



# LUND UNIVERSITY

## Laser Diagnostics Applied to Lean Premixed Swirling Flames - Simultaneous Flow Field and Scalar Measurements

Petersson, Per

2014

[Link to publication](#)

*Citation for published version (APA):*

Petersson, P. (2014). *Laser Diagnostics Applied to Lean Premixed Swirling Flames - Simultaneous Flow Field and Scalar Measurements*. [Doctoral Thesis (compilation), Combustion Physics]. Division of Combustion Physics, Department of Physics, Lund University.

*Total number of authors:*

1

### General rights

Unless other specific re-use rights are stated the following general rights apply:

Copyright and moral rights for the publications made accessible in the public portal are retained by the authors and/or other copyright owners and it is a condition of accessing publications that users recognise and abide by the legal requirements associated with these rights.

- Users may download and print one copy of any publication from the public portal for the purpose of private study or research.
- You may not further distribute the material or use it for any profit-making activity or commercial gain
- You may freely distribute the URL identifying the publication in the public portal

Read more about Creative commons licenses: <https://creativecommons.org/licenses/>

### Take down policy

If you believe that this document breaches copyright please contact us providing details, and we will remove access to the work immediately and investigate your claim.

LUND UNIVERSITY

PO Box 117  
221 00 Lund  
+46 46-222 00 00

# Laser Diagnostics Applied to Lean Premixed Swirling Flames

Simultaneous Flow Field and Scalar Measurements

Doctoral Thesis

Per Petersson

Division of Combustion Physics  
Department of Physics



**LUND**  
UNIVERSITY

© Per Petersson

Printed by Media-Tryck, Lund University  
Lund, Sweden, 2014

Lund Reports on Combustion Physics, LRCP-172

ISBN 978-91-7473-840-7 (Tryck)

ISBN 978-91-7473-841-4 (Pdf)

ISSN 1002-8718

ISRN LUTFD2/TFCP-172

Per Petersson

Division of Combustion Physics Department of  
Physics

Lund University

P.O. Box 118

SE-221 00 Lund, Sweden



# Abstract

The work reported here includes experimental studies of lean premixed swirling flames. Various laser-based optical diagnostic techniques were used to collect information under different operational conditions. Combined flow- and scalar field measurements were performed at high repetition rates for detailed studies of the turbulent flames. The results obtained were used for validation of numerical simulations, carried out by collaborating groups in parallel with the experiments. In a longer perspective the combined work aims at contributing to the development of more efficient, fuel-flexible combustors with reduced levels of emission.

A large part of the work presented concerns experimental studies of lean turbulent premixed flames stabilized by a low-swirl burner. The unconfined flames that were studied were propagating in a divergent flow field and interacted with complex flow structures in the shear layers surrounding them. With the flame lifted above the burner the wrinkling of the flame front, the fuel distribution in the unburnt region and the flow conditions on both sides of the flame front were studied in detail with use of non-intrusive optical diagnostics.

Characterization of the turbulent flow field was carried out primarily by use of Particle Image Velocimetry (PIV), enabling two and three (stereo-PIV) velocity components, respectively, to be assessed in a given plane. Volumetric Velocimetry (3D PIV) was also performed in order to assess the full 3D characteristics of the flow field. In addition, flame-front visualization and fuel distribution measurements were obtained by use of Planar Laser Induced Fluorescence (PLIF). The OH radicals, created in regions in which chemical reactions at high temperature occurred, were used to determine the position, fluctuation, overall shape and wrinkling of the flame front. Simultaneous measurements of the velocity field and of flame location enabled information concerning the flame flow interaction that occurred to be collected. Such combined flow- and scalar field measurements were performed at high repetition rates (several thousand images per second) for detailed studies of the propagation of lean turbulent premixed flames.

The overall aim of the work was to obtain experimental data to assist in the development and validation of Large Eddy Simulations (LES). Today such simulations are able to resolve questions concerning the large scale dynamic behavior of turbulent flames. The close collaboration between experimentalists and modelers was very important in order to obtain a better understanding of the turbulent reacting flows that were investigated and for evaluating the possible strengths and limitations of both the experimental and the numerical techniques involved.

In addition, an investigation of flames close to flashback was carried out in a burner having a variable degree of swirl. PIV and high-speed video of the flame luminosity were used to study the transition to flashback when the degree of swirl was increased.

A demonstration of simultaneous measurements of the flow- and the temperature field was also included. Here, phosphoric particles were used both as flow tracers for PIV and as temperature sensitive particles. The aim was to investigate new measurement techniques that could possibly be used in coming studies to obtain a better understanding of turbulent combustion.

# Populärvetenskaplig sammanfattning

Den värld vi lever i drivs till stora delar av förbränning. Det mesta vi gör kräver energi, elektricitet för matlagning och bensin eller diesel för transporter. Sett över hela världen kommer den största delen av den energi som förbrukas från förbränning. Främst är det fossila bränslen, olja och kol, som används, men en ökande del kommer från förnyelsebara bränslen. Vid förbränning bildas olika miljöfarliga ämnen såsom kväveoxider, svaveloxider, kolmonoxid och oförbrända kolväten. Dessa ämnen kan ge upphov till försurning, smog, och skador på ozonlagret. Vissa ämnen, speciellt koldioxid, bidrar till växthuseffekten som gradvis höjer medeltemperaturen på jorden.

Kväveoxider bildas vid all förbränning i luft vid hög temperatur, oberoende av bränslets kemiska sammansättning. Utsläppen av dessa ämnen kan minskas genom att sänka temperaturen under förbränning. En etablerad metod för att åstadkomma detta är att använda en luft-bränsleblandning med ett stort överskott på luft. Önskvärt är att optimera förbränningsprocessen så att en så låg temperatur som möjligt erhålls, samtidigt som förbränningen hålls stabil. För att studera detta krävs experiment.

I avhandlingen används laserdiagnostik för att studera de kemiska och fysikaliska processer som styr förbränningsprocesser. Laserbaserade mätmetoder stör inte de observerade processerna då inga fysisk mätprober används. Laserljus passerar genom förbränningszonen och mätsignalen samlas in med känsliga kameror. I den mätmetod som främst använts för att karakterisera flödesfält används korta laserpulser som "fotoblixtar". Laserljuset passerar optik som skapar ett tunt laserark som lyser upp den del av flödesfältet som ska studeras. Små partiklar, som blandats in i gasflödet, fungerar som flödesmarkörer. För att hastigheten ska kunna bestämmas tas två bilder med ett avpassat tidsavstånd så att partiklarna hinner flytta sig en kort sträcka. Genom att jämföra partikelmönstret i de två efterföljande bilderna kan medelförflyttningen av partiklar inom små områden beräknas. Genom detta kan hastighetsvektorer beräknas och en ögonblicksbild av hela flödetsfältet byggs upp. I avhandlingen demonstreras även att man med fyra kameror som avbildar en volym med partiklar, upplysta av laserljus, gör det möjligt att ta fram det tre-dimensionella flödesfält. Detta görs i flera steg; först avbildas

partiklarna i volymen från fyra håll, genom informationen i de erhållna bilderna återskapas den avbildade volymen digitalt, sedan kan flyttningen av partiklar inom små områden mellan två efterföljande rekonstruktioner beräknas och hastighetsvektorer presenteras.

För att visualisera flamfronten i de flammor som studerats används också en laserbaserad teknik. Eftersom olika ämnen absorberar olika våglängder kan man välja vilket ämne man vill studera. Ämnet som absorberar laserljusets våglängd exciteras och sänder ut ljus med specifika våglängder som kallad fluorescens. Hydroxylradikaler, OH, bildas i regioner med högtemperaturreaktioner. I de undersökta flammorna kan områden med bränt och obränt separeras genom fördelningen av OH och flamfronten kan definieras av en linje mellan dessa två områden. Genom kombinerade mätningar av flödesfältet och flamfrontens position går det att undersöka hur virvlar som finns i turbulenta flöden påverkar flamfrontens rörelse och karaktär. Speciella laser- och kamera system som kan ta många tusen bilder per sekund krävs för att följa förbränningsförloppet. I Lund har vi haft möjlighet att genomföra sådana tidsupplöst mätningar och skapa filmsekvenser där inverkan av turbulenta virvlar på flamfronters dynamik tydligt kan studeras. Kunskapen om samverkan mellan flödesfält och förbränning är mycket viktigt för att utveckla och förbättra förbränningsapparater för att minska negativ miljö- och klimatpåverkan från förbränning.

Som ett steg att utveckla mätmetoder för mätning av flödesfält samtidigt med skalära storheter genomfördes försök med termografiska fosforer i gasflöden. Dessa fosforer är små temperaturkänsliga partiklar som i de aktuella försöken även fungerade som flödesmarkörer. Försöken visade på goda möjligheter för en fortsatt utvecklingen av tekniken för användning inom förbränningsstudier.

För utveckling av nya brännare används avancerade simuleringsverktyg. Med hjälp av förenklade beskrivningar av de kemiska och fysikaliska processer som sker vid förbränning kan simuleringar allt bättre beräkna förloppet av förbränningsprocesser i industriella brännare. För att detta skall fungera krävs att simuleringar först jämförs mot experimentdata för att kontrollera att modellerna ger rätt resultat. I denna doktorsavhandling har viktiga parameterar för validering av simuleringar samlats in för olika förblandade flammor med hjälp av laserdiagnostik.

# List of Papers

- I. **P. Petersson**, J. Olofsson, C. Brackmann, H. Seyfried, J. Zetterberg, M. Richter, M. Aldén, M. Linne, R.K. Cheng, A. Nauert, D. Geyer, and A. Dreizler, *Simultaneous PIV/OH-PLIF, Rayleigh thermometry/OH-PLIF and stereo PIV measurements in a low-swirl flame*, Applied Optics, 2007. 46(19): p. 3928-3936.
- II. K.J. Nogenmyr, **P. Petersson**, X.S. Bai, A. Nauert, J. Olofsson, C. Brackmann, H. Seyfried, J. Zetterberg, Z.S. Li, M. Richter, A. Dreizler, M. Linne, and M. Aldén, *Large eddy simulation and experiments of stratified lean premixed methane/air turbulent flames*, Proceedings of the Combustion Institute, 2007. 31: p. 1467-1475.
- III. K.J. Nogenmyr, C. Fureby, X.S. Bai, **P. Petersson**, R. Collin, and M. Linne, *Large eddy simulation and laser diagnostic studies on a low swirl stratified premixed flame*, Combustion and Flame, 2009. 156(1): p. 25-36.
- IV. **P. Petersson**, R. Collin, A. Lantz and M. Aldén, *Simultaneous PIV, OH- and fuel-PLIF measurements in a low swirl stratified turbulent lean premixed flame*, 5th European Combustion Meeting, 2011.
- V. K.J. Nogenmyr, **P. Petersson**, X.S. Bai, C. Fureby, R. Collin, A. Lantz, M. Linne, and M. Aldén, *Structure and stabilization mechanism of a stratified premixed low swirl flame*, Proceedings of the Combustion Institute, 2011. 33: p. 1567-1574.
- VI. **P. Petersson**, R. Wellander, J. Olofsson, H. Carlsson, C. Carlsson, B. Beltoft Watz, M. Richter, M. Aldén, L. Fuchs, and X.S. Bai, *Simultaneous high-speed PIV and OH PLIF measurements and modal analysis for investigating flame-flow interaction in a low swirl flame*, 16th Int. Symp. on Applications of Laser Techniques to Fluid Mechanics, Lisbon, (2012).

- VII. **P. Petersson**, M. Gesnik, J. Olofsson, V. Jaunet, M. Aldén, *Volumetric Velocimetry in lifted turbulent premixed low-swirl flames*, 6th European Combustion Meeting, 2013.
- VIII. A. Nauert, **P. Petersson**, M. Linne, and A. Dreizler, *Experimental analysis of flashback in lean premixed swirling flames: conditions close to flashback*, Experiments in Fluids, 2007. 43(1): p. 89-100.
- IX. A. Omrane, **P. Petersson**, M. Aldén, and M. Linne, *Simultaneous 2D flow velocity and gas temperature measurements using thermographic phosphors*, Applied Physics B-Lasers and Optics, 2008. 92(1): p. 99-102.

## Related work

- A. A. Lantz, R. Collin, J. Sjöholm, Z.S. Li, **P. Petersson**, and M. Aldén, *High-Speed Fuel/Hydroxyl Radical Imaging in a Gas Turbine Pilot Burner*, AIAA Journal, 2012. 50(4): p. 971-976.
- B. H. Carlsson, **P. Petersson**, C. Carlsson, R. Wellander, M. Richter, L. Fuchs, X.S. Bai, M. Aldén, *Flame Speed Analysis in a Methane/Air Low Swirl Premixed Flame*, 6th European Combustion Meeting, 2013.
- C. H. Carlsson, E. Nordström, A. Bohlin, **P. Petersson**, Y. Wu, R. Collin, M. Aldén, P.E. Bengtsson, X.S. Bai, *Large Eddy Simulations and Rotational CARS Measurements of a Lean Premixed Low Swirl Stabilized Flame*, submitted to Combustion and Flame.
- D. A. Ehn, J. Zhu, **P. Petersson**, Z. Li, M. Aldén, C. Fureby, T. Hurtig, N. Zettervall, A. Larsson and J. Larfeldt, *Plasma Assisted Combustion: Effects of O<sub>3</sub> on Large Scale Turbulent Combustion Studied with Laser Diagnostics and Large Eddy Simulations*, submitted to Proceedings of the Combustion Institute 2014.

# Contents

Abstract		i
Populärvetenskaplig sammanfattning		iii
List of Papers		v
Related work		vi
Contents		vii
Chapter 1	Introduction	1
1.1	Outline of the thesis	4
Chapter 2	Turbulent Flows	5
2.1	The nature of turbulence	6
2.2	Statistical description of turbulent flows	7
2.3	Scales in turbulent flows	8
2.4	The energy spectrum	10
Chapter 3	Premixed Combustion	13
3.1	Chemistry	13
3.1.1	Reaction Rate	14
3.1.2	Flammability limits	14
3.2	Laminar flame speed and flame thickness	15
3.3	The structure of laminar flames	17
3.4	Regimes in premixed combustion	18
3.5	Turbulent flame speed	22
3.6	Turbulent flame stabilization	23
Chapter 4	Diagnostic Techniques	27
4.1	Particle image velocimetry	28

4.1.1	Basic principles	28
4.1.2	3D PIV - Volumetric Velocimetry	33
4.1.3	Measurement equipment used for PIV	34
4.1.4	Seeding	34
4.2	Laser Doppler anemometry	35
4.3	Chemiluminescence imaging	37
4.4	Laser-induced fluorescence	38
4.4.1	Basic theory of LIF	39
4.5	Phosphor thermometry	41
Chapter 5	Laboratory Burners	43
5.1	The low-swirl burner	43
5.2	Burner with variable degree of swirl	45
Chapter 6	Results - Low-Swirl Lean Premixed Flames	47
6.1	Background	47
6.2	Characteristics of the flow field and the flame	47
6.3	Paper I - Flow- and scalar field measurements	49
6.4	Paper II - LES and experiments	52
6.5	Paper III - Experiments and comparison of two LES models	53
6.6	Paper IV - Simultaneous PIV, OH- and fuel-PLIF measurements	55
6.7	Paper V - LES and Experiments, flame stabilization	57
6.8	Paper VI - Simultaneous high-speed PIV and OH PLIF	57
6.9	Paper VII - Volumetric Velocimetry (3D PIV)	61
Chapter 7	Results - Swirling Flames close to Flashback	65
7.1	Paper VIII - Swirling flames: conditions close to flashback	65
Chapter 8	Results - Flow and Temperature Field Measurements	67
8.1	Paper IX – Flow and temperature field measurements by use of thermographic phosphors	67

Chapter 9	Concluding Remarks	69
	Acknowledgements	71
Appendix	Geometry of the low-swirl burner	73
	References	77
	Contributions to the Papers	83



# Chapter 1 Introduction

The earliest evidence of a regularly used fireplace in an archaeological context dates back one million years. A campfire, famous today, was placed inside the Wonderwerk Cave in South Africa, one of the oldest known locations of human habitation [1]. The control of fire for cooking food, providing light and heat, and stimulating human interactions is believed to be a major turning point in human evolution. Most of the energy we use today for electricity, transportation, propulsion, heating and industrial processing still comes from fire - now in the form of controlled combustion of primarily fossil fuels inside industrial combustion devices. Such devices include internal combustion engines, gas turbines, furnaces and various burners, used in industrial processes. Fossil fuels (coal, oil, gasoline and natural gas) presently contribute to 81% of the world's total energy consumption. Different alternative fuels obtained from biomass and waste, such as biofuels, satisfy some 10% of the world's energy demands. The approximately 9% of the energy needs remaining are met by nuclear and hydropower and by renewable energy sources, such as solar and wind power. The necessary shift from fossil fuels to renewable energy sources has been slow and must also be stimulated by subsidies and by insofar as possible a globally accepted agreement concerning a price on carbon emissions. The use of fossil fuels continues to rise, however, depleting the resources available. Nevertheless, it is estimated that fossil fuels will be a major energy source for several decades to come [2].

Combustion of fossil fuels in furnaces and gas turbines leads to hazardous emissions (e.g. CO, UHC, NO<sub>x</sub>, and particles) and production of greenhouse gases (mainly CO<sub>2</sub>) that result in global heating. Whereas the emission of carbon dioxide CO<sub>2</sub> cannot be avoided during combustion of fuels containing carbon, emissions of other species can be lowered if the combustion process can be optimized and controlled. New combustion strategies are thus continuously being investigated and existing technologies being refined so as to become more efficient and at the same time reduce emissions. In addition, fuel-flexible designs of combustors, able to operate on both conventional fuels and a range of alternative fuels or mixtures thereof are sought. Solutions aimed at reducing CO<sub>2</sub> emissions include switching to more carbon neutral fuels (such as syngas) and hydrogen-rich fuels, strategies that increase the energy conversion efficiency in combustors and also the costly carbon capture and

storage (CCS) strategy. Sadly enough, at the same time, the ongoing process of deforestation reduces the presence of natural CO<sub>2</sub> sinks.

Nitrogen oxides (NO<sub>x</sub>) including NO and NO<sub>2</sub> are involved in the formation of hazardous groundlevel ozone, photochemical smog and acid rain. Fortunately, NO<sub>x</sub> emissions can be reduced by controlled combustion conditions. One established approach to lowering NO<sub>x</sub> emissions involves lowering the temperature by the lean premixing of fuel and air. Different versions of this approach are commonly employed in modern gas turbine combustors and prototypes thereof [3]. However, the lean operation of combustors makes them prone to combustion instabilities and to flame extinction [3]. Also, lowering the production of NO<sub>x</sub> can increase the emissions of CO if the temperature becomes too low. In order to enable lean premixed combustion technology to be developed further, so as to improve flame stability and lower emissions, the understanding of the turbulence-chemistry interaction needs to be improved and to be investigated under different combustion conditions. Part of this work which is called for includes fundamental research carried out under laboratory conditions and in suitable burners. The low-swirl approach, for stabilizing lean premixed flames, initiated in 1995 by R.K Cheng and co-workers has proved useful for such fundamental investigations [4, 5]. A burner of low-swirl design can stabilize very lean flames in a divergent turbulent flow field. There, the flame is lifted above the burner, making the burner under such conditions ideal for detailed optical diagnostics.

Laser-based optical diagnostic methods in particular are used for detailed studies of turbulent flames and flow fields. Lasers diagnostics enable measurements of extremely high temporal resolution to be obtained, important for “freezing” the flow field being investigated, under certain conditions, this can also be true for chemical reactions that are investigated. In general, optical methods are non-intrusive. This is an important feature in collecting information of high validity in combustion environments. Flame temperature and specific species and radicals of very low concentration can be studied with use of lasers and dedicated sensors. Specific short-lived radicals created where chemical reactions occur can be used to visualize the flame location. Measurements can be divided into point measurement, where traversing of the measurement point is required to map a flame region, and field measurement (2D) able in each acquisition to obtain information regarding the region of interest. Point measurements typically provide data of high spatial and temporal resolution, enabling a large statistical data base to be obtained. Examples of these are Coherent anti-Stokes Raman spectroscopy (CARS) for temperature and oxygen concentration and Laser Doppler Anemometry (LDA) for velocity measurements and characterization of turbulence. Field measurement can provide information, for example,

concerning the velocity field as well as flame location and its structural characteristics. Particle Image Velocimetry (PIV) is used for velocity field measurements and can measure two to three (stereo-PIV) velocity components in a given plane. Flame-front visualization and fuel distribution measurements can be achieved by means of Planar Laser Induced Fluorescence (PLIF). Characterization of the structure of turbulent flames can be based on measurements of suitable flame front markers, such as the CH or the OH radical, the aims being to determine the flame front position, fluctuation, overall shape and wrinkling. In particular, simultaneous measurements of the velocity field and of flame location enable information concerning the flame/flow interaction and estimates of the turbulent flame speed to be obtained. Such combined measurements can be performed today at high repetition rates (several thousand images per second) so as to be able to study the propagation of a premixed flame in a turbulent flow field in detail for example. The recent development of volumetric or tomographic, 3D, measurements for obtaining detailed information concerning the gradients of a flow field or for visualizing the flame region within a given volume, enables complicated flow fields and turbulent combustion phenomena to be explored further. Clearly, the rapid advancements made in experimental methods during the past decade have improved the understanding of turbulent combustion processes considerably.

In addition, in connection with experiments, much attention has been paid to the development of simulation tools for assessing turbulent reactive flows to assist in the designing of next-generation combustors. This has generated considerable interest in Large Eddy Simulations (LES) in recent years [6]. LES has proved to perform well in addressing various classes of combustion problems in which difficulties connected with the use of traditional computational fluid dynamics (CFD) approaches have been experienced. Particularly LES has showed improvements in prediction in situations in which there is significant unsteadiness involving large-scale flow-flame interactions, which is the case in most industrial combustors. LES needs to be validated, however, on the basis of experimental results obtained in dedicated laboratory burners to ensure adequate performance and refine combustion models. Non-premixed combustion target flames have been studied extensively within the framework of the Turbulent Non-Premixed Flames (TNF) workshop [7], this making dedicated validation databases available. In connection with lean premixed turbulent combustion, however, comprehensive data sets for use as validation data for LES are sparse. A validation database should include both the initial and boundary conditions and the relevant physical properties of the flames that are investigated, such as information concerning the mean flame front location and flame topology, as well as temperature and species concentrations, and the velocity field. A

sufficient amount of data, spatially covering the entire region of interest needs to be acquired with use of suitable measurement techniques.

In the thesis, various optical diagnostic methods are used for studying turbulent lean premixed flames under different operational conditions. The major aim of the work was to provide experimental data from lean premixed flames to assist in the development and validation of LES. The close collaboration between experimentalists and modelers throughout this study has been very important for providing a better understanding of the turbulent reacting flows that were studied and for evaluating the possible strengths and limitations of both the experimental and the numerical techniques involved. In addition, a proof-of-concept of the combined measurement of the velocity and the temperature field was performed with the aim to investigate new measurement techniques. Here, phosphoric particles were used both as flow tracers in PIV and as temperature sensitive particles. In the last set of measurements carried out, a new insight into turbulent fluid flow was gained through the possibility of performing 3D flow field measurements.

## 1.1 Outline of the thesis

Following on this introduction the thesis starts with a brief account of turbulent flow in Chapter 2 to provide a theoretical basis for an understanding of the sections in Chapter 3 concerning premixed turbulent combustion. In Chapter 4 the main experimental methods used for flow field characterization are presented together with a brief overview of relevant methods for measurements of scalar quantities. In the chapter that follows the laboratory burners used during the work are presented. Selected results from the low-swirl flame study are presented in Chapter 6. The results include the flow field characteristics as obtained from PIV. In addition, results from the first measurements with Volumetric Velocimetry (3D PIV) are presented. Several examples of PLIF measurements concerning the flame front are included to illustrate the flame structure. Also, results of simultaneous measurements of the velocity field, the flame location and the fuel field distribution are presented. In Chapter 7, work carried out to characterize flames close to flashback in a burner with a variable degree of swirl is presented. The investigation of the combined flow field and temperature field measurements using phosphoric particles as both flow tracers in PIV and as temperature sensitive particles provided a demonstration of the concept as presented in Chapter 8. A brief summary of the work reported on followed by a discussion of future work are provided in Chapter 9, which ends the presentation. The papers included in the thesis are attached at the end.

# Chapter 2      Turbulent Flows

“Ladies and gentlemen, we are experiencing some turbulence. Please return to your seats and fasten your seatbelts.” Most of us have heard this message when traveling in an aircraft, nervous fliers fearing it and thinking of turbulence as a dangerous menace. A turbulent flow is composed mainly of complex flow structures of different sizes moving in a chaotic manner in all directions. An airplane flying through a turbulent wind streak thus shakes. Besides causing *shaking* to occur, turbulence can also result in *mixing*, this feature of turbulent flows being frequently used in practical industrial applications to enhance exchange between fluids and increase the interaction between a fluid and the surfaces involved. The mixer found in most kitchens is an example of a common device in which turbulence is utilized. The rotating impeller sets the fluids to be mixed in motion – an overall blending of the entire contents, together with local, small scale and intense mixing close to the impeller, takes place. The different scales of the structures in the flow field cooperate, thus refining the mixing stepwise until a homogenous mixture is obtained.

In combustion applications generally, many different properties of turbulence can be exploited. In *non-premixed combustion*, the fuel and the oxidizer are initially separate, the reactions that occur being unable to proceed faster than the supply of completely mixed fuel and oxidizer permits. One can readily understand that under such conditions the mixing required to sustain the reactions can be significantly enhanced by turbulence. In *premixed combustion*, on the other hand, the fuel and the oxidizer are already mixed and prepared for “reaction” from the start - so that one can wonder what use further turbulent mixing can have. In fact, under these conditions turbulent structures can wrinkle the reaction surface, i.e. the flame front, and thus increase the fuel consuming area of the flame. With increasing intensity, turbulence can also enhance the mixing of reactants with the hot products, this stimulating the reactions underway increasing the fuel conversion rate and supporting flame stabilization. These features are utilized in gas turbines, in which the high mass throughputs that a high power density requires create a highly turbulent combustion environment. Further details regarding the effects turbulence has on premixed flames are found in Chapter 3.

## 2.1 The nature of turbulence

In 1883, Osborne Reynolds showed for the first time that the distinction between *regular* (laminar) and *eddy motion* (the latter today termed turbulent flow) depends upon the relationship between the dimensions of space and velocity. This dimensionless relationship is the Reynolds number:

$$Re = \frac{UL}{\nu} \quad (2.1)$$

where  $U$  is a characteristic velocity,  $L$  a characteristic length scale (e.g. the diameter of a nozzle or of a combustion chamber) and  $\nu$  the fluid kinematic viscosity. The Reynolds number describes the ratio of inertial (convective) to viscous forces. The viscous forces act at the molecular level and dissipate kinetic energy in the flow - their damping motion unsteadiness. At a level above a certain critical Reynolds number, the inertial forces exceed the viscous forces, so that a small disturbance occurring in an initially laminar flow is not damped, but increases and spreads resulting in the flow becoming turbulent. The level at which the transition to turbulent flow occurs depends upon the specific system and the experimental conditions involved. For pipe flows, the flow typically remains laminar at a level below  $Re < 2000$  and is turbulent at  $Re > 4000$ , somewhere between these two points there being a transition region in which the flow can be either laminar or turbulent.

In addition to the requirement of the Reynolds number being sufficiently large, there are several other qualitative characteristics of turbulent flows that are usually listed, by Tennekes and Lumley (1972) [8], for example, several of these features being the following:

- Turbulent flows are irregular, showing a random behavior in terms of space and time
- The irregularity is produced by characteristic fluctuating three-dimensional vortices or eddies.
- The different sizes and velocities of the eddies results in a continuous spectrum of time and length scales, as well as in an
- Enhanced transfer of mass, momentum and heat, and in a
- High level of dissipation, a continuous feed of kinetic energy being required to sustain the turbulence.

The understanding of turbulent flows has benefited very much from advances made in experimental measurement techniques and Direct Numerical Simulations (DNS). With use of state-of-the art tools, analysis of the 3D

velocity field over the entire spectrum of the involved scales in small domains at moderate Reynolds numbers is becoming a reality. However, turbulent flows are still commonly characterized by use of statistical methods.

## 2.2 Statistical description of turbulent flows

As briefly outlined above, turbulent flows are complex, there thus being no precise description or exact mathematical definition of them. The complexity is connected with the wide range of scales involved, and the random fluctuations occurring on all of them. However, in stationary processes statistical tools can be employed to operationally quantify and compare important properties of turbulent flows. An example of a time trace of a particular velocity component within a turbulent flow field is shown in Figure 2.1.

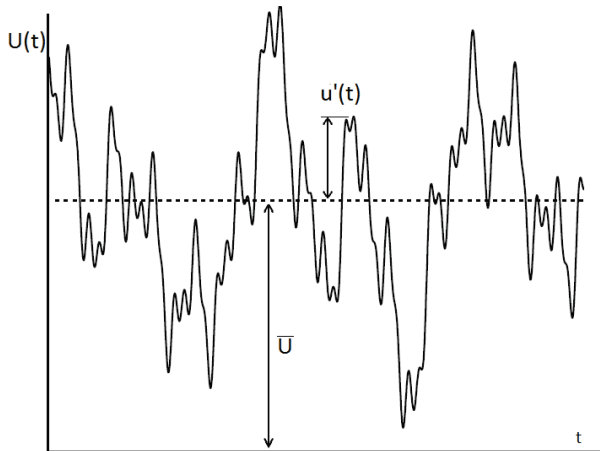


Figure 2.1 The fluctuation occurring over time around the mean level of  $U$ , a particular velocity component in a turbulent flow field.

As indicated in Figure 2.1, the quantity  $U$  can be decomposed into a mean  $\bar{U}$  and a fluctuating part  $u'(t)$ :

$$U(t) = \bar{U} + u'(t) \quad (2.2)$$

$$\bar{U} = \frac{1}{N} \sum_i^N U(t), \quad \frac{1}{N} \sum_i^N u'(t) = 0 \quad (2.3)$$

Here  $\bar{U}$  is the statistical mean obtained by averaging a given number  $N$  of samples (e.g. measured values). In practice, a time average is also frequently employed. The ergodic hypothesis states that if the flow is statistically steady and the averages converge properly the two averages are equivalent.

The standard deviation, representing the root-mean-square of  $u'(t)$ , also termed the RMS value, is used to represent and quantify the turbulent fluctuations:

$$u_{rms} = \left[ \frac{1}{N-1} \sum_i^N (u'(t))^2 \right]^{1/2} \quad (2.4)$$

The RMS value can be interpreted being the contribution of the fluctuations in velocity to the specific turbulent kinetic energy  $k$ . The kinetic energy in a turbulent flow field can be calculated on the basis of information concerning the fluctuations in velocity in the three directions,  $(u_{rms}, v_{rms}, w_{rms})$ :

$$k = \frac{1}{2} (u_{rms}^2 + v_{rms}^2 + w_{rms}^2) \quad (2.5)$$

Probability density functions are used to describe fully the distributions around the mean of any random (turbulent) quantity see e.g. [9].

## 2.3 Scales in turbulent flows

As described briefly above, fluid motion at a sufficiently high Reynolds number can be characterized by a system of unsteady structures or eddies spread over a large range of different sizes (scales). The largest eddies; created by strong mean shear, contain most of the turbulent kinetic energy in the system. The size of these large structures is determined by the dimensions of the flow device, such as the diameter of a pipe. Due to their large size, the damping by viscous forces that occurs is negligible, most of the kinetic energy being transferred to scales of smaller size. The energy transfer is accomplished by the dynamic stretching of the large scales involved, their breaking up so as to produce smaller eddies. This process continues all the way down to the smallest scales, where the kinetic energy is finally dissipated into heat through the effect of molecular viscosity. This transfer of kinetic energy in the so called energy cascade was introduced by Richardson (1922) [10]; see Figure 2.2.

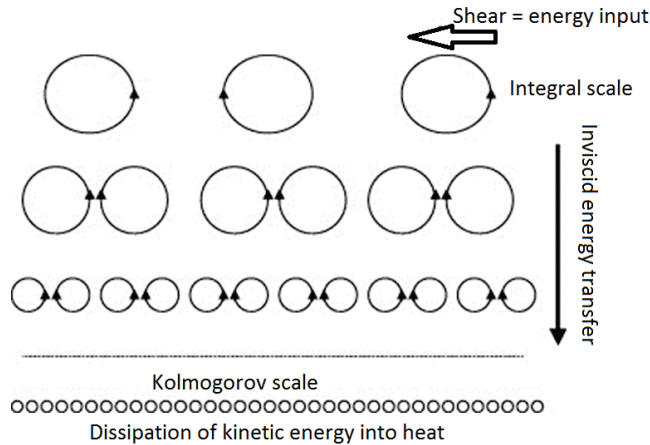


Figure 2.2 A schematic representation of the Richardson energy cascade.

Three typical length scales - the integral, the Taylor and the Kolmogorov scales - are generally used to describe the structure of a turbulent flow.

**Integral scales:** The integral length scale,  $l_0$ , relates to the largest eddies in the flow field and is limited by the physical boundaries of the flow only. It is the kinetic energy at these scales that feeds the cascade. An integral time scale,  $t_0$ , and a velocity scale,  $u_0=l_0/t_0$ , can also be defined. A dedicated Reynolds number based on these scales can be used to characterize the turbulence:

$$Re_t = \frac{u_0 l_0}{\nu} \quad (2.6)$$

The integral time scale is an important parameter for determining a sufficiently long sampling time for performing measurements in turbulent flows (and the computational time in LES). Typically, the sampling time should be at least one magnitude larger than  $t_0$  to ensure that the average values converge.

**Taylor micro-length scale  $\lambda$ :** This scale does not have the same clear physical interpretation as the integral scale but is often referred to as the average dimension of the smallest eddies [11]. It is eddies larger than this scale that carry the major portion of the turbulent kinetic energy in the flow. The Taylor scale can thus be a useful measure of the degree of spatial resolution in experiments which is desired, to ensure that the most important energetic structures of the flow field are resolved. This scale is also relevant for selecting an optimal filter width in simulations capable of resolving the energetic

portion of the flow structures (e.g. LES), see the energy spectrum in the next section.

**Kolmogorov scales:** Kolmogorov [12] developed the cascade theory further and introduced expressions for the scales of the smallest type of eddy in the cascade. The Kolmogorov length ( $\eta$ ), the time ( $t_\eta$ ) and the velocity scale ( $u_\eta$ ) are expressed by

$$\eta \equiv \left(\frac{\nu^3}{\epsilon}\right)^{\frac{1}{4}}, \quad t_\eta \equiv \left(\frac{\nu}{\epsilon}\right)^{\frac{1}{2}}, \quad u_\eta \equiv \frac{\eta}{t_\eta} = (\nu\epsilon)^{\frac{1}{4}} \quad (2.7)$$

where  $\nu$  is the fluid viscosity and  $\epsilon$  is the rate at which turbulent kinetic energy is transferred in the cascade.

At the end of the energy cascade the inertial forces are balanced by viscous forces. This and the fact that the size of the smallest scales is independent of the geometrical dimension and size of the largest eddies implies there to be a universal behavior of the smallest scales. Assuming there to be a balance between the production of turbulent kinetic energy (measured on the integral scale) and the dissipation (measured on the Kolmogorov scale) enables relations between the integral and the Kolmogorov scales to be derived:

$$\frac{\eta}{l_0} \sim Re^{-\frac{3}{4}}, \quad \frac{t_\eta}{\tau_0} \sim Re^{-\frac{1}{2}} \quad (2.8)$$

From this one can see that the Kolmogorov length decreases with an increasing Reynolds number. Accordingly, issues related to spatial averaging both in experiments and simulations become increasingly important as the Reynolds number increases.

## 2.4 The energy spectrum

The energy spectrum of the turbulence is used to describe the distribution of the turbulent kinetic energy among the eddies in a turbulent flow. The energy spectrum in Figure 2.3 shows the energy density as a function of wave number. The size of a scale is inversely proportional to the wavenumber in question; the previously defined integral-, Taylor- and Kolmogorov scales are marked in Figure 2.3. Three distinct ranges can be defined: that of the integral scales, together with the inertial subrange and the viscous- or dissipative subrange. It is at the largest scales where energy is fed into the system, the

major part of the energy being found in the integral scales. The energy is transferred then into smaller and smaller eddies. As can be seen from the spectrum, the energy density (energy content per unit wavenumber) decreases with the wavenumber. At the smallest scales, the Kolmogorov scales, all of the kinetic energy is finally dissipated into heat.

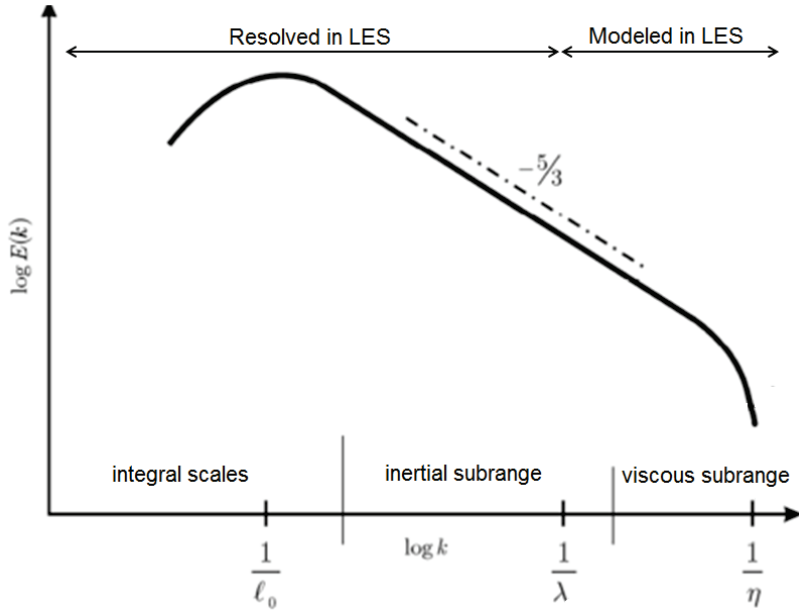


Figure 2.3 The energy spectrum of turbulence.

For a sufficiently large  $Re$ , a range is found in which turbulent kinetic energy is neither produced nor destroyed. This range, termed the inertial subrange, is characterized by negligible energy content and a constant energy density decay,  $k^{-5/3}$ . At large wavenumber the energy density drops quickly. This can be explained physically by the presence of very small eddies and the very large velocity gradients related to these eddies [13]. Under such conditions, fluid viscosity is a significant factor in dissipating the energy through friction (the friction being proportional to the viscosity and to the velocity gradients).

One can estimate the size of the scales that need to be resolved in measurements and simulations on the basis of the spectrum properties involved. It is the energetic scales that need to be resolved in LES, whereas the smaller scales of limited energy content can be modeled. Typically the Taylor scale (within the inertial subrange) serves as a limit for the filter width in LES.



# Chapter 3 Premixed Combustion

Combustion is truly a multi-disciplinary field of science, involving the areas of chemical kinetics, fluid dynamics and thermodynamics. In the present chapter only a limited portion of the theory pertaining to the main topic dealt with in the thesis – premixed combustion – is presented. Further portions of the theory, related to turbulent flow, are found in Chapter 2.

Combustion can be classified as being either premixed or non-premixed, depending upon whether the reactants are mixed or are separated from one another before entering the reaction zone. In the non-premixed case, the fuel and the oxidizer are initially separated from one another and need to be mixed at a molecular level before combustion can take place. The yellow flames of a candle light and those around a fuel droplet in a diesel engine are both examples of non-premixed combustion. In premixed combustion, the reactants are mixed before entering the reaction zone. The blue flame above a Bunsen burner and the combustion occurring in gasoline-fueled internal combustion engines are examples of premixed combustion. The thesis concerns only premixed combustion and the present section provides a brief overview of the basic theory involved.

## 3.1 Chemistry

In the thesis, premixed methane-air flames are investigated. Although methane is the very simplest hydrocarbon fuel, it can be regarded as a model fuel nevertheless, since it is the main component of natural gas, which is widely used in gas turbines. The ideal complete combustion of methane in air (oxygen serving as the oxidizer) under stoichiometric conditions can be expressed in terms of a single-step reaction path:



This reaction path provides a very simplified, or *global*, description of the overall oxidation of methane, it is simply identifying the (ideal) initial and final state, of the process, ignoring the details of what occurs from the initial to

the final state, but it can be used for simple analyses, such as in calculating the heat release obtained. A detailed description of the elementary reactions involved in the oxidation of methane and the formation of reaction products requires hundreds of steps and can include a large number of short-lived chemical species and radicals. Detailed kinetics mechanisms are typically required for an adequate prediction of complex combustion behavior, including ignition, flame propagation and the formation of pollutants such as  $\text{NO}_x$ ,  $\text{CO}$ , unburned hydrocarbons and soot. In three-dimensional simulations, detailed mechanisms become too expensive, in terms of the computations that would be required. The study of simpler reduced mechanisms thus being called for. The reduced reaction mechanisms are ones developed through making systematic approximations of the detailed mechanisms involved.

### 3.1.1 Reaction Rate

An important task of chemical kinetics in the present case is to determine the rate of chemical reactions that takes place. For the one-step reaction describing the oxidation of the fuel  $F$  by the oxidizer  $O$ ,  $F + O \rightarrow P$ , ( $P$  denotes the products) the reaction rate can be expressed by:

$$\frac{-d[F]}{dt} = AT^n \exp\left[-\frac{E_a}{R_u T}\right] [F]^a [O]^b \quad (3.2)$$

where  $A$ ,  $n$ ,  $E_a$  (the activation energy),  $a$ , and  $b$  being parameters obtained from experiments.  $T$  is the temperature (in kelvin) and  $R_u$  is the Universal gas constant. The mole concentration of fuel and oxidizer is  $[F]$  and  $[O]$  respectively. The reaction rate is highly dependent on temperature. Due to this dependence the reaction rate can also be very sensitive to equivalence ratio as it influences the flame temperature.

### 3.1.2 Flammability limits

For a mixture to burn, it must be within specific flammability limits. Flammability is defined as the ability of an ignited mixture to enable flame propagation to take place without further addition of heat. When the composition of the mixture is such that at the completion of the combustion there is ideally no fuel or oxidizer left, carbon dioxide and water being the only products, the mixture is said to be under stoichiometric conditions. Normalizing the fuel-to-oxidizer mass fraction (or mole fraction) involved by the stoichiometric fuel-to-oxidizer mass fraction (or mole fraction) gives the equivalence ratio,  $\phi$ :

$$\phi = \frac{Y_{fuel}/Y_{oxidizer}}{(Y_{fuel}/Y_{oxidizer})_{stoichiometric}} \quad (3.3)$$

where  $Y$  denotes the mass fraction.

If the equivalence ratio  $\phi < 1$ , there is a deficit of fuel, the mixture being termed lean. When there is an excess of fuel as compared with the amount of oxidizer present, the mixture is said to be rich,  $\phi > 1$ . The maximum adiabatic flame temperature for hydrocarbon/air mixtures is reached under close to stoichiometric conditions, the peak there being slightly rich-shifted due to the product dissociation being greater on the lean side, so that the amount of heat release on the lean side is reduced [14]. With an increase in the amount of air (lean conditions) or of fuel (rich conditions), the flame temperature is lowered in relation to the maximum adiabatic temperature, this serving to reduce the formation of thermal NO<sub>x</sub>. Flammability limits are a function of temperature and of pressure, at atmospheric pressure and 25°C most hydrocarbon-air mixtures being flammable in the range of about  $0.6 < \phi < 1.4$ . In what are termed stratified flames the equivalence ratio can change over time and space such as through entrainment of air in an initially well-defined fuel stream. The unconfined low-swirl flames studied in the thesis are stratified due to the entrainment of ambient air; see Papers II and IV, for example.

### 3.2 Laminar flame speed and flame thickness

A characteristic property of premixed flames is the fact that in these the flame front propagates relative to the premixed gas. This distinguishes flames of this sort from non-premixed flames, as these are restricted to follow along the contour of stoichiometric composition determined by the local mixing. A consequence of the property of premixed flames described above is that potentially dangerous flashbacks into e.g. the mixing tube in which the premixing took place can occur under certain conditions. A simple experiment can be performed in which a long tube is filled with a flammable mixture and closed at both ends. When both end covers are quickly removed and the mixture at one end is ignited a planar flame front propagates towards the unburned side, as shown in Figure 3.1. At the walls of the tube the flame is normally extinguished, quenched, through losses of heat. If the mixture is perfectly at rest prior to ignition, the front travels through the unburnt mixture at a constant speed. This propagation speed in relation to the unburned gas is termed the laminar flame speed ( $S_L$ ). For hydrocarbon-air

mixtures,  $S_L$  is low, about 0.4 - 0.6 m/s under stoichiometric conditions. The laminar flame speed depends on fluid properties, the type of fuel involved, its concentration, temperature and pressure and the oxidizer employed [13].

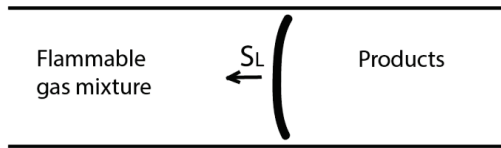


Figure 3.1 Example of a premixed flame propagating in a tube, with a constant cross-sectional area, filled with a flammable gas mixture.

If one instead uses a slightly conical tube and lets a flammable premixed gas flow through it in the direction of increasing cross-sectional area, the concept of the stabilization of freely propagating flames can be introduced. If the mixture is ignited at the end of the tube where the velocity is lowest (i.e. with the largest cross-sectional area), a laminar flame front can propagate upstream as long as the mixtures burning velocity  $S_L$  exceeds the velocity of the gas flow. Since the increase in the cross-sectional area in the downstream direction results in a decrease in flow rate a section can be found in which  $S_L$  is equal and is opposite in sign to that of the gas flow, the propagating laminar flame front being said to be *stabilized* there, see Figure 3.2. A slight increase in the mass flow rate would lead to the flame moving downstream, where the cross-sectional area is larger, to a point at which the local flow rate again matches  $S_L$ . Similarly, if a slight increase in the burning velocity of the mixture occurs (e.g. through an increase in the equivalence ratio or in the temperature of the mixture) the flame moves upstream to a new position in order to compensate for this change.

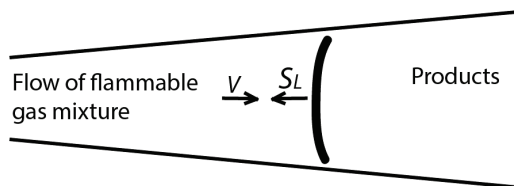


Figure 3.2 Illustration of a laminar premixed flame stabilized at a location at which the laminar flame speed is equal and opposite in sign to that of the approaching premixed gas flow.

Not only the flame speed ( $S_L$ ) but also the flame thickness,  $l_f$ , is important for classifying laminar premixed flames. Several methods of estimating the flame

thickness are described in the literature. One method is based on the thermal diffusivity,  $D$ , and the laminar flame speed. A relevant time scale for the flame,  $t_F$ , can be defined by considering the time required for the flame to propagate a distance equal to the thickness of the flame.

$$l_f = \frac{D}{s_L}, \quad t_F = \frac{l_F}{s_L} = \frac{D}{s_L^2} \quad (3.4)$$

### 3.3 The structure of laminar flames

In Figure 3.3 the schematic one-dimensional structure of a premixed methane flame front is plotted in relation to the flame coordinate. The development of the temperature profile can be followed across the front, together with the changing concentrations of reactants, products and generic intermediates (short-lived radicals formed through exothermic reactions). Four different layers or zones can be identified: the preheat zone, the inner layer, the oxidation layer and the post-flame zone [15]. In the preheat zone it is mainly the diffusion of heat and mass from the reactions in the inner layer that gradually changes the temperature and the concentrations of the fresh mixture. The overall temperature increase in the preheat zone is slight and chemical reactions are limited. By definition, it is first at the entrance to the inner layer that the *cross-over* temperature (around 1000 K) is reached and that self-sustained chemical reactions can occur. The fuel and the oxidizer are quickly consumed in the inner layer, most of the heat being released then, resulting in a steep temperature increase. Intermediate species, CO and other radicals (CH, CH<sub>2</sub>O, OH etc.), reach peak concentrations in the inner layer. Some of these intermediates are possible to use as flame-front markers in laser diagnostics, see Chapter 4. Most of the intermediates are rapidly oxidized in the oxidation layer, the product species approaching steady state. The temperature reaches its maximum value and the profile flattens out then, since most of the chemical reactions reach equilibrium in the post-flame zone. Due to the high temperature, certain reactions still occur, some of them related to undesired or harmful pollutants such as the formation of NO<sub>x</sub>, whereas other reactions concern the oxidation of radicals such as OH, which peaks in the oxidation layer. In practical applications the residence time in the high temperature post-flame zone is an important factor in controlling the formation of harmful pollutants and ensuring a complete combustion of CO and of possible unburnt hydrocarbons (UHC).

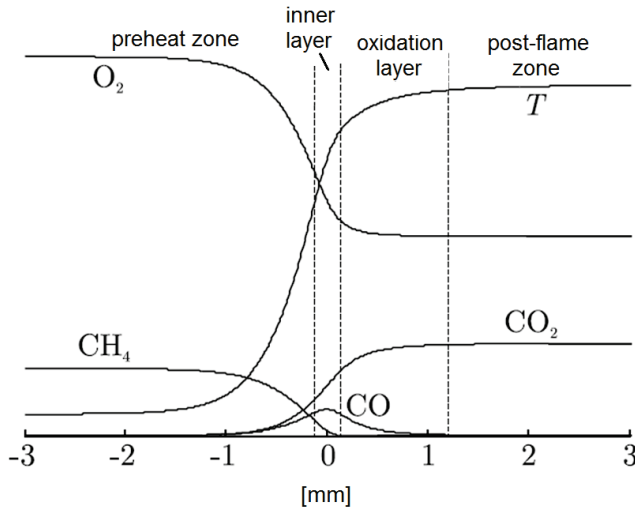


Figure 3.3 The detailed structure of a laminar freely propagating planar premixed flame.

### 3.4 Regimes in premixed combustion

In the previous section, laminar premixed flames were characterized by the laminar flame speed,  $S_L$ . In addition, two flame length scales were defined: the laminar flame thickness,  $l_f$ , (order of 1 mm), and the much thinner inner-layer,  $l_\delta$ , (order of 0.1 mm). A relevant time scale for the flame can also be obtained by dividing the flame thickness by the flame speed. As will be seen below, these well-defined laminar properties are also used in the classification of turbulent flames. However, turbulent premixed flames are more difficult to characterize than their laminar counterparts. The complexity involved is connected in part with the large variety of turbulent scales - eddies of different sizes and velocities - that can affect the flame in various ways. The effects can be purely kinematic, such as in the mild wrinkling of a flame by large eddies. The turbulence can also affect the reaction rates directly. This requires the presence of small eddies that can increase the mixing within the flame itself. If the turbulence is too intense, the flame fronts can break, resulting in local extinction.

Thus, the characteristics of the turbulent flow field (the scales and the intensities involved) are physical quantities of relevance in describing the turbulent flame behavior. The large scales relating to turbulence are characterized by the turbulent integral length scale,  $l_0$ , and the turbulence intensity by the large scale fluctuation  $u_0$ . At the other end of the spectrum,

the Kolmogorov scales are used to characterize the smallest scales. In the Borghi diagram shown in Figure 3.4, premixed flames are categorized in terms of length-scale ( $l_0/l_F$ ) and velocity-scale ( $u_0/S_L$ ) ratios [13]. Three non-dimensional numbers are used in discussing the different regimes and to describing the competition between the chemical reactions and the fluid-dynamical processes involved. For convenience sake these numbers are expressed in the regime diagram in terms of the coordinates that are applicable, and when relevant in terms of the smallest scales of turbulence (Kolmogorov scales) and of the flame (e.g. the inner-layer thickness). Only the order of magnitude is important here, several approximations being used to simplify the analysis, equal diffusivity of mass and momentum is assumed ( $Sc = \nu/D = 1$ ), for example.

The turbulent Reynolds number, introduced in Equation (2.6), used to characterize the large scale of turbulence, can here be written

$$Re_t = \frac{u_0 l_0}{\nu} = \frac{u_0 l_0}{S_L l_F} \quad (3.5)$$

The *Damköhler number*,  $Da$ , is the ratio of the characteristic time scale of the turbulence, as based on the integral length scale, to the characteristic time scale of the flame. For  $Da > 1$  the chemical reactions are fast and the reaction zone thin so that the front can be regarded as a discontinuity separating the burnt from the unburnt.

$$Da = \frac{t_0}{t_F} = \frac{S_L l_0}{l_F u_0} \quad (3.6)$$

The *Karlovitz number*,  $Ka$ , compares the flame time scales with the smallest scales of turbulence, the Kolmogorov time scales. It can be written as

$$Ka = \frac{t_F}{t_\eta} = \frac{l_F^2}{\eta^2} \quad (3.7)$$

In Equation (3.7),  $Ka$  also relates the laminar flame thickness to the smallest flow scales, represented by the Kolmogorov scale. From this one can determine whether or not the turbulence affects the transport mechanisms within the flame. To characterize the interaction of the smallest turbulence scales with the thin layer in which the main reactions takes place, a second Karlovitz number based on the characteristics of the inner-layer is employed. The inner-layer typically has a thickness one-tenth that of the flame thickness, the following relationship is applying:

$$Ka_\delta = \frac{l_\delta^2}{\eta^2} = \frac{1}{100} Ka \quad (3.8)$$

Thus for  $Ka > 100$  ( $Ka_\delta > 1$ ), turbulence can distort the inner layer. With the range of  $1 < Ka < 100$ , turbulence can only affect the preheat layer.

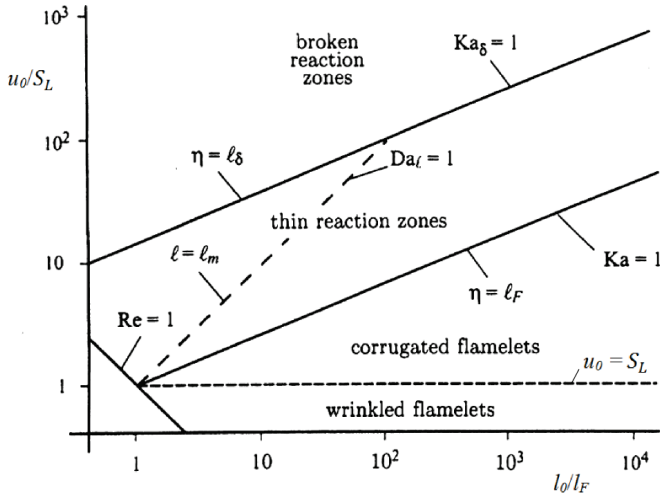


Figure 3.4 The Borghi diagram showing the different combustion regimes applying to premixed flames [13].

In the version of the Borghi diagram used here, five different regimes can be seen, one of them for the laminar case ( $Re_t < 1$ ) and the other four for turbulent premixed flames ( $Re_t > 1$ ). The turbulent regimes are separated by primarily three straight lines:  $Ka = 1$ ,  $Ka_\delta = 1$  and  $u_0 = S_L$ . A brief description of the turbulent flame regimes follows.

#### Turbulence wrinkles and strains the flame without modifying its structure:

**$Ka < 1$ .** The smallest turbulent structures are larger than the thickness of the laminar flame. The flame can be seen as embedded in Kolmogorov eddies. Since the flow inside these smallest eddies is by definition laminar, it cannot disturb the local laminar-like flame structure directly. Two *flamelet* sub-regimes exist:

$u_0 < S_L$ : **Wrinkled flame regime**, the turbulence intensity here being weak, even the large eddies being able to compete with the flame propagation. Turbulence here can thus only wrinkle the flame, no flame front corrugations occurring. For a wrinkled flame, the main contribution to the increase in

flame speed there in comparison to the laminar case is proportional in size to the increase in effective flame area.

$u_0 > S_L$ : **Corrugated flame regime**, the turbulence here being sufficiently strong to corrugate the flame front, i.e. to form multiple connected reaction sheets. The formation of pockets of burnt and fresh gas is also possible, due to the merging of neighboring fronts in the corrugated structure. Because of the straining induced by the turbulent fluctuations, the inner structure and the local flame speed can differ slightly from that of a purely laminar flame [16].

Turbulence modifies the flame structure:

$1 < Ka < 100$ , ( $Ka_\delta < 1$ ). **Thin reaction zones regime**, the smallest turbulent structures here being smaller in size than the laminar flame thickness, vortices being able to mix and thus thicken the preheat zone but being unable to modify the inner-layer, which retains a *thin* laminar structure. The increased heat and mass transfer within the preheat zone can increase the flame speed.

$Ka > 100$ , ( $Ka_\delta > 1$ ). **Broken reaction zones regime**, in which turbulent eddies are smaller in size than the thickness of the inner-layer and the entire flame structure can be modified. Eddies that survive inside the inner (fuel-consumption) layer can perturb the chemical reactions directly by increasing the heat and mass transport. If the turbulent mixing becomes extensive, the flame front can *break*, so that local extinction occurs. The turbulence interaction can become so intense that finally flame structures can no longer be identified, the term *well-stirred reactor* being used to describe the combustion that occurs.

In engineering applications, strongly turbulent flows are utilized to increase considerably the energy released per unit volume. The corrugated flame regime, the thin reaction zones regime, and the broken reaction zones regime thus all of practical importance. The wrinkled flame regime is often encountered in fundamental studies of flame flow interaction in laboratory flames.

In the wrinkled and corrugated flame regimes, where the turbulence not directly does interfere with the internal flame structure turbulent flames can be described with use what is termed the *flamelet concept* [17, 18]. Here the structure of turbulent flames can be simplified by regarding them as laminar flamelets embedded in a turbulent flow. The flamelets can be wrinkled or corrugated but still retain their laminar flame-front properties, in which there is a thin reaction layer that separates distinctly reactants from the burnt gases.

Accordingly, laminar flame properties can be used to describe the chemical kinetics involved. The flamelet concept has also been extended on the basis of experimental observations to encompass the thin reaction zones regime, in low-swirl flames for example [19]. The flamelet approach is attractive for modeling turbulent premixed combustion, since laminar flame properties that have been tabulated can be used in a simulation then, rather than performing costly calculations.

In analyzing real flames, it is important to realize that the turbulence quantities, and hence most of the non-dimensional numbers used to characterize flames are fluctuating quantities that can change markedly over space and time.

### 3.5 Turbulent flame speed

It is clear, on the basis both of the flame structure and of the flame dynamics in the different turbulent premixed combustion regimes, that the propagation speed of the mean turbulent flame front there differs clearly from the laminar case. The concept of turbulent flame speed is used to quantify the propagation of a turbulent flame front. Different mechanisms that affect the propagation speed, these being based on the flame-flow interaction were briefly introduced above, such as an increase in the effective flame area, and straining of the flame (due to wrinkling) and an increased (turbulent) diffusion within the flame.

In the wrinkled and corrugated flame regimes the effects of turbulence are attributed mainly to the wrinkling and stretching of the flame front. The resulting change in effective flame area as compared to the laminar case ( $A_T/A_L$ ) results in a corresponding increase in the mean propagation speed ( $S_T$ ) of the turbulent flame:

$$\frac{S_T}{S_L} = \frac{A_T}{A_L} \quad (3.9)$$

*Damköhler* [20] suggested there to be an increase in laminar flame speed of the turbulence intensity ahead of the flame front:

$$S_T = S_L + u' , \quad \frac{S_T}{S_L} = 1 + \frac{u'}{S_L} \quad (3.10)$$

For a regime in which turbulence affects the transport properties within the preheat layer, *Damköhler* suggested that:

$$\frac{S_T}{S_L} = 1 + C \left( \frac{u'}{S_L} \right)^n \quad (3.11)$$

where  $C$  and  $n$  are coefficients sought by experimental and numerical investigations. However, with the increased understanding of turbulent flame propagation, studied under various conditions, the turbulent flame speed is found to be a function of a larger number of parameters than originally proposed by Damköhler. A few significant parameters are geometry of the burner, stabilization method, Reynolds number, flame stretch and diffusivity [18, 21].

### 3.6 Turbulent flame stabilization

As shown above, a laminar flame can be stabilized in a region in which the flame speed matches the flow velocity. For a turbulent flame, it is the local turbulent flame speed that needs to be considered, in particular, this being a property which can be dependent upon such factors as the fuel mixture, temperature, and the flow field characteristics, which thus also can change both over time and in regard to the location within a combustor. In addition, the combustion of lean-premixed fuel, utilized to reduce emissions, is more sensitive to flow fluctuations than are flames under close to stoichiometric conditions. Therefore, the stabilization mechanisms utilized in turbulent combustion need to be robust and to be optimized insofar as possible for the application at hand. With the high mass-flow rates needed to reach a desired output in a gas turbine, flame stabilization is commonly achieved by creating regions of recirculating flow. Recirculation zones can be produced by introducing a bluff body in the flow or by an abrupt expansion of the combustion chamber for example [22]. One possible drawback of such an approach is that the thermal load on the material reduces the lifetime of the device.

A more refined way of creating a recirculation zone is to do so by aerodynamic means [3, 23]. Through imparting swirl to the inflow into the combustion chamber a central region of low pressure, termed the vortex core can be created. At some distance from the inlet, through radial expansion of the flow, produced by the swirl and by the geometry of the chamber, the pressure in the center gradually increases. If the swirl is sufficiently strong, the adverse pressure gradient can overcome the axial momentum involved, a reverse flow being established along the center axis, resulting in what is termed *vortex breakdown*. A central recirculation zone is thus created (Figure 3.5 a) in which

hot combustion products are trapped and constantly mix with and ignite the fresh mixture to ensure stabilization of the flame [3]. A calculated drawback is that the recirculation increases the retention time of the combustion products in regions of high temperature, this often being accompanied by an increase in  $\text{NO}_x$  formation.

In some applications or combustion devices, flames can be stabilized aerodynamically without the need of a recirculating flow. In the low-swirl burner as it is called [4, 5], the swirl is limited but is sufficient nevertheless to create a diverging flow field, Figure 3.5 b. In the central divergence zone (CDZ) the axial velocity is decelerated and at sufficiently high Reynolds number the flame can find a position enabling the propagation speed of the flame to balance the flow velocity [20]. In the downstream direction, the flow approaches stagnation and a weak recirculation can occur, its strength depending upon the burner configuration and combustion conditions present. A version of the low-swirl burner was used in the thesis and under the operational conditions used it was found that dynamics in the shear layer surrounding the CDZ were important for the flame dynamic and the flame stabilization, see Papers V and VI.

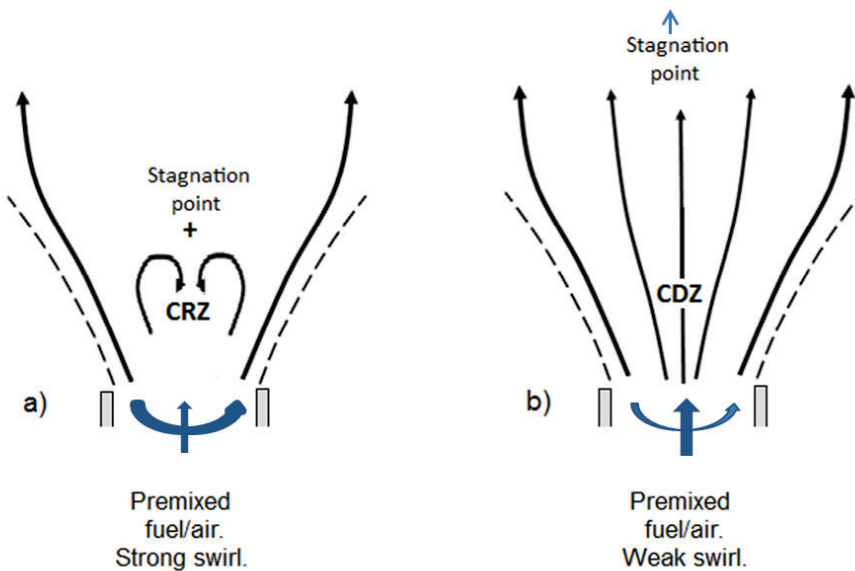


Figure 3.5 A swirling flow with a) a strong swirl (CRZ = central recirculation zone) and b) a low- to moderate swirl (CDZ = central divergence zone). The broken line indicates the outer shear layer towards the ambient.

The degree of swirl can be quantified by comparing the axial flux of the swirl momentum ( $G_\theta$ ) with the axial flux of the axial momentum ( $G_x$ ) in a non-dimensional swirl number [23, 24]:

$$S = \frac{G_\theta}{R G_x} = \frac{\iint_A U_x U_\theta r dA}{R \iint_A (U_x^2 - \frac{p}{\rho}) dA} \quad (3.12)$$

In practical applications the pressure term is often omitted (or is approximated by use of the circumferential velocity distribution),  $R$  being taken as the radius of the exit nozzle or of the flow section of interest. The swirl is typically imparted by a swirler arrangement, and the geometry of the swirler (such as swirler vane angle and central body blockage) together with the geometry of the chamber determining the radial distribution of the swirl produced. The swirl number alone is thus not enough to determine the pressure effects in the inflow section of a combustion chamber. If the swirl becomes too strong, the adverse pressure gradient can result in an upstream flow all the way into the exit nozzle. In combustion applications, this causes a flashback that, if persistent, can destroy the exit nozzle or the injector.



# Chapter 4 Diagnostic Techniques

Several different diagnostic techniques have been used in the experiments included in the work. The main techniques are presented here, information concerning Rayleigh thermometry used in Paper I is found in [25] and [26]. For investigation of turbulent flow fields Particle Image Velocimetry (PIV) has been frequently used and is presented in section 4.1. Laser Doppler Anemometry (LDA), used for point measurements of flow velocities, is shortly described in 4.2.

For investigation of scalar properties, optical diagnostic techniques of different complexity were utilized. In initial investigations of lean flames in the thesis work the natural emitted light from the flames was recorded to collect information integrated over the line-of sight. The light emitted from species excited by chemical reactions is called chemiluminescence. Section 4.3 gives relevant information on this topic. When lasers are used to excite molecules or atoms for the purpose of species specific measurements the technique is named Laser Induced Fluorescence (LIF), presented in section 4.4. Finally thermometry based on the use of thermographic phosphors is described in section 4.5.

In several of the papers, flow and scalar field information is acquired simultaneously to obtain instantaneous information of the interaction between the flow, flame front dynamics and entrainment of ambient air into the fuel stream. In the first paper (Paper I), single-shot PIV was combined with multi-frame OH PLIF and gave the first information on the flame/flow interaction. In Paper VI simultaneous high-speed PIV and OH PLIF measurements were performed to further study this interaction. In Paper IX the feasibility of simultaneous measurement of temperature and velocity fields are presented using thermographic phosphors as temperature sensitive particles and acting as tracer particles for velocity measurements at the same time.

## 4.1 Particle image velocimetry

Particle Image Velocimetry (PIV) is an optical technique for measuring velocity fields in both gaseous (reacting and non-reacting) and liquid medium. The ability to capture the instantaneous velocity distribution in large regions at once, often with a high resolution, makes PIV very useful for acquiring data to be compared with LES. PIV is like LDA an indirect technique, in which the motion of seeding particles that are added makes it possible to measure the fluid velocity. It is considered to be a non-intrusive technique as compared with measurement techniques involving the use of physical sensors. PIV can also be combined with other planar optical measurement techniques, such as PLIF, to measure simultaneously both the flow field and flame species in combustion applications. However, in combustion applications, flame radiation, gas expansion, and regions with non-uniform refractive index makes PIV more challenging than in many other areas. Thanks to development of new hardware and evaluation algorithms PIV systems are now available in the kHz range, enabling time-resolved PIV [27]. With the development of tomographic PIV it is now also possible to obtain volumetric (3D) flow field data [27, 28]. These PIV techniques are utilized in Paper VI and VII respectively.

### 4.1.1 Basic principles

The basic principle for determining the flow velocity by use of PIV relies on accurate information of the displacement of imaged particles in small regions and the time for the displacement. A simple illustration of the basic hardware for the imaging and the evaluation steps that are required is given in Figure 4.1. With the arrangement shown the two velocity components (2C) in-plane of the light sheet (2D) can be acquired, often referred to as a 2D2C configuration. By adding a second CCD sensor and arranging the two sensors in a stereoscopic manner, both the out-of-plane velocity and the two in-plane velocity components can be measured. This method is called stereo-PIV (SPIV) or 2D3C PIV. PIV generally consists of the following stages:

- Camera calibration
- Image acquisition
- Image interrogation and calculation of velocity vectors
- Post processing of data (final vector field)

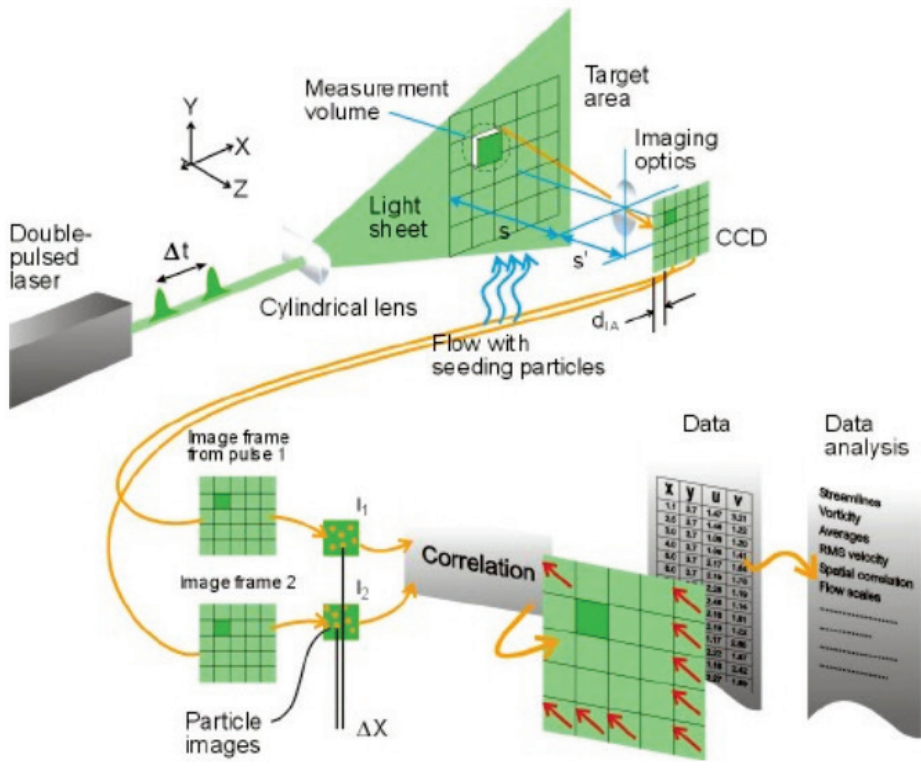


Figure 4.1 The working principles of PIV. Courtesy of Dantec Dynamics A/S.

**Camera calibration:** A calibration procedure is required for relating the image plane to the object plane; the calibration will also determine the optical magnification. For 2D2C PIV, this procedure is simple and requires only an image of a planar target. For SPIV, a mapping of the volume of the light sheet to camera pixel is needed. This can be obtained by using a two-level target aligned with the laser sheet. Different functions or models are available for the mapping; the requirement being that the calibration account for perspective viewing and optical distortions [29]. In SPIV, a refinement of a first calibration, such as one performed using a target, can be made by making use of the information from particle images simultaneously recorded by the two cameras [30].

**Image acquisition:** In order to provide precise imaging, the two laser pulses are expanded into a thin sheet by a lens system. Typically, the sheet thickness is 0.5-1 mm for 2D2C PIV and ~2 mm for SPIV. The duration of the pulses, typically ~10 ns, defines the effective exposure time of the particles and enables the particles to be imaged without being blurred, even at high velocities. The

time separation,  $\Delta t$ , between the two laser pulses can be set with a high degree of accuracy. The laser pulses are synchronized with cameras capable of taking two images with a very short time delay. The laser pulses act as very precise planar photo flashes illuminating the particles in the light sheet that crosses the target area. Scattered laser light in the Mie regime [31] from the seeding particles is then imaged onto the sensor array. The seeding density should be relatively high and preferably uniform.

**Image interrogation and calculation of velocity vectors:** In this step the two consecutive image frames are divided into small interrogation windows (IW's). Individual particles cannot be tracked with the seeding densities used in PIV, instead a cross-correlation of the intensity patterns (created by many individual particle images) in the two images obtained is performed. A correlation plane is then generated for each pair of IW's, as shown in Figure 4.2.

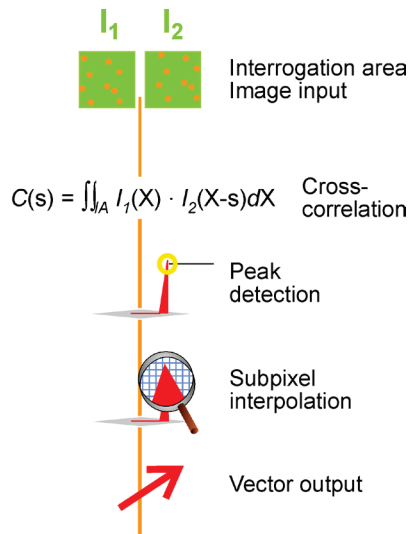


Figure 4.2 The correlation of the intensity distribution in two interrogation windows (IW's) separated in time by  $\Delta t$ . The peak location represents the average particle displacement from which the velocity vector can be determined knowing  $\Delta t$  and the magnification. Courtesy of Dantec Dynamics A/S.

The location of the strongest correlation peak represents the average particle image displacement. By fitting e.g. a Gaussian function to the shape of the peak, the location of the peak, in the correlation plane, can be determined with sub-pixel precision,  $\sim 0.1$  pixels. It is partly the degree of precision in the peak detection and the number of particle images used in the correlation that determines the accuracy of the measured displacement and thus also the

accuracy of calculated velocity. The vector of the local flow velocity (in the plane of the light sheet) is calculated taking into account both  $\Delta t$  and the magnification determined in the calibration step. The described process is repeated for each pair of IWs to be able to obtain the complete 2D velocity vector map (see Figure 4.1).

In SPIV the information from two cameras in a stereoscopic arrangement is used in the evaluation procedure, see Figure 4.3. By combination of the projections obtained by the two cameras it is possible to reconstruct the particle displacement inside the overlapping IWs and thereby evaluate the three velocity components [32].

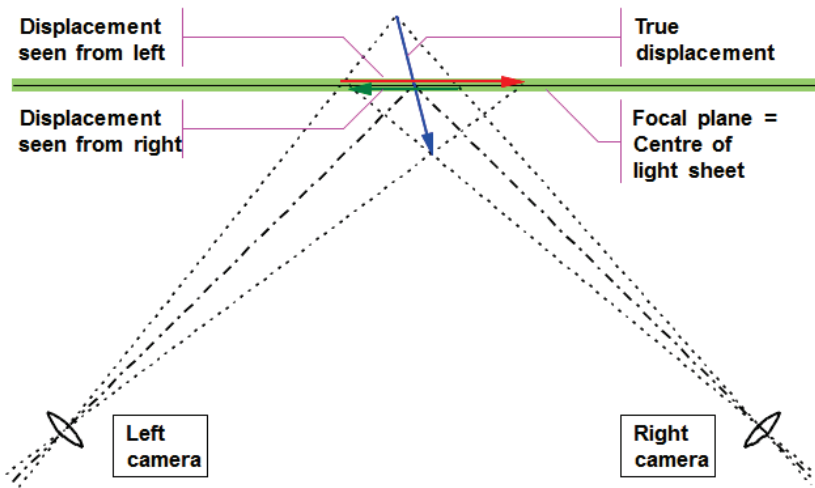


Figure 4.3 The stereoscopic camera arrangement used to derive the out-of-plane velocity component. Courtesy of Dantec Dynamics A/S.

**Post-processing of data:** Normal practice includes measures taken to reduce the noise occurring during image acquisition; avoid reflections and optimize the laser power. In view of the many steps involved in the data collection, noise cannot be avoided entirely, however. In addition, there can be regions with few or no particle images useful for the correlation, such regions can e.g. occur in the hot expanded regions found in flames. Post-processing is therefore necessary and involves data validation, removal of erroneous data, replacement of removed data, and possibly smoothing of data. A typical criterion used for eliminating unreliable vectors is that of the ratio of the largest to the second largest peak in the cross-correlations. If the ratio exceeds a threshold value then there are two values for the velocity that can be correct. In such cases the

dubious velocity vector can be replaced by interpolating from a group of valid neighbors.

From the description above, it is evident that the sensing domain for PIV is a volume defined by the size of the IW and the thickness of the laser sheet. Also, as the particle displacement is measured over  $\Delta t$ , the velocity vector is averaged over exactly this time interval. Due to this built-in averaging effect, and to assure accurate results, it is necessary to optimize the size of the IWs, the laser sheet thickness, and  $\Delta t$  on the basis of flow field (e.g. the highest out-of-plane velocity), the seeding density and the optical arrangement employed [32, 33]. The number of particles evaluated (i.e. present in both images) in each pair of IWs should be  $\sim 10-15$  in order for the strongest correlation peak to be an adequate representation of the average displacement. If the seeding density is sufficient for the size of IW employed, the particles should as a rule move no more than  $\frac{1}{4}$  of the length of the IW to reduce in-plane losses. Similarly, to reduce out-of-plane losses, particles should not move a distance greater than  $\frac{1}{4}$  of the laser sheet thickness.

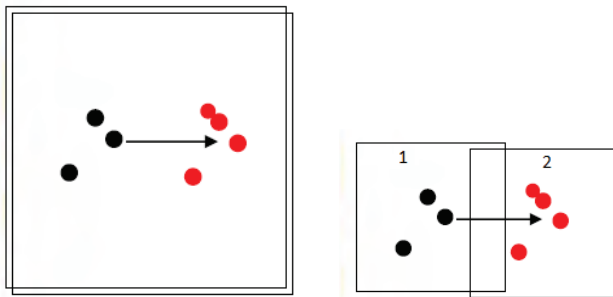


Figure 4.4 Adaptive cross-correlation Step 1 (left): large IWs without offset. Step 2 (right): smaller IWs can be employed. The second IW is shifted on the basis of information from Step 1.

Different multi-pass adaptive cross-correlation techniques have been developed aimed at improving the correlation strength, to achieve a higher spatial resolution and to increase the dynamic velocity range [33]. One approach, shown in Figure 4.4, is to employ a standard cross-correlation in the first step, in combination with a large IW. The size of the IW in the second step can be reduced since the IW is shifted (in all directions) in accordance with the estimated displacement vector obtained in the first step. This procedure is repeated several times normally until a final selected size of the IW is reached, typically  $32 \times 32$  pixels. Ideally, the final size of the IW used should be sufficiently small to prevent sharp velocity gradients from affecting the results [33]. This adaptive approach allows the in-plane displacements to be larger,

meaning that the dynamic velocity range can be increased. Therefore, in turbulent flows and especially in swirling flows, the out-of-plane motion (limited to  $\frac{1}{4}$  of the laser sheet thickness) thus typically setting the upper limit for  $\Delta t$ . The adaptive technique is developed further by use of deforming windows that adapt to rotation or deformation in the IW to strengthen the correlation even further.

#### 4.1.2 3D PIV - Volumetric Velocimetry

With the introduction of 3D PIV or tomographic PIV [28] a new possibility to investigate complex flow fields became a reality. An overview of the major developments in 3D velocity field measurements related to tomographic PIV methods is given in [34]. With the tomographic approach the measurement volume is illuminated at once and scattered light from seeding particles in the volume are imaged from several different viewing directions simultaneously, see Figure 4.5.

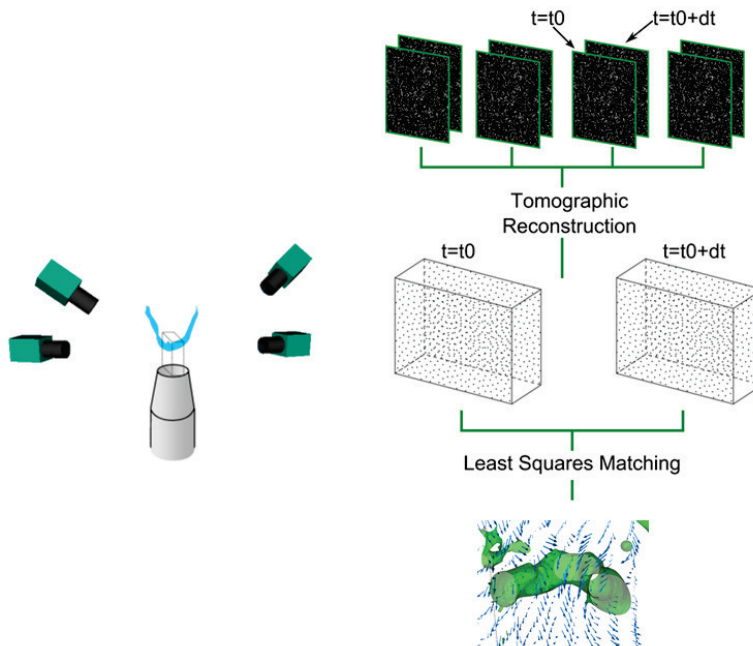


Figure 4.5 The camera arrangement used in Paper VII (right). Reconstruction of the volume from four simultaneous views of the particles (left). With two successive reconstructed voxel spaces the three-component velocity vector distribution can then be obtained by means of a 3D cross-correlation or an iterative algorithm (LSM).

From the simultaneous views of the illuminated particles a 3D array of light intensity discretized over voxels is reconstructed. With two exposures separated in time the intensities representing the particles in the volume can then be analyzed by means of a 3D cross-correlation or an iterative algorithm to calculate the three-component velocity vector distribution over the measurement volume. The two step procedure used in Paper VII is shown in Figure 4.5.

#### **4.1.3 Measurement equipment used for PIV**

Lasers are used as the primary light source due to their ability to produce high-power light beams with short pulse durations. Typically, frequency-double flashlamp pumped Nd:YAG lasers are used for low repetition rate systems (Hz) and, due to an improved thermal stability, diode pumped Nd:YLF lasers are employed for high-speed systems (kHz). To allow for very short time separations together with maximal pulse power, two lasers are combined to create a dedicated PIV-laser. The classic cameras used for PIV are based on interline transfer CCD sensors designed with the purpose of taking the two required images with a short time delay [35]. For acquiring images at high-speed, CMOS cameras are typically employed. The tradeoff to reach the kHz range is a much reduced laser power and of cameras that are less light sensitive than the hardware available for low-repetition rate (in the Hz range) PIV.

#### **4.1.4 Seeding**

Seeding particles used in combustion applications must withstand the highest temperatures reached. This limits the choice of particles to e.g. commercially available ceramic materials:  $\text{TiO}_2$ ,  $\text{MgO}$ ,  $\text{ZrO}_2$  and  $\text{ZrSiO}_4$ . The particles must be small and light enough to follow the fluctuations in the flow. The density for these particles are in the range of 3-5  $\text{kg/m}^3$  and to follow moderate fluctuations (1 kHz) particles should be in the 2-3  $\mu\text{m}$  range [36]. The behavior of small particles in the thermal expansion regions and strong temperature gradients in flames is complex. A flamelet Stokes number defined as the ratio between the particle relaxation time and the flame front time scale, was reported to be the proper parameter to characterize the particle dynamics in a premixed flame [37]. In practical combustion applications an in-homogenous seeding concentration cannot be avoided due to the thermal gas expansion. This can make it difficult to follow the rule of thumb of 10 particles within the IW. A new approach to come around this is an algorithm that adapts the size of the IW to the local seeding density [38].

## 4.2 Laser Doppler anemometry

Laser Doppler Anemometry (LDA) or Laser Doppler Velocimetry (LDV) is a well-established technique for measurements of velocities and for turbulence characterization [39]. The technique is based on the detection of the frequency shift of laser light that has been scattered by small particles that follows the flow. The particles are typically of the same types as used for PIV. The scattered light is frequency shifted in accordance with the Doppler principle, the light containing information concerning the velocity of the particle from which the radiation was scattered. To detect the Doppler shift LDA utilizes the intersection of two laser beams of the same wavelength, both originating from the same laser. The measurement principle can be explained by observing the interference phenomenon that occurs where the light from the two beams canceling each other out in some regions and in other regions complementing each other due to the coherent properties of the laser light. A pattern of alternatively dark and bright planes called fringes is formed inside the measurement volume defined by the intersection of the two beams, see Figure 4.6. The distance between the fringes, the fringe spacing,  $d_f$  is only dependent on the wavelength of the laser light and the intersection angle of the beams. The fringe spacing is the calibration constant for the system and can be determined once and for all for the optical system used. A particle that passes through the measurement volume crosses the fringe pattern and scatters a periodic light flux, a burst. This modulated light flux is detected as a frequency,  $f_d$  by the receiving optics, a Photo Multiplier Tube (PMT). The detected frequency is proportional to the particle velocity perpendicular to the fringes. This velocity,  $V_y$ , is obtained by multiplying the fringe spacing,  $d_f$  by the output frequency,  $f_d$  the latter being the number of fringes traversed per unit time:

$$V_y = f_d d_f \quad (4.1)$$

With the basic method described above there is a direction ambiguity with respect to the particle velocity. In order to overcome this problem one of the intersecting laser beams is frequency-shifted with a by means of a Bragg cell. This result in a movement of the fringes in the measuring volume with a frequency of the shift frequency, and the number of fringe passes will be increased accordingly. A zero velocity will correspond to the shift frequency, and the flow direction relative to the fringe movement can easily be determined.

In the LDA system used in the present study, the light source was a low-power argon-ion laser generating a mixed beam. This beam is split into two mixed beams of which one is passed through a Bragg cell and appropriately shifted. Each of the resulting beams, the shifted and unshifted, are further separated into one blue (488 nm) and one green (514 nm) beam. The two pair of beams, the shifted and unshifted beam for each wavelength, are transmitted through fiber optics to the measurement probe. The initial beam spacing is 50 mm and the four beams are focused to intersect by a 350 mm lens. The two measuring volumes, created at the beam intersection point, will overlap with the fringes of each volume oriented perpendicular to each other. Thus, two perpendicular velocities can be measured simultaneously. Due to the Gaussian intensity distribution in the laser beam the effective measuring volume, one for each color, becomes ellipsoidal about 1 mm long and 0.2 mm in diameter. The signal is collected in a back-scatter mode, with the signal receiving optics incorporated in the probe.

The temporal resolution depends on the passage of seeding particles but is usually in the kHz range. Since the measurements are made one point at a time, and thus theoretically only one particle at a time needs to be in the measurement volume, the demand for the seeding density being dense and homogenous is relaxed compared with PIV. Being a point measurement technique one has to either traverse the LDA probe (two probes for a three component systems) or the measurement object to acquire velocity profiles over the field of interest.

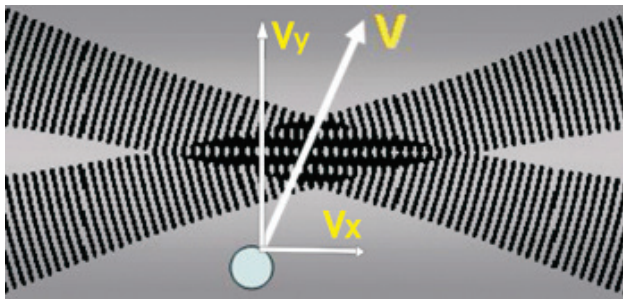


Figure 4.6 The interference phenomenon at the intersection of two coherent laser beams where an ellipsoid measurement volume is created. The velocity component perpendicular to the fringes,  $V_y$ , is measured on basis of the scattered light from particles crossing the beam intersection.

### 4.3 Chemiluminescence imaging

The light naturally emitted by flames is termed luminescence, and includes both chemiluminescence and gray and blackbody radiation from soot and other particulates [31]. Chemiluminescence is the electromagnetic radiation emitted through the de-excitation of electronically excited species formed by chemical reactions in the thin reaction zone. It occurs in flames due to the high temperatures in the reaction zone, which leads to the spontaneous emission of light. In hydrocarbon-air flames, much of the visible and ultraviolet light is emitted by e.g. the CH, OH, and C<sub>2</sub> radicals [40]. The flame luminosity can provide information useful in combustion sensing (by optical sensors) and in diagnostic applications (through spatially resolved signals) and can also be a source of interference in PLIF and PIV measurements [41].

The recording of flame chemiluminescence is one of the simplest methods of visualizing flames. This natural (passive) radiation can be observed by the naked eye or can be recorded with a camera. The equipment required for this imaging is simply a sufficiently light-sensitive camera, together with filters, when desired, for selecting a part of the emission spectra, the ultraviolet radiation of the OH radicals, for example. A drawback of this technique is its line-of-sight nature, which needs to be taken into account when interpreting images of chemiluminescence. Since the signal is averaged over the volume of the flame as a whole, the local (2D) structure of it is not revealed. Due to its simplicity, this technique is employed routinely to detect the global position and shape of the combustion region in industrial combustors. In premixed flames, it is also possible to interpret the radiation intensity of free radicals in terms of fluctuations in the heat release. This approach is used in studies of combustion dynamics in which the imaging of fluctuations in heat release can be carried out spatially and temporally resolved (high-speed imaging), keeping in mind the integration over the line-of-sight.

In Paper VIII, spectrally integrated chemiluminescence, monitored by an intensified CMOS camera at a frame rate of 7 kHz, was used to study flames at and approaching flashback. In the study, the flames rotated around a central bluff-body during flashback and the imaging was performed perpendicular to the central axis of the burner through a glass cylinder. The line-of-sight was thus reduced to the flame segment obtained in the annular section, 15 mm wide, located between the bluff body and the cylinder wall. Under these conditions, the chemiluminescence images provided a relatively clear picture of the flame propagation taking place.

## 4.4 Laser-induced fluorescence

Fluorescence is the spontaneous emission of radiation by which the molecule or atom relaxes from an upper energy level to the ground level. In Laser Induced Fluorescence (LIF), the optical excitation is by means of a laser pulse, carefully tuned to a transition from a lower to an upper state of the targeted species. LIF is an important tool in combustion diagnostics and can be used to investigate species distributions, flame-front propagation and temperature fields.

If the target molecule is resonantly excited by the laser radiation, a photon of energy  $h\nu$  is absorbed, bringing the molecule from a ground state to a certain vibrational and rotational level in a higher electronic state. Here,  $h$  is Planck's constant and  $\nu$  is the tuned frequency. The population in the new state is unstable, due to collisions between molecules. Rapid energy redistribution occurs immediately after excitation, resulting in a population of closely-lying rotational levels. Shortly thereafter, the molecule spontaneously emits another photon (fluorescence) of energy  $h\nu$  or lower, before it decays to the rotational and vibrational sub-levels in the ground electronic state. Due to the energy redistribution in the excited state, fluorescence occurs not only at the excitation wavelength (resonant fluorescence), but also at other wavelengths, mainly shifted towards longer wavelengths. This property is an advantage in the detection of the fluorescence, generally done at non-resonant wavelengths to minimize interference by seeding particles (Mie) or spurious laser scattering. The fluorescence signal can be collected by an intensified CCD camera (2D measurements) or by a PMT (point measurements).

Since each species has unique absorption and fluorescence patterns, this technique enables species-selective measurements. For this to work in practice, a tunable laser source is required such as a dye laser. The success of LIF is clearly linked to the high sensitivity that can be achieved through the relatively large cross-sections of the resonant absorption process involved. In the combustion area, LIF can be used to detect flame radicals, reaction intermediates and pollutants at ppm (parts per million) and even at sub-ppm levels. The high sensitivity also enables planar (2D) laser-induced fluorescence (PLIF) imaging to be carried out.

For flame visualization, qualitative information obtained by PLIF of a suitable flame radical is often sufficient. If quantitative information (such as absolute species concentrations) is sought a thorough understanding of the energy transfer processes involved in LIF, how this affects the signal, and how to put this knowledge into practical use is required.

### 4.4.1 Basic theory of LIF

An excited atom or molecule does not necessarily emit radiation, since several other processes can compete with fluorescence. Some of these are dissociation, energy transfer through collisions with other species, other internal energy states and chemical reaction. The losses due to collisions between molecules, collisional quenching, reduce the major part of fluorescence. Predissociation is the probability of the specific excited states, to decay without emitting radiation into neutral atoms, for example.

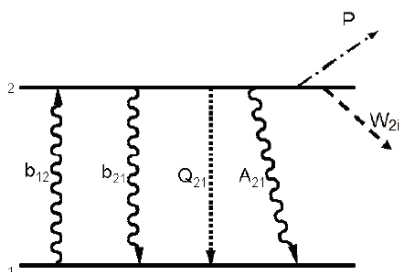


Figure 4.7 A two-energy-level diagram of the energy transfer processes involved in LIF.

An overview of the energy processes involved in single-photon LIF is provided in Figure 4.7, in which a simple two-energy-level model is used to describe the system. Levels 1 and 2 are the lower and the upper electronic energy level, respectively. The outline of the theory and the used notations follows those of Eckbreth [31]. The arrows, representing the optical and collisional processes involved, are denoted by their corresponding rate constants. The rate constants for stimulated absorption and stimulated emission,  $b_{12}$  and  $b_{21}$ , are related to the Einstein coefficient,  $B$ , for the corresponding process. The relation can be written as

$$b = \frac{BI_\nu}{c} \quad (4.2)$$

where  $I_\nu$  is the spectral irradiance of the incident laser light and  $c$  is the speed of light. In this approximation  $b_{12}$  and  $b_{21}$  thus, depend linearly on the incident laser field. Parameter  $A_{21}$  is the rate constant for spontaneous emission, given by the Einstein  $A$  coefficient.  $Q_{21}$  corresponds to the collisional quenching, discussed briefly above.  $P$  corresponds to photoionization and  $W_{2i}$  to predissociation. The rate equations for the population densities of the two energy levels,  $N_1$  and  $N_2$ , as based on the processes outlined in Figure 4.7 can be written as

$$\frac{dN_1}{dt} = -N_1 b_{12} + N_2 (b_{21} + A_{21} + Q_{21}) \quad (4.3)$$

$$\frac{dN_2}{dt} = N_1 b_{12} - N_2 (b_{21} + A_{21} + Q_{21} + P + W_{2i}) \quad (4.4)$$

The signal of interest for LIF is the fluorescence signal,  $F$ . A first observation one can make is that  $F$  is proportional to  $N_2 A_{21}$ . However, to deduce the species concentration prior to laser excitation from  $F$ , a relation linking  $N_2$  to the population in the lower level prior to excitation,  $N_1^0$ , is required. To simplify matters further, the effects of the two loss terms ( $P$  and  $W_{2i}$ ) can usually be neglected. This can be regarded as a valid simplification since photoionization can be avoided by simply adjusting the laser power, and since most excited states are not predissociative. It follows that if no loss terms are present, the number of states at the two levels, respectively, is constant. From this, the time-dependent population at level 2 can be obtained from Equation (4.4) above. Assuming further that after a short period of time the populations at both levels have reached a steady state yields Equation (4.5) below.

$$N_2 = N_1^0 \frac{b_{12}}{b_{12} + b_{21}} \frac{1}{1 + \frac{A_{21} + Q_{21}}{b_{12} + b_{21}}} \quad (4.5)$$

With use of the definition of the saturation energy according to Equation (4.6) below, the relationship for the fluorescence signal power,  $F$ , can be expressed as in Equation (4.7), in which  $h\nu$  is the energy of the photons emitted by the laser,  $\Omega/4\pi$  is the collection solid angle,  $l$  and  $A$  are the length and the area of the active volume as determined by the laser sheet and the detection optics and  $I_\nu$  represent the laser energy.

$$I_{sat} = c \frac{A_{21} + Q_{21}}{b_{12} + b_{21}} \quad (4.6)$$

$$F = h\nu \frac{\Omega}{4\pi} l A N_1^0 \frac{b_{12}}{b_{12} + b_{21}} \frac{1}{1 + \frac{I_{sat}}{I_\nu}} \quad (4.7)$$

As can be seen, the fluorescence signal power is linearly proportional to the laser irradiance. In addition, the fluorescence is proportional to the number of molecules of the probed species,  $lAN_1^0$ , in the measurement volume. In this linear LIF regime, however, the time between excitation and fluorescence emission is sufficiently long for some of the molecules to lose their excitation energy in collisions with other molecules prior to fluorescence being emitted. This makes it very difficult to quantify the species concentration on the basis of the recorded signal. It is necessary, therefore, to handle the quenching rate

constant when using LIF if quantitative results are desired. This is complicated since the quenching rate is dependent on temperature, pressure and species composition. Under certain conditions and assumptions, such as that the quenching is reasonably constant throughout the measurement volume, linear LIF can provide a satisfactory qualitative representation of the spatial distribution of the species being studied.

## 4.5 Phosphor thermometry

A relatively new technique for thermometry in combustion environments makes use of the physical properties of phosphor particles to measure temperature. Phosphor is a solid luminescent material, consisting typically of a ceramic host material doped with a small amount of rare earth elements [42]. A large number of different phosphors are available in the form of a fine powder typically having particle sizes of 1-10  $\mu\text{m}$ . The main use of particles of these types is in commercial products such as lamps, screens and paint. The particles exhibit a high degree of temperature sensitivity for temperatures ranging from cryogenic temperatures up to 2,000 K, and referred to, when used in thermometry, as thermographic phosphors (TP) [43].

The most common use of TP is for surface thermometry. In such applications the TP are deposited in a very thin layer on the surface of interest and are excited by a suitable wavelength, UV or near UV, often produced by a laser. The host material in the particles is optically transparent for the radiation, the laser energy being absorbed by the doping agent. After excitation, an intense luminescent light, phosphorescence, is emitted and is detected using either a point light detector, such as a PMT or an image detector, such as an intensified CCD camera. The phosphorescence decay lifetime [43, 44] or the spectral intensity ratio of two or several emission lines [43, 45, 46], assuming thermal equilibrium, can be compared with previous calibrations in order to infer the actual surface temperature.

The possibility to achieve close to non-intrusive remote two-dimensional measurements is attractive in many application areas. In addition, the high quantum yield, high temporal resolution and high degree of accuracy make the technique well-suited for combustion diagnostics. Measurements are performed to assess such as wall and component temperatures in internal combustion engines [47, 48] and in gas turbines [46, 49]. In addition to measurements on surfaces, the suitability of the technique for measurements in sprays [50, 51] and for thermometry in gaseous media has been investigated in recent years [52, 53]. In Paper IX, the simultaneous measurements of gas

temperature field, by use of TP, and of the velocity field was demonstrated. In these measurements, TP were used as temperature-sensitive particles, and also acting, at the same time, as tracer particles for PIV.

The fine phosphor powders have characteristics very similar to the ceramic materials used as seeding for PIV in combustion applications. Typical characteristics are; densities of 4-2 kg/dm<sup>3</sup>, a melting point above 2,000 K and a white or light color. For accurate measurement of both velocity and temperature, the particles used should be as small as possible. For the rather heavy ceramic powders it is important that the size is around 2-3 μm for the particles to be able to follow moderately fast fluctuations in a turbulent flow [36]. In addition, the rapid temperature changes and large temperature gradients often encountered in combustion applications require a careful investigation to ensure that the response time of the particles to such temperature fluctuations is sufficient [43].

# Chapter 5      Laboratory Burners

In laboratory studies of lean premixed flames, use of suitable generic burners that can stabilize such flames is important. The major part of the work presented in the thesis was carried out using what is termed a low-swirl burner. Use of such burners, initiated by R.K Cheng and co-workers in 1995 [4, 5] has proved to be useful in investigations of a fundamental character and for the validation of LES. A burner of this sort generates a divergent turbulent flow field in which the axial velocity decreases along the center axis. The characteristic lifted flames thus obtained are optimal for optical diagnostics in both the unburnt and the burnt regions.

In paper III another burner, in which the degree of swirl could be altered during operation, was utilized to study flashback phenomena. In order to enable optical observation of the transient flame to be performed during flashback, a cylindrical glass tube was employed here as an exit nozzle. Both of these burners are described in greater detail below.

## 5.1      The low-swirl burner

For the work presented in the thesis, a new version of a low-swirl burner (LSB) was developed jointly by the Lund University, the Technical University Darmstadt and the Lawrence Berkley National Laboratory (LBNL). Three copies of the newly designed burner were made for comparative studies at different locations. To produce exactly the same swirl conditions in all three burners, fixed swirl vanes were used for producing the swirl in the flow, rather than tangential jets of the type found in the original design being employed [4, 5]. An overview of the burner design and the configuration of the swirler arrangement is presented in Figure 5.1. The LSB nozzle has an inner diameter of 50 mm, the swirler being placed 68 mm upstream of its exit plane. The annular (outer) section of the swirler is provided with eight curved vanes of constant thickness, each having an inlet angle of 90 degrees and a long section with a constant discharge angle of 37 degrees. The central channel is 38 mm in diameter and is fitted with a perforated plate 3.6 mm in diameter having 37 holes. In the current configuration, the approximate split of the mass flow is

such that 60% of it passes through the swirler vanes and 40% through the perforated plate, resulting in a swirl number of about  $S=0.55$  according to Equation (3.12) and data from stereo-PIV measurements reported in Paper I and III. After passing through the swirler and the perforated plate, the flow discharges through a nozzle (50 mm in diameter) into a coflow of air. The thickness of the nozzle wall is reduced towards the exit, so that the inner flow does not change in area before exiting into the surroundings. This design is aimed at reducing the generation of recirculating eddies at the nozzle exit that a thick wall would create. Premixed air and fuel (methane) enters the burner via four pipes leading into the plenum in the lower part of the burner. A distributor plate in the plenum and a total of five perforated plates, break down the large flow structures generated upstream before the gas reaches the swirler (see Appendix). The burner assembly is mounted in a 300 mm wide coflow of air. The coflow is used to protect the nozzle flow and the flames from disturbances caused by the ambient flow and thereby ensure reproducibility.

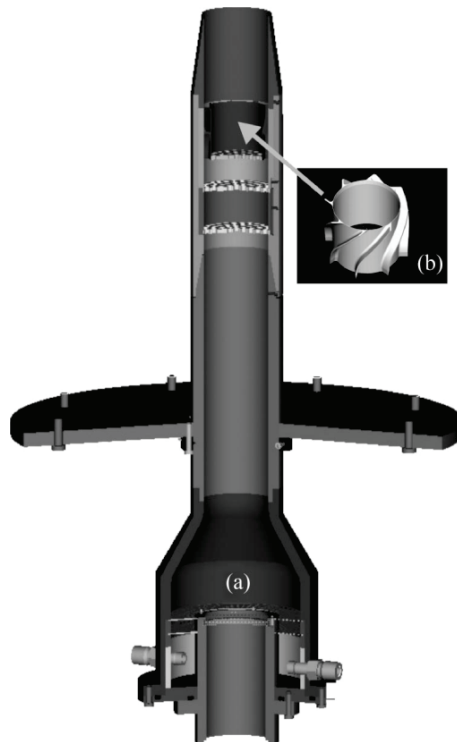


Figure 5.1 (a) Cross-section of a burner without the swirl assembly. Premixed air and fuel enter by way of four nozzles (two of the visible here) and pass through several perforated plates before reaching the swirler. (b) The swirl assembly, the arrow indicating where the assembly is installed.

Mass Flow Controllers (MFC), Bronkhurst (Hi-Tec, EL-Flow), were used to provide the burner with the correct amounts of air and methane. The measurement principle of these controllers is based on the decrease in temperature of the gas passing through a narrow bypass duct parallel to the main gas flow. By use of this technique, the rate of the mass flow through the MFC, and not the volumetric flow rate, can be controlled (calculated). The particular advantage of this technique is that with use of it the mass flow rate which is given (calculated) does not depend upon variations in either the pressure or the temperature of the MFC. The uncertainty of control of these MFCs is typically ~1-3% provided that they are calibrated and are used at levels above 10% of the specified maximum flow rate of the device.

## 5.2 Burner with variable degree of swirl

A burner equipped with moveable-block swirl generators was employed in the studies of flames close to flashback reported in Paper VIII. The swirl generators were situated upstream of the nozzle and allowed the degree of swirl to be adjusted. The fluid flow enters the moveable block in a radial direction and is injected radially upstream of the moveable block through eight nozzles, as can be seen from the arrows in the Figure 5.2. This moveable-block consists of upper as well as lower segments each segment having an angular bend in the radial direction. Turning of the lower segment of the moveable block allows the burner to be operated at various swirl numbers. A schematic cross-sectional view of the burner arrangement is shown in Figure 5.3. Upstream the moveable-block, methane is injected into the air flow by a perforated tube. Downstream of the mixing chamber, the flow passes through the swirler assembly. Thereafter, the flow reaches a cylindrical, vertically orientated, 15 mm wide annular slot that encloses a central bluff-body 30 mm in diameter. To ensure constant and reproducible boundary conditions, the bluff-body is water-cooled.

To enable a thorough investigation of the transition from stable to flashback conditions to be carried out, the length of the central bluff-body was extended by 20 mm as compared with its original design. This enabled the transitional regime between stable conditions and flashback to be extended and to be made experimentally accessible for observation times of sufficient length. To make optical observation of the transient flame during flashback possible, the outer cylindrical wall of the annular slot was replaced in some of the experiments by a cylindrical glass tube. Its inner diameter of 60 mm was matched by its stainless-steel counterpart. For easy control of the degree of swirl, the moveable block was equipped with an electrical stepper motor.

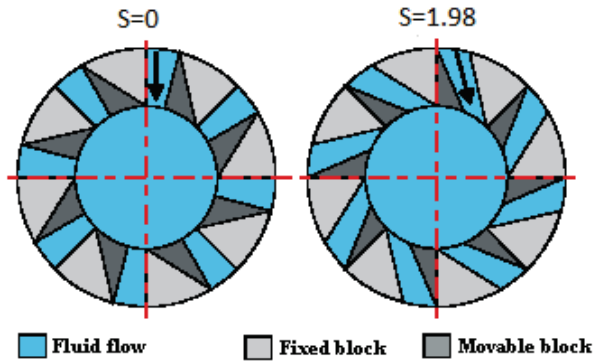


Figure 5.2 The arrangement of movable blocks (swirl generators) used to adjust the swirl. The block configuration at the left shows no swirl ( $S=0$ ) and at the right strong swirl ( $S=1.98$ ).

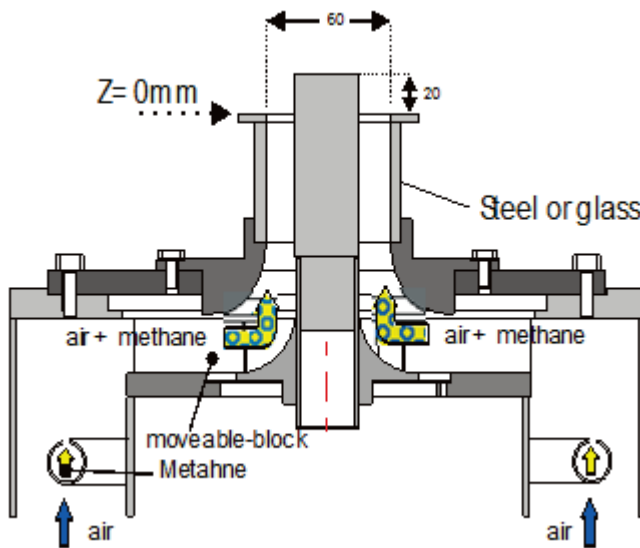


Figure 5.3 A cross-sectional view of the nozzle as adapted by extending the length of the central bluff-body and providing optical access to the annular slot.

# Chapter 6 Results - Low-Swirl Lean Premixed Flames

## 6.1 Background

This section concerns the characterization of unconfined lean premixed flames, stabilized by a low-swirl burner, as presented in Paper I -VII. The work has been carried out in close cooperation with groups performing numerical simulations (LES). Several of the papers presented in the thesis include LES from Prof. X.S Bai's group at Lund University and from Prof. C. Fureby at FOI, Stockholm. Different groups have investigated low-swirl flames in a wide range of inlet conditions [54, 55], for different fuels [56-58] as well as investigated the potential of the low-swirl approach for practical applications [59-61].

## 6.2 Characteristics of the flow field and the flame

To help the reader a schematic overview of the burner, the flow field and the lifted flame is given in Figure 6.1. Details of the burner design are found in Section 5.1 and in the Appendix. Two methane/air flames are used as baseline conditions throughout this study, both with  $\phi=0.62$ . The laminar flame speed is about 12 cm/s [62]. The Reynolds number based on the bulk flow velocity (6.2 and 9.3 m/s) and diameter at the burner exit are about  $Re=20,000$ , and  $Re=30,000$ .

As illustrated in Figure 6.1 the investigated flames are lifted and are propagating in an inner low-speed region created by the divergent flow field. In mean an approximately bowl-shaped flame region is displayed. Mean flame position at the centerline is 32 mm above the nozzle for  $Re=20,000$ , and slightly lower for  $Re=30,000$ . The outer region of the flame interacts with large vortices in the inner shear layer; this interaction is believed to be

important for the flame stabilization. The flame flow interaction and flame stabilization are discussed in Paper V and VI. Since the flame is lifted and unconfined, surrounding air can be entrained into the outer part of the mixture ahead of the flame, causing a stratification of the mixture at the outer sections of the flame front, see e.g. Paper V.

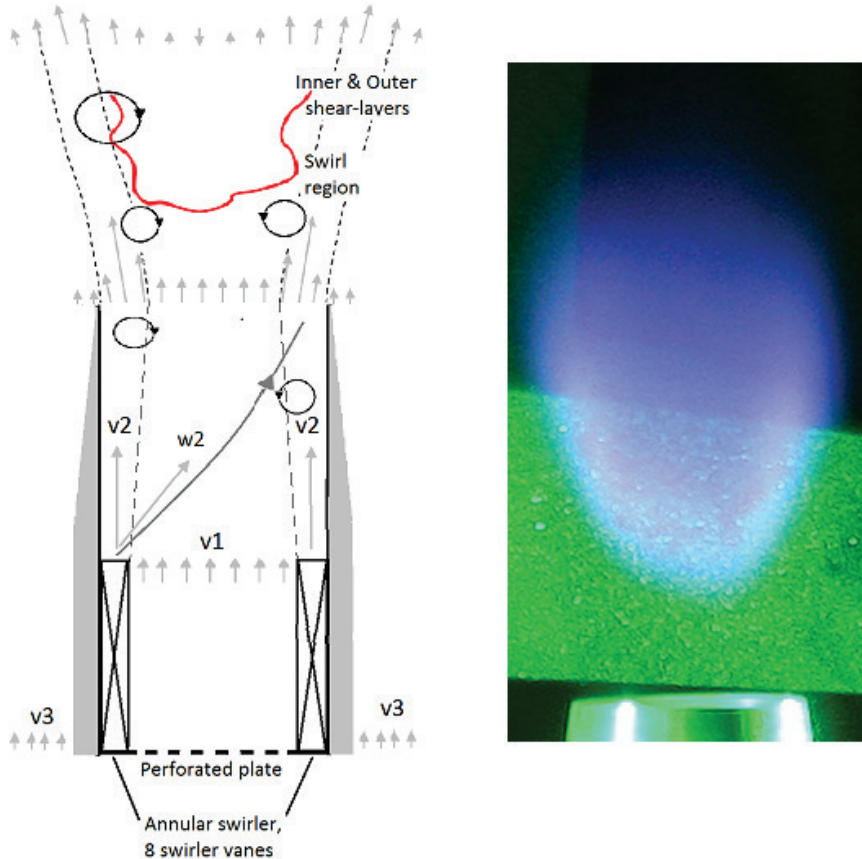


Figure 6.1 (left) Schematic drawing of the burner, the flow field and the lifted flame. The flow is split through the perforated plate ( $v_1$ ) and the swirler ( $v_2$ : axial component and  $w_2$ : azimuthal component), outside the nozzle is a weak coflow ( $v_3$ ). The helical path of one of the jets leaving the swirler is indicated. (right) The lifted flame and a crossing laser sheet seen by scattered light from seeding particles (photo H. Bladh).

Inside the burner the flow of premixed methane/air is split through the perforated plate ( $\sim 40\%$  of the flow) and the swirler ( $\sim 60\%$  of the flow) yielding a swirl-number  $S \approx 0.55$ , see Paper I. The eight jets (and wakes) leaving the swirler follow helical paths as indicated in Figure 6.1. Based on the discharge angle of 37 degrees at the exit from the swirler the vertical distance

(pitch) required for one revolution for each jet leaving the swirler is  $\sim 119$  mm. Accordingly, the vertical separation between the eight helical jet paths inside the nozzle is  $\sim 15$  mm. The part of the flow passing through the central perforated plate initially consists of individual jets emanating from the 37 circular holes in the plate (hole diameter = 3.6 mm). As the flow develops in the downstream direction the jets mix and the grid turbulence gradually dissipates. At the point where the core flow meets and starts to interact with the helical jets and wakes leaving the swirler the inner-shear layer starts to develop. Characteristic velocities (see Figure 6.1) above the swirl arrangement for  $Re = 20,000$  are;  $v_1 = 5$  m/s,  $v_2 = 12$  m/s,  $w_2 = 10$  m/s. Where  $v_2$  is the peak axial velocity and  $w_2$  the peak azimuthal velocity leaving the swirler passages, see Figure 6 in Paper I for details. Outside the nozzle is a weak coflow  $v_3 \sim 0.3$  m/s. When the flow exits the nozzle the axial flow velocity along the radial direction varies from 2 m/s (around the axis) to about a peak velocity of 10 m/s in the outer swirling region. The signatures of the individual jets (and wakes) are still present in the outer region of the flow field downstream of the nozzle exit, see Paper III. Results from stereo-PIV showing the non-reacting and reacting flow field above the nozzle ( $Re = 30,000$ ) is found in Section 6.3 below. In Paper VI sequences of results from high-speed PIV is found, illustrating the complex flow structures found in the inner shear layer region.

### 6.3 Paper I - Flow- and scalar field measurements

Results of the first series of experiments that were carried out concerning low-swirl flames are presented in this paper. The measurements were performed at Lund University in cooperation with Technical University of Darmstadt, Germany. Stereo-PIV was employed for assessing the three velocity components in the region above the nozzle in both the vertical and the horizontal plane. Measurements were also carried out above the swirler (with the nozzle removed), which enabled for an approximate evaluation of the split of the flow between the swirler and the perforated plate to be carried out. LDA measurements were performed for comparison of these with PIV results and for estimating the integral-length scales. In addition, simultaneous measurements of the velocity fields (PIV) and the OH distribution, as well as simultaneous measurements of the temperature fields and the OH distribution were performed.

Stereo-PIV was performed using two pulses from a frequency-doubled Nd:YAG laser and two interline-transfer CCD cameras to collect the Mie scattered light from seeding particles that were added into the gas flow. Both cameras were fitted with Scheimpflug adaptors and were so arranged that the

angle between the two cameras was  $\sim 90$  degrees. A stereoscopic calibration was performed using a two-level calibration plate. The calibration carried out was followed by a refinement procedure involving a comparison of a hundred pairs of simultaneously acquired images of the seeding particles from both cameras [30]. With use of the stereoscopic setup, as just described, and a sufficiently ( $\sim 2$  mm) thick light-sheet, the out-of plane motion of the particles could be evaluated, along with the in-plane motion taking place. In this particular flow field, the high out-of plane velocities close to the nozzle determine the upper limit for the separation in time between two consecutive images required to evaluate the velocities involved. In Figure 6.2 (not shown in the paper) the three velocity components for the condition  $Re=30,000$  is shown for both the non-reacting (cold) and the reacting (flame) case. A broadening of the flow field can be seen in the reacting as compared with the non-reacting case. The broadening is caused by the hot, expanding flame region increasing the divergence of the flow. Stagnation occurs in the downstream direction along the center axis for both cases. For the reacting case, a reverse flow can be seen along the axis in the upper part of the flow field. It can be noted that there is a difference between the peak axial velocity at the left and at the right side of the centerline for profiles close to the nozzle. This difference was found to be an artifact of the non-symmetric flow field in the circumferential direction, this being caused by the flow passing through the swirler. This was investigated further by performing stereo-PIV in horizontal planes above the nozzle, the results being used to generate boundary conditions, as discussed in Paper III.

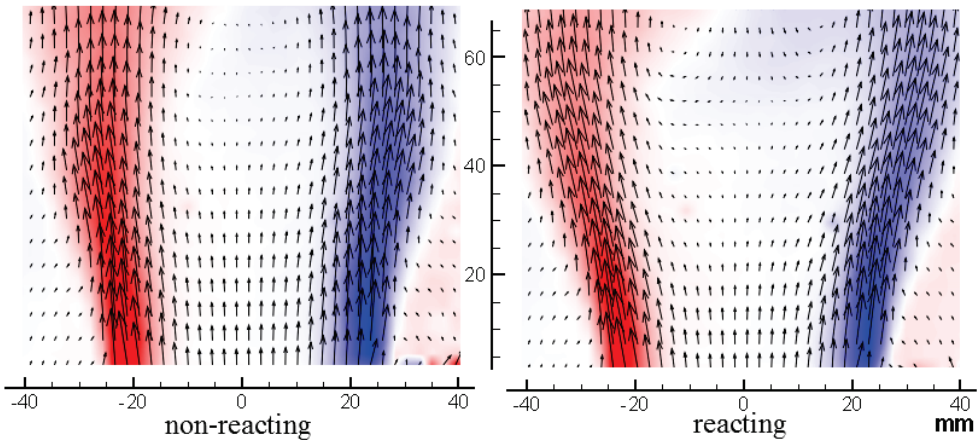


Figure 6.2. The time-averaged velocity field for non-reacting and reacting cases obtained from stereo-PIV,  $Re=30,000$ . The arrows represent the axial ( $U$ ) and the radial ( $V$ ) velocity components, respectively. The background color represents the circumferential velocity ( $W$ ). The peak velocities at the nozzle exit are  $U_{\max} = 16$  m/s and  $W_{\max} = 12$  m/s.

The two laser sheets were overlapped above the burner when simultaneous OH PLIF and PIV measurements were carried out. The OH PLIF imaging was performed at a high repetition rate, using a multi-dye laser cluster pumped by a multi-YAG system. The OH radicals were excited at approximately 283 nm, the resulting fluorescence (at close to 310 nm) was collected by a dedicated high-speed framing camera equipped with a UV lens. A large number of sequences of four OH images were collected. The temporal separation between the consecutive OH PLIF images was varied, typically in the range 200 – 400  $\mu\text{s}$ , for tracking the movements of the flame front over time. The flame dynamic, including fluctuation of the flame base position and wrinkling was noted. Occasional out-of-plane motion of the flame was detected through the appearance of islands of OH, representing burnt gas, below the main flame.

For each OH PLIF sequence, a PIV recording was synchronized with the second image in the sequence. A binary mask was created from the instantaneous OH PLIF images, indicating only burned and unburned zones. The flame front was identified as the line separating the two zones. For each flame condition investigated 1500 joint PIV and OH PLIF sequences were collected to generate statistics. Properties such as a mean reaction progress variable and conditional velocities were extracted from the measurement data.

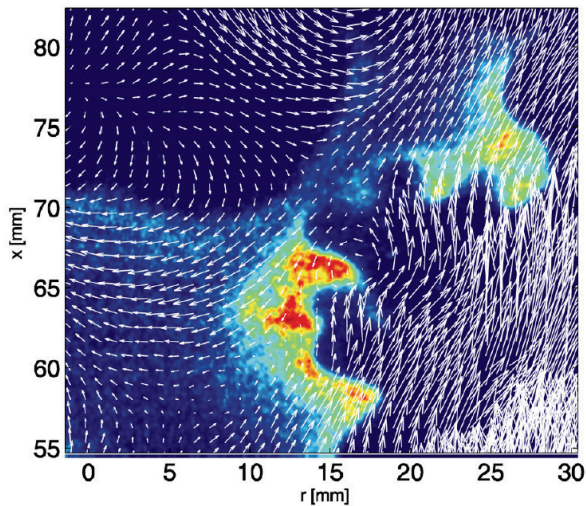


Figure 6.3 Combined OH PLIF and flow field images from PIV measurements obtained in the low-swirl flame ( $Re$  30,000).

Simultaneous single-shot OH PLIF and PIV was also performed using a different camera setup for the OH imaging, enabling a stronger signal and

higher spatial resolution to be obtained. An example of the OH distribution together with the flow field from the PIV is shown in Figure 6.3. The displayed region is located at the trailing edge of the flame. Both the flow field and thus the interaction between the flame and flow as well, become increasingly complex. In addition, dilution of the mixture occurs, due to entrainment of air from the surrounding coflow. This stratification can lead to the mixture along the trailing edge becoming too lean and local extinction may occur.

Filtered Rayleigh Scattering (FRS) was employed for studying the temperature distribution. This technique was selected partly because of its potential of suppressing Mie scattered light from seeding particles that remained in the gas flow from PIV. FRS exploits the fact that Doppler broadening increases with temperature. Using narrowband excitation for Rayleigh scattering together with an atomic notch filter, served to suppress the excitation wavelength (and thus the Mie radiation), and enabled the Doppler broadened signal to be separated out. The FRS approach employed is described in detail in [25]. Simultaneous OH PLIF and FRS measurements were also performed. Simultaneous PIV and FRS were not successful, however, due to the high seeding densities required for PIV. Radial profiles of mean temperature and fluctuations in temperature are presented in the paper. The temperature distribution along the central axis was extracted and was used for later comparison with LES, presented in Papers II and III. In a recent investigation Rotational Coherent Anti-Stokes Raman Spectroscopy (RCARS) was carried out along the center axis of the burner for the  $Re=20,000$  condition [63]. The mean temperature along the center axis was in reasonable close agreement with the FRS data presented in Paper I. The FRS data display a larger scatter than the RCARS data do. The measured peak temperature in the post flame region is close to the adiabatic flame temperature ( $\sim 1700$  K).

## 6.4 Paper II - LES and experiments

The paper is the first presentation of the joint results of experiments and of LES that had been carried out. Most of the experimental results presented in Paper I were available at the time except for those concerning the stereo-PIV measurements. On the basis of the combined PIV and OH PLIF results, a number of characteristic features of the flames that had been investigated could be detected, these being described and discussed. Important features included a large scale wrinkling, and an axial fluctuation of the flame base and an intense flame flow interaction in the inner shear layer. A continuous flame front that separated burnt and unburnt was also extracted from the OH

images, suggested a flamelet-like behavior at both the leading and the trailing edge of the flame. The vortex shedding in the shear-layer region was likewise observed, both in the experiments and in LES. A consequence of the dynamics evident in the shear-layer region was a strong tendency of the coflowing air and the already lean methane air mixture to mix with another, which can possibly lead to the flame being quenched by the entrained air. A model dealing with stratified premixed combustion of this kind is presented in the paper. The model was validated by the experimental data, a reasonable degree of support for the quantitative and qualitative predictions made being obtained.

## 6.5 Paper III - Experiments and comparison of two LES models

In this paper the experimental data obtained were used for comparing LES turbulent combustion models of two separate types for  $Re=20,000$ . One model is based on a level-set G-equation (G-LES) and flamelet chemistry, and the other on finite rate chemistry including reduced kinetics (F-LES). The effects of the numerical solvers employed and of the boundary conditions on the flame and flow predictions made on the basis of the respective combustion models were examined. Radial profiles of the mean axial and radial velocities and the corresponding rms-fluctuations were extracted from the experimental data and used for comparing these results with those obtained from LES. Data from Filtered Rayleigh scattering were used to examine the temperature field in the leading flame front.

Newer results, concerning simultaneous OH- and fuel-PLIF (or acetone-PLIF) measurements, were also introduced for comparison with LES. The information regarding the fuel distribution enabled further investigation of the entrainment of air from ambient region into the methane air stream. Engulfed pockets of air were found to be transported towards reacting zones, creating 'holes' in the flame front, as the reactions terminates due to a too lean mixture. The entrainment process of this sort occurring both in the experiments and in the LES is shown in Figures 3 and 4 in the paper.

Two different inflow boundary conditions (at the exit of the burner) are used in G-LES, separately from one another, to examining the effects on the flow field of the characteristics of the swirler. The first approach is based on the stereo-PIV data obtained just above the burner exit plane. The mean axial velocity field at the nozzle exit is shown in Figure 6.4. The data involved is

phase-averaged for use as part of the boundary conditions, the original PIV data being presented in the paper. The signatures of the eight jets and wakes formed by the flow through the swirler are visible there as the peaks and valleys found in the outer region in the flow field. An artificial turbulence generation algorithm was applied to reconstruct a time-dependent inflow velocity [64]. The inflow conditions generated in this manner are referred to in the paper as modeled inflow conditions (M-BC). In the second approach, the flow through the swirler and nozzle is simulated using LES and the velocity data at the burner exit is sampled and tabulated. These inflow conditions are referred to in the paper as the simulated inflow condition (S-BC). In connection with S-BC, large vortices are introduced, these emerging from the burner and entering the G-LES domain. A significant greater degree of mixing in the inner shear layer and flame wrinkling are found to occur when S-BC rather than M-BC is involved (see Figure 3 in the paper). The effects of the boundary condition are studied further in Paper V. It is concluded on the basis of the investigations carried out that resolving the flow within the burner is important for studying flames of these types.

In the experiments and in the LES results the flames were found to display a marked bowl shaped (slightly W-shaped in a cross-sectional view) structure, with wrinkles along the flame front, which in mean became stabilized about 32 mm above the burner rim. The G-LES results appear to predict a more wrinkled slightly broader flame, since the vortices in the outer shear layer continuously interacts with the flame front. In the predictions from the F-LES model, these vortices pass in a region outside of the flame.

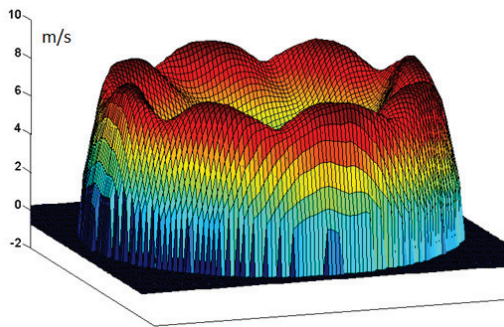


Figure 6.4 The mean axial velocity field obtained using stereo-PIV 2 mm above the nozzle. The flow field is phase-averaged and is used as a part of a certain optional boundary conditions in LES as described in Paper III.

## 6.6 Paper IV - Simultaneous PIV, OH- and fuel-PLIF measurements

This paper presents the experimental work involving simultaneous PIV, OH- and fuel-PLIF measurements in low-swirl flames. Since methane does not fluoresce, gaseous acetone was added as a fuel tracer in employing the PLIF technique to study the fuel stream. The experiments were conducted at acetone concentrations of ~0.3% – a compromise between obtaining a sufficiently strong LIF signal and keeping the effects on the flame at a minimum. The methane concentration was reduced to compensate for the acetone that was introduced – this enabling the equivalence ratio to remain unchanged at 0.62 in the premixed gas.

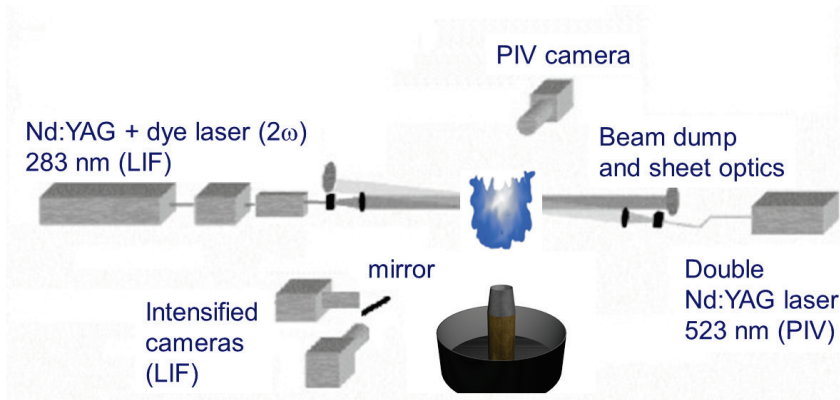


Figure 6.5 A schematic view of the combined PLIF and PIV experimental arrangement. A high-reflective bandpass mirror at a 45-degree angle to the burner reflects the OH signal and transmits the acetone (fuel tracer) signal to the respective detectors.

Two separate laser systems were used for simultaneous PIV and PLIF measurements that were obtained. The laser beams were formed into overlapping sheets to illuminate a planar region of the flame, one crossing the vertical centerline of the burner, see Figure 6.5. For PIV, doubled Nd:YAG lasers at 532 nm were employed. An interline-transfer CCD camera (1376 $\times$ 1040 pixels) was used to image the full width of the lifted flame. A cross-correlation algorithm employed in conjunction with an adaptive multipass method was employed for the evaluation of the velocities. The laser source employed for the PLIF measurements was a dye laser pumped by a frequency-doubled Nd:YAG laser. The OH radicals were excited near 283 nm, detection of the resulting fluorescence occurring at around 310 nm. Acetone

was excited using the same laser as used for the OH, i.e. at  $\sim 283$  nm. The resulting fluorescence from acetone was emitted in the blue band between 350-500 nm. Two image-intensified CCD detectors equipped with UV lenses were used for recording the fluorescence signals.

An example of combined images of the three techniques is shown in Figure 6.6. These results provide increased insight into the flame behavior, including flame flow interaction and the entrainment of ambient air. Pockets of unburnt reactants are often found downstream of the main flame front. Also islands of OH are found below the main flame front, these being attributed to the 3D nature of the flame. The fuel distribution was found to be uniform in the lower central parts of the fuel stream, whereas in the outer parts, the entrainment of air can be seen, partly diluting the mixture. In the combined OH- and fuel-PLIF images, a thin black non-signal region ( $\sim 1$  mm wide) can be seen, separating the unburnt from the burnt regions. The fact that these two regions do not overlap can be seen as an illustration of the flamelet combustion concept.

Profiles of the approximate fuel mass fractions at 20, 30, 40 and 50 mm above the nozzle under both operating conditions were extracted from these measurements for later use in the validation of LES. The laser sheet profile was normalized by use of data obtained along the center axis involving fuel-PLIF images acquired for the non-reacting case. For the reacting case the fuel mass fraction was known,  $\phi = 0.62$ , close to the axis at the nozzle exit enabling a calibration of the images to be carried out.

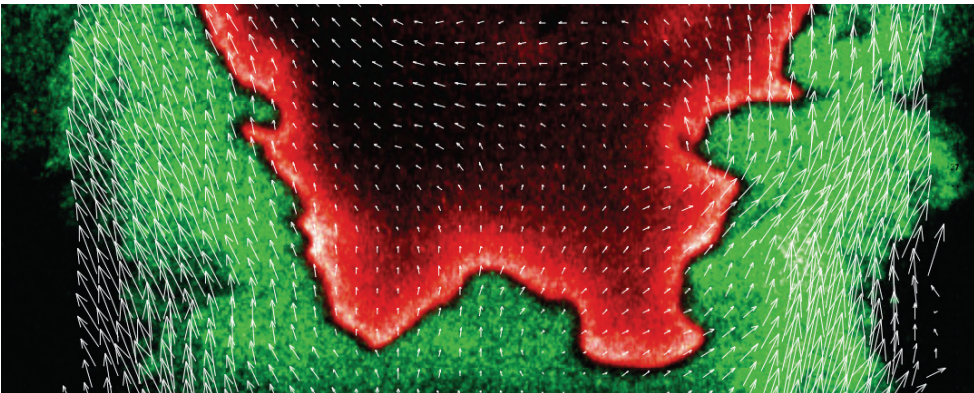


Figure 6.6 A cross-section through the flame showing the fuel-distribution (below and outside the flame), the burnt region (OH) and the superimposed flow field from PIV.

## 6.7 Paper V - LES and Experiments, flame stabilization

In this paper the flame dynamics and the stabilization mechanisms of the low swirl flames were investigated, and were discussed on basis of both experimental results and LES. LDA and PIV results were also employed in studying the flow fields. Combined OH- and fuel-PLIF data were used to identify the position and the structure of the flames as well as the entrainment of air that created stratification along the trailing edge of the flames. The flame dynamics were investigated using multi-frame OH PLIF images in combination with single-shot PIV, as reported in Paper I. In addition, high-speed chemiluminescence recordings of the flame motion were obtained. The time evolution of simulated flames was studied, employing each of the two different boundary conditions presented in Paper III. Large eddies in the inner shear layer, present in both experiments and the simulations and emerging from the nozzle, were found to be important in predicting the flame dynamics and for the stabilization of the flame. The influence of the shear layer on the flame was found to be similar to that encountered in lifted jet-flames [65]. In simulations ( $Re=20,000$ ) in which these burner flow structures were omitted, blow-out of the flames occurred.

Discussions concerning flame stabilization led to decision to carry out the following experimental study concerning simultaneous high-speed measurements of the flow field and the flame front location.

## 6.8 Paper VI - Simultaneous high-speed PIV and OH PLIF

Simultaneous high-speed (4 kHz) OH PLIF and PIV measurements were performed to investigate flame flow interactions in the low-swirl flames. Two separate laser systems were used in the combined measurements. For PIV, a double cavity diode pumped Nd:YLF laser and a high-speed camera were used. With the reduced light budget, compared to previous PIV measurements in the Hz-range, the laser sheet was limited in height and was focused at the center of the target area above the burner. One set of measurements was performed with a sheet height of ~40 mm and for a second set ~25 mm was used. Different seeding particles and camera settings were tested during these measurements to optimize the correlation strength and reduce peak-locking in the evaluation procedure. A diode pumped Nd:YAG laser in combination with a high repetition rate dye laser were used to excite the OH radicals. For a

repetition rate of 4 kHz, the pulse energy of the 283 nm radiation was about 300  $\mu$ J. The excited OH radicals were imaged by use of an intensified high-speed camera. The laser beams generated by the two systems were formed into overlapping sheets to illuminate a planar region of the flow field and the flame, see Figure 6.7. A large number of simultaneous consecutive images were recorded and combined to film sequences.

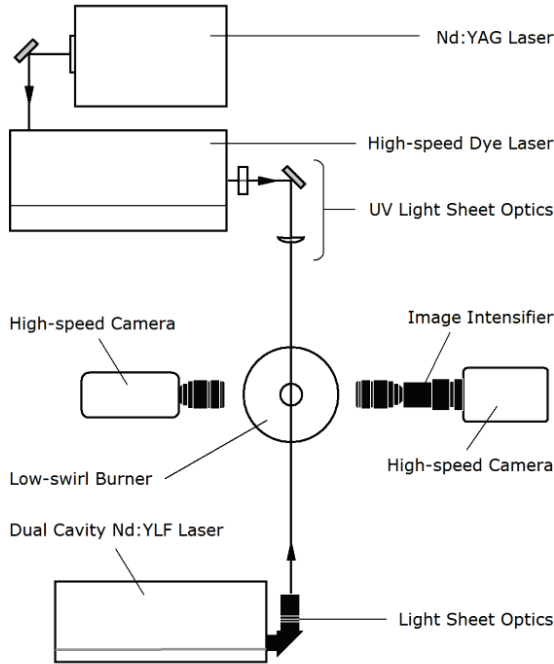


Figure 6.7 The combined high-speed PLIF and PIV experimental arrangement used for the measurements in Paper VI.

A short sequence of the flow field and the lifted flame is shown in Figure 6.8. The fluctuating part of the flow field (the mean value of each velocity vector is subtracted) is shown to reveal vortices hidden by the convection. Several sequences of 2,000 combined images, at a sampling rate of 4 kHz, were collected for both of the two operational conditions, making it possible to investigate in qualitative terms the interaction between the flow and the flame.

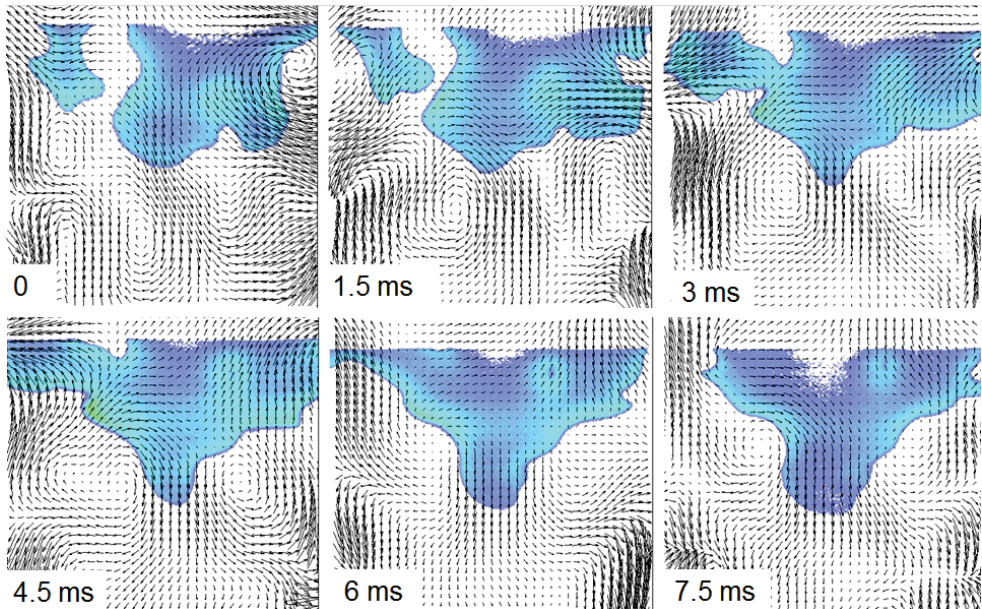


Figure 6.8 The fluctuating part of the flow field and the lifted flame visualized by the OH radical. Flow structures created upstream of the flame are convected downstream and interact with the flame. The time between images is 1.5 ms ( $Re=30,000$ ). The images cover the width of the nozzle; the lower edge is located 5 mm above the nozzle.

The characteristic features that were identified for both the investigated Reynolds numbers include the large-scale vortex structures that were convected within the inner shear layer. Some of these vortices were strong enough to create regions with flow reversals that convected the flame upstream and in the radial direction. These vortices that surrounded the flame region appeared to be important for the stabilization of the investigated flames. Vortices of lower strength that often appeared in the shear layer as vortex-pairs wrinkled the flame locally. In the inner, low-speed region, the freely propagating flames responded to local fluctuations in the flow field. A schematic overview of observations made from the film sequences is included in Table 6.1 below (not included in the paper).

To investigate this further, modal analyses of the PIV data were performed to identify any cyclic processes that observations of the film sequences indicated to be present. These processes were assumed to be related to vortex shedding in both the axial and azimuthal shear layers that surrounded the inner low-speed region [66, 67]. Results of the simulations (LES) are also included in the paper to demonstrate the complex 3D flame flow dynamics, especially in the shear-layer region. Oscillating Pattern decomposition (OPD) is applied on the time-resolved data for characterization of the flow field in different regions

whereas Dynamic Mode Decomposition (DMD) are applied on 3D LES data for visualization of coherent large scale helical structures in the flow field. Ongoing work includes coupled analysis of the flame and flow field, such analysis are being performed on both experimental data and LES.

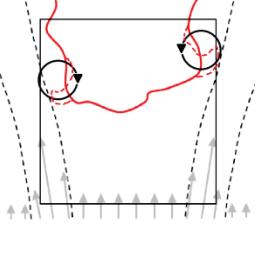
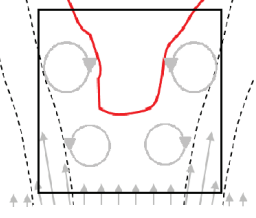
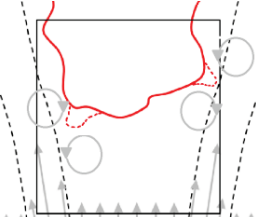
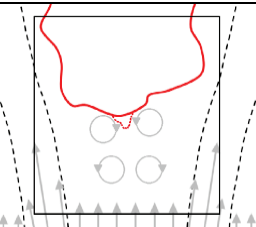
<b>Characteristics</b> The field-of-view used in the analysis is marked. Dotted lines indicate the inner and outer shear-layers.	<b>Schematic flow/flame interactions</b> Flow reversal:  Fluctuation: 
Strong vortices, creating flow reversal, following the inner shear layer. These vortices pull the flame upstream and in the radial direction, are believed to be important for the flame stabilization.	
Large weak vortices, symmetric around the flame. Affects the inner low-speed region and thus the flame base position. The rotational direction alters.	
Pairs of counter-rotating vortices. Present in the inner shear layer. The rotational direction alters and wrinkles the flame accordingly.	
Pairs of counter-rotating vortices. Present in the inner low-speed region. The rotational direction alters and wrinkles the flame accordingly.	

Table 6.1 Schematic representation of typically occurring interactions between resolved flow structures and the flame. The field-of-view starts 5 mm above the nozzle.

## 6.9 Paper VII - Volumetric Velocimetry (3D PIV)

In the last investigation concerned with the low-swirl burner, the feasibility of Volumetric Velocimetry, also known as 3D PIV or Tomographic PIV, was tested under both reacting and non-reacting conditions. The measurement system consisted of four CCD cameras mounted on Scheimpflug adaptors to ensure the overlapping of the different depths-of-field. The cross-wise arrangement of the cameras around the lifted flame is shown in Figure 6.9. The two combined Nd:YAG lasers used in earlier PIV measurements were used for illumination. Each laser delivered approximately 300 mJ of energy per pulse at a wavelength of 532 nm. With the light intensity inversely proportional to the thickness of the measurement volume, tests with 5 - 20 mm thick light sheets were performed. Different seeding particles and seeding densities were tested during this work. For final measurements the seeding density was about 0.035 ppp (particles per pixel) in dense regions and 0.025 ppp in the expanded post- flame region.



Figure 6.9 The camera arrangement used for measurements in vertically oriented volumes above the burner. The height of the measurement volume was ~50 mm. (Photo and editing A. & A. Petersson.)

The positions of the particles were reconstructed from the four camera views through use of a tomographic technique, in an array of typically 500x450x200

voxels at a voxel resolution of 0.1 mm. Two successive voxel spaces that were reconstructed were then analyzed by means of an iterative algorithm, providing both the three-component velocity vector distribution and the full gradient tensor across the measurement volume. The spatial resolution, as based on the size of the cuboids that were evaluated was  $4.5 \times 4.5 \times 4.5 \text{ mm}^3$ . With an overlap (shift) of 30% in the evaluation process, the obtained vector spacing was 1.5 mm. The results presented include both the mean and the instantaneous 3D flow field upstream and downstream of the main flame region. The mean flow field data enable the symmetry and the position of the bowl-shaped low-speed region created by the diverging flow field and the flame to be visualized (see Figure 7 in the paper). Measurements were also performed in the post-flame region above the stagnation region. The mean flow field in Figure 6.10 shows a symmetric stagnation region at approximately 60 mm above the nozzle.

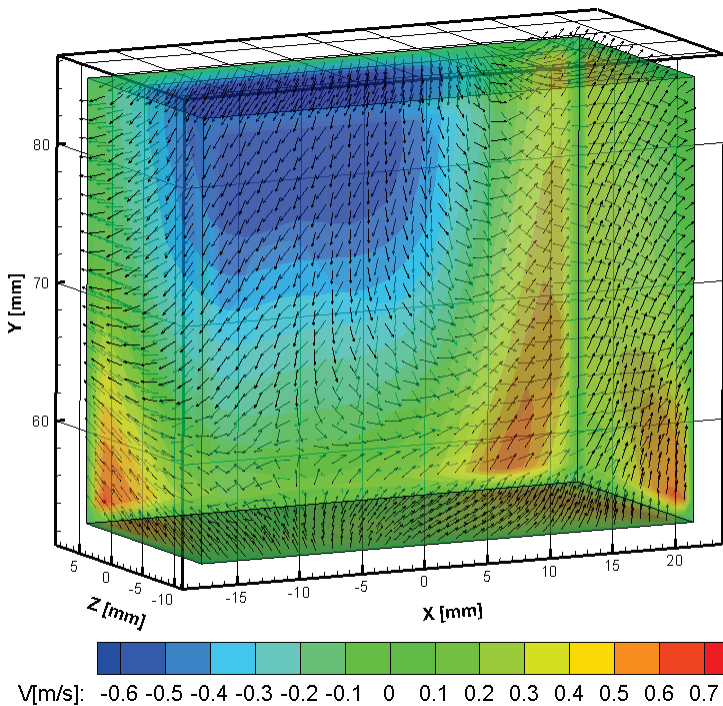


Figure 6.10. The stagnation zone in the post-flame region, shown as the average of 200 images,  $Re=20,000$ .  $V$  is the axial velocity component. Velocity vectors are presented with a uniform length.

An example of the instantaneous flow field in the post-flame region is displayed in Figure 6.11. The position of the stagnation region is shown in the

lower part of the image. Since the iso-surfaces in the figure visualize the magnitude of the vorticity they can be used to identify vortex cores in the flow field. Detection of vortex cores is performed by use of the Q-criterion [68], utilizing information generated by the LSM algorithm of the velocity gradient tensor. With the limited spatial resolution only large structures can be regarded as significant, the threshold related to the vorticity is set accordingly. The slightly tilted view of the measurement volume in the figure makes it possible to identify a part of a large vortex structure located in the X-Z plane. The direction of rotation of the vortex structure (as indicated by the large arrows in the figure) is consistent with the radial flow towards the center at  $Y=70$  mm, and the upstream (reverse axial flow) along the center axis towards the instantaneous stagnation region created at  $Y=50$  mm in this case. On the basis of observations made from the 500 instantaneous flow field data collected, the visualized structure shown in Figure 6.11 is suggested to be a part of a vortex ring encircling an inner flow region.

The results obtained in this investigation clearly stimulate further work with use of this technique. A possible next step would be to compare results obtained using stereo-PIV with results obtained using 3D PIV data in thin volumes to be able to address questions of measurement accuracy.

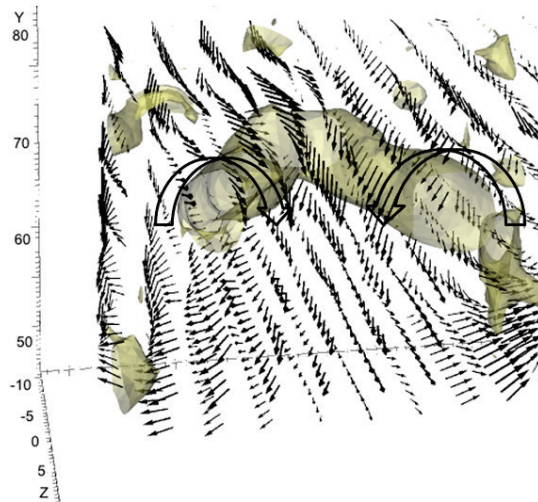


Figure 6.11. An example of the instantaneous flow field in the post-flame region. The iso-surfaces represent the magnitude of vorticity and are used to identifying vortex cores. The visualized large structure is suggested to be a part of a vortex ring encircling an inner flow region.



# Chapter 7 Results - Swirling Flames close to Flashback

## 7.1 Paper VIII - Swirling flames: conditions close to flashback

In this paper an investigation of flames close to flashback was carried out. The work was initiated by Prof. A. Dreizler and was carried out partly in Lund and partly at the TU Darmstadt. A burner having a variable degree of swirl, presented in Section 5.2, was used and when a critical swirl number was exceeded the flame flashed back into the burner nozzle. The critical swirl number was found to depend on equivalence ratio and geometry. A transparent nozzle enabled the flashback to be studied by recording of the transient flame luminosity, see Figure 7.1 below. Such recording was carried out using a CMOS camera at a frame rate of up to 10 kHz. The flashback velocity was found to be much higher than the estimated burning velocity of the flame, accordingly, the flashback was attributed a convection directed upstream.

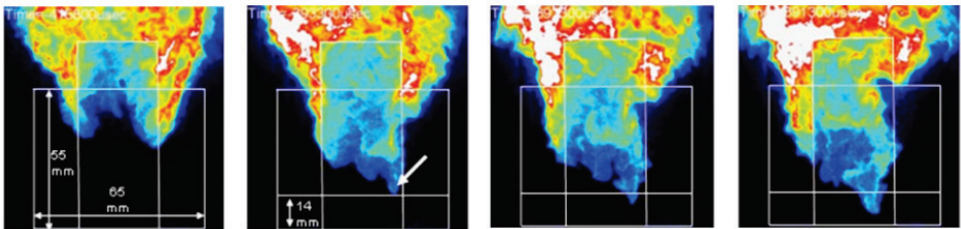


Figure 7.1 Temporal sequence of the flame during flashback, time between images is 1 ms. White lines sketch the extensions of the central bluff-body and the outer wall of the annular slot. The actual flashback is triggered by the leading edge of the flame highlighted by the arrow in the second image (see Figure 6 in the paper for details).

In Lund the reacting flow field was investigated by use of PIV to supplement previously performed LDA and hot-wire measurements of the non-reacting

case. Radial profiles of the mean axial velocity component 5 mm above the burner measured by PIV is shown in Figure 7.2. The outward shift of the location of the peak axial velocity, together with the high degree of fluctuations in the shear layers (the inner and the outer) are characteristics induced by the strong swirl. The mean progress variable obtained from OH PLIF images indicated how the mean flame position was following the location of the inner shear layer as the swirl was increased (see Figure 12 in the paper).

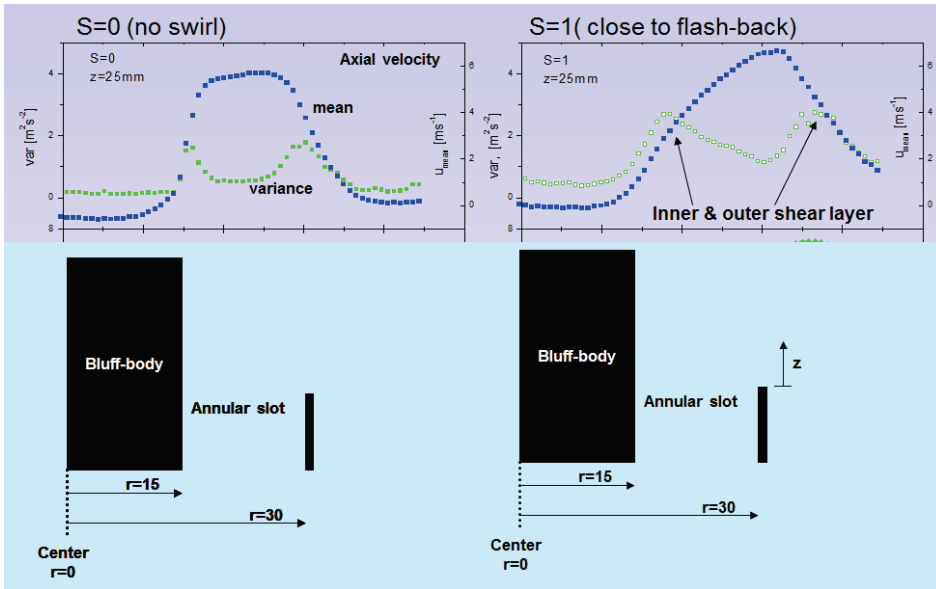


Figure 7.2 Radial profiles of the mean axial velocity component and its fluctuations 5 mm above the bluff-body, as measured by PIV; see Figure 9 in the paper for details.

To investigate the flashback process further the group at TU Darmstadt later performed measurements of OH PLIF at 10 kHz and PIV at 20 kHz [69]. A hypothesis for the flame propagation was proposed in the paper were, at the initial phase of the flashback, the separation of the boundary layer from the bluff body wall was linked to the existence of an adverse pressure gradient, i.e., the rise in static pressure in stream-wise direction. The separation of the wall boundary layer created a wide enough region for the flame to propagate upstream, further increasing the strength of the adverse pressure gradient or shifting the location of the adverse pressure gradient in an upstream direction. A complete explanation of the driving mechanism could not be determined due to the involved interactions between large-scale coherent motion, turbulence and chemical reactions.

# Chapter 8 Results - Flow and Temperature Field Measurements

## 8.1 Paper IX – Flow and temperature field measurements by use of thermographic phosphors

In this paper combined flow- and gas temperature field measurements using thermographic phosphor (TP) particles as both flow tracers in PIV and as temperature sensitive particles was demonstration for the first time. A heated air flow was used as a test case. The phosphoric particles,  $Mg_4FGeO_6:Mn$ , were dispersed in alcohol and transported by compressed air streaming through a nebulizer creating a fine spray carrying the particles. During the passage through the heated tube the alcohol evaporated and particles and air were heated gradually to approximately 400 C before exiting into the ambient. Two separate laser and detector systems were used for the simultaneous velocity (PIV) and temperature measurements as shown in Figure 8.1.

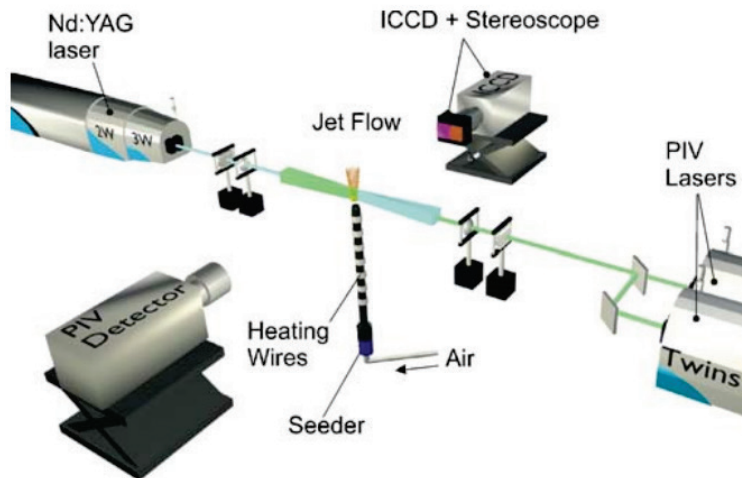


Figure 8.1 The experimental setup used for the measurements reported in Paper IX.

The two laser beams were formed into overlapping sheets to illuminate a planar region along the centerline of the flow to be investigated. A standard PIV approach was used to evaluate velocity vectors in the measurement plane. To assess the gas temperature field the third harmonic generation of an Nd:YAG laser at 355 nm, with a pulse duration of 7 ns and a repetition rate of 10 Hz, was used to excite the particles in the air flow. The subsequent phosphorescence from two emission lines was detected by an intensified CCD camera together with an imaging stereoscope. The collected emission first passes through separate filters before encountering the stereoscope, producing identical images of the same object on corresponding halves of the CCD chip. The intensity-ratio method was then employed for assessing the gas temperature field. An example of the obtained results is shown in Figure 8.2. Here, the heated air flow passes a conical bluff body creating a recirculating flow in the center. The data were produced by averaging 50 instantaneous samples. Point measurements using the temporal decay method were also performed. The phosphorescence decay was analyzed and was compared with previous calibration data of lifetime versus temperature.

Further studies of TP's applied for thermometry in gaseous free-flows can be found in [52], in the paper issues with potential laser-induced heating were investigated. A recent demonstration of simultaneous gas-phase temperature and velocity imaging using TP's particles at a repetition rate of 3 kHz repetition rate is found in [70].

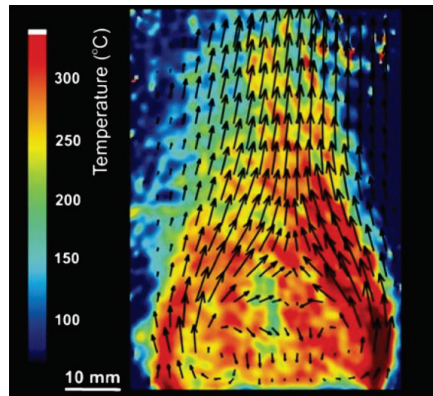


Figure 8.2 Result from simultaneous measurements of temperature and of the flow behind a conical bluff body.

# Chapter 9      Concluding Remarks

Experimental results concerning lean premixed flames studied under various operational conditions have been presented. A large part of the work presented involves studies of turbulent lean premixed flames stabilized by a low-swirl burner of a newly designed type. The characteristic features of the unconfined flames reported on here concerned their interactions with complex flow structures in the surrounding shear layers. The characterization of the flow field was based primarily on results of Particle Image Velocimetry (PIV) used to assess two and three velocity components, respectively, in both horizontal and vertical planes above the burners. The potential of Volumetric Velocimetry (3D PIV) was investigated in low-swirl flames and used to assess the 3D characteristics of the flow field. Flame-front visualization and fuel distribution measurements were carried out using Planar Laser Induced Fluorescence (PLIF). PLIF of OH radicals was employed to determining the position, as well as the fluctuation, overall shape and wrinkling of the flame front. Simultaneous flow- and scalar field measurements were performed at high repetition rates for detailed studies of the propagation of turbulent lean premixed flames.

The experimental data were used to assist in the development and validation of Large Eddy Simulations (LES). The potential of such simulations for resolving the large-scale dynamic behavior and mean properties of the low-swirl flames was investigated stepwise. The work with low-swirl flames conducted demonstrated clearly the need for use of well-characterized boundary conditions in LES. Recent results from non-reacting LES, including the flow through the swirler arrangement and the nozzle, is presently used to provide the boundary condition for combustion LES [71]. High-speed 3D PIV measurements of high spatial resolution are clearly desired in order to adequately map velocity gradient tensor field as a whole at the nozzle exit. With the limited light budget available in the kHz range the depth (thickness) of a volume will be limited to a few mm. An alternative to this approach is to perform simultaneous dual-plane stereo-PIV (kHz) above the nozzle exit. To separate the light, scattered by seeding particles in the two separated light sheets, onto the individual stereo camera pairs requires the use of two different laser wavelengths in conjunction with suitable filters [72]. Here, the thickness

of the light sheet could be limited to around 2 mm and the light budget could allow measurements to be performed at very high-repetition rates,  $\sim 20$  kHz. The light budget can be further improved by arranging the cameras to collect forward scattered light and using suitable seeding particles.

With demonstration recently of time-resolved (kHz) 3D imaging of OH PLIF in a premixed flame [73], the possibility to visualizing the behavior of turbulent flames has taken a new step forward. It appears feasible to combine such measurements with high-speed 3D PIV in investigating the temporal 3D flame flow interactions in small segments of suitable flames. In low-swirl flames, the inner region demonstrates propagating flames, of varying complexity with radial distance from the center axis, which could be suitable for demonstration of simultaneous 3D flame front visualization and 3D flow field measurements within the kHz range. If this is successful, information regarding the local 3D displacement velocity of such propagating premixed flames could be derived.

# Acknowledgements

The work was supported by the Swedish Energy Agency through CECOST, Center for Combustion Science and Technology and partially supported by the Swedish Research Council (VR).

I am very grateful to Marcus Aldén who made it possible for me to work in this exiting field and at this pleasant work place – Division of Combustion Physics in Lund.

I am also very grateful to Mark Linne for always believing in me and for introducing me to the study of turbulent flames.

Many thanks to Sven-Inge Möller and Annika Lindholm for assistance and encouragement during the work with pulsating combustion, and specially to Sven-Inge for valuable advice during the writing of the thesis.

Thanks also to Rutger Lorensen for introducing me to the high-pressure combustion facility and for always being a helping hand.

I would like to thank all my present and former colleagues at Combustion Physics for making it such a pleasant place: some I worked with - Christian Brackmann, Robert Collin, Ala Omrane, Hans Seyfried, Johan Zetterberg, Andreas Lantz, Andreas Ehn, Emil Nordstöm, Rikard Wellander, JiaJian Zhu, David Sedarsky; others have always been supporting, helpful and good teachers - Henrik Bladh, Ronald Whiddon, Moah Christensen, Mattias Richter, Per-Erik Bengtsson, Zhongshan Li, Fredrik Ossler, Joakim Bood, and many more..

I would also like to thank my roommate Fahed Abou Nada for his friendliness and for assistance during the preparation of the thesis.

To Minna Ramkull, Cecilia Bille, Anneli Nilsson and Igor Buzuk - thank you for helping med with all the practical things and most important for your friendliness during the years.

A special thanks to Jimmy Olofsson for being a support, for the cooperation with the papers, and sharing my enthusiasm for combustion diagnostics both in Lund and at Dantec.

Many thanks to my former colleagues at Dantec Dynamics, especially to Palle Gjelstrup for taking me into his group and for making the cooperation within CECOST possible.

Many thanks to Xue-Song Bai for guidance within the field of turbulent combustion. Thanks also to his former student, Kalle Nogenmyr, and present students for fruitful discussions and cooperation with the papers in the low-swirl flame study. I would also like to thank Andreas Dreizler, Robert K. Cheng, Christer Fureby, Mohammad Irannezhad, and Andreas Nauert for inspiring discussion and assistance during the low-swirl flame study.

I would also like to thank Magnus Larson, Lennart Jönsson and Lars Bengtsson for introducing me to the field of fluid mechanics.

To friends in Lund and elsewhere - thanks for introducing me to other things than work.

Finally, I would like to thank my family for all love and support during this work – Thank you all!



Perforated plate at the swirler arrangement:

The central channel in the swirler arrangement is 38 mm in diameter, and the entrance is fitted with a perforated plate that has 37 circular holes. Concentric hole distribution, hole diameter  $d=3.6$  mm. Blockage 69.3 %. The plate diameter is 39.6 mm to allow mounting.

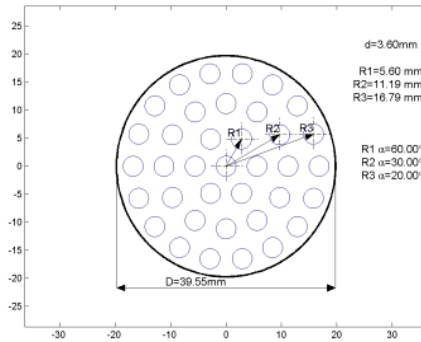


Figure 2 Measures of the perforated plate at the swirler arrangement.

The two perforated plates immediately upstream of the swirler:

First plate 20 mm distance plus (1-2) mm upstream of swirler.

Second plate 30 mm upstream of the first plate.

Both plates has a concentric hole distribution, hole diameter  $d=4.8$  mm. Blockage 45.5 %.

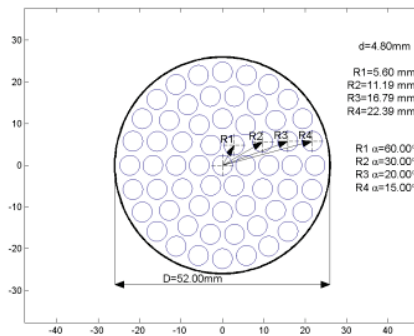


Figure 3 Measures of the perforated plates upstream of the swirler arrangement.

### **3.) Screens in lower part of the burner – plenum**

Order of stainless-steel-screens. Concentric hole distribution, hole diameter  $d=4.8$  mm.

Screen

4 mm Distance ring

Screen

5 mm Distance ring

Screen

10 mm Distance ring

Screen

Inflow ring, tightened by screws

The four inflow tubes into the plenum: 8 mm diameter, 60 mm long.

### **4.) Coflow**

In Lund the coflow diameter was 300 mm to be able to reach a resulting coflow air velocity of  $\sim 0.35$  m/s with the available pressurized air supply.



# References

1. F. Berna, P. Goldberg, L.K. Horwitz, J. Brink, S. Holt, M. Bamford, and M. Chazan, *Microstratigraphic evidence of in situ fire in the Acheulean strata of Wonderwerk Cave, Northern Cape province, South Africa*. Proceedings of the National Academy of Sciences of the United States of America, 2012. **109**(20): p. E1215-E1220.
2. *Key World Energy Statistics*. IEA: International Energy Agency, 2013.
3. Y. Huang and V. Yang, *Dynamics and stability of lean-premixed swirl-stabilized combustion*. Progress in Energy and Combustion Science, 2009. **35**(4): p. 293-364.
4. B. Bedat and R.K. Cheng, *Experimental-Study of Premixed Flames in Intense Isotropic Turbulence*. Combustion and Flame, 1995. **100**(3): p. 485-494.
5. R.K. Cheng, *Velocity and Scalar Characteristics of Premixed Turbulent Flames Stabilized by Weak Swirl*. Combustion and Flame, 1995. **101**(1-2): p. 1-14.
6. H. Pitsch, *Large-eddy simulation of turbulent combustion*. Annual Review of Fluid Mechanics, 2006. **38**: p. 453-482.
7. R. Barlow, *International Workshop on Measurement and Computation of Turbulent NonPremixed Flames*.  
<http://public.ca.sandia.gov/TNF/abstract.html>.
8. H. Tennekes and J.L. Lumley, *A first course in turbulence*, 1972, Cambridge, Mass.,: MIT Press. 300 p.
9. S.B. Pope, *Turbulent flows*, 2000, Cambridge ; New York: Cambridge University Press. 771 p.
10. L.F. Richardson, *Weather Prediction by Numerical Process*. Cambridge University Press, 1922.
11. J.O. Hinze, *Turbulence*. 2d ed. McGraw-Hill series in mechanical engineering 1975, New York: McGraw-Hill. 790 p.
12. A.N. Kolmogorov, *The local structure of turbulence in incompressible viscous fluid for very large Reynolds numbers*. Proceedings of the USSR Academy of Sciences, 1941. **30**: p. 299-303.
13. R. Borghi, M. Destriau, and G. De Soete, *Combustion and flames: chemical and physical principles*, 1998, Paris: Editions Technip. 371 p.
14. C.K. Law, A. Makino, and T.F. Lu, *On the off-stoichiometric peaking of adiabatic flame temperature*. Combustion and Flame, 2006. **145**(4): p. 808-819.
15. H. Pitsch and N. Peters, *A consistent flamelet formulation for non-premixed combustion considering differential diffusion effects*. Combustion and Flame, 1998. **114**(1-2): p. 26-40.

16. T. Poinso, D. Veynante, and S. Candel, *Quenching Processes and Premixed Turbulent Combustion Diagrams*. Journal of Fluid Mechanics, 1991. **228**: p. 561-606.
17. N. Peters, *Laminar flamelet concept in turbulent combustion*. Proceedings of the Combustion Institute, 1988. **21**(1): p. 1231-1250.
18. C.K. Law and C.J. Sung, *Structure, aerodynamics, and geometry of premixed flamelets*. Progress in Energy and Combustion Science, 2000. **26**(4-6): p. 459-505.
19. I.G. Shepherd and R.K. Cheng, *The burning rate of premixed flames in moderate and intense turbulence*. Combustion and Flame, 2001. **127**(3): p. 2066-2075.
20. G. Damköhler, *Elektrochem. Angew. Phys. Chem.*, 1940. **46**.
21. J.F. Driscoll, *Turbulent premixed combustion: Flamelet structure and its effect on turbulent burning velocities*. Progress in Energy and Combustion Science, 2008. **34**(1): p. 91-134.
22. C. Bruno and M. Losurdo, *The trapped vortex combustor: An advanced combustion technology for aerospace and gas turbine applications*. Advanced Combustion and Aerothermal Technologies: Environmental Protection and Pollution Reductions, 2007: p. 365-384.
23. S. Candel, D. Durox, T. Schuller, J.F. Bourgouin, and J.P. Moeck, *Dynamics of Swirling Flames*. Annual Review of Fluid Mechanics, 2014. **Vol. 46**: p. 147-173.
24. A.K. Gupta, D.G. Lilley, and N. Syred, *Swirl flows*, . Energy and engineering science series 1984, Tunbridge Wells, Kent: Abacus Press. 475 p.
25. Z.S. Li, M. Afzelius, J. Zetterberg, and M. Alden, *Applications of a single-longitudinal-mode alexandrite laser for diagnostics of parameters of combustion interest*. Review of Scientific Instruments, 2004. **75**(10): p. 3208-3215.
26. J. Zetterberg, Z.S. Li, M. Afzelius, and M. Alden, *Two-dimensional temperature measurements in flames using filtered Rayleigh scattering at 254 nm*. Applied Spectroscopy, 2008. **62**(7): p. 778-783.
27. J. Westerweel, G.E. Elsinga, and R.J. Adrian, *Particle Image Velocimetry for Complex and Turbulent Flows*. Annual Review of Fluid Mechanics, Vol 45, 2013. **45**: p. 409-+.
28. G.E. Elsinga, F. Scarano, B. Wieneke, and B.W. van Oudheusden, *Tomographic particle image velocimetry*. Experiments in Fluids, 2006. **41**(6): p. 933-947.
29. C.E. Willert, *Assessment of camera models for use in planar velocimetry calibration*. Experiments in Fluids, 2006. **41**(1): p. 135-143.
30. B. Wieneke, *Stereo-PIV using self-calibration on particle images*. Experiments in Fluids, 2005. **39**(2): p. 267-280.
31. A.C. Eckbreth, *Laser diagnostics for combustion temperature and species*. 2.ed. 1996: Gordon & Breach, Amsterdam,.
32. M. Raffel, *Particle image velocimetry : a practical guide*. 2nd ed 2007, Heidelberg ; New York: Springer. 448 p.
33. R.J. Adrian and J. Westerweel, *Particle Image Velocimetry*. Cambridge Aerospace Series 2011, Cambridge ; New York: Cambridge University Press. 558 pages.

34. F. Scarano, *Tomographic PIV: principles and practice*. Measurement Science & Technology, 2013. **24**(1).
35. W.T. Lai, D.C. Bjorkquist, M.P. Abbott, and A.A. Naqwi, *Video systems for PIV recording*. Measurement Science & Technology, 1998. **9**(3): p. 297-308.
36. A. Melling, *Tracer particles and seeding for particle image velocimetry*. Measurement Science & Technology, 1997. **8**(12): p. 1406-1416.
37. F. Battista, F. Picano, G. Troiani, and C.M. Casciola, *Particle clustering in turbulent premixed flames*. Cost Action Mp0806 Particles in Turbulence: International Conference on Fundamentals, Experiments, Numeric and Applications, 2011. **333**.
38. R. Theunissen, F. Scarano, and M.L. Riethmuller, *An adaptive sampling and windowing interrogation method in PIV*. Measurement Science & Technology, 2007. **18**(1): p. 275-287.
39. J.W. Czarske, *Laser Doppler velocimetry using powerful solid-state light sources*. Measurement Science & Technology, 2006. **17**(7): p. R71-R91.
40. A.G. Gaydon and H.G. Wolfhard, *Flames, their structure, radiation, and temperature*. 4th ed 1979: Chapman & Hall.
41. K. Kohse-Höinghaus and J.B. Jeffries, *Applied combustion diagnostics*. Combustion, an international series, 2002, New York: Taylor & Francis. 705 p.
42. W.M. Yen, S. Shionoya, and H. Yamamoto, *Phosphor handbook*. 2nd ed. The CRC Press laser and optical science and technology series 2007, Boca Raton, FL: CRC Press/Taylor and Francis. 1051 p.
43. M. Alden, A. Omrane, M. Richter, and G. Sarner, *Thermographic phosphors for thermometry: A survey of combustion applications*. Progress in Energy and Combustion Science, 2011. **37**(4): p. 422-461.
44. A. Omrane, F. Ossler, and M. Alden, *Two-dimensional surface temperature measurements of burning materials*. Proceedings of the Combustion Institute, 2002. **29**: p. 2653-2659.
45. L.P. Goss, A.A. Smith, and M.E. Post, *Surface Thermometry by Laser-Induced Fluorescence*. Review of Scientific Instruments, 1989. **60**(12): p. 3702-3706.
46. S. Alaruri, T. Bonsett, A. Brewington, E. McPheeters, and M. Wilson, *Mapping the surface temperature of ceramic and superalloy turbine engine components using laser-induced fluorescence of thermographic phosphor*. Optics and Lasers in Engineering, 1999. **31**(5): p. 345-351.
47. N. Fuhrmann, T. Kissel, A. Dreizler, and J. Brubach, *Gd<sub>3</sub>Ga<sub>5</sub>O<sub>12</sub>:Cr-a phosphor for two-dimensional thermometry in internal combustion engines*. Measurement Science & Technology, 2011. **22**(4).
48. J.S. Armfield, R.L. Graves, D.L. Beshears, M.R. Cates, T.V. Smith, and S.W. Allison, *Phosphor thermometry for internal combustion engines*. SAE Technical Papers, 971642, 1997.
49. J.P. Feist, A.L. Heyes, and S. Seefelt, *Thermographic phosphor thermometry for film cooling studies in gas turbine combustors*. Proceedings of the Institution of Mechanical Engineers Part a-Journal of Power and Energy, 2003. **217**(A2): p. 193-200.

50. A. Omrane, G. Sarner, and M. Alden, *2D-temperature imaging of single droplets and sprays using thermographic phosphors*. Applied Physics B-Lasers and Optics, 2004. **79**(4): p. 431-434.
51. J. Brubach, A. Patt, and A. Dreizler, *Spray thermometry using thermographic phosphors*. Applied Physics B-Lasers and Optics, 2006. **83**(4): p. 499-502.
52. J. Linden, N. Takada, B. Johansson, M. Richter, and M. Alden, *Investigation of potential laser-induced heating effects when using thermographic phosphors for gas-phase thermometry*. Applied Physics B-Lasers and Optics, 2009. **96**(2-3): p. 237-240.
53. A. Omrane, P. Petersson, M. Alden, and M.A. Linne, *Simultaneous 2D flow velocity and gas temperature measurements using thermographic phosphors*. Applied Physics B-Lasers and Optics, 2008. **92**(1): p. 99-102.
54. M. Day, S. Tachibana, J. Bell, M. Lijewski, V. Beckner, and R.K. Cheng, *A combined computational and experimental characterization of lean premixed turbulent low swirl laboratory flames I. Methane flames*. Combustion and Flame, 2012. **159**(1): p. 275-290.
55. G.E. Ballachey and M.R. Johnson, *Prediction of blowoff in a fully controllable low-swirl burner burning alternative fuels: Effects of burner geometry, swirl, and fuel composition*. Proceedings of the Combustion Institute, 2013. **34**(2): p. 3193-3201.
56. J.B. Bell, M.S. Day, and M.J. Lijewski, *Simulation of nitrogen emissions in a premixed hydrogen flame stabilized on a low swirl burner*. Proceedings of the Combustion Institute, 2013. **34**(1): p. 1173-1182.
57. P.L. Therkelsen, J.E. Portillo, D. Littlejohn, S.M. Martin, and R.K. Cheng, *Self-induced unstable behaviors of CH<sub>4</sub> and H<sub>2</sub>/CH<sub>4</sub> flames in a model combustor with a low-swirl injector*. Combustion and Flame, 2013. **160**(2): p. 307-321.
58. R.K. Cheng and D. Littlejohn, *Effects of Combustor Geometry on the Flowfields and Flame Properties of a Low-Swirl Injector*. Proceedings of the Asme Turbo Expo 2008, Vol 3, Pts a and B, 2008: p. 393-407.
59. M. Koyama and S. Tachibana, *Technical applicability of low-swirl fuel nozzle for liquid-fueled industrial gas turbine combustor*. Fuel, 2013. **107**: p. 766-776.
60. W. Nazeer, K. Smith, P. Sheppard, R. Cheng, and D. Littlejohn, *Full scale testing of a low swirl fuel injector concept for ultra-low NO<sub>x</sub> gas turbine combustion systems*. Proceedings of the ASME Turbo Expo 2006, Vol 1, 2006: p. 107-115.
61. M.R. Johnson, D. Littlejohn, W.A. Nazeer, K.O. Smith, and R.K. Cheng, *A comparison of the flowfields and emissions of high-swirl injectors and low-swirl injectors for lean premixed gas turbines*. Proceedings of the Combustion Institute, 2005. **30**: p. 2867-2874.
62. N. Peters and B. Rogg, *Reduced kinetic mechanisms for applications in combustion systems*. Lecture notes in physics New series m, Monographs 1993, Berlin ; New York: Springer-Verlag. x, 360 p.
63. A. Bohlin, E. Nordstrom, H. Carlsson, X.S. Bai, and P.E. Bengtsson, *Pure rotational CARS measurements of temperature and relative O<sub>2</sub>-concentration in a low swirl turbulent premixed flame*. Proceedings of the Combustion Institute, 2013. **34**: p. 3629-3636.

64. M. Klein, A. Sadiki, and J. Janicka, *A digital filter based generation of inflow data for spatially developing direct numerical or large eddy simulations*. Journal of Computational Physics, 2003. **186**(2): p. 652-665.
65. K.M. Lyons, *Towards and understanding of the stabilization mechanism of lifted turbulent jet flames: Experiments*. Progress in Energy and Combustion Science, 2007. **33**: p. 211-231.
66. M. Legrand, J. Nogueira, A. Lecuona, S. Nauri, and P.A. Rodriguez, *Atmospheric low swirl burner flow characterization with stereo PIV*. Experiments in Fluids, 2010. **48**(5): p. 901-913.
67. H.Z. Liang and T. Maxworthy, *An experimental investigation of swirling jets*. Journal of Fluid Mechanics, 2005. **525**: p. 115-159.
68. J.C.R. Hunt, A.A. Wray, and P. Moin, *Eddies, stream, and convergence zones in turbulent flows*. Center for Turbulence Research Report, 1988. **CTR-S88**: p. 193-208.
69. C. Heeger, R.L. Gordon, M.J. Tummers, T. Sattelmayer, and A. Dreizler, *Experimental analysis of flashback in lean premixed swirling flames: upstream flame propagation*. Experiments in Fluids, 2010. **49**(4): p. 853-863.
70. C. Abram, B. Fond, A.L. Heyes, and F. Beyrau, *High-speed planar thermometry and velocimetry using thermographic phosphor particles*. Applied Physics B-Lasers and Optics, 2013. **111**(2): p. 155-160.
71. H. Carlsson, E. Nordström, A. Bohlin, Y. Wu, P.-E. Bengtsson, and X.-S. Bai, *Numerical and Experimental study of Flame Propagation and Quenching of Lean Premixed Turbulent Low Swirl Flames at Different Reynolds Numbers*. Submitted for publication.
72. J.A. Mullin and W.J.A. Dahm, *Dual-plane stereo particle image velocimetry (DSPIV) for measuring velocity gradient fields at intermediate and small scales of turbulent flows*. Experiments in Fluids, 2005. **38**(2): p. 185-196.
73. R. Wellander, M. Richter, and M. Aldén, *Time resolved (kHz) 3D imaging of OH PLIF in a flame*. Submitted for publication.



# Contributions to the Papers

## **Paper I**

Simultaneous measurements of the velocity fields (PIV) and the OH distribution, as well as simultaneous measurements of the temperature fields and the OH distribution are presented. Multi-frame OH PLIF simultaneous with single-shot PIV was used for investigate the flame dynamic. Stereo-PIV was applied to capture the three velocity components in both vertically and horizontally planes above the nozzle.

*I participated in the simultaneous PIV and OH PLIF and performed the stereo-PIV measurements. The PLIF measurements and evaluation of the OH data were performed by J. Olofsson together with C. Brackmann and H. Seyfried. Rayleigh thermometry was performed by J. Zetterberg. A. Nauert operated the burner and extracted the statistics from the measurements. The paper was written by me together with A. Nauert, M. Linné, A. Dreizler and with contributions from the persons above performing the PLIF measurements and the Rayleigh thermometry.*

## **Paper II**

This paper includes the first analyses of the flame structure and a comparison between experiments and LES.

*Analyses of the flow and flame properties were performed together with K.J. Nogenmyr who also performed the LES. The paper was written by K.J. Nogenmyr and X.S Bai, with contribution from me and the experimental groups on relevant sections.*

## **Paper III**

In this paper the experimental data were used for comparison with two types of LES turbulent combustion models. New results from simultaneous OH- and fuel-PLIF measurements in low-swirl flames are presented. The effect of combustion models, the numerical solvers and boundary conditions on the flame and flow predictions is systematically examined. Two different inflow boundary conditions are used in order to examine the influence of the details of the swirler on the flow field.

*The new PLIF measurements, presented in detail in Paper IV and V, were performed by R. Collin and A. Lantz. The LES were performed by K.J. Nogenmyr and C. Fureby. The paper was written by K.J. Nogenmyr, me, C. Fureby and X.S. Bai.*

#### **Paper IV**

This paper presents the experimental work concerning simultaneous PIV, OH- and fuel-PLIF measurements in low-swirl flames.

I was responsible for the flow field measurements. R. Collin and A. Lantz performed the PLIF measurements and the post processing of the data. The laser systems were aligned and the data acquisition synchronized with joint forces. The paper was written by me together with R. Collin and A. Lantz.

#### **Paper V**

In this paper the stabilization mechanism of the low swirl flame was investigated and discussed on basis of both experimental results and LES.

*I participated in all the performed measurements, and was responsible for the flow field measurements. R. Collin and A. Lantz performed the PLIF measurements and the post processing of the data. The paper was written by K.J. Nogenmyr, X.S. Bai and with contributions on the experimental part by me, R. Collin and A. Lantz.*

#### **Paper VI**

In this paper simultaneous high-speed PIV and OH PLIF measurements were performed in the low swirl flame. Results were compared with LES.

*I performed the flow field measurements and analyses together with. J. Olofsson. PLIF measurements were performed by R. Wellander who also performed the post processing of the OH images. H. Carlsson was responsible for the LES. He also performed analysis of the LES data together with C. Carlsson. I wrote the experimental part of the paper together with R. Wellander with contribution from B. Beltoft Watz on the modal analyses. H. Carlsson and C. Carlsson wrote the LES part of the paper.*

#### **Paper VII**

Volumetric velocimetry was performed in low-swirl flames.

*The measurements were performed by me together with M. Gesnik, J. Olofsson and V. Jaunet from Dantec. by the candidate. I performed relevant post-processing and wrote the paper with contributions from V. Jaunet and J. Olofsson.*

### **Paper VIII**

In this paper the high-speed chemiluminescence imaging was used to study flames approaching flashback. The reacting flow field was investigated using PIV to add to previously performed LDA and hot-wire measurements of the non-reacting case. The mean flame position prior to flashback was obtained from OH PLIF images. This work was initiated by Prof. A. Dreizler and was carried out partly in Lund and partly at the TU Darmstadt.

*I participated in the measurements performed in Lund. I performed the PIV measurements and relevant post-processing. The paper was written together with A. Nauert, M. Linné and A. Dreizler.*

### **Paper IX**

In the measurement thermographic phosphors were used as temperature sensitive particles and acting as tracer particles for velocity measurements at the same time.

*I was responsible for flow field experiments and relevant post-processing. A. Omrane was in charge of the temperature measurements. The paper was written by A. Omrane with contributions from me concerning the flow field diagnostics.*



# Paper I



# Simultaneous PIV/OH-PLIF, Rayleigh thermometry/OH-PLIF and stereo PIV measurements in a low-swirl flame

Per Petersson,<sup>1,\*</sup> Jimmy Olofsson,<sup>1</sup> Christian Brackman,<sup>1</sup> Hans Seyfried,<sup>1</sup> Johan Zetterberg,<sup>1</sup>  
Mattias Richter,<sup>1</sup> Marcus Aldén,<sup>1</sup> Mark A. Linne,<sup>2</sup> Robert K. Cheng,<sup>3</sup> Andreas Nauert,<sup>4</sup>  
Dirk Geyer,<sup>4</sup> and Andreas Dreizler<sup>4</sup>

<sup>1</sup>Department of Combustion Physics, Lund University, SE-221 00 Lund, Sweden

<sup>2</sup>Sandia National Laboratories, P.O. Box 969, Livermore, California 94551-0969

<sup>3</sup>Environmental Energy Technologies Division, Ernest Orlando Lawrence National Laboratory, Berkeley, California 94720

<sup>4</sup>Energie- und Kraftwerkstechnik, Technische Universität Darmstadt, Petersenstrasse 30, 64287 Darmstadt, Germany

\*Corresponding author: per.petersson@forbrf.lth.se

Received 29 September 2006; revised 14 February 2007; accepted 28 February 2007;  
posted 1 March 2007 (Doc. ID 75632); published 12 June 2007

The diagnostic techniques for simultaneous velocity and relative OH distribution, simultaneous temperature and relative OH distribution, and three component velocity mapping are described. The data extracted from the measurements include statistical moments for inflow fluid dynamics, temperature, conditional velocities, and scalar flux. The work is a first step in the development of a detailed large eddy simulation (LES) validation database for a turbulent, premixed flame. The low-swirl burner used in this investigation has many of the necessary attributes for LES model validation, including a simplified interior geometry; it operates well into the thin reaction zone for turbulent premixed flames, and flame stabilization is based entirely on the flow field and not on hardware or pilot flames. © 2007 Optical Society of America

*OCIS codes:* 120.1740, 280.1740, 280.2470, 280.2490.

## 1. Introduction

One emerging approach to lower NO<sub>x</sub> emissions for applied combustion processes is based on lean premixing of fuel and air. To achieve lowest NO<sub>x</sub> emissions in practical devices, it is desirable to operate these flames close to their lean blow-off limit (LBO). As one example, this concept is commonly applied to modern prototype gas turbine combustors. Unfortunately, lean operation in combustors makes them prone to thermoacoustic instabilities and flame extinction. To mitigate such problems during the development of new combustors, a more detailed understanding based on a deterministic numerical simulation of swirling turbulent premixed flames is necessary [1,2].

The emerging design tools for lean premixed combustors are based on large eddy simulation [3,4] (LES). At the present stage of development, underlying models [subgrid models most often transferred from Reynolds averaged Navier Stokes (RANS) simulations] need to be validated in the context of LES. Although turbulent premixed flames (classified as oblique [5], envelope [6], and unattached flames [7,8]) have been extensively studied experimentally, at present just a few databases suitable for LES validation exist (see, e.g., Ref. 6). Such a validation database should contain information similar to the databases provided for non-premixed target flames studied recently in the framework of the Turbulent Non-Premixed Flames (TNF) workshop [9]. Most important are well-characterized inflow and boundary conditions, information on statistical moments of velocity, temperature, and species concentrations at various locations, structural information such as thermal dissipation, flame surface density, reaction progress, and turbulent length and time

scales. In a combined effort such a database is currently being developed by the authors of this paper. In the work reported here simultaneous PIV (particle image velocimetry) and multishot OH-PLIF (planar laser-induced fluorescence) and simultaneous filtered Rayleigh thermometry and multishot OH-PLIF and stereo PIV experiments are presented.

A suitable generic burner for stabilizing lean premixed flames is required to develop a validation database. The design features of the burner nozzle should make it easy to apply structured meshes common to most research codes used for the numerical simulation of turbulent flames. Complex fluid-flow structures such as intense recirculation zones or even coherent motion and pilot flames for stabilization should be avoided. Despite these constraints, however, a nozzle geometry that is applicable to industrial applications is desirable. The low-swirl concept initiated in 1995 by Cheng and co-workers [10,11] meets most of these conditions. The main characteristics are a detached flame that propagates freely in a diverging, intensely turbulent flow field. Thus very lean flames can be stabilized in a divergent flow that slows in a linear fashion without producing recirculation. This concept has been shown to generate very low  $\text{NO}_x$  levels and is a promising solution for attaining ultralow emission targets [ $<5$  ppm  $\text{NO}_x$  (15%  $\text{O}_2$ ) in stationary gas turbines [12]].

Low-swirl flames have been investigated in a number of laboratories. Unfortunately, no standard design has been employed. Most of the studies use a set of four tangential air jets that superimpose a weak swirl on the turbulent flow of the premixed fuel-air stream [8,13–16]. In other studies the swirl was generated by an annular swirler [12,17]. Although flame series have been partly investigated [14], these different low-swirl flames have served primarily for investigation of the validity of different regime diagrams [14,15], to compare emission characteristics with high swirling flames [12], to investigate systematic changes in flame structure by varying the ratio between turbulence intensity and laminar flame speed ( $u'/s_l$ ) [8], and by varying flame speeds, flow acceleration, and flame crossing frequencies [13]. The operational conditions of these previous studies differ too much to be used collectively for LES validation purposes.

For this project a new low-swirl burner was designed. The burner design includes an annular swirler consisting of eight curved vanes used in connection with a perforated plate fitted to the entrance of the center channel (Fig. 1). This choice of swirl generation was made to avoid dilution of the lean gas mixture by four tangential air jets. Three copies of the newly designed burner were made for comparative studies in different locations. Reproducibility between several burners was then of paramount importance. To reproduce the same swirl condition in three different burners in three locations would be more certain with fixed vanes than with air jets. The matched burners were fabricated in the same machine shop at the same time, and tolerances were very tightly held.

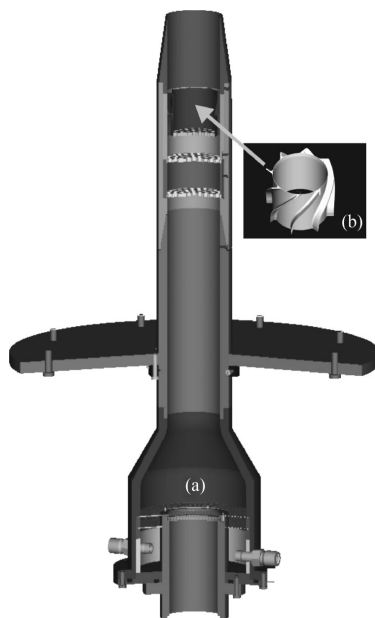


Fig. 1. (a) Cross section of burner without swirl assembly. Premixed air and fuel enter via four nozzles (two visible) and pass several perforated plates before reaching the swirler. (b) Swirl assembly; arrow marks the location where the assembly is installed.

## 2. Experimental Methods

The low-swirl burner used here is different from the original design [8] in that eight vanes are used to impart swirl in the flow rather than four tangential jets. In addition, this burner has a nozzle with a long bezel on the outside so that the inner flow does not change area before exiting into the surroundings. The inner diameter of the nozzle is 50 mm. This design also avoids generating any recirculation at the nozzle exit. Furthermore, the burner assembly was mounted in a 600 mm wide co-flow of air. This necessitated a slim outer shape of the burner, and any obstacles (e.g., air swirler tubes) in the co-flow needed to be avoided. A wide co-flow was necessary to ensure that no dust particles were entrained from the laboratory environment. This is crucial especially for single-shot 1D Raman and conventional Rayleigh measurements on the same flames where dust caused optical breakdown otherwise [18]. All mass flows were controlled by electronic mass flow controllers (Bronkhorst, The Netherlands).

Two operational points were selected for study, LSF-1 (27 kW) and LSF-2 (40 kW), both with a fuel-air ratio  $\phi = 0.62$  (see Table 1). The flames were classified to lie within the thin reaction zone of the revised regime diagram [19]. To infer this designation, the laminar flame speed  $s_l$  and the corresponding laminar flame thickness  $l_f$  were based on data

**Table 1. Operational Points and Characteristics of Lean Premixed Methane–Air Flames**

Flow Designator	$u_{\text{exit}}$ [m/s]	$Re_{\text{exit}}$	P [kW]	$\phi$
LSF-1	6.2	20,000	27	0.62
LSF-2	9.3	30,000	40	0.62

taken from a flamelet library [20]. Taylor’s hypothesis of frozen turbulence was used to obtain the integral length scales from measured laser Doppler velocimetry (LDV) time series.

For flows such as this one, the swirl number  $S$  is expected to land in the range of 0.5 [21], but to accurately calculate the value of  $S$  based on geometry is difficult because it depends on the pressure drop across the various flow channels (the holes in the perforated plate and the swirler channels in this case). Here stereo PIV data taken in the horizontal plane for flow LSF-1 at a position 2 mm above the nozzle were used to calculate the swirl number, based on the ratio of the axial flux of tangential momentum over the axial flux of axial momentum. In the current configuration a relatively large fraction is passing through the perforated plate, approximately 40% by volume, yielding a swirl number  $S \approx 0.55$ .

Two separate laser systems were used for simultaneous PIV/PLIF measurements. The counterpropagating laser beams were formed into overlapping sheets to illuminate a planar region of the flame, crossing the vertical centerline of the burner. A schematic of the setup is shown in Fig. 2. A similar arrangement was used for the simultaneous Rayleigh thermometry/PLIF measurements. To simplify the alignment of the setup special alignment tools were manufactured. One tool had a transparent grid for the alignment of the cameras, and one tool had a centered slit for alignment of the counterpropagating laser sheets and for PIV sheet thickness control. The tools had a perfect fit in the burner nozzle and could easily be mounted for alignment.

For PIV the beams from two frequency doubled Nd:YAG lasers (Quantel, France) were overlapped to provide successive Mie scattering from the seed particles. In the probe volume the light sheet had a height of 60 mm and a thickness of  $\sim 700 \mu\text{m}$  for the two-component measurements and  $\sim 1 \text{ mm}$  for the three-component measurements. The energy in each pulse was approximately 40 mJ, and the pulse separation was optimized for each field of view and choice of interrogation window.

When the full width of the flame was imaged the field of view was approximately  $60 \text{ mm} \times 50 \text{ mm}$ , and a relatively short pulse separation,  $\Delta t = 30\text{--}50 \mu\text{s}$ , was applied to capture high axial and out of plane velocities in the outer part of the flame. When only the low velocity core of the flow field was investigated the field of view was  $30 \text{ mm} \times 25 \text{ mm}$ , and a  $\Delta t = 100\text{--}200$  could be used. For imaging an interline-transfer CCD camera (Flowmaster 3S, La Vision, Germany) with  $1280 \times 1024$  pixels was used. For evaluation of the velocities, a cross-correlation algorithm with an adaptive multi-pass method developed by LaVision was used. The spatial resolution for the PIV measurements equals the sizes of the interrogation windows, for both cases  $32 \times 32$  pixels, and the sheet thickness. Hence the spatial resolution is approximately  $0.8 \text{ mm} \times 0.8 \text{ mm} \times 0.7 \text{ mm}$  (1 mm for stereo PIV) for the high spatial resolution case, and  $1.6 \text{ mm} \times 1.6 \text{ mm} \times 0.7 \text{ mm}$  (1 mm for stereo PIV) for the low spatial resolution case.

For stereo PIV a second CCD camera (Imager Intense 1376  $\times$  1040, La Vision) was installed, and both cameras were fitted with Scheimpflug adaptors. The angle between the image plane of the cameras and the object plane was  $45^\circ$ . A two-level calibration plate (La Vision) was used for alignment of the laser sheet, cameras and for sheet thickness adjustment ( $\sim 1 \text{ mm}$ ). With the two-level plate two different calibration planes can easily be imaged without moving the plate. To relate the coordinate system of the two cameras to the laboratory reference frame, four mapping functions are necessary, one for each calibration plane. The mapping functions are based on a pinhole model (software Davis 7.0, La Vision) that also makes it possible to use a self-calibration procedure based on cross correlation on simultaneous exposed images by the two cameras. In case of any displacement between the calibration plate and the light sheet a field of disparity vectors is created and used for misalignment corrections [22].

Dry  $0.5 \mu\text{m}$  sized  $\text{ZrSiO}_4$  particles were used as seed material. Velocity fluctuations up to 7 kHz could be resolved with a slip of less than 1%. Two seeders were installed to provide seeding to the methane–air mixture and the co-flowing air individually. To assure stable and reproducible seeding densities, the  $\text{ZrSiO}_4$  was sieved into a bypass of the respective gas flows. For this purpose a combination of static mesh and rotating brush was installed at the bottom of an adequately dimensioned  $\text{ZrSiO}_4$  storage tank. The speed of the motor driving the rotating mesh and the bypass ratio determined the seeding density. The seeding density was adjusted to meet the standard PIV criterion of a minimum of ten particles in the interrogation windows, even in the hot expanded region.

To achieve laser-induced fluorescence from OH, and to track the OH propagation in time, the multi-YAG laser cluster at LTH Lund was used (see Fig. 3). The system is described thoroughly in Ref. 23. The cluster consists of four individual, Q-switched

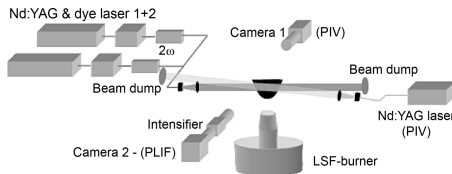


**Fig. 2. Schematic of the experimental setup for simultaneous PIV/OH-PLIF measurements.**

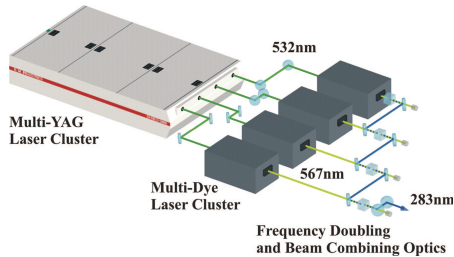


Fig. 3. (Color online) Multi-YAG laser cluster at LTH Lund.

Nd:YAG lasers (BMI), with an output wavelength of 532 nm. Each of these was used to pump a dye laser (Sirah) operating on a Rhodamine 590 dye solution in methanol. The problems with beam profile deterioration and severe pulse energy losses, which occur when a single dye laser is pumped by a rapid burst from the multi-YAG, are circumvented when using several dye lasers. The outputs from the dye lasers were then frequency doubled and superimposed to a single beam path by means of dichroic mirrors. The UV laser beams were formed into sheets of thickness  $\sim 300 \mu\text{m}$  in the probe volume region. The energy in each pulse was approximately 2 mJ. OH radicals were excited via the  $Q_1(8)$  transition of the ( $v' = 1, v'' = 0$ ) band in the A-X system at approximately 283 nm (Ref. 24) with a fairly temperature-insensitive population distribution in the  $N = 8$  level. Fluorescence from the A-X (1, 1) and (0, 0) bands (near 310 nm) was detected using an UV lens (Nikkor, Japan,  $f = 105 \text{ mm}$ ,  $f/\# = 4.5$ ). A bandpass filter and a *UG11*-filter (Schott, Germany) suppressed spurious light efficiently, while long-pass OH detection filters included a high reflector from 275–295 nm and a highly transmissive filter for wavelengths greater than 295 nm.

To allow for multiframe, time-resolved PLIF images, a high-speed framing camera (Hadland, UK) with eight individual ICCD modules was used [23], enabling acquisition of up to eight frames in rapid succession. The camera was fitted with an image intensifier unit for UV detection and the smallest resolvable unit for this arrangement was approximately  $300 \mu\text{m}$ . For this investigation a sequence of four PLIF images was captured with this camera with a  $\Delta t = 200\text{--}400 \mu\text{s}$ . The time delay was chosen so that the flame front motion could be studied. For each OH-PLIF sequence, a PIV recording was synchronized with the second image in the sequence. The PIV and PLIF imaging were controlled from different computers. The synchronization of the 8 Hz PIV lasers and the 10 Hz LIF lasers was achieved with external timing equipment. For each investigated flame condition 1500 joint PIV and OH-PLIF sequences were collected to generate statistics.

For higher spatial resolution fluorescence detection a second interline-transfer CCD camera (Imager Intense  $1376 \times 1040$ , La Vision) was equipped with an

image intensifier (Hamamatsu, Japan). With this setup and a field of view of  $34 \text{ mm} \times 26 \text{ mm}$  the smallest resolvable unit was approximately  $100 \mu\text{m}$ . By using two of the Nd:YAG lasers in the laser cluster a sequence of two OH-PLIF images could be captured for tracking the flame front movement. The camera was connected to the PIV computer, allowing both PIV raw data and OH-PLIF images to be collected and stored in the same image file. This simplified the data evaluation considerably. Laser irradiance profiles were recorded online by reflecting the laser sheets into a cell containing fluorescing dye. The resulting dye LIF signals were imaged onto the detector concurrently with the OH-PLIF images. The beam profiles were used in a postprocessing step to normalize OH-PLIF data on a shot-by-shot basis. Previous experience has established that OH and dye PLIF signals are linear when the system is operated as it was in this work.

For Rayleigh thermometry the filtered Rayleigh scattering [25] (FRS) approach was used. FRS exploits the fact that Doppler broadening increases with temperature. By using a narrowband excitation for Rayleigh scattering in connection with an atomic or molecular notch filter resonant with the excitation wavelength in front of a camera system, increasing Doppler widths are converted to enlarged leakage around the notch, generating increasing signal levels. By proper calibration and modeling of the convolution among spectral profiles of the laser, notch, and Doppler width, signal strengths can be transformed into temperatures. The present FRS approach is described in detail in Ref. 26. In brief, a single-longitudinal mode pulsed (90 ns) alexandrite laser (PAL 101, Light Age, Somerset, New Jersey) with a linewidth of 100 MHz and a pulse energy of 30 mJ was tuned on the resonance of single-isotope atomic mercury  $\text{Hg}^{202}$  at 254 nm. Mercury was contained at 300 K in a 7 cm long quartz cell ( $10^{-3}$  Torr) directly in front of an ICCD camera (Roper Scientific, Germany, PIMAX). The mercury absorption notch width of  $\sim 2$  GHz was dominated by Doppler broadening under these conditions. The use of isotope-enhanced mercury simplified the absorption profile of the filter to produce a single hyperfine line structure. This facilitated a proper notch filter model. The Rayleigh scattering line profile was modeled with the S6 model to include Brillouin contributions, and the total Rayleigh cross section in the burned gases was estimated with the unburned gases. The cross section for a burned gas composition for complete reaction of methane differs from that of the unburned gases by less than 1.3%. The potential of FRS to suppress Mie scatter from seed particles is an attractive feature, the goal being simultaneous PIV and FRS. In the present study the seeding density required for good PIV spatial resolution was relatively high, to facilitate extraction of statistical moments across the flame front. Unfortunately, the Mie scattering from particles in the flow proved too large to be removed by the atomic filter. Future experiments will reduce the seed density so

that only features at typical LES grid scales and larger are imaged simultaneously with FRS. For this investigation, simultaneous FRS and multishot OH-PLIF were captured in a similar manner as for the PIV/OH-PLIF imaging. For each investigated flame condition 600 joint FRS and OH-PLIF sequences were collected to generate statistics.

### 3. Results and Discussions

The measurement techniques, the specific flow rates and the equivalence ratios selected for this work are somewhat different from those of Cheng and co-workers [8,10–14,16,17], but the findings of the program described here are consistent with the results published by that group.

Figure 4 shows an ensemble averaged image of 500 stereo PIV recordings for LSF-2. One can see that the flow slows approximately linearly with height, reaching a very slow zone in the core at  $x = 61$  mm, and that no mean tangential component (e.g., swirl) exists in the core. In the core region turbulent flames are hydrodynamically stabilized where the mean flow has slowed to a point where it matches the flame propagation. The swirling flow at the outer edge is symmetric and reproducible, offering opportunities for investigation of a sheared, stratified premixed flame. Stereo PIV taken in horizontal planes demonstrates that the eight vanes actually impose a small but observable structure in the swirling flow, but this does not propagate to the center, and it decays with height. Figure 5 shows a combined PIV/OH-PLIF image of the LSF-2 flame, and it illustrates a common, reoccurring flame shape.

To capture the inflow conditions, stereo PIV was applied to the outlet of the annular swirl assembly

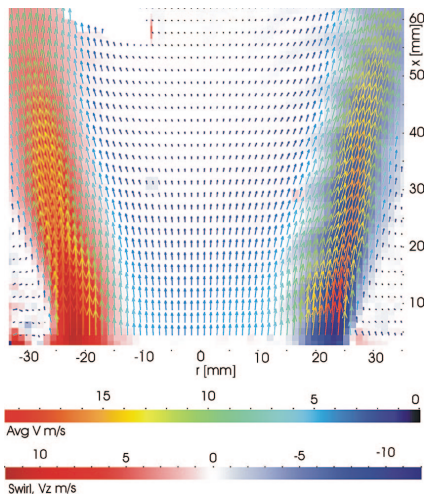


Fig. 4. (Color online) Ensemble average of 500 single-shot stereo PIV images for LSF-2 (flow is going into the paper on the right side; note that a few vectors were lost in the upper left of the image).

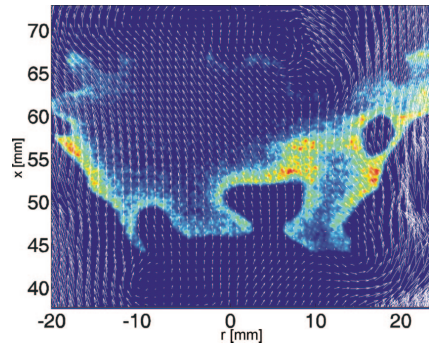


Fig. 5. (Color online) Combined single-shot PIV/OH-PLIF image for LSF-2 ( $r$  = radial distance,  $x$  = height above nozzle).

and at the outlet of the nozzle as it entered the surroundings. Radial profiles of mean and fluctuations of velocity components at the exit of the swirler are presented in Fig. 6. These results were acquired with the nozzle removed, thereby imposing a radial component that does not exist at that location when the nozzle is in place. The data are useful as a specific test of a swirler model, however, if the swirler has been included in a computational domain. One can observe that there are significant differences between the data extracted just above a swirler passage and those extracted just above a swirler vane, but this is not surprising. The profiles, however, are fairly symmetric. Next, radial profiles of mean and fluctuations of velocity components at the exit of the nozzle are presented in Fig. 7. One can observe relatively symmetric mean profiles, no swirl at the center, and the rms values reach a minimum at the centerline.

Figure 8 shows a single-shot FRS temperature recording (top) followed by a sequence of four OH-PLIF images with a  $\Delta t = 400 \mu\text{s}$ . It can be seen from the OH field that the inner part of the flame, where the flow is close to 2D on average, is not changing significantly. In the outer regions the swirl, the average flow velocity, and the flow fluctuations all increase in

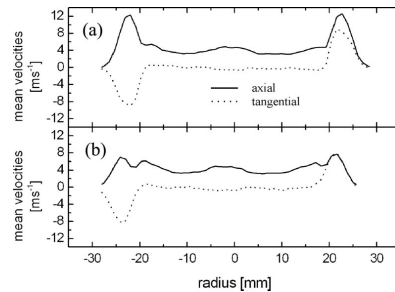


Fig. 6. Exit velocity profiles of swirler for LSF-1 (2 mm downstream). Mean axial and tangential velocities (a) crossing over the center of a flow passage and (b) crossing over the center of a vane.

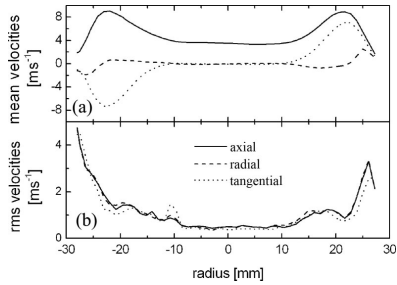


Fig. 7. Exit velocity profiles of nozzle for LSF-1 (2 mm downstream). (a) Mean axial, radial, and tangential velocities and (b) respective rms values.

strength. All these factors increase the interaction between the flame and the flow, and rapid changes in the observed flame structure can occur. The single-shot FRS recording is synchronized with the second image in the OH-PLIF sequence. The resolution in the single-shot FRS image is sufficient to match the PLIF and FRS images and to deduce temperature data around the flame front, the single-shot signal-to-noise ratio for FRS in the present setup is 5–10:1 depending on temperature.

Figure 9 contains radial profiles of temperature from both LSF-1 and LSF-2, acquired using FRS. The adiabatic flame temperature for such a flame is 1705 K, which is almost reached in the postflame zones (at 40–45 mm, the flow is almost always in the burned flame zone), especially for LSF-2. The rms values for each profile are also shown, and they indicate wide variation in temperature at each location, especially for LSF-1. Note also that the peak temperature for LSF-1 at  $x = 35.4$  mm is well below 1700 K. This is caused mainly by the fact that measurements are made sometimes in burned and sometimes in unburned gases owing to the large-scale structures of the flame front, (see Fig. 5), and the front dynamics. This fact can also explain the high rms fluctuations encountered.

A 2D plot of the Reynolds mean reaction progress variable  $\bar{c}$  is shown in Fig. 10 for flow LSF-2. The mean reaction progress variable,  $\bar{c}$ , is 0 in the unburned state and 1 in the fully reacted state. The values between 0 and 1 correspond to locations within the turbulent flame brush. A binary mask is created from the instantaneous OH-PLIF images, indicating only burned and unburned zones. Ensemble averaging of all the instantaneous mask images (approximately 6000 images) provides the Reynolds mean reaction progress [27–29]. Axial plots of  $\bar{c}$  are shown in Fig. 11. From these one can extract the mean flame front location (at  $\bar{c} = 0.5$ ); for LSF-1 it is 33 mm, and for LSF-2 it is 32 mm. In addition, the distance between  $\bar{c} = 0.1$  and  $\bar{c} = 0.9$  can be taken as the width of the flame brush; it is equal to 17 mm for LSF-1 and 15 mm for LSF-2.

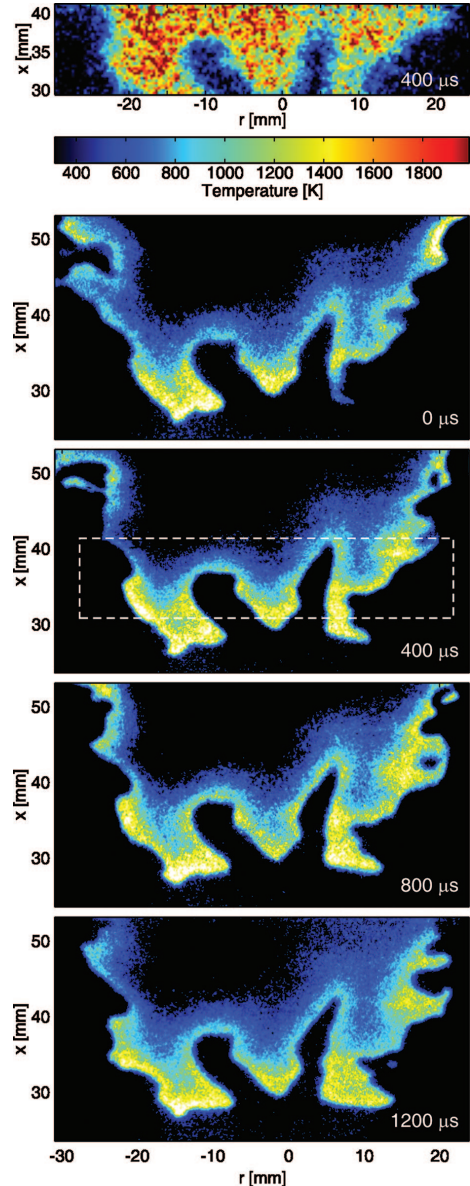


Fig. 8. (Color online) Single-shot FRS temperature image (top) followed by a sequence of four OH-PLIF images with a  $\Delta t = 400 \mu\text{s}$ .

The results from the simultaneous PIV and PLIF measurements were used to determine the conditional velocities (see below) and for increased understanding of the flame–flow interaction. Figure 12

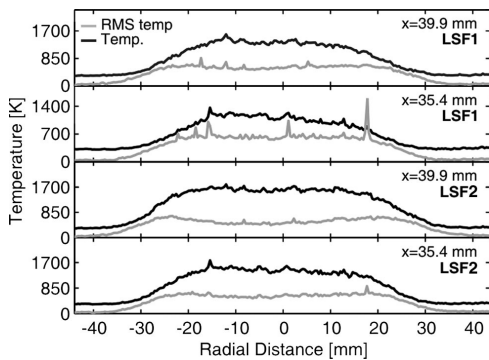


Fig. 9. Radial profiles of temperature and rms values.

shows a combined PIV/OH-PLIF image in the upper part of the flame for LSF-2. In this region of the flame the flow field is more complicated and the flame–flow interaction strong. The entrainment of air also successively dilutes the air–fuel mixture, and extinction can finally occur. This phenomenon was important to study and became a challenge to capture in the ongoing LES modeling of the present flame [30].

Conditional velocities were extracted using combined PIV and OH-PLIF images at three different radial positions (centerline, 6 mm from the centerline, and 12 mm from the centerline). As shown in Fig. 5 the flame is highly contorted, and, for this reason, conditional velocities were extracted normal to the flame front. For each radial location data were collected from five adjacent cells, centered around the investigated radial location, with a cell size of  $32 \times 32$  pixels. The flame front location for each OH image was identified near the center and at the left and right border of each cell. Using these data the best corresponding velocity vector on both sides of the flame front could be taken from the PIV data. Therefore only velocity vectors immediately adjacent to the

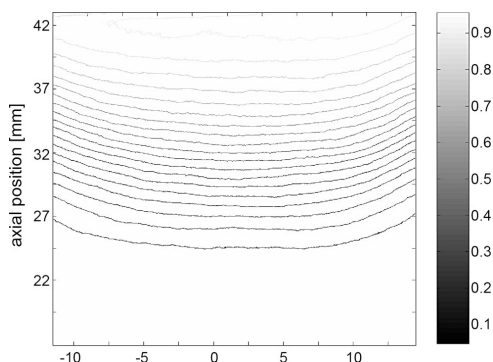


Fig. 10. Contour plot of the mean reaction progress variable for LSF-2.

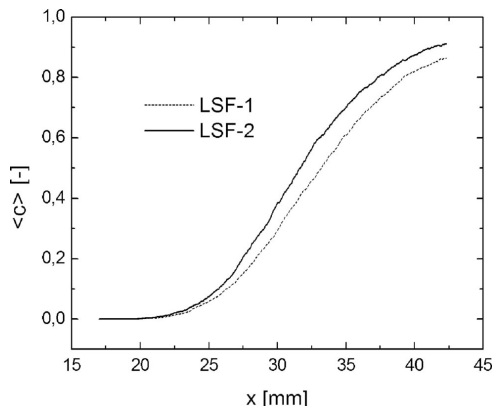


Fig. 11. Axial dependence of the mean reaction progress variable.

flame front (within approximately 1 mm) are considered. This corresponds to the strip-conditioned velocities introduced in Ref. 28. Also, the local flame front angle was determined for extracting the velocity components normal to the flame front. The influence of the flame front angle on the conditional velocities was further investigated by processing data with low flame angle ( $<45^\circ$ ) and steep flame angles ( $>45^\circ$ ), respectively. No conclusive differences in the conditional data were observed for these two flame angle intervals. The uncertainties attributable to particle thermophoretic transport were estimated in Ref. 28 for premixed methane–air flames of  $\phi = 0.6$  to be  $\bar{u}_{TP,b} = 0.02$  m/s at the burned side and independent of strain. This value is low compared to the mean velocities at locations where  $\bar{c} = 0.5$  and can thus be neglected.

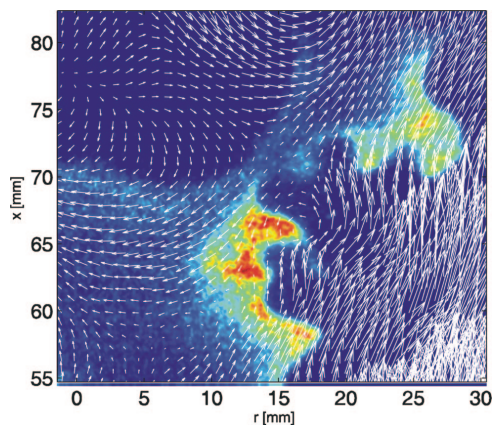


Fig. 12. (Color online) Combined single-shot PIV/OH-PLIF image in the upper part of the flame for LSF-2.

Table 2. Conditional Velocities and Scalar Fluxes at  $\bar{c} = 0.5$  for the Flames Described in Table 1

Flow Designator	Location	$\bar{u}_b$ [m/s]	rms <sub>b</sub> [m/s]	$\bar{u}_u$ [m/s]	rms <sub>u</sub> [m/s]	$\overline{\rho u'' c''}$ [kg/sm <sup>2</sup> ]
LSF-1	cl <sup>a</sup>	0.46	0.35	0.33	0.34	0.01095
LSF-1	6 mm from cl	0.51	0.46	0.37	0.46	0.01149
LSF-1	12 mm from cl	0.28	0.72	0.20	0.60	0.00663
LSF-2	cl	0.49	0.44	0.41	0.45	0.00694
LSF-2	6 mm from cl	0.37	0.55	0.31	0.58	0.00495
LSF-2	12 mm from cl	0.20	0.78	0.16	0.81	0.00211

<sup>a</sup>cl denotes centerline.

The conditional velocity data for  $\bar{c} = 0.5$  are presented in Table 2. The quantities  $\bar{u}_b$  and  $\bar{u}_u$  denote conditional mean velocities in the burned and unburned regions deduced from the conditional PIV data. For flame LSF-1 and for all three radial positions considered,  $\bar{u}_b$  exceeds  $\bar{u}_u$  by approximately 40%, which is clearly above the uncertainties related to thermophoretic transport. Thus countergradient diffusion associated with thermal expansion and the acceleration of fluid passing the flame front dominates in this flow. For flame LSF-2 the Reynolds number is higher than for LSF-1. However, the measurements of the conditional velocities indicate as well that  $\bar{u}_b$  exceeds  $\bar{u}_u$  but only by approximately 20%. Countergradient diffusion still dominates this flame.

As is obvious from Table 2, the conditional turbulence level increases with increasing radial position. This is in accordance with the trends depicted in Fig. 7(b). The enhanced velocity fluctuations farther away from the centerline are attributable to higher shear.

Scalar fluxes were extracted from the data by applying the BML model [31], as described in Refs. 28, 32, and 33, via the following:

$$\overline{\rho u'' c''} = \bar{\rho} \bar{c} (1 - \bar{c}) (\bar{u}_b - \bar{u}_u). \quad (1)$$

The Favre-averaged reaction progress  $\bar{c}$  is calculated from

$$\bar{c} = \frac{\bar{c}}{\bar{c} + \frac{\rho_u}{\rho_b} (1 - \bar{c})}. \quad (2)$$

The densities in the burned ( $\rho_b$ ) and unburned regions ( $\rho_u$ ) are taken from laminar flamelet calculations assuming adiabatic conditions (CHEM1D [34], 16-step reaction mechanism [35]). The Reynolds mean reaction progress variable  $\bar{c}$  is taken from the ensemble averaged binarized instantaneous OH images as previously described.

The calculated scalar fluxes are also contained in Table 2. More data will be extracted from new measurements higher up in the flame brush for  $\bar{c} > 0.8$ .

#### 4. Conclusions

A number of laser diagnostics were applied to a low-swirl flame to measure flow-field velocity, relative OH distribution, and temperature. In keeping with the

spatial orientation of LES, imaging and statistical moments extracted from the images are emphasized. We report statistical moments for inflow fluid dynamics, temperature, and conditional velocities. In addition, the progress variable was extracted from the OH distributions, and from this the scalar flux was deduced. We have described the initial results in the development of a detailed validation database for a turbulent, premixed flame.

The low-swirl design has been chosen for this work because it has many of the necessary attributes for LES model validation, including a simplified interior geometry, it operates well into the thin reaction zone of the regime diagram, and flame stabilization based entirely on the flow field and not on hardware or pilot flames. Initial experiments have demonstrated that a stable and symmetric flame can be achieved and that various regions of the flame offer opportunities to study 2D turbulent flames in the core, while the outer edge offers the opportunity to investigate stratified lean, premixed flames with local extinction.

Future work will focus on further analysis of the data, additional temperature measurements, and measurement of the flow inside the nozzle. The data will be organized in a usable form and made available together with information on boundary conditions and estimated measurement accuracies to model developers wishing to make use of it.

Financial support through Sonderforschungsbe- reich 568, project B1 (Darmstadt), the Swedish Energy Agency, the Swedish Research Council, the Swedish Foundation for Strategic Research (Lund), and the European Union Large Scale Facility in Combustion (contract HPRI-CT-2001-00166) is acknowledged.

#### References

1. R. J. Santoro, "Applications of laser-based diagnostics to high pressure rocket and gas turbine combustor studies," in *Proceedings of the 20th AIAA Advanced Measurement and Ground Testing Technology Conference* (AIAA, 1998), paper 98-2698.
2. A. Dreizler and J. Janicka, "Diagnostic challenges for gas turbine combustor model validation," in *Applied Combustion Diagnostics*, K. Kohse-Höinghaus and J. Jeffries, eds. (Taylor & Francis, 2002), p. 561.
3. H. Pitsch, "Large-Eddy simulation of turbulent combustion," *Annu. Rev. Fluid Mech.* **38**, 453–482 (2006).
4. J. Janicka and A. Sadiki, "Large Eddy simulation of turbulent combustion systems," *Proc. Combust. Inst.* **30**, 537–548 (2005).

5. A. Soika, F. Dinkelacker, and A. Leipertz, "Measurement of the resolved flame structure of turbulent premixed flames with constant Reynolds number and varied stoichiometry," *Proc. Combust. Inst.* **27**, 785–792 (1998).
6. Y.-C. Chen, N. Peters, G. A. Schneemann, N. Wruck, U. Renz, and M. S. Mansour, "The detailed structure of highly stretched turbulent premixed methane-air flames," *Combust. Flame* **107**, 223–244 (1996).
7. E. J. Stevens, K. N. C. Bray, and B. Lecordier, "Velocity and scalar statistics for premixed turbulent stagnation flames using PIV," *Proc. Combust. Inst.* **27**, 949–955 (1998).
8. B. Bédard and R. K. Cheng, "Experimental study of premixed flames in intense isotropic turbulence," *Combust. Flame* **100**, 485–494 (1995).
9. R. S. Barlow, International Workshop on Measurement and Computation of Turbulent Non-Premixed Flames, <http://www.ca.sandia.gov/TNF/>
10. C. K. Chan, K. S. Lau, W. K. Chin, and R. K. Cheng, "Freely propagating open premixed turbulent flames stabilized by swirl," *Proc. Combust. Inst.* **24**, 511–518 (1992).
11. R. K. Cheng, D. T. Yegian, M. M. Miyasato, G. S. Samuelsen, R. Pellizzari, P. Loftus, and C. Benson, "Scaling and development of low-swirl burners for low-emission furnaces and boilers" *Proc. Combust. Inst.* **28**, 1305–1313 (2000).
12. M. R. Johnson, D. Littlejohn, W. Nazeer, K. O. Smith, and R. K. Cheng, "A comparison of the flowfields and emissions of high-swirl injectors and low-swirl injectors for lean premixed gas turbines," *Proc. Combust. Inst.* **30**, 2867–2874 (2005).
13. R. K. Cheng, "Velocity and scalar characteristics of premixed turbulent flames stabilized by weak swirl," *Combust. Flame* **101**, 1–14 (1995).
14. R. K. Cheng, I. G. Shepherd, B. Bédard, and L. Talbot, "Premixed turbulent flame structures in moderate and intense isotropic turbulence," *Combust. Sci. Technol.* **174**, 29–59 (2002).
15. C. Kortschik, T. Plessing, and N. Peters, "Laser optical investigation of turbulent transport of temperature ahead of the preheat zone in a premixed flame," *Combust. Flame* **136**, 43–50 (2004).
16. T. Plessing, C. Kortschik, N. Peters, M. S. Mansour, and R. K. Cheng, "Measurements of the turbulent burning velocity and the structure of premixed flames on a low swirl burner," *Proc. Combust. Inst.* **28**, 359–366 (2000).
17. R. K. Cheng, D. Littlejohn, W. Nazeer, and K. O. Smith, "Laboratory studies of the flow field characteristics of low-swirl injectors for adaptation to fuel-flexible turbines," *ASME Turbo Expo GT2006-90878* (2006).
18. D. Geyer, A. Kempf, A. Dreizler, and J. Janicka, "Scalar dissipation rates in isothermal and reactive turbulent opposed jets: 1D-Raman/Rayleigh experiments supported by LES," *Proc. Combust. Inst.* **30**, 681–689 (2005).
19. N. Peters, *Turbulent Combustion* (Cambridge U. Press, 2000), p. 78.
20. P. Wang and X. S. Bai, "Large Eddy simulation of turbulent premixed flames using level-set G-equation," *Proc. Combust. Inst.* **30**, 583–591 (2005).
21. D. Littlejohn, A. J. Majeski, S. Tonse, C. Castaldini, and R. K. Cheng, "Laboratory investigation of an ultra-low NO<sub>x</sub> premixed combustion concept for industrial boilers," *Proc. Combust. Inst.* **29**, 1115–1121 (2002).
22. B. Wieneke, "Stereo-PIV using self-calibration on particle images," *Exp. Fluids* **39**, 267–280 (2005).
23. J. Hult, M. Richter, J. Nygren, M. Aldén, A. Hultqvist, M. Christensen, and B. Johansson, "Application of a high-repetition-rate laser diagnostic system for single-cycle-resolved imaging in internal combustion engines" *Appl. Opt.* **41**, 5002–5014 (2002).
24. LIFBASE: Database and spectral simulation, <http://www.sri.com/psd/lifbase/>.
25. R. B. Miles, J. N. Forkey, and W. R. Lempert, "Filtered Rayleigh scattering measurements in supersonic/hypersonic facilities," *AIAA paper 92-3894* (1992).
26. J. Zetterberg, Z. S. Li, M. Afzelius, and M. Aldén, "Applications of a single-longitudinal-mode alexandrite laser for diagnostics of combustion interest," *Rev. Sci. Instrum.* **75**, 3208–3215 (2004).
27. P. A. M. Kalt, J. H. Frank, and R. W. Bilger, "Laser imaging of conditional velocities in premixed propane/air flames by simultaneous OH PLIF and PIV," *Proc. Combust. Inst.* **27**, 751–758 (1998).
28. J. H. Frank, P. A. M. Kalt, and R. W. Bilger, "Measurement of conditional velocities in turbulent premixed flames by simultaneous OH PLIF and PIV," *Combust. Flame* **116**, 220–232 (1999).
29. A. Nauert and A. Dreizler, "Conditional velocity measurements by simultaneously applied laser Doppler velocimetry and planar laser-induced fluorescence in a swirling natural gas/air flame," *Z. Phys. Chem.* **219**, 635–648 (2005).
30. K.-J. Nogenmyr, P. Petersson, X. S. Bai, A. Nauert, J. Olofsson, C. Brackman, H. Seyfried, J. Zetterberg, Z. S. Li, M. Richter, A. Dreizler, M. Linne, and M. Aldén, "Large Eddy Simulation and experiments of stratified lean premixed methane/air turbulent flames," *Proc. Combust. Inst.* **31**, 1467–1475 (2007).
31. K. N. C. Bray, P. A. Libby, and J. B. Moss, "Flamelet crossing frequencies and mean reaction rates in premixed turbulent combustion," *Combust. Sci. Technol.* **41**, 143–172 (1984).
32. P. A. M. Kalt, Y.-C. Chen, and R. W. Bilger, "Experimental investigation of turbulent scalar flux in premixed stagnation-plate flames," *Combust. Flame* **129**, 401–415 (2002).
33. D. Most, F. Dinkelacker, and A. Leipertz, "Direct determination of the turbulent flux by simultaneous application of filtered Rayleigh scattering thermometry and particle image velocimetry," *Proc. Combust. Inst.* **29**, 2669–2677 (2002).
34. CHEMID, "A one-dimensional laminar flame code," Eindhoven University of Technology, <http://www.combustion.tue.nl/chem1d>.
35. M. D. Smooke and V. Giovangigli, *Reduced Kinetic Mechanisms and Asymptotic Approximations for Methane-Air Flames*, M. D. Smooke, ed. (Springer, 1991), p. 1R28.



## Paper II





ELSEVIER

Available online at [www.sciencedirect.com](http://www.sciencedirect.com)

 ScienceDirect

Proceedings of the Combustion Institute 31 (2007) 1467–1475

Proceedings  
of the  
Combustion  
Institute

[www.elsevier.com/locate/proci](http://www.elsevier.com/locate/proci)

# Large eddy simulation and experiments of stratified lean premixed methane/air turbulent flames

K.-J. Nogenmyr<sup>a</sup>, P. Petersson<sup>b</sup>, X.S. Bai<sup>a,\*</sup>, A. Nauert<sup>c</sup>, J. Olofsson<sup>b</sup>,  
C. Brackman<sup>b</sup>, H. Seyfried<sup>b</sup>, J. Zetterberg<sup>b</sup>, Z.S. Li<sup>b</sup>, M. Richter<sup>b</sup>,  
A. Dreizler<sup>c</sup>, M. Linne<sup>b</sup>, M. Aldén<sup>b</sup>

<sup>a</sup> Department of Energy Sciences, Lund Institute of Technology, Lund, Sweden

<sup>b</sup> Department of Combustion Physics, Lund Institute of Technology, Lund, Sweden

<sup>c</sup> Institute for Energy and Power Plant Technology, Technical University of Darmstadt, Darmstadt, Germany

## Abstract

This paper presents a joint large eddy simulation and laser diagnostic investigation of premixed turbulent low swirl flames. A lean premixed methane/air mixture, of the equivalence ratio 0.60–0.66, is injected from a 50 mm diameter low swirl burner to a low speed co-flowing air at room temperature and pressure. The level-set G-equation is employed to simulate the inner layer flame front. Flamelet chemistry is used to determine the flame properties in the reactive zones. Mixing and heat transfer in the post-flame zone downstream are modeled using transport equations. In addition to large eddy simulation, simultaneous 2-D laser induced fluorescence of OH and 2-D particle image velocimetry are used to characterize the basic flame structure. Laser Doppler velocimetry is employed to further analyze the flow velocity along the central axis above the burner, and 2-D filtered Rayleigh scattering is used to measure the temperature field in the lower part of the flame. A bowl-shaped, highly wrinkled turbulent flame is stabilized at a position about one-half diameter above the burner. The flame consists of two distinct parts; around the burner axis, a premixed flame with uniform mixture fraction is stabilized in the low speed flow region induced by the inflow swirl; off the axis of the burner, a stratified lean premixed flame is found in the shear layer of the flow field. Flame holes (local extinction) owing to overly lean mixtures are observed in the off-axis lean stratified part of the flame. A unified level-set G-equation is developed to model the flame holes. The basic flow and flame structure from the model simulations are compared to the laser diagnostic measurements; the height of flame stabilization (lift-off height), the mean temperature profile, and the mean axial and radial velocity components together with rms velocity components are in fairly good agreement with measurement data.

© 2006 The Combustion Institute. Published by Elsevier Inc. All rights reserved.

*Keywords:* Lean premixed stratified flames; Laser diagnostics; Large eddy simulation; Level-set G-equation

## 1. Introduction

Low swirl stabilized, lean premixed flames (LSF) offer an approach to achieve very low  $\text{NO}_x$  production for gas turbine applications [1] and they also provide a suitable experimental configuration to study the fundamentals of the

\* Corresponding author. Fax: +46 462 224 717.  
E-mail address: [Xue-Song.Bai@vok.lth.se](mailto:Xue-Song.Bai@vok.lth.se) (X.S. Bai).

interaction of turbulence and flames [2–6]. With a low swirl inflow from the burner, vortex breakdown does not occur or occurs rather far away downstream from the burner. The flame is stabilized some distance away from the burner where the turbulence intensity is high and the flow speed is low. The turbulent flame can thus fall within the thin-reaction zone regime that is more relevant to practical engine and gas turbine applications [7]. Another possibility with LSF is the formation of stratified lean mixtures, owing to the dilution of ambient air that leans the mixture from the burner. This allows one to scrutinize the interaction of flame and turbulence in stratified lean premixed flames.

In the present study, a LSF experimental rig is developed based on the original design of Cheng et al. [2,3]. A lean premixed methane/air mixture is injected through a low swirl burner accompanied by low speed co-flowing air. The flame is ‘lifted off’ above the burner, and stabilized in the downstream low-speed region generated by the swirl motion. In the center of the flow field, a rather planar lean premixed flame is stabilized by the mechanism of flame propagation in turbulence. Stratification of the fuel/air mixture occurs in the shear layer. Joint numerical modeling using large eddy simulation (LES) and laser diagnostics using particle image velocimetry (PIV), laser Doppler velocimetry (LDV), planar laser-induced fluorescence (PLIF) of OH, and filtered Rayleigh scattering (FRS) for temperature measurements are carried out to investigate the basic characteristics of the lean premixed/stratified methane/air turbulent flames.

The structure of stratified lean premixed turbulent flames is similar to that of premixed flames [8], yet it introduces additional difficulties since the local equivalence ratio varies spatially; as the mixture becomes too lean, local flame extinction occurs. There are a number of modeling studies concerning stratified/partially premixed flames, for example using the Reynolds Averaged Navier–Stokes (RANS) equations, based on the mixture fraction and progress variable/presumed probability density function (pdf) [9] and a RANS based flame surface density model [10]. Another approach that has been used to simulate premixed turbulent flames is the level-set G-equation model [7,11–15]; the flame front is simulated by the G-equation, and the temperature and species fields are determined by coupling with detailed chemistry, tabulated as flamelet manifolds. The level-set G-equation has also been used to simulate triple flame propagation of lifted turbulent jet diffusion flames [16]. The approach has the advantage of incorporating detailed flamelet chemistry with low computational cost. It is thereby feasible to simulate detailed radical/intermediate species produced in flames. The approach presents difficulties in modeling the local extinction holes on the flame

surface, however, since the G-function becomes singular at the edge of the flame holes. So far the level-set G-equation flamelet approach has been applied mainly to premixed flames without variation of the fuel/air ratio. In this study, we present a LES based level-set G-equation approach that can handle local flame extinction owing to stratification of the mixture. The model is applied to simulate the LSF and the modeling results are compared with laser diagnostics data.

## 2. Modeling of stratified premixed flames

Mixture fraction is used to describe the stratification of the mixture. With varying mixture fraction in the flow field, the local burning velocity and thickness of the flame vary; and the flames can be in different turbulent flame regimes throughout the flow field. Off the burner axis, the flame is in the ‘thin-reaction zone’ regime; in places where mixture fraction becomes too low, local flame extinction may happen. In a recent experimental study of a similar low swirl flame [5] there is evidence that the inner layer flame structure remains similar to that of laminar flames although the flame is in the thin-reaction zone regime. This inner layer is modeled using level-set G-equation as described below.

### 2.1. Level-set G-equation for stratified premixed flames

A level-set G-equation model for the thin-reaction zone regime has been developed by Peters [7] in the framework of RANS modeling. In LES, the level-set G-equation can be written as,

$$\frac{\partial G}{\partial t} + \tilde{u}_j \frac{\partial G}{\partial x_j} = S_{SGS} \left( \frac{\partial G}{\partial x_j} \frac{\partial G}{\partial x_j} \right)^{1/2} \quad (1)$$

where the r.h.s. term represents the self-propagation of the filtered reaction front.  $\tilde{u}_j$  is the density weighted, spatially filtered velocity component in  $x_j$  direction. The zero level-set ( $G = 0$ ) represents the filtered inner layer location at which the consumption and formation of radicals, for example methyl, becomes equal. The propagation speed of the zero level-set,  $S_{SGS}$ , is larger than the actual inner layer displacement speed,  $S_d(Z, s)$ , by a ratio of  $\sigma(Z, s)$ :

$$\begin{aligned} S_{SGS} &= \sigma \langle S_d \rangle, \langle S_d \rangle \\ &= \int_{-\infty}^{\infty} \int_0^1 S_d(Z, s) \wp(Z, s) dZ ds \end{aligned} \quad (2)$$

where  $\wp(Z, s)$  is the joint probability density function (pdf) of mixture fraction ( $Z$ ) and flame stretch ( $s$ ) fluctuations on the sub-grid scale level. The integral in Eq. (2) takes into account the effect of sub-grid scale (SGS) fluctuations of mixture

fraction and flame stretch on  $S_{\text{SGS}}$ , whereas  $\sigma$  accounts mainly for the influence of SGS flame wrinkling. Following a similar approach to Peters [7] a model for  $\sigma$ , valid for both the corrugated flamelet regime and the thin-reaction zone regime, can be derived for LES:

$$\sigma = 1 + \left( 4a \left( \frac{u'_d \Delta}{\langle D \rangle} \right) + a^2 \left( \frac{\langle S_d \rangle \Delta}{\langle D \rangle} \right)^2 \right)^{1/2} - a \left( \frac{\langle S_d \rangle \Delta}{\langle D \rangle} \right) \quad (3)$$

where  $u'_d$  is a characteristic sub-grid fluctuation velocity, calculated using the Smagorinsky model;  $\Delta$  is the width of the LES filter, taken here as the computational grid size.  $a = 0.2$  is a model constant;  $\langle S_d \rangle$  is defined in Eq. (2); and  $D$  is the diffusion coefficient of temperature.  $\langle D \rangle$  is calculated using a pdf integration in the mixture fraction and flame stretch space in the same way as  $\langle S_d \rangle$  in Eq. (2). It should be noted that Eq. (3) implies that as the filter size approaches zero,  $\sigma$  approaches unity; then the LES level-set formulation becomes direct numerical simulation.

$S_d(Z, s)$  and  $D(Z, s)$  used in Eqs. (2) and (3) are determined for different mixture fractions and strain rates from numerical calculations using a detailed chemical kinetic mechanism for methane/air mixture [17] in the counter flow configuration using an in-house code [18]. In the case of quenched flamelet,  $S_d(Z, s)$  is zero.

The level-set equation is well defined only at the zero level-set. A re-initialization procedure, by solving the equation  $(\partial G / \partial x_j)(\partial G / \partial x_j) = 1$ , is used in a narrow band of the zero level-set to convert the G-function into a distance function.

Mixture fraction and flame stretch have been assumed to be statistically independent; following previous work [9,11] the pdf for mixture fraction has been assumed to be a  $\beta$ -function with the mean determined by the transport equation

$$\frac{\partial \bar{\rho} \tilde{Z}}{\partial t} + \frac{\partial \bar{\rho} u_j \tilde{Z}}{\partial x_j} = \frac{\partial}{\partial x_j} \left( \bar{\rho} D \frac{\partial \tilde{Z}}{\partial x_j} \right) + \frac{\partial}{\partial x_j} \left( \bar{\rho} \tilde{u}_j \tilde{Z} - \overline{\rho u_j \tilde{Z}} \right) \quad (4)$$

where the SGS transport flux for mixture fraction (the last term on r.h.s.) has been modeled using the standard Smagorinsky model. The variance of the mixture fraction is modeled using  $\widetilde{Z'^2} = C_Z \Delta^2 \nabla \tilde{Z} \cdot \nabla \tilde{Z}$ , where  $C_Z = 0.2$  [19]. The pdf for the flame stretch has been assumed to be a  $\delta$ -function with the flame stretch on the resolved scale modeled as in [20].

## 2.2. Level-set G-equation for quenched flame holes

Far away from the burner axis, the mixture becomes so lean that it is not possible for the

flame to exist; the zero level-set becomes singular in the flow field. Numerically, it is difficult to treat this singularity. We propose here a model that extends the level-set equation to quenched ‘flame holes’. The level-set equation for the quenched part of the flame is written as

$$\frac{\partial G}{\partial t} + \tilde{u}_j^* \frac{\partial G}{\partial x_j} = 0, \quad \tilde{u}_1^* = |\tilde{u}_1|, \quad \tilde{u}_2^* = \tilde{u}_2, \quad \tilde{u}_3^* = \tilde{u}_3, \quad (5)$$

where  $\tilde{u}_1$  is the axial velocity component on the resolved scale;  $\tilde{u}_2$  and  $\tilde{u}_3$  are the other two components on the resolved scale.  $\tilde{u}_j^*$  is introduced to ensure that the zero level-set on the quenched part of the flame ‘propagates’ downstream if there is a reverse flow. Numerical tests have shown that the zero level-set would be convected to the low flow speed zone if  $\tilde{u}_j^*$  were not ensured to have a positive axial component. If the quenched part of the zero level-set were convected to the low speed zone, it would move towards the burned part of the zero-level set and thereby it would lead to a singularity in the G-function.

## 2.3. Species and temperature distributions in the flame zone

Chemical reactions occur mainly in the narrow band of the zero level-set where we apply an ensemble average of the local laminar flamelet to determine the species and temperature distributions, similar to the flamelet library approach for premixed flames [7,11,12]. The main difference compared to uniform premixed flames is that here the flamelet library manifolds contain an additional coordinate, the mixture fraction.

$$\begin{aligned} \bar{\rho}(x, t) &= \left\{ \int \int \int \frac{\varphi(Z, s) \varphi_G(g)}{\rho_L(Z, s, g)} dZ ds dg \right\}^{-1}, \\ \bar{Y}_j(x, t) &= \int \int \int Y_{j,L}(Z, s, g) \varphi(Z, s) \varphi_G(g) dZ ds dg, \\ \bar{T}(x, t) &= \int \int \int T_L(Z, s, g) \varphi(Z, s) \varphi_G(g) dZ ds dg. \end{aligned} \quad (6)$$

Here,  $\rho_L(Z, \chi, \alpha)$ ,  $Y_{j,L}(Z, \chi, \alpha)$  and  $T_L(Z, \chi, \alpha)$  are density, mass fractions of species  $j$  and temperature that are obtained from the laminar flamelet library, calculated using a counter-flow configuration and detailed chemical kinetics [17].  $\varphi(Z, s)$  has been used in Eq. (2);  $\varphi_G(g)$  is the pdf of the distance function  $G$ , presumed to be a Gaussian distribution. The variance of the distance function is modeled as  $0.2 \Delta^2 \nabla G \cdot \nabla G$ , which implies that the sub-grid scale flame fluctuation is within the filter length. Sub-grid wrinkling effects have been found important for the distribution of intermediate species such as OH and CO. This has been modeled using the ‘re-scaled’ flamelet library integration [11,12], in which the distance function is re-scaled by a factor  $\sigma$  (modeled by Eq. (3)) to represent the

fact that the distance in the narrow band of zero level-set to the flame is shorter than that given by the distance function  $G$ , owing to the sub-grid wrinkling of the flamelets.

#### 2.4. Species and temperature distributions in the downstream zone

In the post-flame zone, two different conditions can be encountered. One is that the local mixture fraction is lower than a critical value ( $Z_{cr} = 0.024$ ,  $Z_{cr}$  corresponds to the lean flammability limit). In this zone, we assume that chemical reaction rates are negligible. This zone is seen mostly in the far downstream where air dilution is high; the leaked fuel remains in the mixture. Combustion products from different upstream flamelets of varying mixture fraction and stretch rate are mixed with air and fuel from the quenched flame zones. The species and temperature distributions are determined from solving transport equations without chemical source terms, similar to the mixture fraction equation, Eq. (4). Thereafter, density is calculated using equation of state. The flame has been assumed adiabatic. In the post-flame zone where  $Z > Z_{cr}$  the fuel leaked through the flame holes is burned continuously. This corresponds to the flame pockets in the post-flame zone. These pockets are the zero level-sets that are separated from the main flame by eddy-flame interaction, and they are captured successfully using the present level-set  $G$ -equation.

#### 2.5. Modeling of velocity field and numerical methods

Spatially filtered Navier–Stokes equations with low Mach number approximation are employed together with the combustion model described above. Flow velocity and combustion are coupled through the density field. The density in the LES is spatially filtered with a top-hat filter using three grid cells. The filtered governing equations are discretized using an implicit finite difference scheme, in which the time derivatives in the continuity equation and transport equations are discretized using a three-level second-order implicit scheme. The spatial derivatives are discretized using a fourth order central difference scheme for all the terms in the continuity equation and all terms in the transport equations except the convective terms. The convective terms are discretized using a third order upwind scheme. The numerical methods have been validated for isothermal turbulent flows [21] and for premixed turbulent flames [12]. More details of the numerical methods are given in [22]. The level-set  $G$ -equation, Eq. (1), is discretized using a third order WENO (weighted essentially non-oscillatory) scheme [23]. The re-initialization equation  $|\nabla G| = 1$  is solved using a ‘sub-cell fix’ scheme [24].

Uniform cartesian grids are used in the LES to minimize the finite difference/filter commutation error and truncation errors. The grid used was set to be slightly anisotropic with a mesh spacing 1.7 mm in the axial direction and 2.0 mm in the remaining two directions. This can be compared with the Taylor and Kolmogorov length scales which are estimated to be 2.5 and 0.5 mm, respectively. The computational domain is cubic with a size of  $400 \times 400 \times 400$  mm; in which a  $200 \times 200 \times 200$  mm domain around the flame is locally refined. The large domain is used to apply far-field conditions whereas the local domain is to resolve the flame and the main flow. The inflow is set at the exit of the burner; a velocity profile from the stereo-PIV (time averaged mean and Reynolds stresses) recorded 1 mm above the burner is imposed as the inflow boundary condition. To simulate the turbulence fluctuations at the inflow a turbulence generation algorithm [25] is applied. The time step used in the LES is  $1.8 \times 10^{-5}$  s.

### 3. Experimental setup and conditions

The low swirl flame (Fig. 1) is unconfined and similar to those reported in [2,3]. The burner is based upon the design described originally by Bédard and Cheng [3]. However, the difference is that eight vanes are used to impart swirl in the flow rather than the original four radial jets. The burner diameter is 50 mm. The burner consists of a lower mixing chamber, a long tube section where the swirl vanes are attached, and the nozzle exit. Before reaching the swirler, the premixed methane and air mixture ( $\phi = 0.62$ ) passes through a perforated plate which breaks down large flow structures generated upstream. The flow then enters a central tube where a second perforated plate is placed, and thereafter the annular swirler. The burner is surrounded by a co-axial air flow at a speed of 0.3 m/s, emanating from a large annular co-flow. The experiments are carried out at room temperature (25 °C) and atmospheric pressure.

Simultaneous two-dimensional PLIF from OH and PIV are used to characterize the flame and to collect information concerning conditional velocities and flame front dynamics. In addition to PIV measurements, LDV is used to measure the velocity distribution in the flame zone and also in the vicinity of the burner exit (1 mm above the burner). The flow velocity along the radial direction at the burner exit varies from 2 m/s (around the axis) to about 10 m/s (outer radius). The Reynolds number based on the burner diameter and bulk flow speed is 20,000.

For PIV measurements, 1  $\mu\text{m}$  sized  $\text{ZrSO}_4$  particles were added to the flow to serve as flow tracers. The time between the two laser pulses used for the PIV imaging was optimized for each field-of-view and choice of interrogative window. For

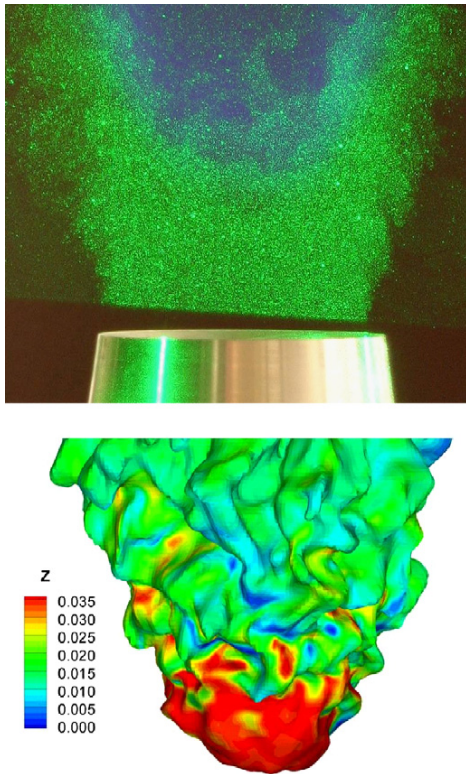


Fig. 1. Top: the burner, the scattered laser light from seeding particles (green dots) and the chemiluminescence of the flame (blue plume, photo by H. Bladh); bottom: instantaneous flame surface ( $G = 0$ ) calculated from the LES. The color contours on the flame surface denote the level of mixture fraction.

the evaluation of the velocities, a cross-correlation algorithm with an adaptive multipass method developed by LaVision was used. The laser sheet thickness was 1 mm to ensure that particles would not move out of plane at locations of high out-of-plane velocity. The spatial resolution of the PIV data presented in this paper is 1.7 mm. Limited measurements with a spatial resolution of 0.85 mm was performed to investigate the inner part of the flame in more detail. A good agreement between the two sets of data was found.

In order to achieve OH-LIF images, the multi-YAG laser cluster at Lund University was used [26]. A recently upgraded version of this instrument was used to acquire multi-shot images of the OH distribution as it progressed through the flow field. For each OH-LIF sequences, a PIV recording was synchronized with one of the images in the sequence. For each investigated flame condition, 500 to 1500 joint PIV and OH-LIF sequences were collected in order to generate statistics.

For temperature measurements FRS was used, the technique and apparatus is described in detail in [27]. Close to 600 single-shot FRS images were acquired at a range between 30 and 45 mm above the burner.

#### 4. Results and discussion

Figure 1 shows a photo of the burner and the flame (the blue plume). The green dots are scattered laser light from seeding particles required for the PIV measurements. The flame has a bowl shape; it was stabilized at about 0.63 diameters above the burner. The length of the visible flame is about 2 burner diameters. A 3-D plot of an instantaneous flame surface calculated from LES is also shown in Fig. 1. The flame surface (the zero level-set,  $G = 0$ ) is highly wrinkled owing to interaction of turbulence and flame. The mixture fraction distribution on the flame surface is shown by the color contours. The bottom part of the flame has a rather uniform mixture fraction, and it is essentially a wrinkled premixed flame. Simultaneous PIV and OH PLIF measurements (not shown here) show large scale flame wrinkling in the bottom part of the flame. The flame propagates back and forth in the axial direction around an equilibrium position, where the ‘lift-off’ height of the flame above the burner may be defined; further discussion about the lift-off height will be given later.

At the upper part of the zero level-set, as a result of dilution by the co-flowing air, the mixture fraction is not uniform; in some part of the zero level-set the fuel/air mixture becomes so lean that local flame extinction occurs (the blue-green region on the surface, Fig. 1). Air and small amount of fuel leakage through the unburned part of the surface is predicted by the present model. The leaked air and fuel mix with the hot combustion products from the bottom part of the flame. The PLIF OH image (Fig. 2) shows that there are zones of low OH in the inner part of the flame. This is likely owing to the dilution of the cold air from the ‘flame holes’ in the upper part of the flame, which has been observed in simultaneous PIV and OH PLIF (not shown here). Qualitatively similar results from LES are shown Fig. 2. Since PLIF gives only relative signals, there has been no attempt to evaluate the quantitative scale of the OH field. There are a few points in the flame front where the OH concentration has a peak, as indicated in both the LES and measurements. According to the LES, the peak OH is owing to the high degree of flame wrinkling in that point.

Instantaneous velocity vector fields from the PIV and LES both show significant vortex shedding in the shear layer at about  $r/R = 0.8 - 1.2$ , owing to Kelvin–Helmholtz instability. Under the present low swirl condition (swirl number

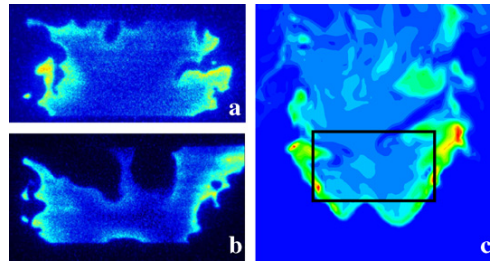


Fig. 2. (a and b) Snap shots of OH LIF on the upper part of the flame (marked area in c). To the right of (a), a flame hole is seen; in (b) two large zones of low OH concentration are shown, indicating cold air entrainment through the flame holes. (c) Instantaneous distribution of OH concentration calculated from LES. Flame holes are also shown.

0.54 defined in [21]), a large bubble-shaped low speed region is formed. The mean flow structure is shown in Figs. 3 and 4. The low speed region starts from about half a burner diameter above the burner and extends a few burner diameters downstream. In the center of the large low speed region, there is only weak reverse flow. Previous studies [21,28,29] of high swirl flows have indicated that with very strong reverse flow, a low frequency vortex core oscillation (precessing vortex core, PVC) appears. PVC can cause noise, com-

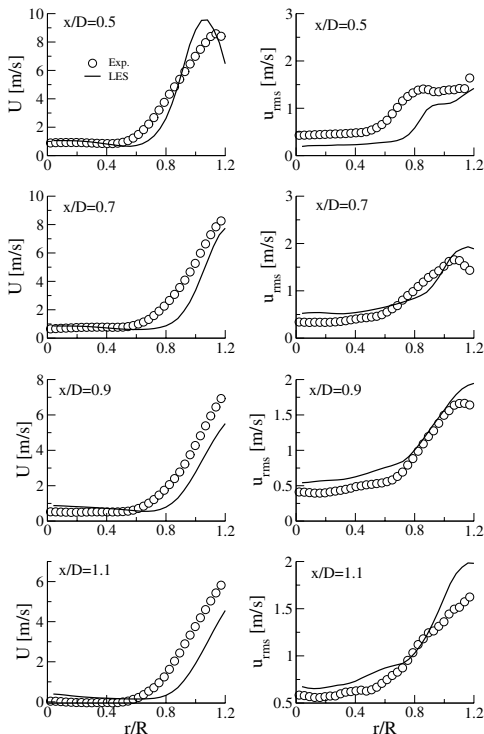


Fig. 3. Mean axial velocity and r.m.s. axial velocity along radial direction at different height above the burner.

bustor structure oscillations and damage. An analysis of the instantaneous velocity from the LDV and the LES both confirmed that there is no significant low frequency PVC in the present flame.

A quantitative comparison of the velocity field is given in Figs. 3 and 4, where the time averaged mean axial and radial velocity components and rms of these components are shown along the radial direction ( $r$ , normalized by the burner radius,  $R$ ) at different height above the burner ( $x$ , normalized with the burner diameter,  $D$ ). Twenty thousands time steps were used for the time average in the LES, whereas 1000 instantaneous PIV samples were used for the mean velocity. The mean axial velocity is positive up to 1.5 diameters downstream; thereafter a weak reverse flow was predicted by LES and confirmed by LDV measurements along the axis of burner. The mean axial velocity is 2–3 times higher than the radial velocity. The rms of the axial and radial velocity components are however on the same order of magnitude, owing to the turbulence eddy interaction. The peaks of the mean and rms velocity components are in the shear layer ( $r/R = 0.8 - 1.2$ ). Certain discrepancy between the LES results and measurements are found in the shear layer region, where the LES over-predicted the rms radial velocities. In general, the LES results and the experimental data are in fairly good agreement.

Comparison of the time averaged temperature profiles along the burner axis is given in Fig. 5. The temperature measurements have been focused mainly on the bottom premixed flame. Time averaged temperature from the LES is in reasonably good agreement with the experimental data.

Figure 6 shows the lift-off height for different equivalence ratios of the inflow mixture but with the same inflow Reynolds number at the burner exit. The lift-off height is determined in the measurement from 20 (statistically independent) chemiluminescence images of the flame, whereas the lift-off height from LES is from the zero level-set. The prediction of lift-off height depends on the modeling of the SGS flame front propagation

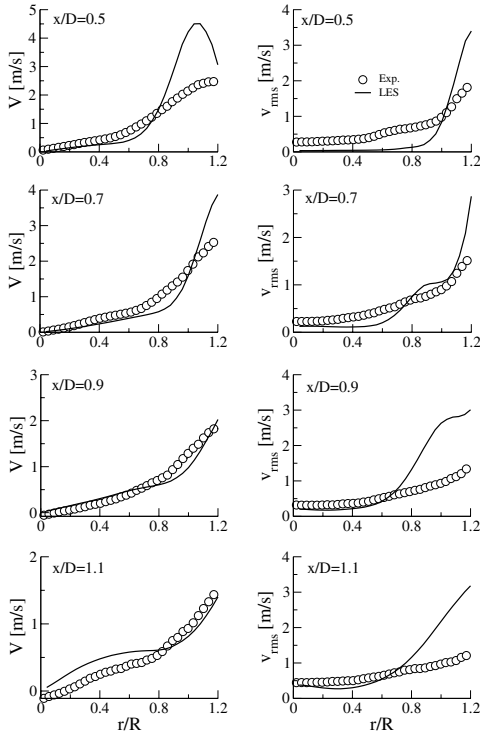


Fig. 4. Mean radial velocity and r.m.s. radial velocity along radial direction at different height above the burner.

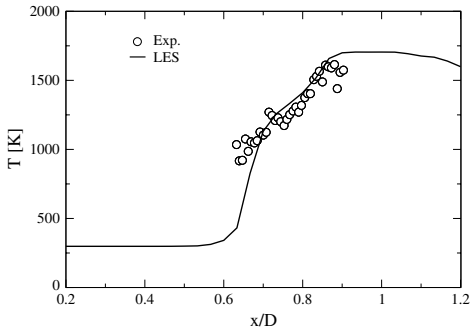


Fig. 5. Mean temperature from FRS measurements and LES along the burner axis.

speed Eq. (2). In the present simulation, model parameter adjustment has not been attempted. Nevertheless, the LES predicted lift-off height agrees with the experiments. At equivalence ratio  $\phi = 0.60$  the predicted lift-off height is 20% lower than the measured one; at  $\phi = 0.66$  the predicted height is almost identical to the measured one. The predicted mean bottom flame is W-shaped,

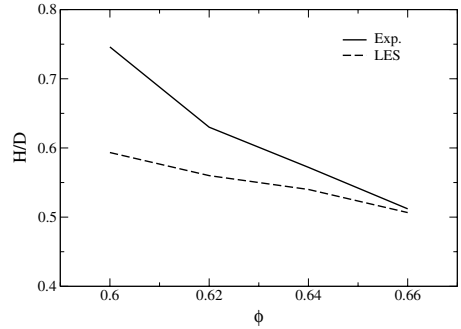


Fig. 6. Mean lift-off height from experiments and LES, at different equivalence ratios but with the same Reynolds number.

as indicated in Fig. 2. The lift-off height from LES has been calculated as an average of the two lowest valleys of the flame surface and the flame surface position at  $r/R = 0$ . This has led to a lower predicted lift-off height. If the lift-off height is defined at the burner axis ( $r/R = 0$ ), the predicted lift-off height for  $\phi = 0.62$  is fairly close to the measurements. This is already observed in the temperature profile along the burner axis (Fig. 5).

### 5. Conclusions

A joint LES and laser diagnostic study on lean premixed methane/air flames above a low swirl burner is carried out. From the LES, PIV, and OH PLIF results, the basic structures of the flame are characterized. Around the burner axis about one-half diameter above the burner, a lean premixed flame is found in the low speed zone induced by the swirl. The flame stabilization can be explained by the mechanism of premixed flame propagation in turbulence. This aspect has been extensively investigated in previous studies on similar burners [2–6]. A new aspect that is emphasized in the present study is the flame structure off the axis of the burner, where a lean stratified premixed flame with varying equivalence ratio is found in the shear layer. Large scale vortex shedding is predicted in LES and characterized by PIV; vortex shedding and turbulence eddy interaction in the shear layer cause strong mixing of the co-flowing air with the fuel/air mixture. OH PLIF shows strong penetration of the air to the downstream post-flame zone; this is likely owing to the flame holes in the shear layer in places where the mixture is too lean. The flame holes are modeled using a revised level-set G-equation, to avoid the singularity of the zero-level set in the flow field. The model results are compared to qualitative OH PLIF images, time averaged velocity and temperature profiles and the lift-off height

of the flames. Reasonably good agreement between LES results and experiments is observed.

### Acknowledgments

This work was supported by the Swedish research funding organizations (STEM, SSF, Ce-COST, and VR), the European Union through the Lund University Combustion Center Large Scale Facility (LTH, TUD), and the Deutsche Forschungsgemeinschaft, SFB 568 project B1 and project DR 347/4-1 (at TUD).

### References

- [1] M.R. Johanson, D. Littlejohn, W.A. Nazeer, K.O. Smith, R.K. Cheng, *Proc. Combust. Inst.* 30 (2005) 2867–2874.
- [2] R.K. Cheng, *Combust. Flame* 101 (1995) 1–14.
- [3] B. Bédard, R.K. Cheng, *Combust. Flame* 100 (1995) 485–494.
- [4] R.K. Cheng, I.G. Sheperd, B. Bédard, L. Talbot, *Combust. Sci. Technol.* 174 (2002) 29–59.
- [5] I.G. Shepherd, R.K. Cheng, T. Plessing, C. Kortschik, N. Peters, *Proc. Combust. Inst.* 29 (2002) 1833–1840.
- [6] C. Kortschik, T. Plessing, N. Peters, *Combust. Flame* 136 (2004) 43–50.
- [7] N. Peters, *Turbulent Combustion*, Cambridge Press, 2000.
- [8] R.W. Bilger, S.B. Pope, K.N.C. Bray, J.F. Driscoll, *Proc. Combust. Inst.* 30 (2005) 21–42.
- [9] D. Bradley, P.H. Gaskell, X.J. Gu, *Proc. Combust. Inst.* 27 (1998) 1199–1206.
- [10] S. Bondi, W.P. Jones, *Proc. Combust. Inst.* 29 (2002) 2123–2129.
- [11] P. Nilsson, X.S. Bai, *Proc. Combust. Inst.* 29 (2002) 1873–1879.
- [12] P. Wang, X.S. Bai, *Proc. Combust. Inst.* 30 (2005) 583–591.
- [13] M. Dusing, A. Kempf, F. Flemming, A. Sadiki, J. Janicka, *Prog. Comput. Fluid Dyn.* 5 (2005) 363–374.
- [14] H. Pitsch, L. Duchamp de Lageneste, *Proc. Combust. Inst.* 29 (2002) 2001–2008.
- [15] H. Pitsch, *Ann. Rev. Fluid Mech.* 38 (2006) 453–482.
- [16] M. Chen, M. Herrmann, N. Peters, *Proc. Combust. Inst.* 28 (2000) 167–174.
- [17] N. Peters, in: N. Peters, B. Rogg (Eds.), *Reduced Kinetic Mechanisms for Applications in Combustion Systems, Lecture Notes in Physics*, vol. m15, Springer-Verlag, Heidelberg, 1993, pp. 1–13, Ch. 1.
- [18] F. Mauss, Ph.D. thesis, RWTH Aachen, 1997.
- [19] F. di Mare, W.P. Jones, K.R. Menzies, *Combust. Flame* 137 (2004) 278–294.
- [20] D. Bradley, P.H. Gaskell, X.J. Gu, *Proc. Combust. Inst.* 27 (1998) 849–856.
- [21] P. Wang, X.S. Bai, *Phys. Fluids* 16 (2004) 3306–3324.
- [22] J. Gullbrand, X.S. Bai, L. Fuchs, *Int. J. Numer. Meth. Fluids* 36 (2001) 687–709.
- [23] G.S. Jiang, D.P. Peng, *SIAM J. Sci. Comput.* 21 (2000) 2126–2143.
- [24] G. Russo, P. Smereka, *J. Comput. Phys.* 163 (2000) 51–67.
- [25] M. Klein, A. Sadiki, J. Janicka, *J. Comput. Phys.* 186 (2002) 652–665.
- [26] C.F. Kaminski, J. Hult, M. Aldén, *Appl. Phys. B* 68 (1999) 757–760.
- [27] Z.S. Li, M. Afzelius, J. Zetterberg, M. Aldén, *Rev. Sci. Instrum.* 75 (2004) 3208–3215.
- [28] F.G. Gouldin, R.N. Halthore, B.T. Vu, *Proc. Combust. Inst.* 20 (1984) 269–276.
- [29] C. Schneider, A. Dreizler, J. Janicka, *Flow Turbul. Combust.* 74 (2005) 103–127.

### Comments

*Bart Merci, Ghent University, Belgium.* How long are the calculations in physical time and how does this compare to typical flow time scales?

Are the velocity RMS values the resolved or the total (resolved and modeled) values?

*Reply.* The mean profiles shown in Figs. 3–5 were obtained from averaging over typically 20,000–30,000 time steps, after the simulated flow field has evolved to be ‘statistically stationary’. The time step in these simulations was 18  $\mu$ s, which corresponds to about 0.5 s of physical time. The ‘flow-through-time’ associated with the locally refined domain is about 40 ms, whereas the integral time scale was estimated to be 10 ms. The physical time is thereby about 10 ‘flow-through-times’ and 50 integral times. To assure that the statistical data were fully

converged, the convergence history of these mean profiles was checked to make sure that no more time steps were needed.

The presented velocity RMS values were the resolved ones only. In the present LES, the filter size was about 3 mm, which is comparable to the estimated Taylor micro-scale of 2.5 mm. According to the Kolmogorov theory of turbulence the un-resolved RMS values below the SGS level is believed to be negligible once the filter length is on the order of the Taylor micro-scale for the case of high Reynolds number flows. If the filter size and the grid size are large, i.e., very large eddy simulation (VLES) is performed, especially when the SGS models are based on a traceless formulation (for example the Smagorinsky formulation), the RMS values from LES may not be comparable to the experimental data [1].

**Reference**

- [1] G.S. Winckelmans, H. Jeanmart, D. Carati, *Phys. Fluids* 14 (2002) 1809–1811.

•

*G.I. Nathan, University of Adelaide, Australia.* Did you assess the effect at the breaks in the flame sheet on combustion performance, such as CO emissions?

*Reply.* The flame holes have significant effect on the combustion process, particularly on the composition field far downstream and on the emissions. The fuel distribution in the flow field has been analyzed using LES. However, due to the limit of paper length, those

results were not shown in the paper. Fuel could leak through the flame holes and most significantly at the trailing edge of the flame and downstream. The simulations showed that the fuel leaked through the holes was partially oxidized when mixed with the hot combustion products transported from the upstream. However, in the far downstream the leaked fuel was not burned at places where the local mixture fraction was too low (the local temperature was too low). In industrial application this may be avoided by controlling the secondary air supply and dilution to the fuel. So far, only major species and OH (not CO) have been calculated and measured. According to our model based on the stationary flamelet library the CO distribution in the flow field should be similar to that of OH (see Fig. 2).



# Paper III





## Large eddy simulation and laser diagnostic studies on a low swirl stratified premixed flame

K.-J. Nogenmyr<sup>a,\*</sup>, C. Fureby<sup>b</sup>, X.S. Bai<sup>a</sup>, P. Petersson<sup>c</sup>, R. Collin<sup>c</sup>, M. Linne<sup>c,1</sup>

<sup>a</sup> Department of Energy Sciences, Lund Institute of Technology, Box 118, 22100 Lund, Sweden

<sup>b</sup> Division of Weapons & Protection, The Swedish Defense Research Agency – FOI, Stockholm, Sweden

<sup>c</sup> Department of Combustion Physics, Lund Institute of Technology, Lund, Sweden

### ARTICLE INFO

#### Article history:

Received 10 July 2007  
Received in revised form 5 June 2008  
Accepted 30 June 2008  
Available online 27 August 2008

#### Keywords:

Lean premixed stratified flames  
Low swirl  
Laser diagnostics  
Large eddy simulation  
Level-set  $G$ -equation  
Finite rate chemistry

### ABSTRACT

This paper presents numerical simulations and laser diagnostic experiments of a swirling lean premixed methane/air flame with an aim to compare different Large Eddy Simulations (LES) models for reactive flows. An atmospheric-pressure laboratory swirl burner has been developed wherein lean premixed methane/air is injected in an unconfined low-speed flow of air. The flame is stabilized above the burner rim in a moderate swirl flow, triggering weak vortex breakdown in the downstream direction. Both stereoscopic (3-component) PIV and 2-component PIV are used to investigate the flow. Filtered Rayleigh scattering is used to examine the temperature field in the leading flame front. Acetone-Planar Laser Induced Fluorescence (PLIF) is applied to examine the fuel distribution. The experimental data are used to assess two different LES models; one based on level-set  $G$ -equation and flamelet chemistry, and the other based on finite rate chemistry with reduced kinetics. The two LES models treat the chemistry differently, which results in different predictions of the flame dynamic behavior and statistics. Yet, great similarity of flame structures was predicted by both models. The LES and experimental data reveal several intrinsic features of the low swirl flame such as the W-shape at the leading front, the highly wrinkled fronts in the shear layers, and the existence of extinction holes in the trailing edge of the flame. The effect of combustion models, the numerical solvers and boundary conditions on the flame and flow predictions was systematically examined.

© 2008 The Combustion Institute. Published by Elsevier Inc. All rights reserved.

### 1. Introduction

Swirling lean premixed flames are frequently used in modern gas turbine combustors since they offer a possibility of controlled flame temperature and thus favorable thermal  $\text{NO}_x$  emissions. However, these flames pose a challenge to engineers as they are inherently unstable; they exhibit not only turbulent motions but also low frequency large-scale coherent structure dynamics [1–3]. This unstable motion could trigger not only noise, but also combustion oscillations and structural damage. Many studies have been carried out to obtain deeper understanding and control of swirl combustion systems, e.g. experimental measurements of swirling lean premixed systems [4–6], and numerical simulations of premixed and stratified premixed swirling flames [7–13]. Gouldin et al. [4] found that under high swirl conditions, two modes of low-frequency non-turbulent large-scale oscillations can exist, one is attributed to the structure of the swirl generator inside the burner and one is caused by the Precessing Vortex Core

(PVC), owing to the breakdown of vortices imposed by the swirling inflow. For high swirl, Benjamin [14] showed that the flow transits from a supercritical to a subcritical mode, where downstream disturbances can travel upstream and modify the combustion process. Escudier et al. [15,16] experimentally demonstrated the subcritical flow nature: by varying the combustor outlet contraction, the flow structures changed from an on-axis bubble-like breakdown to an off-axis annular breakdown. Owing to the complexity of the flow and combustion physics, accurate predictions of swirling flames are challenging. Reynolds Average Navier Stokes (RANS) models with the  $k$ - $\epsilon$  type model were shown to be inadequate to capture the low-frequency rotational flow [17]. In this regard, Large Eddy Simulation (LES) and similar methods [18] offer a greater possibility due to its built-in ability to resolve the coherent structure dynamics.

LES has been successfully used to predict swirling isothermal flows and premixed flames [7–13,19–22]. It is important to note that rather diverse modeling approaches have been applied in these reported LES studies, for example the flamelet models based on level-set  $G$ -equation (e.g. [8,13]), the artificially thickened flame model based on a reaction progress variable (e.g. [11]), the flame surface density models, and models based on direct coupling of fi-

\* Corresponding author. Fax: +46 462224717.

E-mail address: karl-johan.nogenmyr@energy.lth.se (K.-J. Nogenmyr).

<sup>1</sup> Currently at Sandia National Lab.



**Fig. 1.** (a) The burner mounted in the co-flow arrangement. (b, c) The swirl arrangement. In the center of the swirler (axial type swirler) a perforated plate bypasses a fraction of the mixture without imparting swirl.

nite rate chemistry (e.g. [7]). This reflects the fact that the physical process is complex and there is a lack of generally acceptable and universally valid model. It is therefore desirable to systematically investigate the performance of the different models. This can be done by applying different models to simulation of the same flame cases.

A common difficulty in LES of turbulent combustion is the modeling of the reaction zones. The chemical reaction zones are usually below the Taylor micro-scale and are generally not resolved in LES. The resolved flow acts as a boundary condition to the reaction zones, which has led to the development of different subgrid combustion models. One such model is the *G*-equation flamelet model, which combines a flamelet approximation, with the reaction layers tabulated and stored in a flamelet library [23,24], and with a level-set *G*-equation [23–27] predicting the motion of the flame front. The main advantage of this method is the possibility of coupling detailed chemical kinetics to LES, and the drawbacks are the static coupling between the chemical kinetics and the flame front, and issues regarding the capability of predicting extinction and re-ignition. Another method is to employ the chemical kinetics to directly simulate the propagation of the reaction fronts at the resolved scales. This has the potential to capture the flame dynamics more precisely (including extinction and re-ignition) but at a higher computation cost—in particular if detailed kinetics is necessary. An issue with this type of model is how to model the integrated kinetics rates across the reaction zone, taking into account the different boundary conditions imposed on the reaction zones by the resolved flow. These two models are examined in the present paper, with the objective of assessing their performance in predicting swirling flames.

A limitation for the development and validation of combustion models for swirling flames is the lack of well-documented reference data, especially for the inflow and outflow conditions. As pointed out earlier [19,28], boundary conditions can be decisive to the accuracy of the simulations. In view of this, a new laboratory measurement rig was developed [5,8] in which a premixed  $\text{CH}_4/\text{air}$  mixture is injected through a low swirl burner into a co-flowing unconfined atmosphere. The purpose of having an unconfined flame is to separate the influence of the confinement induced outer toroidal vortices off the burner axis and the outlet geometry on the flame from the inflow swirl effect. The basic burner design is similar to that of Cheng et al. [29–31] with an annular swirler and inner perforated plate to generate nearly homogeneous turbulence in the central region and a weak vortex breakdown downstream. To quantify the inflow, 3-component PIV velocity measurements are carried out in the proximity of the burner nozzle orifice. The effect of the swirler geometry is evident in the PIV data and its effect on the flame is examined using LES.

## 2. Burner and experimental setup

The low swirl burner used in this investigation is an enhancement of the original design proposed by Bedat and Cheng [30] for studying premixed flames propagating in turbulence. The goal with the new design is to produce a suitable generic burner for stabilizing lean premixed flames and to create a validation database. The burner used here, Fig. 1, is one of several that were developed and manufactured by the Technical University of Darmstadt [5]. Premixed fuel and air are fed to a mixing chamber, containing perforated grids to assure a uniform mixture, below the burner (not shown). The mixture is transported in a pipe through the co-flow arrangement surrounding the burner. Ahead of the swirler two perforated plates are mounted to disintegrate large turbulent structures formed in the pipe. The swirler consists of an outer part, with eight swirl vanes, and an inner part, which consists of a perforated plate that allows for a certain portion of the flow to pass through the swirler section without gaining swirl, Figs. 1b and 1c. Downstream of the swirler, a nozzle discharges the swirling mixture into a co-flow of air at  $\sim 0.35$  m/s. Two operational conditions have been studied at 27 and 40 kW, both with a fuel–air ratio of  $\phi = 0.62$  [5]; data from the 27 kW case will be discussed here. The swirl number, *S*, can be controlled by changing the perforated plate in the center of the swirler since the more flow blocked in the central perforated plate, the more flow will pass through the outer part and gain swirl. In the current configuration, about 40% by volume passes through the perforated plate, resulting in  $S \approx 0.55$ , which is defined as the ratio of the axial flux of tangential momentum over the axial flux of axial momentum, as estimated using the 3-component PIV data 1 mm above the nozzle.

Owing to the low swirl number, and that the swirl is limited to the outer part of the discharged flow, only weak vortex breakdown is observed in the far downstream post-flame zone. According to the measurement data, negative axial velocities are first encountered at  $x/D \approx 1.20$ , where  $D = 50$  mm is the diameter of the nozzle, and  $x$  is the axial distance to the burner exit. In the core, a lifted flame that propagates freely in a divergent, turbulent flow-field is formed. The mean flame front forms an axisymmetric bowl-shape, with a W-shape cross-section at the leading edge that starts around  $x/D \approx 0.6$ . The width and length of the visible flame are about 1 and 2 diameters of the nozzle, respectively. Since the flame is lifted and unconfined, surrounding air is entrained into the outer part of the mixture ahead of the flame, causing a stratification of the mixture at the reaction front. The core of the swirling jet flow is virtually unaffected by the entrainment, whereas a radial profile of the fuel–air ratio starting at  $\phi \approx 0.62$  in the center decreases towards zero with increasing radial distance.

### 2.1. Performed measurements

The flame has been investigated using Planar Laser Induced Fluorescence (PLIF) to determine the reaction front, and Rayleigh scattering to assess its temperature. Details on these experiments can be found elsewhere [5]. Several additional measurements were carried out recently and data are presented here. First, to quantify the flow and the inflow conditions, 3-component PIV velocity measurements were carried out. Two CCD cameras (Imager Intense 1376 × 1040 and Flowmaster 3S 1280 × 1024 La Vision) fitted with Scheimpflug adaptors were used for these measurements. The angle between the image plane of the cameras and the object plane was 45°. A two-level calibration plate (La Vision) was used for alignment of the laser sheet and the cameras, and for sheet thickness adjustment (~1 mm). To relate the coordinate system of the two cameras to the laboratory reference frame, four mapping functions based on a pinhole model (software Davis 7.0, La Vision) were calculated. A self-calibration algorithm developed by La Vision was used to increase measurement accuracy [5]. To perform PIV measurements the flow needs to be seeded with tracer particles and here 0.5 μm-sized ZrSiO<sub>4</sub> particles were used and velocity fluctuations up to 7 kHz could be resolved with a small slip. The spatial resolution for the PIV measurements equals the sizes of the interrogation windows used for the velocity evaluation and the laser sheet thickness [5]. For the data presented in this paper the spatial resolution is about 1.6 × 1.6 × 1.0 mm<sup>3</sup> for the overall flow field images and about 1.2 × 1.2 × 1.0 mm<sup>3</sup> for the data just above the nozzle assembly.

Second, to characterize the fuel distribution and the flame front structures simultaneous two-dimensional OH and fuel tracer acetone PLIF were used. Gaseous acetone (about 0.3% by volume) was carried into the fuel/air flow by bubbling air through liquid acetone. To also allow for simultaneous PLIF from OH and fuel tracer acetone measurements acetone was excited using the same excitation wavelength as used for OH LIF [5], i.e. ~283 nm and the resultant LIF fluorescence was emitted in the blue band between 350–500 nm. The laser source used for the acetone PLIF measurements was a frequency doubled dye laser, pumped with a frequency doubled Nd:YAG laser. The PLIF signal was detected at 90 degree angles to the laser sheet onto an image-intensified CCD detector (LaVision, Flamestar II) equipped with a Nikkor UV lens ( $f = 105$  mm,  $f\# = 4.5$ ) and appropriate filters (WG 345, SP500).

### 2.2. Measurement uncertainty

The uncertainty of measurements is a combination of fixed errors (accuracy) and random errors (precision) [32]. Fixed errors are always present but can be minimized by a careful setting, proper alignment and choice of measurement equipment. In the present analysis, special alignment tools were manufactured to increase the accuracy. Random errors give an estimate of the scatter, or lack of repeatability, that is expected between consecutive measurements. For measurements of mean quantities in turbulent flows the random errors depend on the flow situation, the measurement technique used, and the amount of independent data or samples used to calculate the mean values. For PIV measurements in combustion applications several other processes also contribute to the random errors [33]. Uncertainties due to particle thermophoretic transport were estimated in [34] to be ~2 cm/s in a similar flame. The influence of refractive index gradients were estimated from images of a steel ruler held inside the flame to be less than 1 cm/s. Typically, 1000 PIV samples collected for a time span of 500 s were used for calculating the mean flow. The random variation, in the measured mean velocities caused by random errors was estimated to ~2.5% of the instantaneous velocity measurement for all components based on a 95% confidence level [32]. The influence of

fixed errors was difficult to determine and instead an attempt was made to directly estimate the total error from repetitive measurements. Thus, the total error in the mean velocities was estimated to be ~5%. The total error in the rms values was in general of the same order.

### 3. LES combustion modeling

The equations governing reactive flows are the conservation equations of mass, momentum and energy describing convection, diffusion and chemical reactions, which after filtering become,

$$\partial_t(\bar{\rho}) + \nabla \cdot (\bar{\rho}\bar{\mathbf{v}}) = m^p, \quad (1a)$$

$$\partial_t(\bar{\rho}\bar{Y}_i) + \nabla \cdot (\bar{\rho}\bar{\mathbf{v}}\bar{Y}_i) = \nabla \cdot (\bar{\mathbf{j}}_i - \mathbf{b}_i) + \bar{w}_i + m^i, \quad (1b)$$

$$\partial_t(\bar{\rho}\bar{\mathbf{v}}) + \nabla \cdot (\bar{\rho}\bar{\mathbf{v}} \otimes \bar{\mathbf{v}}) = -\nabla \bar{p} + \nabla \cdot (\bar{\mathbf{S}} - \mathbf{B}) + \bar{\rho}\bar{\mathbf{f}} + \mathbf{m}^v, \quad (1c)$$

$$\partial_t(\bar{\rho}\bar{h}) + \nabla \cdot (\bar{\rho}\bar{\mathbf{v}}\bar{h}) = \partial_t \bar{p} + \bar{\mathbf{S}} \cdot \bar{\mathbf{D}} + \varepsilon + \nabla \cdot (\bar{\mathbf{h}} - \mathbf{b}_h) + \bar{\rho}\bar{\sigma} + m^h. \quad (1d)$$

Here,  $\rho$  is the density,  $\mathbf{v}$  the velocity vector,  $p$  the pressure,  $\mathbf{S}$  the viscous stress tensor,  $\mathbf{f}$  the body force,  $h$  the enthalpy,  $\mathbf{h}$  the heat flux vector,  $\mathbf{D} = \frac{1}{2}(\nabla\mathbf{v} + \nabla\mathbf{v}^T)$  the rate-of-strain tensor,  $\mathbf{S} \cdot \mathbf{D}$  the net-power,  $\sigma$  the non-mechanical energy supply (i.e. radiation, which is neglected in this study),  $Y_i$  the species mass-fraction,  $\dot{w}_i$  the species reaction-rate and  $\mathbf{j}_i$  the species mass-flux. To close these, additional relations describing the fluid properties and the rate at which species  $i$  is produced or destroyed are needed. Following for example Fureby [35],

$$\bar{\mathbf{j}}_i = \overline{D_i \nabla Y_i} \approx D_i \nabla \bar{Y}_i, \quad (2a)$$

$$\bar{p} = \rho RT \sum_i (Y_i / M_i) \approx \bar{\rho} R \bar{T} \sum_i (\bar{Y}_i / M_i), \quad (2b)$$

$$\bar{\mathbf{S}} = (\lambda + \frac{2}{3}\mu)(\text{tr}\bar{\mathbf{D}})\mathbf{I} + 2\mu\bar{\mathbf{D}}_D \approx (\lambda + \frac{2}{3}\mu)(\text{tr}\bar{\mathbf{D}})\mathbf{I} + 2\mu\bar{\mathbf{D}}_D, \quad (2c)$$

$$\begin{aligned} \bar{h} &= \sum_i (Y_i h_{f,i}^0) + \sum_i \left( Y_i \int_{T_0}^T C_{p,i}(T) dT \right) \\ &\approx \sum_i (\bar{Y}_i h_{f,i}^0) + \sum_i \left( \bar{Y}_i \int_{T_0}^{\bar{T}} C_{p,i}(T) dT \right), \end{aligned} \quad (2d)$$

$$\bar{\mathbf{h}} = \kappa \nabla \bar{T} \approx \kappa \nabla \bar{T}, \quad (2e)$$

$$\begin{aligned} \bar{w}_i &= M_i \sum_{j=1}^M (P''_{ij} - P'_{ij}) \bar{w}_{ij} = M_i \sum_{j=1}^M (P''_{ij} - P'_{ij}) \\ &\quad \times \left[ k_{fj}(T) \rho \sum_i P'_{ij} \prod_{i=1}^N Y_i^{P'_{ij}} - k_{bj}(T) \rho \sum_i P''_{ij} \prod_{i=1}^N Y_i^{P''_{ij}} \right], \end{aligned} \quad (2f)$$

where ‘ $\approx$ ’ indicates that the influence of the subgrid components has been neglected. Here,  $C_{p,i}$  the species heat-capacities,  $h_{f,i}^0$  the species formation enthalpies,  $\lambda$  and  $\mu$  the viscosities of the mixture,  $\kappa$  the heat conductivity of the mixture,  $D_i$  is the diffusivity of species  $i$ . Moreover,  $k_{fj}$  and  $k_{bj}$  are the forward and backward rate constants,  $k_{fj} = A_j \exp(-T_{Aj}/T)$ , where  $A_j$  and  $T_{Aj}$  are the pre-exponential factor and the activation temperature of the  $j$ th reaction step, and  $P_{ij}$  is the stoichiometric matrix. The commutation error terms,  $m^\alpha$ , represent errors due to exchanging the order between filtering and differentiation, and are usually neglected [36] whereas the subgrid stress and flux terms,  $\mathbf{B} = \rho \mathbf{v} \otimes \mathbf{v} - \bar{\rho} \bar{\mathbf{v}} \otimes \bar{\mathbf{v}}$  and  $\mathbf{b}_f = \rho \mathbf{v} \bar{f} - \bar{\rho} \bar{\mathbf{v}} \bar{f}$ , where  $f$  denotes an arbitrary scalar, as well as the dissipation term,  $\varepsilon = \bar{\mathbf{S}} \cdot \bar{\mathbf{D}} - \bar{\mathbf{S}} \cdot \bar{\mathbf{D}}$ , require modeling together with the filtered reaction rate  $\bar{w}_i$ .

There are several different ways of modeling turbulent combustion starting from (1a)–(1d) and (2a)–(2f), cf. [18,37,38], and here we will use two conceptually different models: one flamelet model and one finite rate chemistry model. The difference between these models is the way that the turbulence–chemistry interactions are handled. In the flamelet approach the flame is considered thin compared to the length scales of the flow, and the flame is then viewed as a thin layer (the so-called flamelet) between fuel and oxidizer (for non-premixed combustion) or between reactants and products (for premixed combustion). Because of the separation of scales, it is convenient to decouple the simulation of the flow and the flamelet from that of the chemistry, which can be modeled by the unstretched laminar flame speed,  $S_u^0$ , and by mapping the structure of the flamelet (the species mass fractions, temperature and density across the flamelet). A mixture fraction is conveniently used for non-premixed flames and a progress/regress variable or a kinematic  $G$  field is often used for premixed flames, whereas for stratified combustion both a mixture fraction and a progress/regress or  $G$ -field variable are required. In the finite chemistry model, different methods [35,37] are used to estimate the low-pass filtered reaction rates  $\bar{w}_i = M_i \sum_{j=1}^M (P''_{ij} - P'_{ij}) \bar{w}_{ij}$ , which, due to the exponential temperature dependence, are non-linear, and thus hard to model. However, once this problem is taken care of the prospects of finite rate chemistry are good since it can handle not only non-unity Lewis number cases but also intermediate species.

### 3.1. Flamelet level-set $G$ -equation LES model (G-LES)

A transport equation for the mixture fraction,  $z$ , is solved to capture the mixing of the fluid exiting from the nozzle and the surrounding air. This gives the opportunity to determine the local stoichiometry, which in turn determines the local flame properties. The leading edge of the flame is estimated to be in the thin reactions regime [23]. However, off the axis, the mixture is leaner, and as the laminar flame speed decreases, the local flame enters the distributed reactions regime, in which the flame may be quenched by the entrained air. From previous studies of this type of flames, there is evidence that the structure of the inner layer of the leading edge of the flame is similar to that of a laminar flame [39]. This allows for incorporation of detailed chemistry through the laminar flame speed,  $S_u^0$ , while avoiding incorporating the full set of species concentration equations corresponding to a given reaction mechanism. If the position of the inner layer is tracked, a laminar flamelet library incorporating detailed chemistry can be used for example by using the level-set  $G$ -equation developed by Peters [23] for RANS and recently modified by for LES [25,26] or the progress or regress-variable approach as developed for RANS and LES by Weller et al. [40] and Knikker et al. [41], respectively. In this study, we have employed the level-set  $G$ -equation, for which the kinematic equation [26] can be written,

$$\partial_t(G) + \tilde{\mathbf{v}} \cdot \nabla G = S_{LES} |\nabla G|, \quad (3)$$

where  $S_{LES}$  is the local flame velocity, and in which the rhs describes the self-propagation of the filtered reaction front. The zero-level-set ( $G = 0$ ) represents the position of the filtered inner layer. The local flame velocity for a laminar flame is the displacement speed,  $S_u^0$ , which is usually a function of equivalence ratio, strain rate, and curvature. These quantities are not resolved in LES, and in order to handle this consistently, a PDF-integration has been performed,

$$S_{LES} = \mathcal{Z}(S_u^0) \quad \text{where} \\ \langle S_u^0 \rangle = \int_{-\infty}^{\infty} \int_0^1 S_u^0(z, \sigma) \wp(z, \sigma) dz d\sigma. \quad (4)$$

The laminar flame speed,  $S_u^0$ , is determined from numerical calculations applying detailed chemistry [42] in a counter-flow configuration. The chemical kinetic mechanism [42] consists of 30 species and 82 elementary reactions. It has been used in previous LES studies [8,24,26] and theoretical analyses [42]. A chart of the flame speed in mixture fraction and strain rate space is determined and integrated together with the joint PDF of mixture fraction ( $z$ ) and flame stretch ( $\sigma$ ) on the sub-grid scale level,  $\wp(z, \sigma)$ . This is then tabulated and a look-up routine is used to fetch the flame speed in the code. To account for the increase of flame area due to unresolved turbulent fluctuations, an extension of the Damköhler model to stratified premixed flames is here proposed through a wrinkling model,

$$\mathcal{Z} = 1 + cv' H(S_u^0 - \beta) / S_u^0, \quad (5)$$

where  $v'$  is the sub-grid velocity fluctuations, here estimated from the Smagorinsky model,  $v' = \Delta \sqrt{2S_{ij}S_{ij}}$ ,  $c = 1.0$  and  $\beta = 0.01$  are model constants,  $\Delta$  is the filter size, and  $H$  the Heaviside's function. A small number  $\beta$  is introduced to cut-off the non-physical flame wrinkling when the mixture is close to the lean flammability limit. As this estimation of sub-grid velocity fluctuation has an unphysical peak at the flame front (due to thermal expansion), the zero-level-set of the  $G$ -field is set 2 mm into the pre-heat layer relative to the fuel consumption layer.

The mixture fraction and flame stretch have been assumed to be statistically independent; following previous works, cf. [8], the PDF for mixture fraction has been assumed to be a beta-function with the mean determined by the transport equation,

$$\partial_t(\bar{\rho}\bar{z}) + \nabla \cdot (\bar{\rho}\bar{z}\tilde{\mathbf{v}}) = \nabla \cdot (D_z \nabla \bar{z}) + \nabla \cdot (\bar{\rho}\bar{z}\tilde{\mathbf{v}} - \bar{\rho}\bar{z}\tilde{\mathbf{v}}), \quad (6)$$

where the subgrid transport flux for mixture fraction,  $\bar{\rho}\bar{z}\tilde{\mathbf{v}} - \bar{\rho}\bar{z}\tilde{\mathbf{v}}$ , has been modeled using the same approach as for the velocity components, described below. The variance of the mixture fraction is modeled using  $\bar{z}''^2 = c_z \Delta^2 |\nabla \bar{z}|^2$ , where  $c_z = 0.2$  [43]. The PDF for the flame stretch has been assumed to be a delta-function with the flame stretch on the resolved scale modeled as in [26]. Due to the stratification of the mixture, a fraction of the fuel mixes with surrounding air and leaks through the reaction zone. This fuel is handled using a transport equation similar to Eq. (6).

The unresolved scales of the velocity field are in the G-LES formulation handled implicitly by the numerical discretization; hence, no explicit model has been applied. This approach has been studied extensively [44], and is generally acceptable if the flow is reasonably well-resolved, and only a small fraction of the total turbulent kinetic energy is left unresolved. The requirement on the subgrid model is primarily to drain kinetic energy from the resolved scales at the correct rate; a constraint fulfilled by the odd ordered discretization of the convective term in the momentum equations, as discussed in [45].

### 3.2. Finite rate chemistry LES model (F-LES)

In the finite rate chemistry approach different techniques are employed to estimate the low-pass filtered reaction rates  $\bar{w}_i = M_i \sum_{j=1}^M (P''_{ij} - P'_{ij}) \bar{w}_{ij}$ , which, due to the exponential temperature dependence, are non-linear, and thus hard to model. To highlight the effects of the filtering we consider a rate expression of the form  $\bar{w}(\rho, Y_F, Y_O, T) = A \rho^{(a+b)} Y_F^a Y_O^b e^{-T_a/T}$ . By inserting the LES decomposition  $Y_i = \bar{Y}_i + Y'_i$  and  $T = \bar{T} + T'$  into this reaction rate expression we find that,

$$\bar{w} = \overline{A \rho^{(a+b)} Y_F^a Y_O^b e^{-T_a/T}} \\ = \left[ \frac{(\bar{Y}_F + Y'_F)^a (\bar{Y}_O + Y'_O)^b e^{-\frac{T_a T'}{(\bar{T} + T')}}}{\bar{Y}_F^a \bar{Y}_O^b} \right] A \bar{\rho}^{(a+b)} \bar{Y}_F^a \bar{Y}_O^b e^{-T_a/\bar{T}} \\ \approx \kappa A \bar{\rho}^{(a+b)} \bar{Y}_F^a \bar{Y}_O^b e^{-T_a/\bar{T}}, \quad (7)$$

in which  $\kappa$  is the generalized segregation factor that expresses the influence of the subgrid fluctuations on the reaction rate. If these fluctuations can be estimated, a direct closure is obtained. Equation (7) has not yet been exploited for LES of reacting flows, but may become practical together with deconvolution-based LES models, e.g. [46].

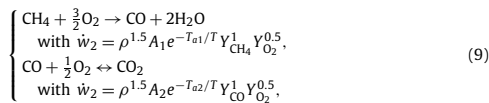
The partially stirred reactor model that will be used here to estimate the segregation factor is developed to phenomenologically incorporate the sequential processes of micro-mixing and chemical reactions. The micro-scale processes responsible for the molecular mixing, as well as the dissipation of turbulent kinetic energy, are highly intermittent, i.e. concentrated in isolated regions, and occupy only a small fraction of the fluid volume. As a consequence, combustion takes place in these well-mixed regions provided that the temperature is sufficiently high. These structures are often organized as tubes or sheets, whose characteristic dimensions are small compared to  $\Delta$ . Hence, each LES cell can be viewed as partially stirred reactor containing the reactive fine structures (perfectly stirred reactors), exchanging mass and energy with its surroundings. The reacting volume fraction,  $\kappa$ , may be estimated as the ratio between the chemical reaction time ( $\tau_c$ ) and the reactor conversion time, i.e. the sum of the micro-mixing time ( $\tau_m$ ) and the chemical reaction time, such that  $\kappa = \tau_c / (\tau_c + \tau_m)$ , and thus,

$$\overline{w_{ij}} \approx \kappa \left[ k_{fj}(\bar{T}) \bar{\rho}^{\sum_i p'_{ij}} \prod_{i=1}^N \bar{Y}_i^{p'_{ij}} - k_{bj}(\bar{T}) \bar{\rho}^{\sum_i p''_{ij}} \prod_{i=1}^N \bar{Y}_i^{p''_{ij}} \right]. \quad (8)$$

Here, the chemical reaction time is estimated from the laminar flame speed at the laminar flame thickness such that  $\tau_c = \delta_f^0 / S_u^0 \approx D / (S_u^0)^2$ , whereas the mixing time, ranging from the subgrid time,  $\tau_k = \Delta / (\varepsilon^{1/3} \Delta^{5/3})$ , to the Kolmogorov time,  $\tau_K = (\nu / \varepsilon)^{1/2}$ , is modeled as the geometrical mean of the two, i.e.  $\tau_m = \sqrt{\tau_k \tau_K} = \nu^{1/4} \Delta^{-1/4} k^{-5/8}$ . In addition, the well-known Eddy Dissipation Concept (EDC) of Magnussen [47], and the earlier model of Vulis [48], are two other examples of models of this type, and note also the similarity of this model with (7).

In the finite rate chemistry LES we have used the Mixed Model (MM) [49] in which  $\mathbf{B} = \bar{\rho}(\bar{\mathbf{v}} \otimes \bar{\mathbf{v}} - \bar{\mathbf{v}} \otimes \bar{\mathbf{v}}) - 2\mu_k \bar{\mathbf{D}}_D$  and  $\mathbf{b}_f = \bar{\rho}(\bar{\mathbf{v}} \bar{f} - \bar{\mathbf{v}} \bar{f}) - \mu_k \nabla \bar{f}$ , where the subgrid viscosity  $\mu_k = c_k \Delta k^{1/2}$  is obtained from the One Equation Eddy Viscosity Model (OEEVM) [46]. This model also provides an estimate of the subgrid dissipation,  $\varepsilon = c_\varepsilon k^{3/2} / \Delta$ , where  $k$  is the subgrid kinetic energy.

For this investigation, involving lean CH<sub>4</sub>-air combustion, we have used the reduced two-step reaction rate mechanism (9), which in turn is based on the GRI 2.1 mechanism (32 species and 177 reactions). In (9) the rate parameters (i.e. the pre-exponential factors,  $A_i$ , the activation temperatures,  $T_{A,i}$ , and the species mass fraction exponents,  $n_j$ ) of the reduced mechanism are individually tuned to make the reduced mechanism mimic the reference mechanism.



where  $A_1 = 1.91 \times 10^9 \text{ m}^{1.5} \text{ s}^{-1} \text{ kg}^{-1.5} \text{ mol}$ ,  $T_{a1} = 10072 \text{ K}$ ,  $A_2 = 14.01 \times 10^8 \text{ m}^{1.5} \text{ s}^{-1} \text{ kg}^{-1.5} \text{ mol}$  and  $T_{a2} = 6047 \text{ K}$ . Associated with the reaction mechanism is the treatment of molecular diffusion. Most chemistry packages use polynomial fits for the diffusion coefficients,  $D_k$ . This technique is accurate but expensive, and may be replaced by a simpler approximation based on the observation that the species Schmidt numbers,  $\text{Sc}_k = \mu / D_k$ , are virtually constant. Therefore, the diffusion coefficient of species  $k$  is defined as

$D_k = \mu / \text{Sc}_k$  in the present study. It should be pointed out that other methods exist for coupling of finite-rate chemistry, such as Filtered Density Function [50] and the Linear Eddy Model [51], the in-situ adaptive tabulation (ISAT) coupled with probability density function approach [52], the flame prolongation of ILDM (FPI) approach [53,54], or the thickened flame model [11,55].

### 3.3. Numerics, boundary conditions and physical models

For the G-LES an in-house developed low Mach number finite difference code employing uniform staggered Cartesian grids is used. To speed up convergence multi-grid acceleration is used. A 3rd order upwind scheme [56], is used to discretize the convective term in Eq. (1c). This scheme has the dissipative nature to drain kinetic energy from the resolved scales, as required for implicit modeling of unresolved scales. However, when used for unsteady simulations, fine grids are recommended. The other spatial derivatives in (1c) are discretized using a 4th order central difference scheme. The time derivative is discretized using a second order implicit scheme, and the equations are solved with a CFL number of 0.15, based on the mean inflow velocity. The G-equation, (3), is solved using a 3rd order WENO scheme [57] for the spatial derivative and a 3rd order Runge-Kutta TVD scheme [58] for time integration. The unconfined flame introduces some problems while setting the boundary conditions. For the G-LES, the equations are solved on a rectangular domain with a side length of 0.4 m or 8 burner diameters, Fig. 2a. The grid far away from the flame has a mesh spacing of  $\sim 6 \text{ mm}$  and an aspect ratio of unity, whereas near the flame the mesh spacing is halved in two steps resulting in a mesh spacing of  $\sim 1.5 \text{ mm}$  covering the flame. This resolution conforms approximately to the Taylor scale of the non-reactive flow that was estimated from LDV measurements as about 1.5 mm. At the lateral boundaries, zero velocity boundary condition has been shown to be enough far away not to influence the flame. The co-flowing air outside of the burner is a laminar flow, whereas two different approaches are used to set the boundary conditions at the exit of the burner. In the first approach 3-component stereoscopic PIV measurement data 1 mm above the burner exit are used to approximate the mean velocity at the burner exit. The fluctuation velocity at the burner exit is then reconstructed using the digital filter based artificial turbulence generation method of Klein et al. [59]. The method reproduces the first and second one-point statistics as well as local given auto-correlation function. Hereafter we will refer this inflow condition as modeled inflow condition or M-BC. The second method consists of using tabulated inflow data sampled from a through-the-vane non-reacting LES, employing the unstructured grid finite volume code used for the F-LES. This inflow condition is referred hereafter as simulated inflow condition, or S-BC. On the far downstream boundary, a conventional convective out-flow boundary condition is applied [60].

For F-LES, a finite volume method for arbitrary cell-shapes together with a segregated solver, described in [61] is used to discretize the reactive LES equations. The flux-reconstruction procedures used for the velocity fluxes are based on linear interpolation and for the scalar fluxes a TVD scheme is used. To minimize non-orthogonality errors the combined viscous and subgrid fluxes are split into orthogonal and non-orthogonal parts. Central difference approximations are applied to the orthogonal part whilst face interpolation of the gradients of the variables is used for the non-orthogonal parts. A Poisson equation is derived for the pressure to handle pressure-velocity coupling and solved using a Pressure Implicit with Splitting of Operators (PISO) procedure based on a Rhie & Chow type interpolation for the cell-centered data storage structure [62]. The equations are solved sequentially, with iteration over the source terms to obtain rapid convergence, with a local maximum CFL number of less than about 0.3. For this model a dif-

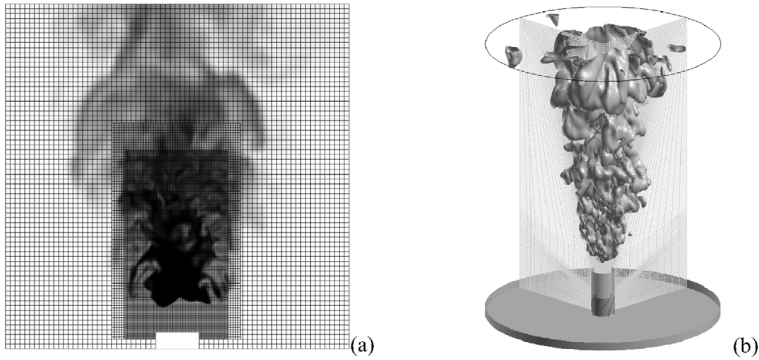


Fig. 2. Schematic of the domain, mesh and boundary conditions of (a) the G-LES model and (b) the F-LES model.

ferent computational domain, including the swirler is used. Here, the external domain consists of a round cylinder with a diameter of 0.30 m or 6 burner diameters at which far-field boundary conditions are applied. At the walls of the swirler and burner, adiabatic no-slip boundary conditions are used, whereas at the outlet, located 0.5 m or 10 burner diameter downstream of the nozzle, wave-transmissive conditions [63] are applied. The swirler inflow is divided into an outer part and an inner part, for which fixed mass flows are specified, whereas outside of the swirler the co-flowing air is modeled as laminar. The baseline grid consists of 3.5 million cells, stretched towards the walls and clustered to the region containing the flame, Fig. 2b. The average cell size is 3 mm. To assess influence of resolution, a simulation with 7.0 million cells was conducted.

As different codes are used for the different combustion models, mainly due to the difficulty of implementing the level-set G-equation model in the unstructured code that was used for the F-LES, it is necessary to examine the difference in numerical results due to the use of different codes. To do so, non-reacting LES have been performed on the same rig, and the results will be discussed in Section 4.3.

#### 4. Results and discussions

To investigate the impact of the two LES models on the numerical simulations, we consider comparing the numerical results in the following two aspects: the prediction of the basic structures of the flame and the prediction of the statistics of the flame. Experimental data obtained previously [5,8] and in this study (e.g. simultaneous acetone and OH PLIF) are used to validate the simulations.

##### 4.1. Characteristics of the flame and flow

Figs. 3a and 3b show cross-sectional views of the instantaneous temperature distribution from F-LES and G-LES, respectively. M-BC is used in the G-LES except that for Fig. 3h where S-BC was used to illustrate the effect of inflow conditions. Fig. 3c shows the PIV seeding density in the flame. The seeding density drops across the jet due to the thermal expansion and the flame front appears as a gradient in the seeding density. The flame is fully detached from the burner and that the highest temperature is found at the leading edge of the flame—the region with the richest mixture. Figs. 3d–3f show snap-shots of the velocity field at the center-plane from (d) F-LES, (e) G-LES M-BC and (f) PIV measurements. As

the weak recirculation starts downstream of the high temperature region, the fluid mixes with surrounding air resulting in a leaner mixture, which in turn yields a lower temperature in the downstream part of the flame, cf. Figs. 3a and 3b. The length of the high temperature region would significantly influence the production of thermal NO, whose rate of formation has strong temperature dependence. As seen from the seeding image and the LES results, the flame has a large scale bowl shape (W-shape in a cross-sectional view) structure, with fine scale wrinkling fronts, and is stabilized about  $x/D \approx 0.63$  above the burner rim. G-LES appears to predict a slightly wider flame, and a more wrinkled flame, as the vortices in the outer shear layer tear the flame front more vividly. These vortices pass outside of the flame in the predictions from of the F-LES model. Increasing the grid resolution of F-LES, Fig. 3g, yields somewhat more structures in the interior of the flame, similar to G-LES and the experiments, but does not affect the width of the flame. From the two LES results it appears that these structures are mainly due to mixture non-uniformities.

In Fig. 3h we present results from the G-LES with S-BC. This however required the parameter  $c$  in Eq. (5) to be reduced from 1.0 to 0.5, to obtain a reasonable lift-off height. It is evident from these figures that the boundary condition is important and significantly more mixing and wrinkling are found when S-BC is used. Flame stabilization is improved by the large vortices emerging from the burner, hence the need for a smaller constant in the flame speed model. This shows that resolving the flow in the burner is important for studying these types of flames.

Moreover, as expected from a LES, only the large-scale wrinkling of flame surface is resolved, while the experiments reveal a finer wrinkle scales. Previous simultaneous PIV and OH-PLIF measurements [5] show the large-scale flame wrinkling in the bottom part of the flame. The flame propagates back and forth in the axial direction around an equilibrium position at  $x/D \approx 0.63$ . As the peak velocity in the discharging flow is found on the edges of the jet, and the co-flow is weak, a sharp velocity gradient exists in the mixing layer. This results in unsteady motions in this area, as seen in Figs. 3d–3f, and pockets of air are engulfed from the ambient into the fuel–air stream. As these pockets are transported towards reacting zones, they create ‘holes’ in the flame front, as the reaction terminates in the lean mixtures.

It should be expected that some of the fuel diffuses into the surrounding air and escaping the reaction zone, due to both molecular and turbulent diffusion. Fig. 4 shows snap shots of the fuel distribution obtained with (a) F-LES, (b) G-LES and (c) acetone and OH PLIF. All results suggest fuel loss to the surroundings as a con-

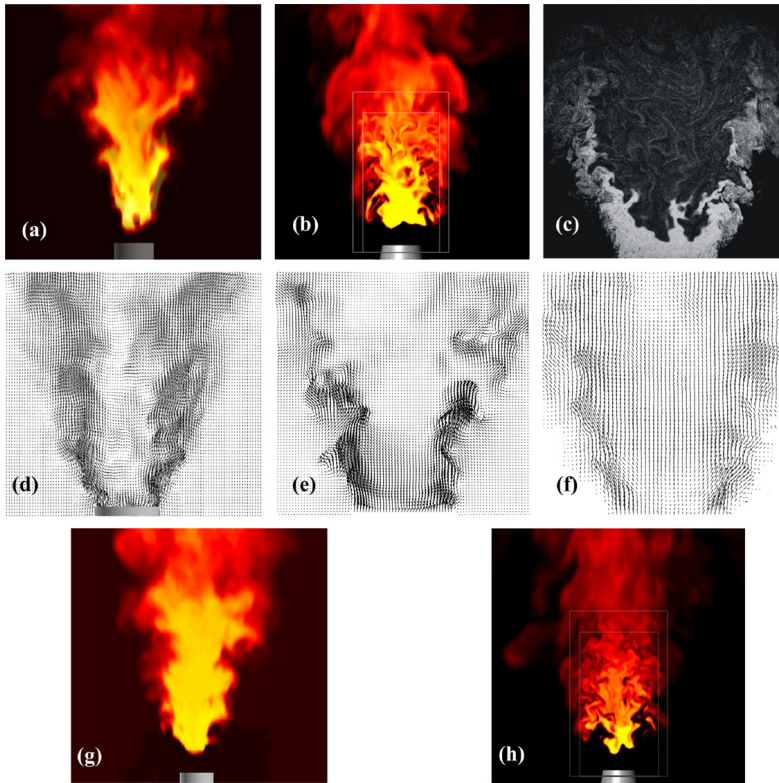


**Fig. 3.** Snap-shot of the temperature, from (a) F-LES, (b) G-LES with M-BC. In (c) we present a snap-shot of the PIV seeding density from experiments (image zoomed in to reveal details). In (d), (e) and (f) we show snap-shot of the velocity field from the F-LES, the G-LES M-BC and from the experiments, respectively. Snap-shot of temperature from (g) F-LES with higher resolution, (h) G-LES with S-BC.

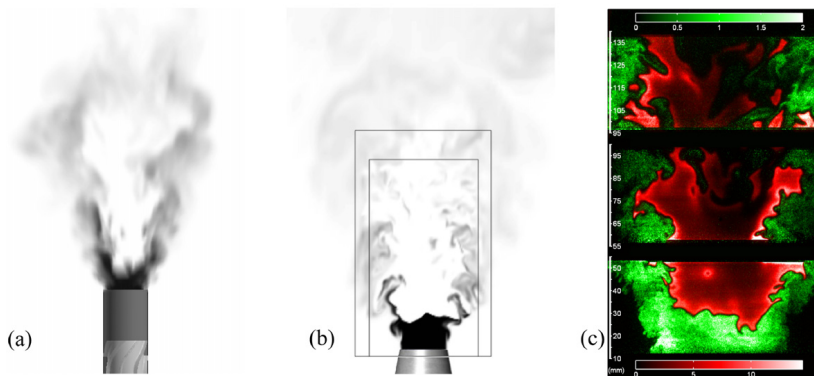


**Fig. 4.** Snap-shot of the fuel distribution from (a) F-LES, (b) G-LES M-BC, and from PLIF of OH and acetone (c). As can be seen, fuel exists far downstream of the main reaction zone. This is quantified below, Fig. 10.

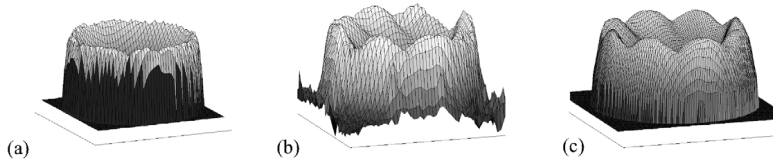


Fig. 5. The time-averaged axial velocity field at the nozzle exit from (a) the F-LES and just above of the burner from (b) the PIV measurement. The phase averaged PIV-field used as boundary condition in the G-LES are shown in (c).

sequence of the lack of confinement. This is also experimentally supported by Fig. 3c, showing a snap shot of the seeding particle density for the PIV measurements. The G-LES model predicts very thin fuel consumption zones at the leading flame front. This is naturally due to the laminar flamelet assumption adopted in the G-LES model. The acetone PLIF indeed shows that the fuel consumption zone is very thin, and the fuel consumption zone and OH zone do not overlap much. This experimental observation supports the use of flamelet type models in the current flame. On the other hand, the F-LES model predicts a much thicker flame, due to the fact that the finite rate chemistry must be resolved completely in the flow field in order to match up the total fuel consumption in the reaction zones. Regarding the instantaneous fuel distributions and the flame structures, it appears that the G-LES model predicts instantaneous flame structures that share greater similarity to the experiments than the F-LES model does.

#### 4.2. Statistical results and comparison with experiments

In Fig. 5 we compare (a) the time-averaged axial velocity from F-LES and (b) the ensemble averaged axial velocity from the stereo-PIV measurement at the exit plane of the burner. Inside the nozzle the flow is very complex. Behind each vane on the swirler, a small wake exists, as evident by the eight peaks in Fig. 5b. In the time averaged F-LES results, these wakes are smeared out, but are clearly visible in the instantaneous F-LES results. As already described, the G-LES model uses either the PIV-measured velocity at the burner exit plane or a time sequence of the non-reacting through-the-vane finite volume LES as inflow conditions. The effects of the jets from the perforated plate in the core is modeled in the F-LES as an elevated value of the subgrid kinetic energy,  $k$ , and implicitly modeled in the G-LES through the measured Reynolds stress tensor, which is reconstructed at the inflow boundary condition [59].

Simulations using the two LES models have been carried out for a sufficiently large number of integral time-scales to provide smooth first and second order statistical moments of velocity, species mass fractions and temperature. The time-average and rms-fluctuations for the velocity field have been extracted along several radii above the burner rim at  $x/D = 0.2, 0.4, 0.6, 0.8, 1.0$  and  $1.2$ . From the experimental campaigns PIV, PLIF and Rayleigh scattering data are available for comparison to the velocity, flame front and temperature. 25,000 time steps of length  $\Delta t = 2.7 \times 10^{-5}$  s were used for the time-average in the G-LES and about 100,000 time steps of length  $\Delta t = 1 \times 10^{-6}$  s were used in the F-LES, whereas 1000 PIV samples during a span of 500 s were used for the mean velocity. No attempts have been made to estimate the contributions from the unresolved scales since the interrogation window in the PIV is of the same order of magnitude in size as is the LES resolution. The spatial resolution for the PIV measurements equals the sizes of the interrogation windows used for the velocity evaluation and the laser sheet thickness. For the data presented in this paper the spatial resolution is about  $1.6 \times 1.6 \times 1.0 \text{ mm}^3$  for the overall flow field images and about  $1.2 \times 1.2 \times 1.0 \text{ mm}^3$  for the data just above the nozzle assembly.

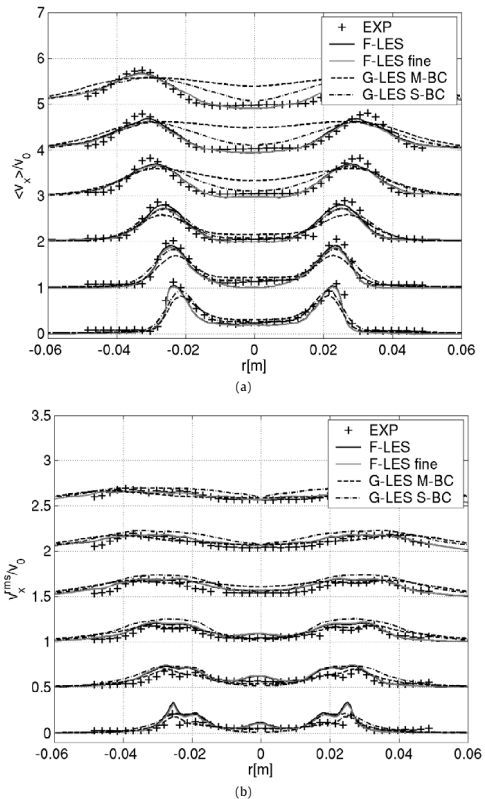


Fig. 6. Time averaged axial velocity profiles (a) and axial rms-velocity fluctuations (b) at  $x/D = 0.2, 0.4, 0.6, 0.8, 1.0$  and  $1.2$ .

In Fig. 6 the mean axial velocity,  $\langle \bar{v}_x \rangle$ , and its rms-fluctuation,  $\bar{v}_x^{rms} = ((\bar{v}_x - \langle \bar{v}_x \rangle)^2)^{1/2}$ , are presented. In general, for  $\langle \bar{v}_x \rangle$  and  $\bar{v}_x^{rms}$ , both the G-LES and F-LES compares reasonably well with the experimental results in the lower part of the flow field. Close to the burner rim, at  $x/D = 0.2$ ,  $\langle \bar{v}_x \rangle$  in the central core zone is lower than that at the edge, this is due to the relatively large blocking of the center plate in the swirler, which allows for a high mass flow through the swirler. The axial velocity profile in swirling pipe flows is known to deviate from its non-swirling counter-part, which has its peak velocity in the center of the pipe. As the flow leaves the burner, the jet starts to spread radially outwards due to the swirl.

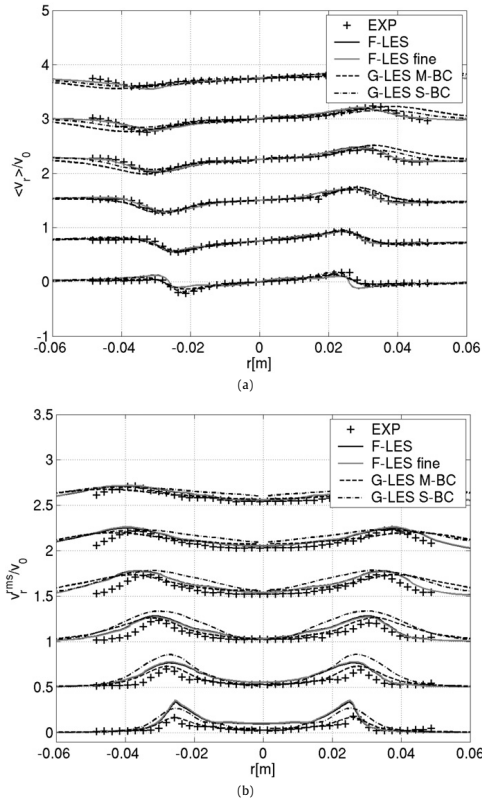


Fig. 7. Time averaged radial velocity profiles (a) and radial rms-velocity fluctuations (b) at  $x/D = 0.2, 0.4, 0.6, 0.8, 1.0$  and  $1.2$ .

This can be seen in Fig. 6a by the position of the peak in  $\langle \tilde{v}_x \rangle$ , which moves radially outwards downstream of the burner. In the region upstream of the flame, i.e. for  $x/D < 0.6$ , the two LES models capture this behavior fairly well, except some under-prediction of the peak value when compared to the PIV-data. In the region where the flame is present, i.e. for  $x/D > 0.6$ , some differences start to show up between the G-LES and F-LES, with the latter comparing very well with the experimental PIV data.

As shown in Fig. 6a, using the time dependent velocity field from the F-LES at the burner exit as boundary condition for the G-LES (i.e. S-BC) improves the results in the downstream region. This reflects the fact that the large-scale flow structures generated by the swirl vanes that are resolved in the F-LES are important to the dynamics of the flame, which in turn affects the velocity downstream the flame. This is also reflected in the time averaged temperature profile as discussed below, where the calculations including the swirler have a smoother temperature profile. Similar observations have been reported previously, e.g. by Roux et al. [64].

The rms-profiles  $\tilde{v}_x^{rms}$ , shown in Fig. 6b, peak in regions of high shear induced by the burner rim. The rms velocity is in general rather low in the current flame. The overall comparison between measured and predicted  $\tilde{v}_x^{rms}$ -profiles is satisfactory.

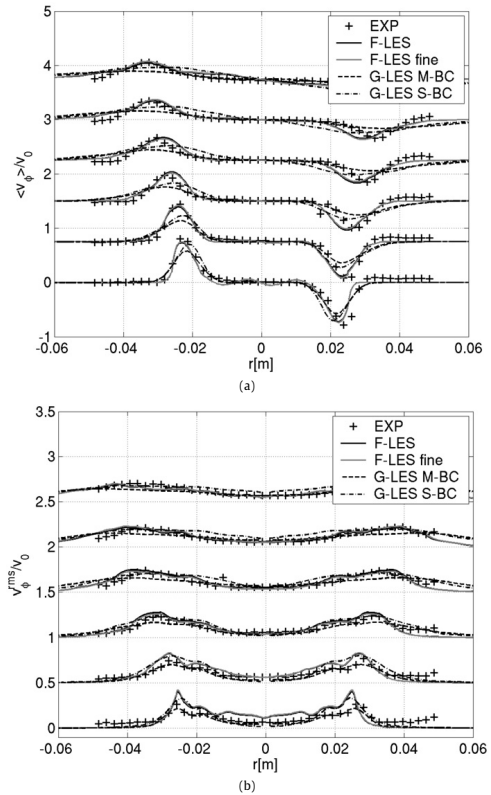


Fig. 8. Time averaged tangential velocity profiles (a) and tangential rms-velocity fluctuations (b) at  $x/D = 0.2, 0.4, 0.6, 0.8, 1.0$  and  $1.2$ .

In Fig. 7 the mean radial velocity,  $\langle \tilde{v}_r \rangle$ , and its rms-fluctuation,  $\tilde{v}_r^{rms} = ((\tilde{v}_r - \langle \tilde{v}_r \rangle)^2)^{1/2}$ , are presented along the same lines as for the axial velocity. In general, for both  $\langle \tilde{v}_r \rangle$  and  $\tilde{v}_r^{rms}$ , both the G-LES and the F-LES compare well with the PIV data. Similar trends as for  $\langle \tilde{v}_x \rangle$  are observed; the peak position is spreading outwards, slightly too fast in the G-LES prediction and satisfactorily in the F-LES predictions. The comparison in the flame zone is somewhat improved here; symmetry forces the profiles to be zero in the center, so discrepancies cannot be expected here. The radial rms velocity profiles  $\tilde{v}_r^{rms}$  have the same general behavior as for  $\tilde{v}_x^{rms}$ ; in regions of intense shear, high rms velocity fluctuations are also observed; whereas in the core where the mean shear is comparatively low, fluctuations still exists. Here, the G-LES with M-BC show somewhat better agreement since the inflow boundary conditions are taken from the experiments, using a model for the turbulent inflow fluctuations, whereas the F-LES, showing somewhat larger differences with the measurement data, does not have a model for the unresolved jets emanating from the perforated plate. Overall, LES and PIV results compare fairly well, with major trends well captured in LES, although certain over-prediction by the LES can be seen at downstream positions.

In Fig. 8 the mean tangential velocity,  $\langle \tilde{v}_\phi \rangle$ , and its rms-fluctuation,  $\tilde{v}_\phi^{rms} = ((\tilde{v}_\phi - \langle \tilde{v}_\phi \rangle)^2)^{1/2}$ , are presented along the same

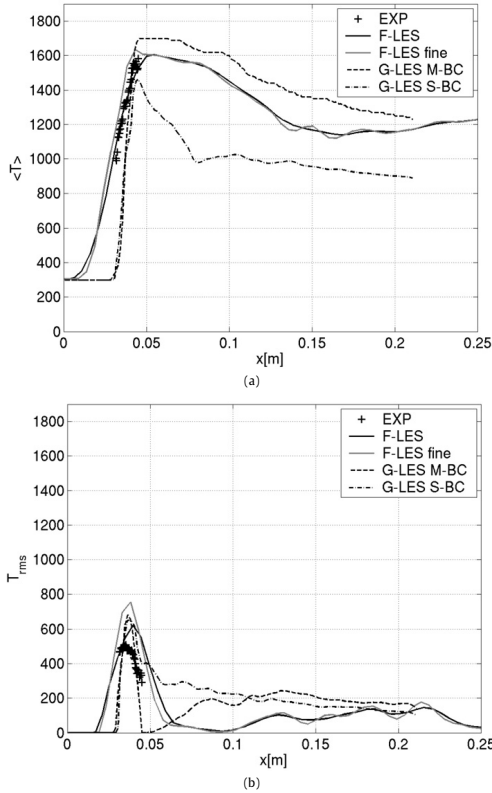


Fig. 9. Temperature profiles along a line along the burner axis. (a) The mean temperature and (b) the temperature rms fluctuations along the centerline of the burner.

lines as for the axial and radial velocities. In general, for  $\langle \bar{v}_\varphi \rangle$  and  $\bar{v}_\varphi^{rms}$ , both the G-LES and the F-LES compare well with the PIV data, with the F-LES giving better agreement with PIV data. G-LES with S-BC gives results closer to the experiments and F-LES results than the G-LES with M-BC does.

Similar to  $\langle \bar{v}_r \rangle$ ,  $\langle \bar{v}_\varphi \rangle$  is also zero in the center. It is evident that  $\langle \bar{v}_\varphi \rangle$  follows similar behavior as for the other two components, and overall,  $\bar{v}_\varphi^{rms}$  obtained from both LES conforms well to the PIV measurements, with the F-LES model showing somewhat better agreement with the PIV data.

The variation of the mean temperature,  $\langle \bar{T} \rangle$ , and the rms-fluctuations,  $\bar{T}^{rms} = ((\bar{T} - \langle \bar{T} \rangle)^2)^{1/2}$ , along the burner axes are presented in Figs. 9a and 9b, respectively. Here, data from Rayleigh scattering has been used for comparison. Good agreement between the G-LES and the F-LES with the experimental data is observed in the region in which experimental data is available. Using the boundary condition from the F-LES for the G-LES affects the temperature, yielding a smoother profile in this region. Large structures formed inside the burner are incident to the flame, and push and pull the flame continuously. Outside of that interval the two LES models behave similarly, but with the F-LES predicting a somewhat lower flame temperature than the adiabatic flame tempera-

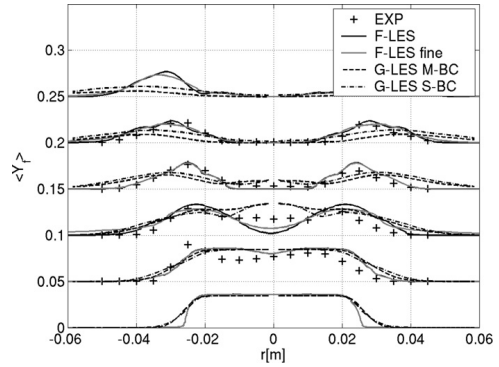


Fig. 10. Time averaged  $\text{CH}_4$  mass fractions at  $x/D = 0.2, 0.4, 0.6, 0.8, 1.0$  and  $1.2$ .

ture predicted (by default) by the G-LES. More important, both LES models predict the lift-off height very well, with the G-LES predicting a slightly larger lift-off and the F-LES predicting a slightly lower lift-off. The flame is located in the region  $0.4 < x/D < 1.0$ , which is clear from the  $\langle \bar{T} \rangle$ -distribution, whereas further downstream,  $\langle \bar{T} \rangle$  decreases monotonically as predicted by the two LES models. This effect is attributed mainly to the entrainment of surrounding cold air and not due to incomplete combustion, as suggested by the fuel distribution in Fig. 4, with fuel leakage occurring primarily at the outer edge of the jet. However, when the G-LES uses the boundary condition from the F-LES, i.e. S-BC, significantly more entrainment is seen. This is due to the coherent structures formed in the swirler which grows rapidly outside the burner and brings surrounding fluid to the core of the jet. In Fig. 9b,  $\bar{T}^{rms}$  is compared along the same line as  $\langle \bar{T} \rangle$ . As can be expected,  $\bar{T}^{rms}$  peaks at the leading edge of the flame, where the local temperature continuously switches from the unburned gas temperature to the adiabatic flame temperature, as can be seen in both LES. In the post-flame zone,  $\bar{T}^{rms}$  drops significantly to low or even zero, which corresponds to the uniform mixture in this region. Again, using the boundary condition S-BC in the G-LES changes the result. The entrainment of surrounding air results in a rather high level of  $\bar{T}^{rms}$ . However, further downstream, all simulations predict elevated values of  $\bar{T}^{rms}$ , due to the entrainment of surrounding air in lean pockets through the flame holes, as discussed earlier [8].

Fig. 10 presents profiles at  $x/D = 0.2, 0.4, 0.6, 0.8, 1.0$  and  $1.2$  of the mean  $\text{CH}_4$  concentrations,  $\langle Y_f \rangle$ , with experimental profiles obtained from acetone PLIF. In general, reasonable agreement between the measured and predicted  $\text{CH}_4$  mass fraction profiles is achieved, with the F-LES showing slightly better agreement with data than the G-LES. At  $x/D = 0.2$  and  $0.4$  we note the difference in spreading of  $\langle Y_f \rangle$  between the G-LES and F-LES, which is primarily caused by the difference in the predicted turbulence mixing field, with the F-LES showing the best agreement with the measurement data. Further downstream, the G-LES results in broader and flatter profiles than the measurement data and the F-LES. This is believed to be caused by the higher velocity fluctuation, affecting both the resolved convective mixing, and the effective flame speed, which in the G-LES is modeled according to Eq. (5). At  $x/D = 0.6$  discrepancies are noticed close to the centerline, where the F-LES under-predicts  $\langle Y_f \rangle$  and the G-LES, over-predicts  $\langle Y_f \rangle$ . This is owing to the W-shape of the flame, which is more pronounced in the G-LES.

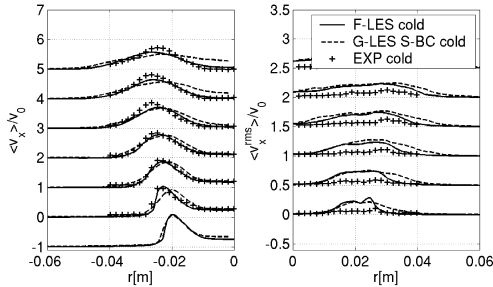


Fig. 11. Time averaged non-reactive flow axial velocity profiles (left) and axial rms-velocity fluctuations (right) at  $x/D = 0, 0.2, 0.4, 0.6, 0.8, 1.0$  and  $1.2$ .

#### 4.3. Discussions on the model comparisons

From the comparison between the two different sets of LES results and the experimental data (cf. Figs. 4, 6–10) it is evident that the flame is sensitive to the conditions at the nozzle, which are either modeled or computed. However, still, under similar nozzle conditions, the two LES models predict the flame differently. The G-LES predict a wider flame, both instantaneously (Figs. 3a, 3b, 3g and 3h) and in the mean (cf. Fig. 10), with a considerably wider and smoother distribution of the mean velocity and rms-velocity fluctuations (cf. Figs. 6a, 6b, 8a and 8b) as compared with experiments and the F-LES. As this occurs also in regions ahead of the flame, this may be due to the different LES solvers. To isolate the behavior of the different LES solvers, additional non-reacting LES was carried out. For the purpose of this study, S-BC was used in the G-LES code to minimize the differences. Fig. 11 shows the mean and rms axial velocity along radial direction at different axial position downstream of the burner exit plane. The finite difference based code (used for the G-LES) gives larger vortices in the outer shear layer which smear out the peak in the axial velocity by turbulent diffusion. The dynamics of this shear layer is rather independent of heat release. It is important to note that similar differences between the two LES models are found in the non-reacting simulations as in the reacting counter part. As stated in Section 3, the two LES solvers differ in several aspects: grid topology, numerical discretization, and SGS models. Additionally, the F-LES resolves the flow inside the swirler whereas the G-LES relies on modeling of the flow at the swirler exit. This will unavoidably lead to certain discrepancy in the predicted results. Based on comparing time-averaged velocity and rms-velocity fluctuation profiles at different distances above the burner rim and the similarity of the discrepancy of mean velocity fields between the reactive flow and non-reactive flow cases, we may conclude that the main discrepancy between the two LES results is to large extent due to the difference in the two LES solvers and the way of the swirler is treated.

From simultaneous acetone- and OH-PLIF the flame was found to be in the flamelet regime, as the fuel tracer vanishes rapidly at the reaction zone. This feature is reproduced well in the flamelet model, while the F-LES model shows a slower fuel consumption at the flame front (Fig. 4a). Also a slower increase of temperature is seen (Fig. 3a), which suggests that the reaction terms are too weak and/or the reaction mechanism is too simplified to accurately capture the flame structures, and the results are similar to what a thickened flame model would give.

Although both LES models can qualitatively simulate the flame structures and the mean flame, both models are subjected to limitations. A drawback with the G-LES model is the requirement of a

subgrid model for the effective (or turbulent) flame speed. In the literature several different closure models are proposed, all based on the laminar flame speed and an estimation of the subgrid fluctuations. However, the problem is significantly more complicated in the presence of a stratified mixture, where the equivalence ratio varies. In this case, the flame speed model directly affects the prediction of the 'lift-off' height and the width of the flame. It is rather difficult to predict both the lift-off height and width of the flame at the same time. A drawback of the F-LES is the determination of the filtered reaction terms which requires adjustment of the reaction rate and the reacting volume fraction in Eq. (8).

#### 5. Concluding remarks

Experimental and LES studies are carried out on a low swirl stratified premixed flame to evaluate two different LES models, and also to deepen the understanding of stratified premixed turbulent low swirl flames. The two LES models are respectively based on a G-equation level-set formulation with pre-tabulated chemistry, and direct coupling of two-step finite rate chemistry with the flow. Two different inflow boundary conditions are also used in order to examine the influence of the details of the swirler. PIV and PLIF of OH radicals and acetone fuel-tracer measurements are performed to characterize the velocity field and the flame structures. The LES predictions are compared with experimental data for velocity, temperature and fuel concentration, as well as snap-shot of simultaneous acetone- and OH-PLIF. The LES and experiments show that the flame is fully detached from the burner nozzle, with a lift-off height of about  $0.63D$ , where  $D$  is the nozzle-diameter. The fuel consumption zone is very thin and it overlaps little with the OH-zone, showing flamelet-like combustion behavior. Owing to the stratification of the mixture, pockets of lean fuel are engulfed by large scale flow motion into the flame, and pockets of fuel are also found to escape the reaction zone, making the modeling of this flame extremely challenging. The G-LES model properly reproduced the thin reaction zone behavior, the flame holes at far downstream and also the high degree of flame wrinkling. The F-LES predicted a thicker fuel consumption zone and less degree of wrinkling. Despite these drastic discrepancies in the prediction of the instantaneous flame structures, the two LES models predicted similar mean and rms flow field and fuel distribution, with the F-LES model predicted a mean and rms field in closer agreement with the experiments. The discrepancies between the G-LES and F-LES results are found to be mainly due to the inflow boundary conditions used in the two simulations, and also due to the difference in the numerical solvers (codes). It appears that the two combustion models themselves do not cause great discrepancies to predictions of the mean and rms velocity field and fuel distributions as one would expect.

#### Acknowledgments

This work was supported by the Swedish research funding organizations (STEM, SSF, CeCOST, and VR), European Union Large Scale Facility in Combustion (contract no. HPRI-CT-2001-00166) and the Swedish Armed Forces.

#### References

- [1] A.K. Gupta, D.G. Lilley, N. Syred, Swirl Flows, Tunbridge Wells, Abacus Press, UK, 1984.
- [2] O. Lucca-Negro, T. O'Doherty, Prog. Energy Combust. Sci. 27 (2001) 431–481.
- [3] N. Syred, Prog. Energy Combust. Sci. 32 (2006) 93–161.
- [4] F.G. Gouldin, R.N. Halthore, B.T. Vu, Proc. Combust. Inst. 20 (1984) 269–276.
- [5] P. Petersson, A. Nauert, J. Olofsson, C. Brackman, H. Seyfried, J. Zetterberg, M. Richter, A. Dreizler, D. Geyer, M. Linne, M. Aldén, R.K. Cheng, Appl. Opt. 46 (19) (2007) 3928–3936.

- [6] N.D. Joshi, M.J. Epstein, S. Durlak, S. Marakovits, P.E. Sabla, ASME Paper 94-GT-253, June 1994.
- [7] F.F. Grinstein, C. Fureby, *Proc. Combust. Inst.* 30 (2004) 1791–1798.
- [8] K.J. Nogenmyr, P. Petersson, X.S. Bai, A. Nauert, J. Olofsson, C. Brackman, H. Seyfried, J. Zetterberg, Z.S. Li, M. Richter, A. Dreizler, M. Linne, M. Alden, *Proc. Combust. Inst.* 31 (2007) 1467–1475.
- [9] W.P. Jones, *Comput. Phys. Commun.* 147 (2002) 533–537.
- [10] W.W. Kim, S. Menon, H.C. Mongia, *Combust. Sci. Technol.* 143 (1999) 25–62.
- [11] P. Schmitt, T. Poinso, B. Schuermans, K.P. Geigle, *J. Fluid Mech.* 570 (2007) 17–46.
- [12] Y. Huang, V. Yang, *Proc. Combust. Inst.* 30 (2005) 1775–1782.
- [13] C. Duwig, L. Fuchs, P. Griebel, P. Siewert, E. Boschek, *AIAA J.* 45 (2007) 624–639.
- [14] T.B. Benjamin, *J. Fluid Mech.* 14 (1962) 593–629.
- [15] M.P. Escudier, J. Bornstein, N. Zehnder, *J. Fluid Mech.* 98 (1980) 49–63.
- [16] M.P. Escudier, A.K. Nickson, R.J. Poole, *Phys. Fluids* 18 (2006) 125103.
- [17] R. Weber, B.M. Visser, F. Boysan, *Int. J. Heat Fluid Flow* 11 (1990) 225–235.
- [18] J. Janicka, A. Sadiki, *Proc. Combust. Inst.* 30 (2005) 537–547.
- [19] C.D. Pierce, P. Moin, in: 29th AIAA Fluid Dyn. Conf., AIAA 98-2892, Albuquerque, NM, 15–18 June 1998.
- [20] F.F. Grinstein, T.R. Young, E.J. Gutmark, G. Li, G. Hsiao, H.C. Mongia, *J. Turb.* 3 (2002) 1–19.
- [21] P. Wang, X.S. Bai, M. Wessman, J. Klingmann, *Phys. Fluids* 16 (2004) 3306–3324.
- [22] C. Fureby, F.F. Grinstein, G. Li, E. Gutmark, *Proc. Combust. Inst.* 31 (2007) 3107–3114.
- [23] N. Peters, *Turbulent Combustion*, Cambridge Press, UK, 2000.
- [24] P. Nilsson, X.S. Bai, *Proc. Combust. Inst.* 29 (2002) 1873–1879.
- [25] H. Pitsch, L. Duchamp de Lageneste, *Proc. Combust. Inst.* 29 (2002) 2001–2008.
- [26] P. Wang, X.S. Bai, *Proc. Combust. Inst.* 30 (2005) 583–591.
- [27] T.C. Treurniet, F.T.M. Nieuwstadt, B.J. Boersma, *J. Fluid Mech.* 565 (2006) 25–62.
- [28] S. Hogg, M.A. Leschziner, *AIAA J.* 27 (1989) 57–63.
- [29] R.K. Cheng, *Combust. Flame* 101 (1995) 1–14.
- [30] B. Bedat, R.K. Cheng, *Combust. Flame* 100 (1995) 485–494.
- [31] R.K. Cheng, I.G. Sheperd, B. Bedat, L. Talbot, *Combust. Sci. Technol.* 174 (2002) 29–59.
- [32] H.W. Coleman, W.G. Steele, *Experimentation and Uncertainty Analysis for Engineers*, Wiley, New York, 1999.
- [33] A. Stella, G. Guj, J. Kompenhans, M. Raffel, H. Richard, *Exp. Fluids* 30 (2001) 167–180.
- [34] J.H. Frank, P.A.M. Kalt, R.W. Bilger, *Combust. Flame* 116 (1999) 220–232.
- [35] C. Fureby, in: 45th AIAA Aerospace Sci. Meet. & Ex., AIAA 2007-1413, Reno, USA, 8–11 January 2007.
- [36] C. Fureby, G. Tabor, *J. Theor. Comp. Fluid Dyn.* 9 (1997) 85–102.
- [37] T. Poinso, D. Veynante, *Theoretical and Numerical Combustion*, RT. Edwards, Philadelphia, USA, 2000.
- [38] H. Pitsch, *Annu. Rev. Fluid Mech.* 38 (2006) 453–483.
- [39] I.G. Shepherd, R.K. Cheng, T. Plessing, C. Kortschik, N. Peters, *Proc. Combust. Inst.* 29 (2002) 1833–1840.
- [40] H.G. Weller, G. Tabor, A.D. Gosman, C. Fureby, *Proc. Combust. Inst.* 27 (1998) 899–907.
- [41] C. Nottin, R. Knikker, M. Boger, D. Veynante, *Proc. Combust. Inst.* 28 (2000) 67–73.
- [42] N. Peters, in: N. Peters, B. Rogg (Eds.), *Reduced Kinetic Mechanisms for Applications in Combustion Systems*, in: *Lecture Notes in Physics*, vol. m15, Springer-Verlag, Heidelberg, 1993, Chap. 1, pp. 1–3.
- [43] F. di Mare, W.P. Jones, K.R. Menzies, *Combust. Flame* 137 (2004) 278–294.
- [44] F.F. Grinstein, L.G. Margolin, W.J. Rider (Eds.), *Implicit Large Eddy Simulation, Computing Turbulent Fluid Dynamics*, Cambridge University Press, UK, 2007.
- [45] C. Fureby, F.F. Grinstein, *J. Comput. Phys.* 181 (2002) 68–97.
- [46] P. Sagaut, *Large Eddy Simulation for Incompressible Flows*, Springer-Verlag, Heidelberg, 2001.
- [47] B.F. Magnussen, in: 19th AIAA Aerospace Sci. Meet., St. Louis, MI, USA, 12–15 January 1981.
- [48] L. Vulis, *Thermal Regime of Combustion*, McGraw-Hill, 1966, Chap. 3.
- [49] C. Fureby, R. Bensow, T. Persson, *Turbulent Shear Flow Phenom. IV* (2005) 1077.
- [50] P. Givi, *AIAA J.* 44 (1) (2006) 16–23.
- [51] I. Porumbel, S. Menon, *AIAA-2006-0152* (2006) 1–17.
- [52] L. Lu, Z. Ren, V. Raman, S.B. Pope, H. Pitsch, *Proc. CTR Summer Program 2004, Center Turb. Res.*, 2004, pp. 283–294.
- [53] O. Gicquel, N. Darabiha, D. Thevenin, *Proc. Combust. Inst.* 28 (2000) 1901–1908.
- [54] L. Vervisch, R. Hauguel, P. Domingo, M. Rullaud, *J. Turb.* 5 (2004), Article N4.
- [55] L. Selle, G. Lartigue, T. Poinso, R. Koch, K.U. Schildmacher, W. Krebs, B. Prade, P. Kaufmann, D. Veynante, *Combust. Flame* 137 (2004) 489.
- [56] M.M. Rai, P. Moin, *J. Comput. Phys.* 96 (1) (1991) 15–53.
- [57] G.S. Jiang, D.P. Peng, *SIAM J. Sci. Comp.* 21 (6) (2000) 2126–2143.
- [58] S. Gottlieb, C.W. Shu, *Math. Comp.* 67 (221) (1998) 73–85.
- [59] M. Klein, A. Sadiki, J. Janicka, *J. Comput. Phys.* 186 (2002) 652–665.
- [60] K. Akselvoll, P. Moin, *J. Fluid Mech.* 315 (1996) 387–411.
- [61] H.G. Weller, G. Tabor, H. Jasak, C. Fureby, *Comp. Phys.* 12 (1997) 620–631.
- [62] R.I. Issa, *J. Comput. Phys.* 62 (1986) 40–65.
- [63] T.J. Poinso, S.K. Lele, *J. Comput. Phys.* 101 (1992) 104–129.
- [64] S. Roux, G. Lartigue, T. Poinso, U. Meier, C. Berat, *Combust. Flame* 141 (2005) 40–54.

# Paper IV



# Simultaneous PIV, OH- and fuel-PLIF measurements in a low-swirl stratified turbulent lean premixed flame

P. Petersson<sup>1\*</sup>, R. Collin<sup>2</sup>, A. Lantz<sup>2</sup>, M. Aldén<sup>2</sup>

<sup>1</sup>Dantec Dynamics A/S, DK-2740, Skovlunde, Denmark

<sup>2</sup>Division of Combustion Physics, Lund University, Lund, Sweden

## Abstract

Simultaneous OH-, fuel- planar laser induced fluorescence (PLIF) and particle image velocimetry (PIV) measurements were performed in turbulent low-swirl stratified premixed flames. The combined PIV/PLIF images revealed e.g. the fuel distribution, entrainment of ambient air, mixing with the air/fuel stream and the resulting stratification in the trailing edge of the flame. Flame-flow interaction was also investigated including the large-scale vortex structures continuously created in the outer shear layer and its influence on the flame stabilization.

## Introduction

The structure and dynamics of turbulent premixed stratified flames are influenced by many parameters e.g. local gas velocity, entrainment, large-scale structures, curvature, and flame strain. The stabilization of premixed flames is also expected to be influenced by the mixing of the fuel/air mixture with the hot products produced in the reaction zones. In order to understand local flame behaviour, stabilization mechanism and to validate large eddy simulation (LES) and combustion models it is therefore necessary to perform simultaneous measurements of the velocity field, the fuel distribution, and of an appropriate flame front marker. Combustion models are required to capture the processes that cannot be simulated, partly due to the fact that they are occurring in the very thin reaction layer that cannot be resolved in e.g. LES. Experimental data, e.g. velocity conditioned on the flame front [1], are often the only information available to validate and develop new combustion models [2]. Furthermore, increased insight in flame flow interaction and possible flame stabilization mechanisms also requires combined measurements of the velocity field and scalars [3][4]. In this content planar laser induced fluorescence (PLIF) is frequently used to investigate turbulent premixed flame structure and fuel distribution, and particle image velocimetry (PIV) is used to measure velocity fields. Preferably all velocity components are measured using stereo PIV.

Depending on e.g. the investigated flame regime (thin flame, distributed flame) and the available laser diagnostic techniques, different flame front markers can be utilized. The OH-radical (hydroxyl) is often a first choice due to a strong signal compared to minor species like the CH-radical. OH is a combustion product reaching high-, super-equilibrium-, levels at the flame front and thereafter decaying as the temperature decreases in the post flame region. The OH region therefore primarily

marks the burnt region in the flame but the maximum gradient of the OH signal is often used as an approximate representation of the flame front. The CH-radical is a combustion intermediate formed in the thin reaction zone and due to a very short lifetime the concentrations drops quickly, making the CH-radical a more precise marker of the reaction zone than OH. However, in highly turbulent flames, especially in the distributed regime, the information from only the CH-radical can be insufficient to correctly interpret the flame structures. Kiefer *et al.* [5] performed simultaneous CH- and OH-PLIF measurements to study the reaction layer structure in a turbulent jet flame. By combining the information from both radicals the location of products and reactants could be clarified even in highly turbulent regions. The authors reported that for a highly turbulent flame a locally broken CH-layer was observed whereas OH showed a continuous flame front.

The fuel distribution can also be investigated using PLIF but in gaseous hydrocarbon fuels that do not fluoresce a fuel tracer is required. Acetone ( $[\text{CH}_3]_2\text{CO}$ ) is often used as a tracer because of suitable gas and fuel properties in combination with well-known photochemistry including a strong absorption and fluorescence [6][7]. Filatyev *et al.* [8] used stereo PIV simultaneously with double-pulsed acetone PLIF in a turbulent premixed flame. With the double acetone images changes in the front position could be followed. Nakamura *et al.* [9] used a set-up with one laser and one detector to simultaneously excite and detect both acetone and OH in a turbulent flame. The broad absorption peak of acetone and the fact that the emission spectra of OH and acetone are well separated makes this single laser and single detector approach possible. A single LIF-detector applied with a double image splitter was used for combined OH-, fuel-PLIF and PIV measurements in a research swirl burner [4]. Simultaneous stereo PIV and CH-/OH-PLIF measurements in turbulent premixed flames were reported in [10]. The out-of-plane velocity component was found to be a significant factor in the flame dynamic and reported

---

\*Corresponding author:

per.petersson@dantecdynamics.com

Proceedings of the European Combustion Meeting 2011

to be required to better understand 3D effects and turbulent transports in flames.

In the present study simultaneous PIV, OH- and fuel-PLIF imaging was applied in a low-swirl lean premixed methane/air flame. The combined images from the three techniques gave increased insight in the flame behaviour, including flow flame interaction, air entrainment and occurrence of “islands” of reactants in the product region.

## 2. Experimental Set-up and Methods

For this investigation the same burner set-up presented in previous work performed at Lund University were used [11][12]. To assure well-controlled experimental conditions the set-up includes the low-swirl burner (Fig.1), calibrated mass flow controllers for methane and air (Bronckhorst Hi-Tec, EL-Flow), and co-flow and exhaust arrangement.



Figure 1. The low-swirl burner placed in a coflow region of air.

The low-swirl burner is based on the design by Bedat & Cheng [13] but updated with a different swirl arrangement. The low-swirl flow is created by an outer annular swirler, with eight swirl-vanes, in combination with an inner perforated plate that allows for about 40% by volume of the mixture to pass through (Fig.2) [11].

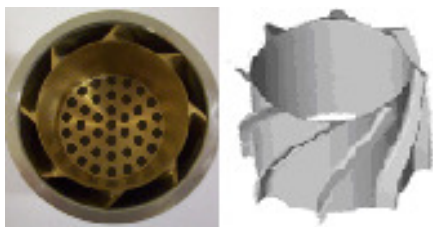


Figure 2. The annular swirler and the inner perforated plate.

After passing the swirler/perforated plate the premixed methane/air mixture of equivalence ratio 0.62 discharges through a 50mm nozzle into a co-

flow of air at about 0.35m/s. The resulting outflow from the nozzle has an inner low velocity non-swirling region ( $-10 \text{ mm} < r < 10 \text{ mm}$ ,  $r = \text{radius}$ ) and an outer region with higher axial and tangential velocities [11].

The turbulent flames considered here are categorized in the laminar flamelet regime and has previously been investigated using Planar Laser Induced Fluorescence (PLIF) to determine the reaction front, Rayleigh scattering to assess its temperature [11] and simultaneous OH- and acetone-PLIF [3]. Results from stereo (3-component) PIV in both cold and reactive flows have also been presented and used for LES validation [3][11]. In this investigation simultaneous two-dimensional PLIF from OH and fuel tracer acetone and PIV were used to characterize the flame structures, fuel distribution and flame flow interaction. A schematic diagram of the experimental apparatus for the combined measurements is shown in Fig. 3.

Since methane does not fluoresce acetone was added as a fuel tracer to apply the PLIF technique to study the fuel stream. The high vapour pressure of acetone made it also easy to seed at a sufficient concentration into a gas stream. In the present study a sealed steel container, volume=1.5 dm<sup>3</sup>, was filled to 50% with acetone and by bubbling air through a perforated ring submersed into the liquid - gaseous acetone at about 0.3% by volume was carried into the fuel/air flow before entering the burner. The acetone seeder was placed in a water bath to keep a constant temperature and controlling the acetone vapour pressure.

OH-radicals were excited through the Q<sub>1</sub>(8) transition near 283 nm in the  $v'' = 0 \rightarrow v' = 1$  band of the  $A^2\Sigma \leftarrow X^2\Pi$  system [14]. The detection of the resulting fluorescence occurs at around 310 nm. To isolate the OH-signal from background fluorescence and scattered laser light the signal was reflected via a high-reflective band-pass mirror centered at 308 nm. Furthermore, 283 nm long-pass filter and an UG11-filter was employed.

Acetone has a broad absorption peak in the UV (250 nm to 350 nm) and was in this investigation excited using the same excitation wavelength as used for the OH-LIF, i.e. ~283 nm. Accordingly, both OH and acetone could be excited with the same laser. The resultant PLIF fluorescence from the acetone was emitted in the blue band between 350-500 nm.

Two separate laser systems were used for the simultaneous PIV/PLIF measurements. The counter-propagating laser beams were formed into overlapping sheets to illuminate a planar region of the flame, crossing the vertical centerline of the burner (Fig. 3). For PIV the beams from two frequency doubled Nd:YAG lasers (Quantel) were overlapped to provide successive Mie scattering from the seed particles. In the probe volume the light sheets had a height of ~65 mm and a thickness of ~1mm.

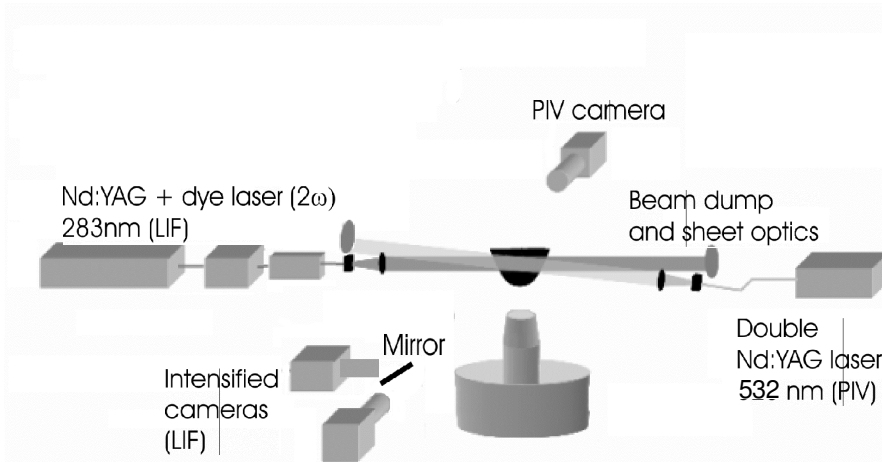


Figure 3. Schematic of the combined PLIF and PIV experimental arrangement. A high-reflective band-pass mirror at 45-degree angle to the burner reflects the OH signal and transmits the acetone (fuel tracer) signal to respective LIF detectors.

For the PIV a relatively short pulse separation,  $\Delta t = 30 \mu\text{s}$ , was required to capture the high axial and tangential (out-of-plane) velocities in the outer part of the flame. For imaging an interline-transfer CCD camera (PCO) with  $1376 \times 1040$  pixels was used. For the evaluation of the velocities, a cross-correlation algorithm with an adaptive multipass method was used. For the final pass refinement of the correlation peak displacement based on Whittaker reconstruction was used to increase the accuracy in the low velocity regions where sub-pixel displacements of the correlation peaks are possible. To capture large portions of both the unburnt and burnt regions a Field-of-View (FoV) of approximately  $60 \times 50 \text{ mm}^2$  was used. The spatial resolution for the PIV measurements equals the sizes of the interrogation windows,  $32 \times 32$  pixels, and the sheet thickness. Hence, the spatial resolution is approximately  $1.5 \text{ mm} \times 1.5 \text{ mm} \times 1 \text{ mm}$ . To perform PIV measurements the flow needs to be seeded with tracer particles that can withstand the high temperature in the flame, here  $\sim 1 \mu\text{m}$ -sized  $\text{ZrSiO}_4$  particles were used.

The laser source used for the OH- and acetone PLIF measurements was a frequency doubled dye laser, pumped with a frequency doubled Nd:YAG laser. Two image-intensified CCD detectors (LaVision, Flamestar II) equipped with Nikkor UV lenses ( $f/4.5$ ,  $f=105 \text{ mm}$ ) were positioned at 90-degree angle to each. A high-reflective band-pass mirror, centered at 308 nm, at 45-degree angle to the burner, was used to reflect the OH-PLIF signal and transmit

the acetone PLIF to the respective detectors. The resulting PLIF images were therefore mapped at 90-degree angles with respect to the propagation direction of the laser sheet. By applying separate detectors for the OH- and acetone-LIF signals an optimization of each detector could be performed. Furthermore, with the two PLIF-images on separate frames the post-processing e.g. threshold setting, filtering and a final edge detection were simplified. However, the experimental set-up, alignment and the following combination of the two images became more complicated than if a single LIF-detector combined with a double image splitter had been applied.

The simultaneous acquisition of velocity and scalars requires a precise superposition of the measurement volumes in the post-processing. In order to perform this a transparent calibration target designed to fit the burner nozzle was imaged on all cameras. In the post-processing the PLIF images were mirrored to fit the PIV coordinate system prior to superposition. The theoretical PLIF image spatial resolution was estimated to be  $0.1 \text{ mm/pixel}$ .

The synchronization of the lasers and cameras involved in the measurements was complicated by the fact that the PIV laser operated at 8Hz (to match the PCO camera) and the LIF laser at 10Hz. The simultaneous acquisition could therefore run at maximum of 2Hz, corresponding to every 4<sup>th</sup> PIV and 5<sup>th</sup> LIF recording respectively. A 2Hz master pulse, generated by a digital delay generator (Stanford Research Systems), combined with a trigger signal from the PIV system indicated when the PIV were collecting data and this signal were used to reassure simultaneous OH and acetone images. The 283 nm laser pulse was fired  $5\mu\text{s}$  before the first PIV pulse to eliminate PIV particle light scattering - but still close in time to freeze the flow/flame behaviour. To eliminate flame emission a narrowband 532 nm ( $\pm 10 \text{ nm}$ ) interference filter was mounted on the PIV camera.

### 3. Results and Discussion

Two methane/air flames were investigated using the combined PIV and PLIF measurements both with equivalence ratio of 0.62. With an inlet gas temperature of 300K and pressure of 1 atm the laminar flame speed calculated using Peters' mechanism [15] is 12 cm/s. The volume flow rates for the two cases were 44.5, and 62.7m<sup>3</sup>/h, respectively. The Reynolds numbers ( $Re$ ) based on the bulk flow velocity (6.2 and 9.3m/s) and diameter at the burner exit were about 20000, and 30000.

The experiments presented in this paper was conducted at acetone concentrations of ~0.3% – a compromise between a sufficiently high LIF signal and a minimum influence on the flame. The methane concentration was reduced to compensate for the introduced acetone – keeping the equivalence ratio of 0.62 unchanged in the premixed gas. To investigate the influence of the acetone seeding on the flame the average flame height and width was investigated using OH PLIF images for cases with and without seeded acetone. The results did not show any visible differences indicating that the acetone seeding gave limited effect on the overall flame behaviour.

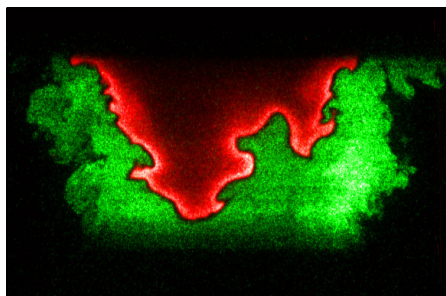


Figure 4. A combined acetone- (unburnt fuel, upstream and outside of the flame in the center), and OH-PLIF image in the low-swirl flame.

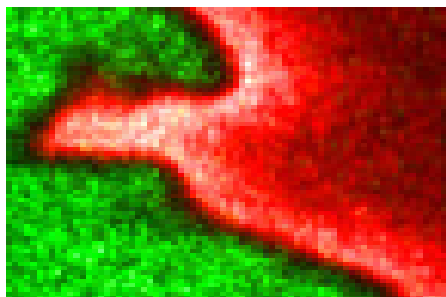


Figure 5 The non-signal region zoomed in, this region includes part of the preheat layer and the reaction layer. Unburnt (acetone) to the left and burnt (OH) to the right.

To detect the flame boundary the acetone- and OH-PLIF images were combined, an example is shown in Fig. 4 and 5 for case  $Re = 20000$ . In the combined images a thin black, non-signal, region is separating the unburnt and the burnt regions. Acetone starts to decompose in the preheat layer and is totally decomposed and oxidized at temperatures above ~1000K [6]. Accordingly, the boarder of the acetone fluorescence signal corresponds fairly well with to the edge of the unburned zone. However, the fluorescence quantum yield of acetone is decreasing with increasing temperature [6] and the acetone-PLIF boundary appears relative diffuse, Fig. 5. The OH-radical peaks slightly after the end of the reaction layer at the location where maximum heat release is expected. In Fig. 6 the maximum gradient of the OH signal visualizes this exothermic reaction zone, an approximate representation of the flame front.



Figure 6. The maximum gradient of the OH-signal, giving an approximate representation of the flame front location for the flame in Fig. 3.

For detailed investigations of the flame region it should be noted that acetone could enhance the radical production (of e.g. OH and CH) especially in lean methane flames and that peak concentrations are shifted towards the unburnt region [6]. Based on the above discussion the non-signal region comprises part of the preheat layer (including the fuel consumption zone) and the OH formation zone (reaction layer) and is here in average ~0.8 mm wide. That these two zones do not overlap can be seen as a good representation of the flamelet combustion concept. The thickness of the region between unburnt and burnt (acetone and OH) is reported to become larger with lower equivalence ratios due to a lower flame temperature [9]. This is not observed in the present investigation, however, thicker non-signal regions are randomly occurring along the flame front (Fig. 4 and 5) and are here interpreted as an effect of the 3D flame structure.

The combined images clearly visualize some of the characters of the unconfined swirling flame. The fuel distribution is uniform in the lower central part of the fuel stream whereas towards the outer parts the entrainment of air is visible, partly diluting the mixture, Fig. 4.

By combining the velocity field with the PLIF-images different aspects of the flame motion and the interaction of the reaction zone with the velocity field and e.g. its influence on the flame stabilization can be investigated. In Fig. 7 large differences in axial velocity in the low velocity core ( $-10 \text{ mm} < r < 10 \text{ mm}$ ) and in the outer region, where the flow origins from the passages in the vanes, are shown. Previously reported stereo PIV measurements show that the tangential velocity is of the same order as the axial in this outer region (in the center the tangential velocity is zero in average)[3].

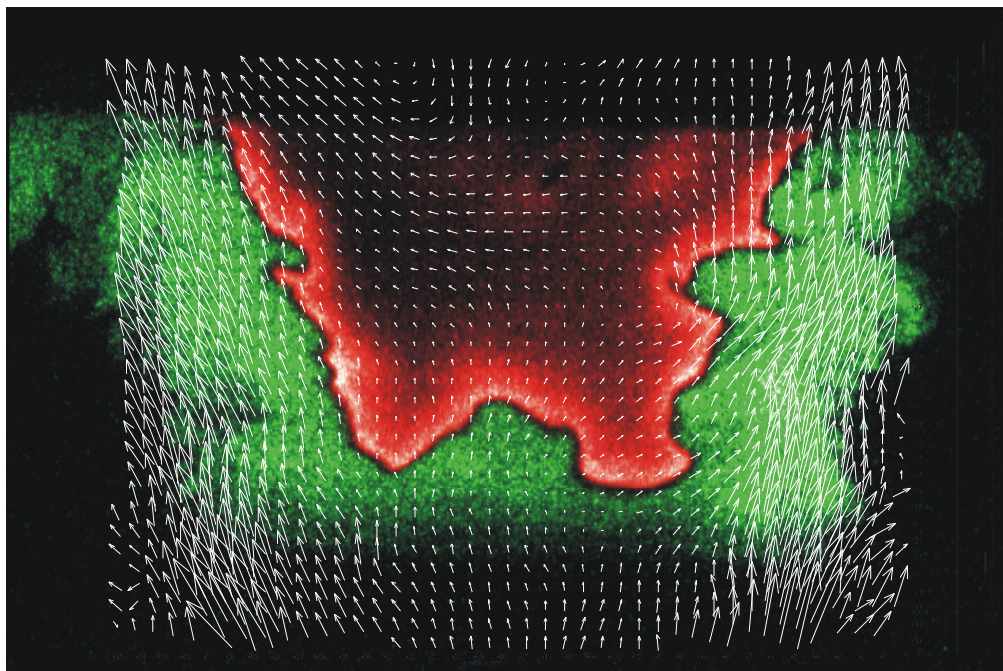


Figure 7. A cross-section through the flame showing the fuel-distribution (below and outside the flame), the burnt region (OH) and the superimposed flow-field from PIV. In the upper part of the post-flame region a weak recirculation is observed.

A strong shear is created on both (inner region and co-flow region) sides of this high velocity swirling flow region. In Fig. 7 the leading edge flame front is observed to exhibit large-scale flame front wrinkling resulting in a W-shaped front. This structure is formed due to the interaction of flame front with the large-scale flow motion in the inner low speed zone and the outer high-speed shear-layer of the burner and are believed to be an important part of the stabilization of the present flame [3]. In the upper part of the flame in Fig. 7 a weak recirculation occurs. Pockets of unburnt reactants are often found downstream of the main flame front. This pocket formation is a normal phenomenon in wrinkled flames. These pockets can occur when wrinkled

fronts propagate towards each other forming a neck that burns through and finally forming a pocket. Also islands of OH are found below the main flame front - this was phenomena were previously investigated by time resolved OH imaging and was for the present flame mainly an effect of the 3D nature of the flame [11].

#### 4. Summary and Conclusions

The simultaneous acetone-, OH-PLIF and PIV measurements were performed to investigate turbulent flame behaviour in a lean low swirl premixed flame. The preheat- and reaction layer was visualized by combining the PLIF images; in average a  $\sim 0.8 \text{ mm}$  non-signal region between acetone and OH was recorded. The simultaneous PIV/PLIF images revealed that large-scale vortex structures had an important influence on the flame stabilization mechanism. The fuel distribution was uniform in the lower central part of the fuel stream whereas towards the outer parts the entrainment of air is visible, partly diluting the mixture.

#### Acknowledgements

This work was supported by the Swedish research funding organizations; STEM, SSF, CECOST, and VR.

## References

- [1] J.H. Frank, P.A.M.Kalt, R.W. Bilger, *Combust. Flame*, 116, (199), 220-232
- [2] B.Böhm, J. Brübach, C. Ertem, A. Dreizler, *Flow Turb. Combust.* 80 (2008) 507-529
- [3] K.J. Nogenmyr, C. Fureby, X.S. Bai, P. Petersson, R.Collin, M. Linne, *Combust. Flame*, 156, 1 (2009), 25-36.
- [4] P. Ludiciano, S.M. Hosseini, R. Zoltan-Szasz, C. Duwig, L. Fuchs, R. Collin, A. Lantz, M. Aldén, E.J.Gutmark. *Proc. ASME TurboExpo (2009)* GT2009-60278.
- [5] J. Kiefer, Z.S. Li, J. Zetterberg, X.S. Bai, M. Aldén, *Combust. Flame*, 154, 4 (2008), 802-818
- [6] O.Dégardin, B.Renou, A.M. Boukhalfa, *Exp. in Fluids* 40 (2006) 452-463
- [7] M.C. Thurber, F. Grisch, B.J. Kirby, M. Votsmeier, R.K. Hanson, *Appl. Opt.* 37 (1998) 4963-4978.
- [8] S.A. Filatyev, M.P. Thariyan, R.P. Lucht, J.P. Gore, *Combust. Flame*, 150, (2007), 201-209.
- [9] Y.Nakamura, S. Manome, H. Yamashita, 13<sup>th</sup> Symp. *Appl. Laser Tech. to Fluid Mech.* (2006) 33-37
- [10] M. Tanahashi, S. Murakami, G-M. Choi, Y. Fukuchi, T. Miyauchi *Proc. Combust. Inst.* 30, (2005), 1665-1672.
- [11] P. Petersson, J. Olofsson, C. Brackman, H. Seyfried, J. Zetterberg, M. Richter, M. Aldén, M. Linne, R. K. Cheng, A. Nauert, D. Geyer, A. Dreizler, *Appl. Opt.* 46 (19) (2007) 3928-3936.
- [12] K.J. Nogenmyr, P. Petersson, X.S. Bai, A. Nauert, J. Olofsson, C. Brackman, H. Seyfried, J. Zetterberg, Z-S. Li, M. Richter, A. Dreizler, M. Linne, M. Aldén. *Proc. Combust. Inst.* 31 (2007) 1467-1475.
- [13] B. Bedat, R.K. Cheng, *Combust. Flame* 100 (3) (1995) 485-494.
- [14] LIFBASE: Database and spectral simulation, <http://www.sri.com/psd/lifbase/>.
- [15] N. Peters, in: N. Peters, B. Rogg (Eds.), *Reduced Kinetic Mechanisms for Applications in Combustion Systems*, Vol. m15 of *Lecture Notes in Physics*, Springer-Verlag, Heidelberg, 1993, Ch. 1, pp.1-13.

# Paper V



# Structure and stabilization mechanism of a stratified premixed low swirl flame

K.-J. Nogenmyr<sup>a</sup>, P. Petersson<sup>c,d</sup>, X.S. Bai<sup>a,\*</sup>, C. Fureby<sup>b</sup>, R. Collin<sup>c</sup>,  
A. Lantz<sup>c</sup>, M. Linne<sup>c</sup>, M. Aldén<sup>c</sup>

<sup>a</sup> Division of Fluid Mechanics, Lund University, Lund, Sweden

<sup>b</sup> Defense Security Systems Technology, The Swedish Defense Research Agency – FOI, Stockholm, Sweden

<sup>c</sup> Division of Combustion Physics, Lund University, Lund, Sweden

<sup>d</sup> DantecDynamics, DK-2740, Skovlunde, Denmark

Available online 11 August 2010

## Abstract

This paper presents numerical and experimental investigations of the structure and stabilization of a low swirl turbulent stratified lean premixed methane/air flame. Large-eddy simulations are performed using a two-scalar flamelet model based on mixture fraction for predicting the stratification in the fuel/air mixture and a level-set G-function for tracking the flame. Measurements are carried out with LDV for velocity field and simultaneous PLIF of OH radicals and fuel tracer acetone to identify the structures of the flame. The leading edge flame front is observed to exhibit large-scale flame front wrinkling with a particular W-shaped front frequently occurring. This structure is formed due to the interaction of flame front with the large-scale flow motion in the inner low speed zone and the outer high-speed shear-layer of the burner. The W-structures are formed and destroyed periodically at 15 Hz. The flame stabilization is shown to be dictated by the large-scale vortex rings in the shear-layer. This flame stabilization mechanism is rather different from that found in typical bluff-body stabilized flames and high-swirl flames.

© 2010 The Combustion Institute. Published by Elsevier Inc. All rights reserved.

**Keywords:** Low-swirl flame; Lean premixed flame stabilization; Flame structures; Laser diagnostics; Large eddy simulation

## 1. Introduction

Understanding and modeling the structure and stabilization of turbulent lean premixed and partially premixed flames are of great industrial importance due to the wide range of application of this type of flames in gas turbines and internal

combustion engines. The stabilization of premixed flames is governed by the chemical kinetics and its interaction with the mixing of the fuel/air mixture with the hot products produced in the reaction zones. Flame extinction and blow-out may occur when the Damköhler number is low, i.e. the ratio of flow mixing time to the chemical reaction time is not high enough [1–3]. In practical applications, flame stabilization is often achieved by using bluff-body flame holders or swirl burners, where the flame is stabilized in the recirculation zone behind the bluff-bodies [4–7], or in the internal recirculation zone downstream of the swirl burners [8–14]. The internal recirculation zone is formed due to

\* Corresponding author. Address: Division of Fluid Mechanics, Lund University, S 221 00 Lund, Sweden. Fax: +46 462224717.

E-mail address: [xue-song.bai@energy.lth.se](mailto:xue-song.bai@energy.lth.se) (X.S. Bai).

vortex breakdown of the swirling flow at sufficiently high swirl number [12]. In both bluff-body stabilized flames and high-swirl flames, hot products in the recirculation zones are circulated back to the unburned fuel/air mixture and thereby increasing the mixing time between the unburned mixture and the hot products. There are other types of flames where the flame is not stabilized in recirculation zones. Examples are the lifted jet flames [15,16], and the low-swirl premixed flames [17–19]. Contrary to high-swirl and bluff-body stabilized flames, there are no significant recirculation zones in the jet flames and low-swirl flames.

The main objective of the present study is to improve the understanding of the structure and stabilization mechanism of the low-swirl flame investigated at Lund University. The low-swirl burner developed by Cheng et al. and its modified versions have been used in several research groups [17–25] to study the fundamental structure of turbulent premixed flames, where the interaction between turbulence eddies and the chemical reactions occurs in both the laminar flamelet regimes and the distributed reaction-zones of the turbulent premixed flame regime diagram [19,20]. The statistical mean fields of the low swirl flames have been discussed in [23–25], where model predictions of the flame statistics were also presented. In the measurements with simultaneous Particle Imaging Velocimetry (PIV) and Planar Laser Induced Fluorescence (PLIF) of OH radicals [23–25] and also tomography images of Cheng et al. [19], it was found that the instantaneous flame front can be randomly shifted to one side of the burner close to the high speed shear-layer. The implication of flame front shifting to the high speed shear-layer on the flame structures and stabilization has not been well understood, and it is investigated in this work.

To characterize the flow/flame interaction, measurements are carried out with Laser Doppler Velocimetry (LDV) together with simultaneous PLIF of OH radicals and a fuel tracer acetone. To quantify the temporal evolution (i.e. dynamics) of the flame propagation and three dimensional structures of the flame front, Large Eddy Simulation (LES) is performed with the two-scalar flamelet model based on mixture fraction for the mixing process and level-set G-function [24,25] for the flame tracking. Both PLIF and LES results show that there exists a large-scale structure correlated with both the inner low speed and the outer high-speed shear-layer. The flame is essentially stabilized by the vortices in the high speed shear-layer. In the low speed inner zone above the burner exit, the flame front tends to be pushed off downstream. The competition of the two motions leads to the formation of a characteristic W-shaped flame front in the low part of the flame.

## 2. Experimental setup

The low-swirl burner used in this study (Fig. 1) is an extension of the design by Bedat and Cheng [18]. The low-swirl flow is generated by an annular swirler, with eight swirl-vanes, and an inner perforated plate that allows for about 40% of the mixture to pass through, yielding a swirl number of 0.55. The diameter at the burner nozzle is 50 mm. Premixed methane/air mixture of equivalence ratio 0.62 is supplied through the nozzle at a speed of 2–10 m/s, varying along the radial position from the axis to the burner rim. The flame has been analyzed using PLIF of OH to determine the reaction front, Rayleigh scattering to assess temperature and three-component PIV to characterize the flow field. Some details about these measured data and the rig were presented by Petersson et al. [23,24]

Experimental investigations are carried out here for new flow conditions as well as for the baseline conditions reported in [23,24]. Specifically, simultaneous PLIF from OH and fuel tracer acetone are used to characterize the flame structures. LDV is used to measure the velocity distribution in the inner flame zone to quantify the flow field and turbulence fluctuations. A fiber optic two component system from TSI is used. As seeding, 0.5  $\mu\text{m}$ -sized  $\text{ZrSiO}_4$  particles are fed into the fuel/air flow by means of a cyclone seeder from LaVision.

The laser source used for the simultaneous OH-PLIF and the acetone PLIF measurements is a frequency doubled dye laser, pumped with a frequency doubled Nd:YAG laser. The two PLIF signals are detected at 90 degree angles to the laser sheet onto two image-intensified CCD detectors (LaVision, Flamestar II), equipped with Nikkor UV lenses ( $f/4.5$ ,  $f = 105$  mm) and appropriate filters. The two detectors are positioned at 90 degree angle to each other but obtained the same field-of-view by applying the high-reflective band-pass mirror centered at 308 nm mirror at 45 degree angle to the burner to reflect the OH-PLIF signal and transmit the acetone PLIF signal to respective detectors.

OH radicals are excited through the  $Q_1(8)$  transition near 283 nm in the  $v'' = 0 \rightarrow v' = 1$  band of the  $A^2\Sigma \leftarrow X^2\Pi$  system [26]. The detection of the resulting fluorescence occurs at around 310 nm. To isolate the OH signal from background fluorescence and scattered laser light the signal is reflected via a high-reflective band-pass mirror centered at 308 nm and a 283 nm long-pass filter and a *UG11*-filter is employed. Further information about detection of the OH radicals in flames can be found in [27].

The high vapor pressure makes acetone an ideal tracer for gaseous flows [28]. A seeder from LaVision normally used for particle seeding is placed in a water bath and filled to 50% with acetone.

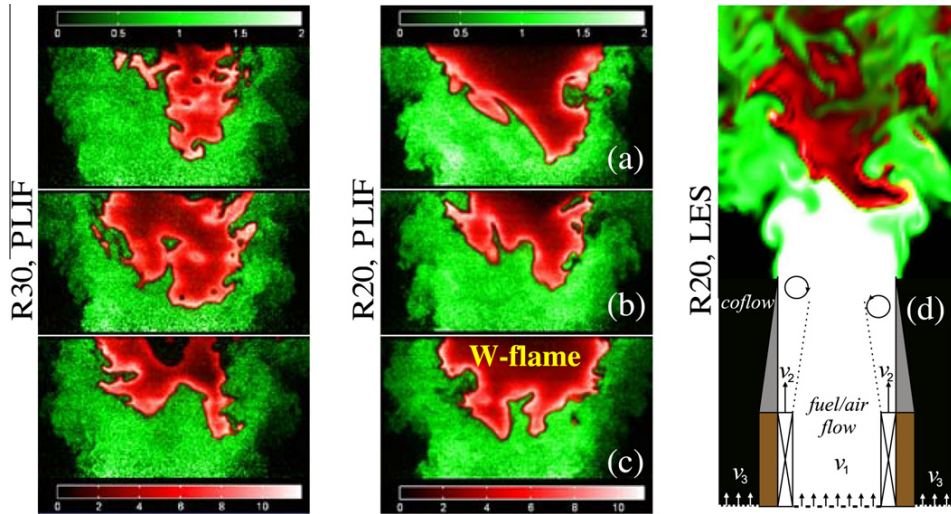


Fig. 1. Flame structures visualized by simultaneous fuel (acetone) PLIF (green) and OH PLIF (red) images and LES. For cases R20: an instantaneous Fuel and OH PLIF image showing V-shape leading flame front tilted to right side of the burner (a); at another instant a W-flame has emerged (b); an unburned fuel pocket penetrates deep into the center flame; the hips of the W-shape flame front move towards each other (c) and eventually merge together to form a V-shaped flame front similar to (a); a schematic illustration of the upper part of the burner and the instantaneous fuel distribution (green) and OH distribution (red) from LES is shown in (d). (For interpretation of the references to color in this figure legend, the reader is referred to the web version of this article.)

By bubbling air through the liquid, gaseous acetone (about 0.3% by volume) is carried into the fuel/air flow. Acetone is excited using the same excitation wavelength as used for OH LIF [29], i.e.  $\sim 283$  nm and the resultant fluorescence is emitted in the blue band between 350 and 500 nm.

Further, a high speed video camera (Phantom v7.1) is used to record the motion of the leading flame front for analyzing the flame dynamics. In the lean flame the visible luminescence was mainly from CH radicals that only exist in a thin layer where fuel is oxidized. Flames at different conditions are recorded as high speed movies with a sampling speed of 600 Hz.

### 3. Computational models

In several investigated low-swirl flames [19,20] with Karlovitz number ranging from 0.13 to 18, i.e. in both the flamelet regime and the thin reaction zone of the turbulent premixed flame regime diagram, the effect of turbulence has been shown to increase the flame surface area, but seldom to quench the reaction zones. This is consistent with the argument of Peters [30] that laminar flamelet models may be valid for rather high Karlovitz numbers. In view of this, a two-scalar flamelet model based on mixture fraction and level-set G-equation [24,25,31,32] is used in the present LES study. The sub-grid scale flame front propa-

gation velocity and re-initialization procedure used here is taken from our previous work [24,25].

The spatially filtered continuity, momentum and energy equations as well as the mixture fraction transport equation are discretized and solved on a uniform staggered Cartesian grid using a finite difference scheme with multi-grid acceleration. A 3rd order upwind-biased scheme is employed for the convective terms, whereas all other spatial derivatives are discretized with a 4th order central scheme, and the time integration is performed by a second order implicit scheme. The level-set G-equation is solved with a 3rd order WENO scheme in combination with a 3rd order TVD Runge–Kutta time integration scheme. The code has been validated against experimental data for several flames [7,24].

Since the flow domain has open boundary a local-grid refinement strategy is used. First, a coarse cubic grid with a spacing of  $\sim 6$  mm in all three directions are used which covers a flow domain of  $8 \times 8 \times 8D$ , where  $D$  is the diameter of the burner exit. The grid is subsequently refined twice in all directions to resolve the flame zone. The fine locally refined flame zone has a flow domain of  $2.4 \times 2.4 \times 4.4D$  in the cross-flow directions and the axial flow direction, respectively, with a mesh spacing of  $\sim 1.4$  mm in all directions. This is approximately on the order of the Taylor scale of the flow. At the lateral far-field boundaries, zero velocity condition has been used.

At far downstream, a convective outflow condition is employed [33]. To assess the influence of inflow boundary condition, two alternative methods are used to determine the boundary condition at the burner exit. In the first approach, the flow field in the burner and swirler is simulated using LES, and the velocity data at the burner exit is sampled and used in the flame simulations. Hereafter, this approach is referred to as the ‘simulated inflow’. A second approach is to use the experimentally measured mean and variance of velocity 1 mm above the burner exit plane. Then, the digital filter based artificial turbulence generation method of Klein et al. [34] is used to reconstruct the time-dependent inflow velocity. The method can reproduce the first and the second one-point statistical moments, as well as auto-correlations, however, the large scale low frequency flow structures developed in the swirler and the burner are not taken into account. This condition is referred to as ‘modeled inflow’ below.

#### 4. Results

Four flames are investigated. In all cases the equivalence ratio is 0.62; the methane/air mixture and the co-flow air have the same temperature of 300 K and pressure of 1 atm. The laminar flame speed calculated using Peters’ mechanism [35] is 12 cm/s. The volume flow rates are, respectively, 32.2, 44.5, 55.0, and 62.7 m<sup>3</sup>/h, which gives Reynolds numbers (based on the bulk flow velocity and diameter at the burner exit) of about 16,000, 20,000, 25,000, and 30,000. These cases are referred to as R16, R20, R25, and R30, respectively. R20 is the baseline case that has been stud-

ied using LES, PIV, LDV, OH-PLIF, acetone PLIF, and filter Rayleigh scattering (FRS) for temperature. R30 has been studied using PIV, OH-PLIF and acetone PLIF. The other two cases have been studied using OH-PLIF. All cases have been studied using the high speed video for flame dynamics.

Figure 1 shows the instantaneous OH and fuel acetone PLIF images for the cases R20 and R30 and LES fuel/OH distribution for R20. In LES the mass fractions of OH are computed using a flamelet tabulation approach considering the effect of flame surface wrinkling [24]. As the Reynolds number increases the wrinkling scale of the flame fronts is shown to become smaller; yet, the fuel and OH images have sharp boundaries indicating that these species do not coexist in thick layers and the reaction zone is thin and flamelet-like, although the Karlovitz numbers are, respectively, 4.0 and 6.3 for cases R20 and R30. This is consistent with the previous results of Cheng et al. [19,20].

Both PLIF and the LES reveal large-scale wrinkling of the flame with several different states. If the flame is cut through its burner axis one can see three different shapes of flame front: a single V-shape tilted towards one side of the burner, a W-shape (two connected V-shapes), and multiple V-flame fronts. One may expect that a single centered V-shape flame front is the natural state of the flame given that the mean velocity field shows a low velocity centre region (about 5 times lower than the peak velocity in the outer shear layer). To understand how these flame shapes emerge, the time evolution of the flame was studied.

Figure 2 shows a sequence of instantaneous velocity vector fields superimposed onto the

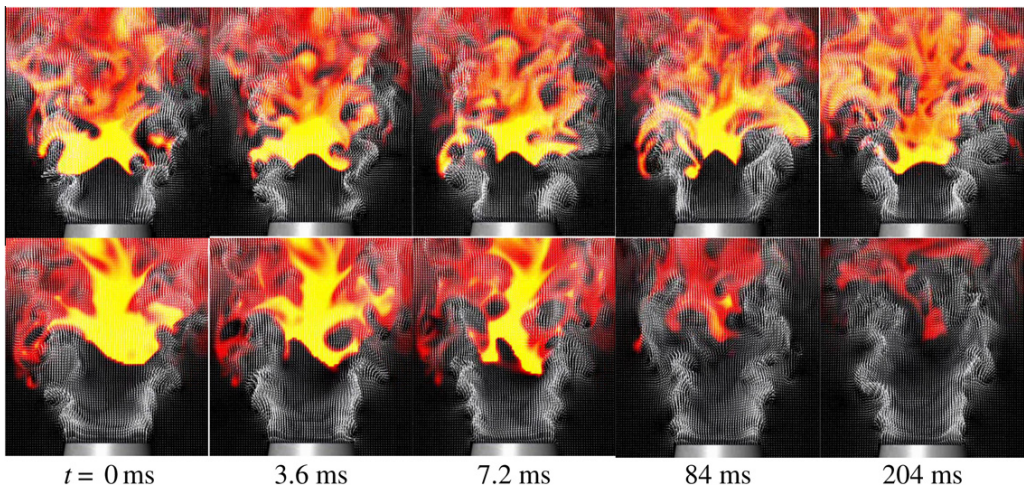


Fig. 2. LES instantaneous temperature field superimposed onto instantaneous velocity vector field, upper row: results from simulated inflow condition; lower row: results from modeled inflow condition.

temperature fields in the axis-symmetric cross-section of the burner of case R20 at a time interval of 3.6 ms for the first three images, and longer interval for the last two images. The results are from LES using the two different inflow boundary conditions. LES with the ‘simulated inflow’ condition (the upper row) results in a statistically stationary flame, as such,  $t = 0$  was chosen arbitrarily in Fig. 2. LES using the ‘modeled inflow’ conditions (lower row) results in blow-out. To illustrate the flame dynamics close to blow-out,  $t = 0$  was set at 220 ms before blow-out. Of particular interest in the figure are the structures of the large-scale vortices in the shear-layers. These large-scale vortices are formed due to the shear-layer instability (Kelvin-Helmholtz instability) outside the burner as well as instabilities inside the burner and swirler, as indicated in Fig. 1d. As the vortices interact with the flame front they are seen to drag the flame downwards, hence, effectively stabilizing the flame. This leads to the frequently appearing W-shape in the axis-symmetric cross-section, as these vortices drag down the outer wings of the flame rather than the central parts.

Similar flame structures are also seen in simultaneous PIV and OH-PLIF images from the multi-YAG experiments described in [23], which gives four snap-shots with a time interval of 1.6 ms, Fig. 3. Similar to Fig. 2,  $t = 0$  was chosen arbitrarily in Fig. 3 due to the statistical stationary nature of the flame. It is seen that the leading edge of the flame front (indicated by the circle) inter-

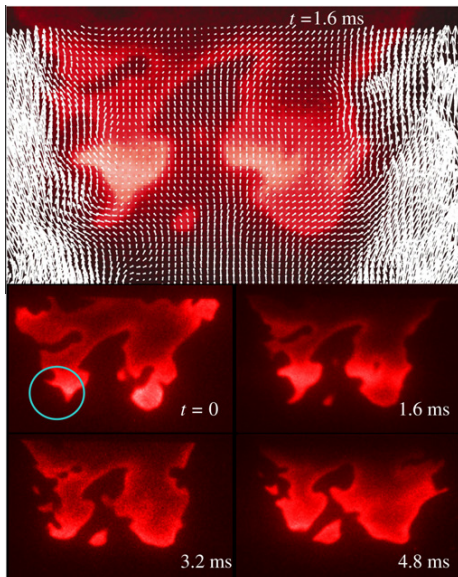


Fig. 3. Simultaneous velocity vector from PIV and OH PLIF from a multi-YAG experiment with a time interval of 1.6 ms.

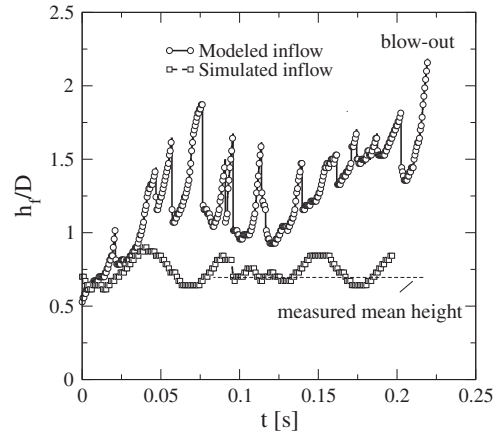


Fig. 4. Instantaneous flame front position at the axis of the burner, calculated from LES for case R20.

acts with the velocity field in a similar fashion as in Fig. 2. The two V-shape structures propagate towards each other and finally they merge into a single V-shape flame front.

Figure 4 shows the LES simulated motion of the flame front in the inner region, i.e. at the axis of the burner for case R20. The LES using the simulated inflow condition (denoted with square symbols in Fig. 4) shows an oscillation of the flame position around a mean position about  $0.65D$  above the burner exit, fairly similar to the experimentally measured flame position of  $0.68D$ . On the other hand LES with the modeled inflow condition results in a blow-out of the flame as time progresses. The blow-out process is already shown in the lower row of Fig. 2. Such significant difference in the flame stabilization behavior underlines the importance of correctly predicting the shear-layer instability in this type of flames. In the two LES simulations all model parameters, except the inflow condition, are identical. In [25] sensitivity of flame front position to the sub-grid flame speed was examined, where it was shown that if the sub-grid scale flame speed is adjusted, a stable flame can be predicted using the modeled inflow condition.

To understand the effect of the two LES inflow conditions, Fig. 5 shows a spectral analysis of the inflow at the burner exit ( $x = 0$ ) and at the downstream position  $x/D = 0.4$ . As seen, there are several low frequency ( $\sim 200$  Hz) peaks in the spectrum from the flow field using the simulated inflow, while no isolated peaks are found in the spectrum from the modeled inflow simulation. This shows that coherent structures generated in the swirler and the burner in LES with simulated inflow condition enhances the shear-layer instability, which produces more energetic vortices in the shear-layer, with vortices noticeably closer to the

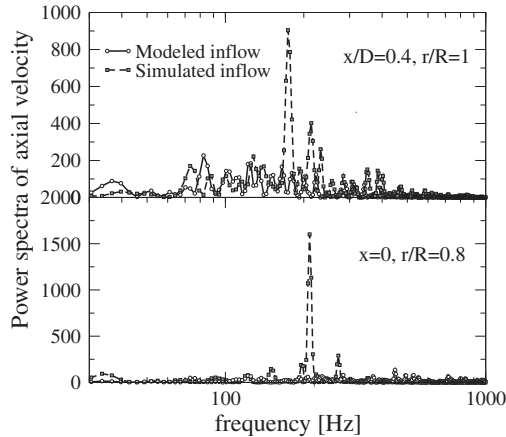


Fig. 5. Power spectra of the axial velocity at the burner exit and in the shear-layer 0.4D above the burner exit.

central low speed region than the LES results using the modeled inflow condition (Fig. 2). If the Kelvin-Helmholtz instability is delayed to further downstream or the large-scale vortices are positioned far away from the center, as in the case of the modeled inflow, the mixture dilution by the ambient air at flame front will decrease the local flamelet propagation speed in the shear-layer due to too lean flame. This will eventually cause a blow-out of the flame as shown in Figs. 2 and 4.

It is worth noting that the stable flame predicted by LES with the simulated inflow has a frequency about 15 Hz. This frequency is much lower than the low frequency motion found in the spectra of the flow at the burner exit and the shear-layer. This inner flame front low frequency motion is related to the large flame structure as shown in Figs. 1–3. When the flame position oscillates to higher position in Fig. 4 the flame shape is a W, i.e. the inner part of the flame is blown upwards, while the wing of the flame is held in the shear-layer. As the W-structure is not stable, the engulfed unburned fuel/air mixture into the flame in the inner region (Fig. 1b and c) starts to burn because of the heating from the neighboring hot zones. Once the fuel pockets are totally burned the flame front returns itself to a V-shape, which corresponds to the low positions shown in Fig. 4. The formation of W–V structures is much slower than the vortex shedding in the shear-layer since it is a large-scale flow phenomenon; a result of the center flame/wing flame interaction. This scenario has been captured in the OH-PLIF images from multi-YAG experiments (Fig. 3), and in the high speed videos at all Reynolds numbers studied, although video images are of a line-of-sight nature and it is difficult to precisely calculate the frequency at which the W and V-fronts are formed and destroyed. Similar flame

holding phenomenon has been reported by Müller et al. [15] for lifted jet flames where the vortices formed in the shear-layer can also drag the flame up and down.

The shear-layer flame stabilization mechanism and the low-frequency formation/destruction of W-structure have an indication that this type of flames may not be easily predicted by Reynolds averaged Navier–Stokes (RANS) equation models which are aimed at calculating the mean flame statistics directly while omitting the dynamics. To illustrate this we apply time averaged level-set G-equation presented in [36] to predict the stabilization position of the flame front at the axis of the burner and in the shear-layer. From the experiments and LES reported earlier [23,24], it is shown that the time averaged flame front in the low speed divergent flow zone is fairly flat and perpendicular to the mean flow stream. This allows for the reduction of the level-set G-equation along the axis of the burner to simply  $U = s_t$ , where  $s_t$  is the turbulent flame speed or the propagation velocity of the time averaged mean flame front and  $U$  is time averaged axial velocity. Figure 6 shows the distribution of  $U$  and the rms velocity ( $u_{rms}$ ) from LDV along the burner axis for case R20. The mean flame position is at about  $x/D = 0.68$  as marked in Fig. 4. Several models have been used to compute the turbulent flame speed, including the Damköhler model, Peters model [30], Gülder's model [37] and Bradley's model [38]. As shown in Fig. 6 all these models predicted the flame position at about  $x/D = 1.1$  (the mean flame position is at  $U = s_t$ ), which is much higher than the measured flame position at  $x/D = 0.68$ .

One can estimate the flame stabilization position in the shear-layer in a similar way. The measured mean axial velocity is about 8 m/s and the

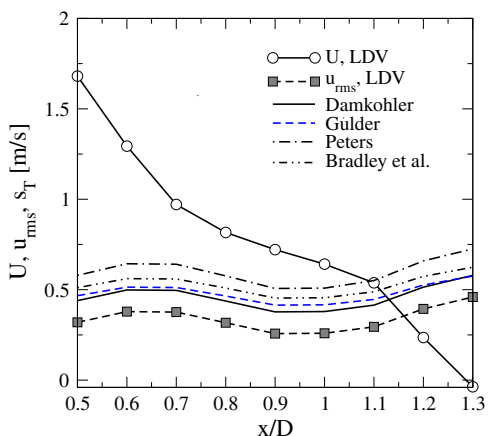


Fig. 6. Time averaged mean axial velocity, rms axial velocity along the axis of the burner from LDV measurement, and turbulent flame speed from different models based on the LDV data, case R20.

rms velocity is about 1.5 m/s [23,24]. All the turbulent flame speed models referred in Fig. 6 would predict a blow-out of the flame also in the shear-layer since the mean flow velocity is approximately 5 times higher than the turbulent flame speed in the shear-layer. This suggests the flame stabilization mechanism in the shear-layer: it is the vortices in the shear-layer which generate local instantaneous downwards flows that tend to help the flame to propagate upstream. Although the vortices are transported downstream, new vortices are continuously formed upstream to take over the duty of flame stabilization.

The dynamics of flames R16, R25, and R30 is qualitatively similar to that of flame R20. All flames show W-shape structures and flame stabilization at the inner shear-layers. Using ensemble averaged OH-PLIF images with 400 snap-shot images, the mean flame front positions along the axis of the burner are determined for flames R16, R20, R25 and R30. The flame positions are found to be at  $x/D = 0.667$ ,  $0.680$ ,  $0.674$ , and  $0.684$ , respectively. The mean flame positions are fairly independent of the burner Reynolds number. This can be explained by the fact that the low frequency vortex shedding in the shear-layer is rather independent of the burner Reynolds number at sufficiently high Reynolds numbers. Thus, the shear-layer flame stabilization would hold the flames at similar heights in different Reynolds number flows.

It should be pointed out that the dynamics of low swirl flames can be different for flames with much higher Reynolds number than studied here. At much higher Reynolds numbers, the flow characteristics may be different and the flames may not be of flamelet type. Local flame extinction may

occur with stronger flame/turbulence interaction, which will affect the structures and stabilization of the flames.

## 5. Conclusions

LDV, high speed video imaging, simultaneous PLIF of OH and acetone and LES with a two-scalar flamelet model are carried out to investigate the structure and stabilization mechanisms of a low-swirl lean premixed methane/air flame. Four different flame conditions are studied, with Reynolds number at the burner exit ranging from 16,000 to 30,000. The Karlovitz numbers are less than 6.3, and the flames are of flamelet-like structures. With increasing Reynolds number (thus turbulence intensity) more fine-scale wrinkling structures appear without local flame extinction. The flames exhibit distinctive large-scale structures characterized by the alternative appearance of V and W-shapes. The W shaped flame structure is originated from the interaction between the flame and the large-scale vortices in the high speed shear-layer. The vortices formed the shear-layer continuously drag the flame downwards, and thereby they effectively stabilize the flame. The large-scale vortices in the shear-layer are shown to be sensitive to the flow structures developed in the burner and the swirler. In simulations where these burner flow structures are omitted, blow-out of flame appears. These flame structures and stabilization mechanisms are shown to be true for all the low swirl flames within the investigated Reynolds numbers.

## Acknowledgements

This work was supported by the Swedish research funding organizations (STEM, SSF, Ce-COST, and VR), and the Swedish Armed Forces. The authors thank Dr. R.K. Cheng at Berkeley Lab for helpful discussions.

## References

- [1] F.A. Williams, *Combustion Theory*, second ed., The Benjamin/Cummings Publishing Company Inc., California, 1985.
- [2] N. Peters, F.A. Williams, *Proc. Combust. Inst.* 22 (1989) 495–503.
- [3] K. Seshadri, N. Peters, *Combust. Flame* 81 (2) (1990) 96–118.
- [4] A. Sjunnesson, P. Henriksson, C. Löfström, *AIAA paper* 92–3650 (1992).
- [5] S.I. Möller, E. Lundgren, C. Fureby, *Proc. Combust. Inst.* 26 (1996) 241–248.
- [6] D. Veynante, J. Piana, J.M. Duclos, C. Martel, *Proc. Combust. Inst.* 26 (1996) 413–420.

- [7] P. Wang, X.S. Bai, *Proc. Combust. Inst.* 30 (2005) 583–591.
- [8] N.D. Joshi, H.C. Mongia, G. Leonard, J.W. Stegmaier, E.C. Vickers, *Dry Low Emission Combustor Development*, ASME paper 98GT-310, 1998.
- [9] F. Dinkelacker, A. Soika, et al., *Proc. Combust. Inst.* 27 (1998) 857–865.
- [10] C. Stone, S. Menon, *Proc. Combust. Inst.* 29 (2002) 155–160.
- [11] Y. Huang, V. Yang, *Proc. Combust. Inst.* 30 (2005) 1775–1782.
- [12] N. Syred, *Prog. Energy Combust. Sci.* 32 (2006) 93–161.
- [13] W. Meier, P. Weigand, X.R. Duan, R. Giezendanner-Thoben, *Combust. Flame* 150 (2007) 2–26.
- [14] P. Schmitt, T. Poinsot, B. Schuemans, K.P. Geigle, *J. Fluid Mech.* 570 (2007) 17–46.
- [15] C.M. Müller, M. Breitbach, N. Peters, *Proc. Combustion Inst.* 25 (1994) 1099–1106.
- [16] C.J. Lawn, *Prog. Energy Combust. Sci.* 35 (2009) 1–30.
- [17] R.K. Cheng, *Combust. Flame* 101 (1–2) (1995) 1–14.
- [18] B. Bedat, B. R.K. Cheng, *Combust. Flame* 100 (3) (1995) 485–494.
- [19] R.K. Cheng, I.G. Sheperd, B. Bedat, L. Talbot, *Combust. Sci. Technol.* 174 (2002) 29–59.
- [20] I.G. Shepherd, R.K. Cheng, T. Plessing, C. Kortschik, N. Peters, *Proc. Combust. Inst.* 29 (2002) 1833–1840.
- [21] M. Mansour, Y.-C. Chen, *Exp. Thermal Fluid Sci.* 32 (2008) 1390–1395.
- [22] D.M. Kang, F.E.C. Culick, A. Ratner, *Combust. Flame* 151 (3) (2007) 412–425.
- [23] P. Petersson, J. Olofsson, C. Brackman, et al., *Appl. Opt.* 46 (19) (2007) 3928–3936.
- [24] K.J. Nogenmyr, P. Petersson, X.S. Bai, et al., *Proc. Combust. Inst.* 31 (2007) 1467–1475.
- [25] K.J. Nogenmyr, C. Fureby, X.S. Bai, P. Petersson, R. Collin, M. Linne, *Combust. Flame* 156 (2009) 25–36.
- [26] R. Collin, J. Nygren, M. Richter, M. Aldén, L. Hildingsson, B. Johansson, *Trans. SAE J. Fuels Lubricants* 112, Paper 2003-01-3218, 2003.
- [27] K. Kohse-Höinghaus, *Prog. Energy Combust. Sci.* 20 (1994) 203–279.
- [28] C. Schulz, V. Sick, *Prog. Energy Combust. Sci.* 31 (2005) 75–121.
- [29] A.D. Hansen, F.K.C. Lee, *J. Chem. Phys.* 62 (1) (1975) 183–189.
- [30] N. Peters, *Turbulent Combustion*, Cambridge University Press, 2000.
- [31] H. Pitsch, *Ann. Rev. Fluid Mech.* 38 (2006) 453–482.
- [32] M. Freitag, J. Janicka, *Proc. Combust. Inst.* 31 (2007) 1477–1485.
- [33] K. Akselvoll, P. Moin, *J. Fluid Mech.* 315 (1996) 387–411.
- [34] M. Klein, A. Sadiki, J. Janicka, *J. Comp. Phys.* 186 (2002) 652–665.
- [35] N. Peters, in: N. Peters, B. Rogg (Eds.), *Reduced kinetic mechanisms for applications in combustion systems, Vol. m15 of Lecture Notes in Physics*, Springer-Verlag, Heidelberg, 1993, pp. 1–13 (Chapter 1).
- [36] P. Nilsson, X.S. Bai, *Proc. Combust. Inst.* 29 (2002) 1873–1879.
- [37] Ö.L. Gülder, *Proc. Combust. Inst.* 23 (1990) 743–750.
- [38] D. Bradley, *Proc. Combust. Inst.* 24 (1992) 247–262.

# Paper VI



## Simultaneous high-speed PIV and OH PLIF measurements and modal analysis for investigating flame-flow interaction in a low swirl flame

Per Petersson<sup>1,2,\*</sup>, Rikard Wellander<sup>1</sup>, Jimmy Olofsson<sup>2</sup>, Henning Carlsson<sup>3</sup>,  
Christian Carlsson<sup>3</sup>, Bo Beltoft Watz<sup>2</sup>, Nicolas Boetkjaer<sup>2</sup>, Mattias Richter<sup>1</sup>,  
Marcus Aldén<sup>1</sup>, Laszlo Fuchs<sup>3</sup>, Xue-Song Bai<sup>3</sup>

1: Division of Combustion Physics, Lund University, Lund, Sweden

2: Dantec Dynamics A/S, Skovlunde, Denmark

3: Division of Fluid Mechanics, Lund University, Lund, Sweden

\* Correspondent author: per.petersson@forbrf.lth.se

---

**Abstract** Simultaneous High-Speed OH planar laser-induced fluorescence (PLIF) and particle image velocimetry (PIV) measurements and Large Eddy Simulations (LES) were performed in turbulent low swirl stratified premixed flames to investigate the flame/flow interaction in detail. The combined PIV and OH PLIF images were captured with up to 4 kHz, sufficient to follow the large-scale spatial and temporal evolution of flame and flow dynamics. Based on the PIV and OH PLIF images collected for two different flame conditions modal analyses were performed to identify the large scale flow structures and their impact of the flame stabilization. Important characteristic features identified from the data include the strong local dilatation of the flow field due to expansion in the flame creating regions with low axial velocity upstream of the flame where the flame can propagate upstream and expand in the radial direction. The fluctuation part of the velocity field shows strong impact of the wrinkling of the flame front. The large-scale vortex structures continuously created in the inner shear layer influence the mixing of unburnt and burnt gases and thereby they allow for the flame stabilization in the low-swirl flame. Oscillating Pattern Decomposition (OPD) is applied on the time-resolved data for characterization of the flow field in different regions whereas Proper Orthogonal Decomposition (POD) and Dynamic Mode Decomposition (DMD) are applied on 3D LES data for visualization of coherent large scale helical structures.

---

### 1. Introduction

Flame/flow interactions are of fundamental importance in combustion science; both the interaction between the flame and large-scale flow structures [1] and the interaction on the micro scale [2] can play an important role in the propagation and stabilization of the flames. The structure and dynamics of turbulent premixed stratified flames are influenced by many parameters, e.g. local gas velocity and turbulence intensity, entrainment of the ambient, large-scale structures of the flow, curvature and strain rate of the flames. To gain an overall insight to the flame flow interaction simultaneous measurements of the velocity field and scalars are required [3,4]. In this context planar laser-induced fluorescence (PLIF) is frequently used to investigate turbulent premixed flame structure and fuel distribution, and particle image velocimetry (PIV) is used to measure velocity fields. The complex time-dependent and three-dimensional nature of the flame-flow interaction is a challenge for both numerical and experimental investigations. In order to capture the important characteristics of the flames it is necessary to perform time-resolved simultaneous measurements of the velocity field and one or several appropriate scalars such as a flame front marker. Depending on e.g. the investigated flame regimes (e.g., flamelets, thin flame, or distributed reaction zone regimes) different flame front markers can be utilized. The OH radical are the first choice for high-speed (kHz) measurements due to the relatively strong signal compared with minor species, e.g. the CH radicals [5]. Being an active species participating in various elementary reactions, OH is reaching the highest levels at the flame front and thereafter it decreases in the post flame region. In flames with a continuous flame surface the maximum gradient of the OH signal may be used to define an

approximate representation of the flame front.

Simultaneous stereo PIV and CH/OH PLIF measurements in turbulent premixed flames were reported in [6]. Boxx et. al. [7] demonstrated the potential of a combined high-speed PIV and PLIF system in lifted-jet and swirl-stabilized flames. The out-of-plane velocity component was found to be a significant factor in the flame dynamics and it is desirable to acquire such data to better understand 3D effects and turbulent transport in flames.

In the present study high-speed simultaneous OH PLIF and PIV were applied to study a low-swirl lean premixed methane/air flame. Various versions of the low-swirl burner have been used in several research groups [8-16] to study the fundamental structure of turbulent premixed flames. Characteristics for the low-swirl flames are that the interaction between turbulence eddies and the chemical reactions occur in both the laminar flamelet and the distributed reaction-zone regimes of the turbulent premixed flame regime diagram [17,18]. In a joint LES and single-shot PIV/OH PLIF study [14,16] it was found that the large scale structures generated in the inner shear layer could be responsible for the flame to be stabilized at a relatively low height. However, due to the lack of time resolved experimental data this finding could not be confirmed experimentally. This has motivated the present investigation in which we perform time resolved (up to 4 kHz), simultaneous OH PLIF and PIV in the leading flame fronts.

The 2D and 3D time resolved data pose a great challenge in the post-processing process. Conventional method such as the decomposition of the instantaneous data to mean and fluctuations can be useful to compute the statistics. Fourier spectrum analysis is often used to identify the energetic scales and low frequency coherent flow structures. Special analysis methods such as Proper Orthogonal Decomposition (POD) are often used to reduce large amount data and to identify the most energetic modes in a flow field or scalar field. To analyze time-resolved experimental data Bi-Orthogonal Decomposition (BOD) and Oscillating Pattern Decomposition (OPD) are applied for visualization and characterization of coherent structures the flow field. Dynamic Mode Decomposition (DMD, [20,21]) are applied on 3D LES data for visualization of coherent large scale helical structures. In this paper we demonstrate several of the above-mentioned techniques in analysis of the flame dynamics of the low swirl stratified premixed flame at two Reynolds numbers.

## 2. Experimental Set-up and Methods

To generate the low-swirl flame the same burner set-up presented in previous work performed at Lund University was used [14-16], Fig. 1a. To assure well-controlled experimental conditions the set-up, newly calibrated mass flow controllers for methane and air (Bronckhorst Hi-Tec, EL-Flow) were used, and the co-flow and exhaust system were adjusted. The low-swirl burner is based on the design by Bedat & Cheng [9] but updated with a different swirl arrangement. The low-swirl flow is created by an outer annular swirler (Fig. 1a) where ~60 % by volume of the mixture pass, with eight swirl-vanes, in combination with an inner perforated plate that allows for about 40% by volume of the mixture to pass through [14]. After passing the swirler/perforated plate the premixed methane/air mixture of equivalence ratio 0.62 discharges through a 60 mm long nozzle (diameter of 50 mm) into a co-flow of air at ~0.25 m/s. The resulting outflow from the nozzle has an inner low velocity non-swirling region ( $r < 10$  mm,  $r$  = radius) and an outer region with higher axial and tangential velocities [14].

The turbulent flames considered here are categorized in the laminar flamelet (leading edge of the flame) and the distributed reaction-zone regimes (typically at the trailing edge of the flame) of the turbulent premixed flame regime diagram and have previously been investigated in several

publications [14-16].

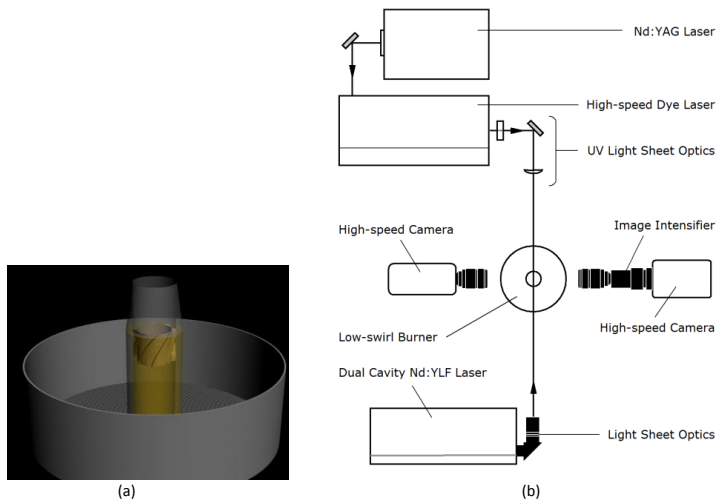


Figure 1. (a) The low-swirl burner placed in a co-flow region of air. The position of the annular swirler is schematically shown. The perforated plate creating the inner non-swirling flow region is not visible; (b) Schematic of the combined high-speed OH PLIF and PIV experimental arrangement.

Two separate laser systems were used for the combined high-speed PIV and PLIF measurements. A schematic diagram of the experimental setup is shown in Fig. 1b. The synchronization of the lasers and cameras was controlled from the DynamicStudio (Dantec) software platform via a high-resolution synchronizer unit.

The high repetition rate laser system, used to excite the OH Q1(6) line in the  $A^2\Sigma-X^2\Pi(1,0)$  band, consists of a diode pumped Nd:YAG laser (EdgeWave HD 40IV-E) in combination with a high repetition rate dye laser (Sirah Credo). For the repetition rates reported in this paper (up to 4 kHz) the pulse energy of the 283 nm radiation is kept at  $\sim 300 \mu\text{J}$ . The laser pulses are formed into  $\sim 27$  mm high laser sheets using ordinary UV-coated sheet forming optics.

The excited OH radicals were imaged onto an image intensified (Lambert HiCATT 25 Gen 2) high-speed camera (Photron Fastcam SA5), which at full resolution ( $1024 \times 1024$  pixels) has a maximum frame rate of 7200 fps. An interference filter, designed to reflect light between 275-295 nm was used to suppress scattered UV laser light. Although not required for detection, a UG 11 band pass filter is used to protect the image intensifier from any scattered PIV laser light.

For PIV double cavity diode pumped kHz Nd:YLF laser (DualPower 1000-10, Dantec) with belonging light sheet optics was used. The laser can generate double laser shots with a repetition rate of up to 10 kHz. For imaging a high-speed camera (SpeedSense 9060) with  $1280 \times 800$  pixels was used. The camera has at full resolution a maximum frame rate of 6242 fps. This means that double-frame images required for PIV can be captured with up to 3.1 fps with full resolution. In the present investigation the active chip size was reduced to  $865 \times 600$  pixels to reach a 4 kHz sampling rate for PIV. To eliminate background light and flame emission a narrowband 532 nm ( $\pm 10$  nm) interference filter was used.

The laser beams generated by the two systems were arranged in a counter-propagating manner and formed into overlapping sheets to illuminate a planar region of the flame, crossing the vertical centerline of the burner, Fig. 1b. In the probe volume the PIV light sheets had a height of  $\sim 50$  mm and a thickness of  $\sim 1$  mm. For PLIF the sheet height was  $\sim 27$  mm. The simultaneous acquisition of velocity and scalars requires a precise superposition of the measurement volumes in the post-processing. In order to perform this, a transparent calibration target designed to fit the burner nozzle was imaged on both cameras. In the post-processing, the PLIF images were mirrored to fit the PIV coordinate system prior to superposition.

The 283 nm laser pulse was fired in between the two PIV pulses to eliminate PIV particle light scattering and to freeze the flow/flame behavior. Typically a pulse separation of  $\sim 30$   $\mu$ s, was required for PIV to resolve the high axial and tangential (out-of-plane) velocities in the outer part of the flame. As flow tracer  $\sim 1$   $\mu$ m-sized  $\text{ZrSiO}_4$  particles were used.

For the evaluation of the velocity field and the following BOD and OPD analysis the DynamicStudio software (v. 3.30) was used.

### 3. Results and Discussion

Two methane/air flames are investigated both with an equivalence ratio of 0.62. The Reynolds numbers ( $Re$ ) based on the bulk flow velocity (6.2 and 9.3 m/s) and diameter at the burner exit are about  $Re=20\,000$ , and  $Re=30\,000$ . The laminar flame speed calculated using Peters' mechanism is 12 cm/s for the inlet gas temperature of 300 K and pressure of 1 atm [19]. An overview of the flow field [14] and mean flame position [14] is given in Fig. 2. The mean flame brush thickness is  $\sim 15$  mm for  $Re=20\,000$ , and  $\sim 17$  mm for  $Re=30\,000$  [14].

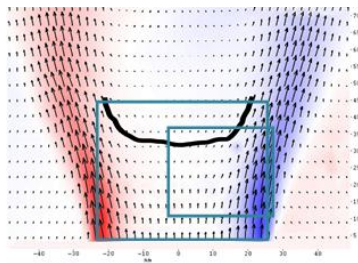


Figure 2. The time-averaged velocity field ( $Re=30\,000$ ) from stereoscopic PIV and the schematic mean flame position. Background color corresponds to the tangential velocity component (swirl). The two regions used for the modal analysis of high-speed PIV data are indicated.

The simultaneous PIV and OH PLIF sequences are used to visualize characteristic flame-flow interaction in the investigated flames. Of particular interest is the vortex motion in the inner shear-layer and how these structures interact with the flame [16]. At the nozzle exit the inner shear-layer is located between the inner low velocity non-swirling region ( $r < 10$  mm) and the outer region with higher axial and tangential velocities [14] (see Fig. 2). In this layer, originated from inside the nozzle, vortices are continuously formed due to the shear-layer instability (Kelvin-Helmholtz instability). A Strouhal number ( $St$ ) based on the characteristic length and velocity scales of high-speed region axial component gives  $St=0.2-0.3$  for frequencies in the range of 100-200 Hz.

Several set simultaneous PIV and PLIF images (each with 2000 samples) were collected for both flame conditions. With a sampling rate of 4 kHz the sample time is 0.5s. An example of a combined PIV and PLIF image is shown in Fig. 3. The color (gray scale) corresponds to the OH PLIF signal indicating the flame front and the burnt region. The OH radicals show the highest level at the flame front and thereafter decreasing to its equilibrium value in the post-flame zone. In the present unconfined flames OH can also decrease in the post-flame zone due to the entrainment of ambient

air which cools down the hot gas. The steepest OH gradient in the most upstream region or leading edge of the flame was here used to define the flame front location. Note that the OH contour resolves only the relative large scale wrinkling of the flame.

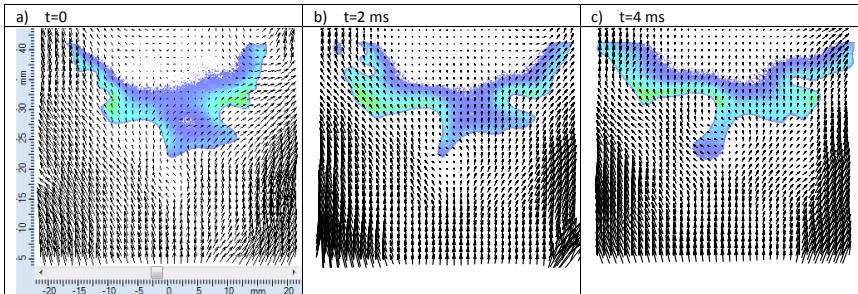


Figure 3. The instantaneous flow field (absolute velocities) and the lifted flame. Images corresponds to Fig.4 a),c) and e) below.

In Fig. 3 the instantaneous flow field, presented with absolute velocities, is shown together with the lifted flame (corresponding to Fig. 4b). Large scale wrinkling of the flame front can be seen in Fig.3, and the wrinkling structure develops with time. The flow appears to diverge around the propagating lower flame segment in the center partly of the images in Fig. 3, creating the low speed regions in both the axial and radial direction (out-of-plane motion is not captured). Careful inspecting the velocity vector in front of the flame front one can see that the flame front tends to propagate to low speed regions. This typical flame-flow interaction can partly be due to a “bluff body effect” of the expanding flame, and partly due to the swirling inflow, which is not strong enough to generate vortex breakdown but strong enough to induce low speed flow region where the flame can reside.

In Fig. 4 (a-f) a short sequence (compare Fig. 3) is shown where the mean value for each velocity vector has been subtracted to reveal the fluctuating part of the flow. The OH PLIF signal showing the flame front and the burnt region are also displayed. As will be shown below the flame flow interaction in the central region can better be understood by observing the flame dynamic in perspective to the fluctuating part of the flow. The following observation can be summarized:

- a) Vortex structures are found in the central region upstream of the flame and further out towards the inner shear layer.
- b) two counter rotating vortex structures convected downstream by the mean flow start to interact with the flame.
- c-d) the region between the two counter rotating vortex structures (here shown as a reverse axial flow with the mean subtracted) allows for the flame to locally propagate upstream.
- e-f) the flame region between the two counter rotating vortex structures expands in the radial direction.

Fig. 3 shows that the absolute flow field corresponding to Fig. 4a),c) and e) is not closely correlated with the local flame shape (dynamics) in the inner region. The mean velocity, which is stationary and determines the mean flame position, is not responsible for the dynamics and evolution of flame wrinkling. The fluctuating velocity, on the other hand, is shown to satisfactorily correlate with the wrinkling and the temporal evolution of the flame front.

Note also that the flame dynamics in the upper outer regions (e.g. upper left region in Fig. 4 a-e) is faster than in the inner region, which is likely due to strong shear in the outer region where Kelvin-Helmholtz instability can induce large scale vortices. Since the flow is swirling, a strong 3D flow exists. The 2D images are limited to explain the 3D nature of the flow and flame in this region. High-speed film sequences indicate a strong erosion of the flame towards the trailing edge of the flame.

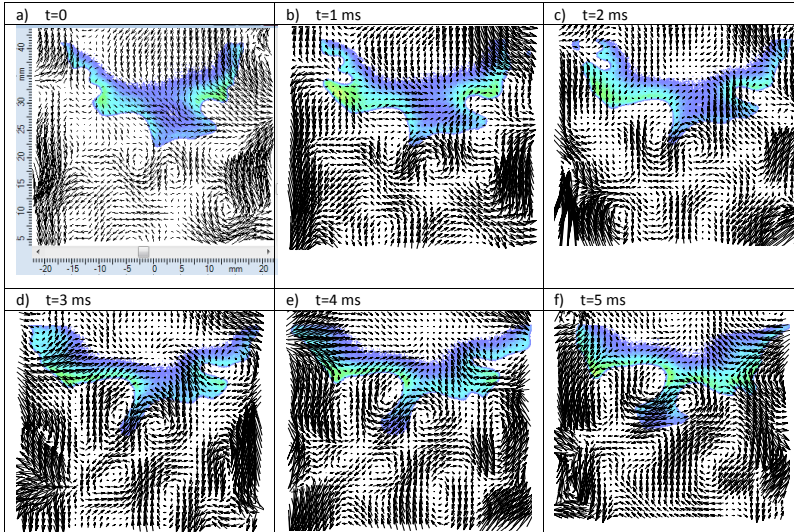


Figure 4. a -f) The fluctuating part of the flow field and the lifted flame. Flow structures created upstream the flame are convected downstream and interacts with the flame. Time between images is 1ms ( $Re=30\,000$ ).

In Fig. 5 a sequence of six simultaneous PIV and OH PLIF images shows the typical roll-up of the outer part of the flame base [16]. Note that the outer counter-clockwise rotating vortex structure creates a reverse flow that can mix burnt and unburnt. This can be compared with the typical flow in the inner region (see Fig. 3) where a reduction of the axial velocity component is created upstream the flame but no flow reversal occurs.

The presented study indicates that vortices in the outer flame region (in shear layers) are frequently created, resulting in large-scale reverse flow structures. The premixed flame front propagates in the same direction as the reverse flow upstream and radially towards the unburned mixture. This observation is consistent with the previous LES and single-shot imaging of the flame [16]. In the inner region the vortices are mainly noticeable in the fluctuating part of the flow (convection speed dominates, cf. Fig. 3 and 4). These vortices may not enhance the macro mixing but can create significant local flame wrinkling. Flame propagation in low speed regions can increase the flame surface that in turn would increase the consumption speed. Flow reversal can randomly occur also in the center region and seems to be related to out-of plane motion of the flame/flow.

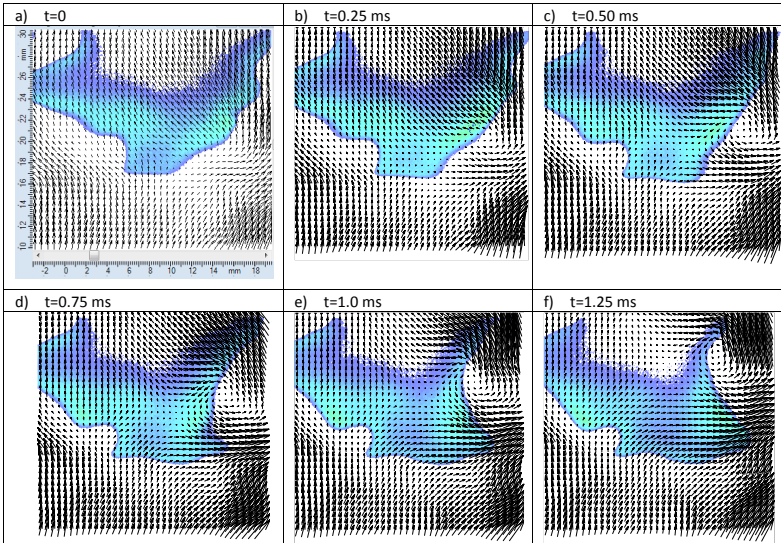


Figure 5. Characteristic flow flame interaction in the outer region (lower flame brush region,  $Re=30\,000$ ).

Further analysis indicates that certain vortex structures may emanate from the nozzle flow although the shear layers downstream of the nozzle are responsible for the generation of turbulence as well as coherent structures. As can be seen in Fig. 4 vortex structures in the inner region are seemingly convected downstream with the (in mean) rather weak swirling flow in this region (see Fig. 2). The vortex structures are captured in a time resolved manner with the planar imaging technique (PIV) due to the low out-of plane motion in this region. In the outer region the swirl is creating complicated flow structures and shear layer(s), Fig. 5. However, the mean and fluctuating part of the velocity vectors are not sufficient to identify the origin of the flow structures. Other analysis methods have to be employed as discussed below.

### Modal analysis - Oscillating Pattern Decomposition (OPD)

For multi-dimensional systems a first order linear differential equation has the form:

$$\overline{X}'(t) = \overline{A} \cdot \overline{X}(t)$$

and the solution can in general be expressed as

$$\overline{X}(t) = \sum c_n \overline{K}_n \exp(\lambda_n t)$$

where  $\lambda_n$  and  $\overline{K}_n$  are eigen-values and eigen-vectors of  $\overline{A}$ .  $\overline{K}_n$  are normalized unit vectors and  $c_n$  scale the contributions from the various terms in the summation above. Eigen-values  $\lambda_n$  of  $\overline{A}$  can be complex, which makes  $\exp(\lambda_n t)$  describe both growth/decay and oscillations:

$$\lambda_n = -1/\tau_n + i\omega_n \Rightarrow \exp(\lambda_n t) = \exp(-t/\tau_n) \exp(i\omega_n t) = \exp(-t/\tau_n) [\cos(\omega_n t) + i \sin(\omega_n t)]$$

It is evident that the imaginary part  $\omega_n$  of each eigen-value determines the frequency (rad/sec), while the real part determines stability in terms of the so-called e-fold time  $\tau_n$  (sec):

$$\tau_n \geq 0 : \text{stable mode (amplitude constant or decaying with time)}$$

$\tau_n < 0$  : unstable mode (amplitude grows with time)

If the underlying, linearized, governing equations are known (and simple) the matrix  $A$  can normally be derived fairly easy, but in many situations they are either unknown or too complex for practical purposes. OPD (and also Dynamic Mode Decomposition (DMD) [20, 21]) strives to estimate the temporal evolution matrix  $A$  from a time series of known state vectors (each state vector describing the state of the dynamic system at a certain point in time). OPD is essentially the same as Principal Oscillation Pattern (POP) analysis [23]. OPD and DMD differ slightly in the way they estimate this matrix from the experimental data, but once  $A$  has been estimated, eigen-values and -vectors can be estimated easily.

To reduce the computational time the OPD analysis is applied on the outcome of a Bi-Orthogonal Decomposition (BOD, related to POD) analysis [24]. BOD (and thus OPD) requires time-resolved data as input. The applied sampling rate of 4 kHz resolved the investigated vortex structures well in time as seen in Fig. 4 and Fig 5. The investigated sequences of 2000 images are sampled with 4 kHz (sample time of 0.5 s). The short sampling time restricts the detection of low frequencies to  $\sim 12$  Hz as at least  $\sim 6$  cycles are required for a reliable result. Following the Nyquist theory frequencies up to half the sampling rate can be resolved; however, with a recommended 6 samples/cycle and a sampling rate of 4 kHz frequencies up to  $\sim 600$  Hz should be possible.

By analyzing several high-speed sequences of the flow and its fluctuations different flow paths and regions where vortex structures are convected (and sometime created) were identified. Based on these findings we present several strong modes (with long decay time) from an OPD analysis to highlight flow structures in different regions of the investigated flow. An overview of the modes is found in Table 1. The full cycles for mode A and B and show below (Fig. 6 & 7). Both investigated flame cases show similar modal behavior.

Mode	$f$ (Hz)	Flow region
A	42.0	Upstream/in flame brush
B	35.3	Inner region/following leading edge of flame brush
C	137.9	Inner shear layer – swirl region
D	68.9	Inner flow path – no swirl

Table 1. Modes from the OPD analysis with frequencies and flow region of importance.

In Fig. 6, a full cycle of a low frequency ( $f = 42$  Hz) mode (mode A) active in the flame region is shown. The background color show the mean OH signal (flame brush) for the same data set. The large coherent structures are created just upstream of the mean flame area (Phase angle 90 and 270) and are convected downstream through the flame. The energy behind these large structures may come from the increased divergence of the mean flow around the lifted expanding (non-enclosed) flame. To confirm this comparison must be made with OPD applied to data from a non-reacting (cold flow) case when available.

Mode B shows flow structures emanating from the nozzle and being convected downstream. The structure follows a path along the leading edge of the flame brush (Fig. 7). These structures are not active in the burnt region (compare mode A).

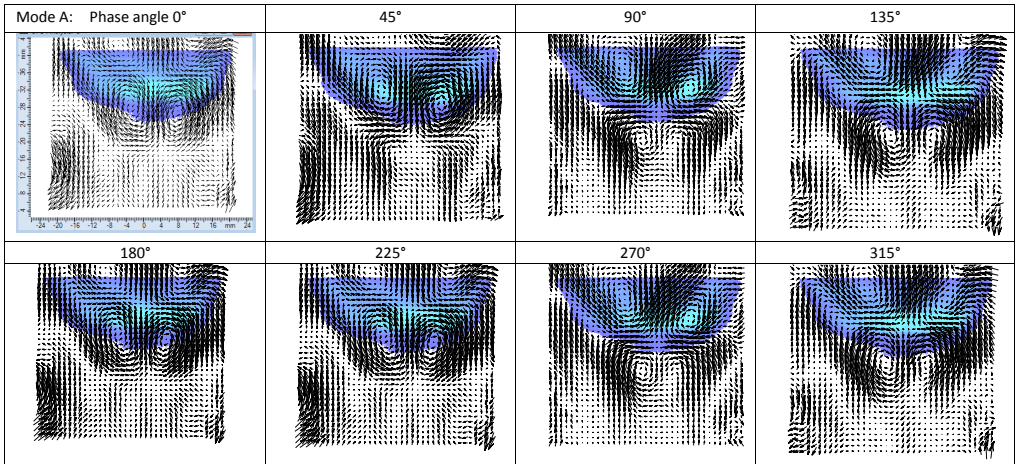


Figure 6. A full cycle for mode A ( $f = 42$  Hz). Large coherent structures are created just upstream of the mean flame area (Phase angle 90 and 270) and are convected downstream through the flame. The background shows the mean OH signal (flame brush) for the same data set. ( $Re=20000$ , 4kHz).

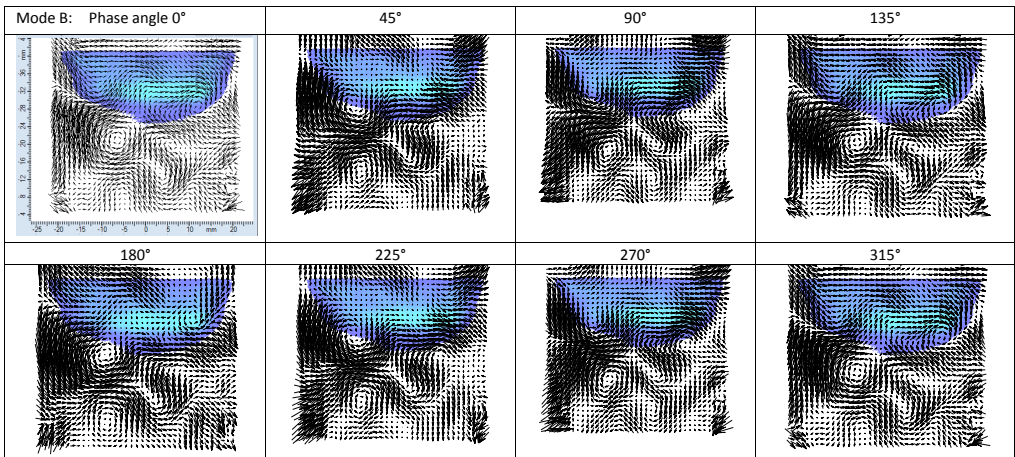


Figure 7. A full cycle for mode B ( $f = 35.3$  Hz). Flow structures emanating from the nozzle are convected downstream. The structure follows a path along the leading edge of the flame brush. ( $Re=20000$ , 4kHz).

### 3D analysis: POD and DMD

The planar data presented above needs to be put into the perspective of the complex 3D nature of the flow field in the flame region. Large eddy simulations (LES) were therefore carried out for the  $Re=20000$  flame. A flamelet model based on mixture fraction and level-set G-equation validated for both flamelet and thin reaction zone regimes was utilized. Details of the sub-grid scale flame front

propagation velocity and modification of the level-set approach accounting for local extinction has been described in [3, 15, 16]. The numerical simulations were performed with an in-house code, where the transport equations are discretized and solved on a uniform staggered Cartesian grid using a high order finite difference scheme [22]. The dimensions of the considered domain was  $8D \times 8D \times 8D$ , where  $D$  is the diameter of the nozzle exit ( $D=5.0$  cm), where two layers of local refinements of the grid were used in the flame zone region  $2.4D \times 2.4D \times 4.4D$  resulting in a mesh spacing of 1.4 mm in all directions. LES was performed to simulate the flow field inside the burner and the swirler to obtain the inflow boundary condition set at the nozzle exit plane. For details about the inflow and other boundary conditions see [3, 15, 16].

The entire 3D data was sampled at 2000 Hz during 0.1 s. 3D POD on this data was carried out, decomposing the flow field into orthogonal flow structures ranked by energy content. Figure 8 shows POD modes 0 and 1 visualized through isosurfaces of tangential vorticity. Mode 0, corresponding to POD average, shows a close to rotationally symmetric inner and outer shear layer where the outer shear layer is bending outwards and the inner shear layer is bending inwards. Mode 1 shows a lot of scattered structures with small coherent structures formed close to the nozzle exit. On the POD obtained time coefficients, Discrete Fourier Transform (DFT) was taken. For the first 15 POD modes, representing more than 87% of the total kinetic energy, the DFTs showed strong influence from two flow frequencies in the vicinity of 200 Hz ( $St = 0.3$ ) as well as some rather low frequency patterns ( $<40$  Hz). As previously presented [16], the obtained flow frequencies in the vicinity of 200 Hz are believed to be highly important in enhancing shear layer instabilities and thereby contributing to the stabilization mechanism.

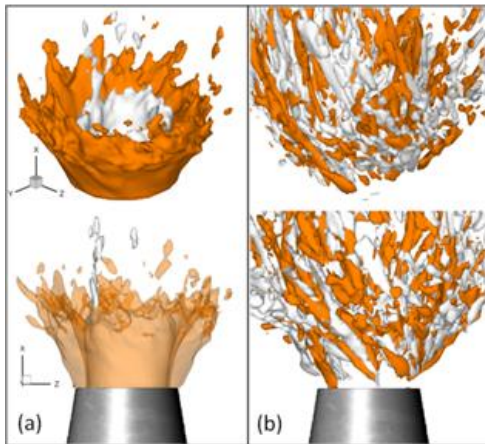


Figure 8. 3D POD modes 0 (a) and 1 (b) visualized through isosurfaces of tangential vorticity with orange and white corresponding to positive and negative vorticity respectively.

For spatial characterization of these frequencies, DMD [20, 21] was performed isolating frequency specific flow motion. Figure 9 (a) and (b) shows the real part of the DMD modes corresponding to the two frequencies obtained in the POD analysis, 175 Hz and 211 Hz respectively visualized through isosurfaces of tangential vorticity. The imaginary part of the modes (not shown here) implies a rotational motion of the modes along and against the swirling direction of the flow for Fig. 9 (a) and (b) respectively. Both modes start from the nozzle exit, where mode (a) shows an origin closer to the nozzle rim while mode (b) has its starting point closer to the nozzle center, corresponding to wall shear layer and inner shear layer induced motion respectively. The modes are

following a helical motion downstream before breaking up at the flame height. Notable is that mode (a) is classified as an  $m=2$  mode whereas mode (b) is classified as an  $m=3$  mode, corresponding to two and three “arms” of positive/negative vorticity. The reason for these numbers of arms and origin of the structures lies in the flow within the nozzle and deserves additional study.

Distinguishing these frequency specific flow patterns with DMD offers a better understanding of the helical structures induced by the swirler and its resulting shear layers than the decomposition obtained with POD.

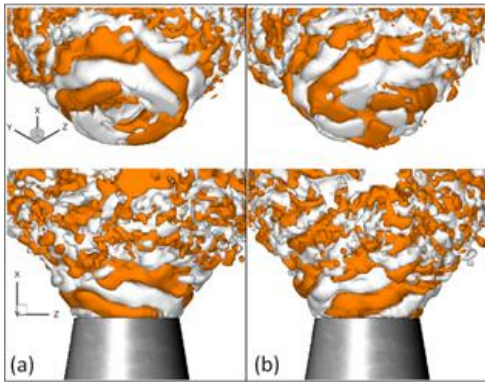


Figure 9. 3D DMD modes corresponding to frequencies 175 Hz (a) and 211 Hz (b) visualized through isosurfaces of tangential vorticity with orange and white corresponding to positive and negative vorticity respectively.

#### 4. Conclusions

High-speed sequences of simultaneous flow field (PIV) and flame front location (OH PLIF) have been obtained. The sequences give insight into the flow dynamics and the flame-flow interaction. Vortex structures emanating from the nozzle flow or created in the shear layers just downstream of the nozzle are convected along different paths. The coherent structures and the paths were also identified in the OPD modes. The results presented above indicated that vortices in the outer flame region create a local flow reversal (recirculation) and thus contribute to the large-scale mixing of burnt and unburnt. In the inner region the vortices are only noticeable in the fluctuating part of the flow (convection speed dominates). These vortices do not enhance the large-scale mixing but can create regions for the flame to propagate (in any direction) and locally increase the flame surface.

The 3D nature of the flow was shown via 3D POD and DMD analysis of LES data and visualized through tangential vorticity. Frequency specific helical structures are found close to the nozzle exit and in the shear layers and surround the inner flow region (and flame region).

#### Acknowledgements

This work was supported by the Swedish Energy Agency and the Swedish Foundation for Strategic Research through CECOST (Centre for Combustion Science and Technology), and the Swedish Research Council.

## References

- [1] C.M. Müller, M. Breitbach, N. Peters, Proc. Combustion Inst. 25 (1994) 1099-1106.
- [2] F.A. Williams (1985) Combustion Theory, 2nd edition, The Benjamin/Cummings Publishing Company, Inc. California.
- [3] K.J. Nogenmyr, C. Fureby, X.S. Bai, P. Petersson, R. Collin, M. Linne, Combust. Flame, 156, 1 (2009), 25-36.
- [4] P. Ludiciano, S.M. Hosseini, R.Z. Szasz, C. Duwig, L. Fuchs, R. Collin, A. Lantz, M. Aldén, E.J. Gutmark. Proc. ASME TurboExpo (2009) GT2009-60278.
- [5] C. Kittler, A. Dreizler, Appl. Phys. B 89 (2007), 163–166.
- [6] M. Tanahashi, S. Murakami, G-M. Choi, Y. Fukuchi, T. Miyauchi. Proc. Combust. Inst. 30, (2005), 1665-1672.
- [7] I.Boxx, M. Stöhr, C. Carter and W. Meier, Appl. Phys. B 95 (2009), 23-29.
- [8] R.K. Cheng, Combust. Flame 101 (1-2) (1995) 1-14.
- [9] B. Bedat B, R.K. Cheng, Combust. Flame 100 (3) (1995) 485-494.
- [10] R.K. Cheng, I.G. Sheperd, B. Bedat, L. Talbot. Combust. Sci. Technol. 174 (2002) 29-59.
- [11] I.G. Shepherd, R.K. Cheng, T. Plessing, C. Kortschik, N. Peters, Proc. Combust. Inst. 29 (2002) 1833-1840.
- [12] M. Mansour, Y-C. Chen, Experimental Thermal Fluid Sci. 32 (7) (2007) 1390-1395.
- [13] D.M. Kang, F.E.C. Culick, A. Ratner, Combust. Flame 151 (3) (2007) 412-425.
- [14] P. Petersson, J. Olofsson, C. Brackman, H. Seyfried, J. Zetterberg, M. Richter, M. Aldén, M. A. Linne, R. K. Cheng, A. Nauert, D. Geyer, A. Dreizler, Appl. Opt. 46 (19) (2007) 3928-3936.
- [15] K.J. Nogenmyr, P. Petersson P, X.S. Bai, A. Nauert, J. Olofsson, C. Brackman, H. Seyfried, J. Zetterberg, Z-S. Li, M. Richter, A. Dreizler, M. Linne, M. Aldén. Proc. Combust. Inst. 31 (2007) 1467-1475.
- [16] K.-J. Nogenmyr, P. Petersson, X.S. Bai, C. Fureby, R. Collin, A. Lantz, M. Linne, M. Aldén. Proc. Combust. Inst. 33 (2011) 1567-1574.
- [17] R.K. Cheng, I.G. Sheperd, B. Bedat, L. Talbot. Combust. Sci. Technol. 174 (2002) 29-59.
- [18] I.G. Shepherd, R.K. Cheng, T. Plessing, C. Kortschik, N. Peters, Proc. Combust. Inst. 29 (2002) 1833-1840.
- [19] N. Peters, in: N. Peters, B. Rogg (Eds.), Reduced Kinetic Mechanisms for Applications in Combustion Systems, Vol. m15 of Lecture Notes in Physics, Springer-Verlag, Heidelberg, 1993, Ch. 1, pp.1-13.
- [20] C.W. Rowley and I. Mezić and S. Bagheri and P. Schlatter and D.S. Henningson, J. Fluid Mech. 641 (2009) 115-127.
- [21] P.J Schmid, J. Fluid Mech. 656 (2010) 5-28
- [22] J. Gullbrand, X.S. Bai, L. Fuchs, Int. J. Numer, Meth. Fluids 36 (2001) 687-709.
- [23] K. Hasselmann, Journal of Geophysical Research, 93, D9, (1988) 11.015-11.021.
- [24] N. Aubry, R. Guyonnet, R. Lima, Journal of Statistical Physics", vol. 64, Nos. 2/3, 1991, pp.683-739.

# Paper VII



# Volumetric velocimetry in lifted turbulent premixed low-swirl flames

P. Petersson<sup>1</sup>, M. Gesnik<sup>2</sup>, J. Olofsson<sup>2</sup>, V. Jaunet<sup>2</sup>, M. Aldén<sup>1</sup>

<sup>1</sup> Division of Combustion Physics, Lund University, Lund, Sweden

<sup>2</sup> Dantec Dynamics A/S, Skovlunde, Denmark

## Abstract

Volumetric velocimetry was successfully performed in lifted turbulent premixed low-swirl flames. A four camera setup in combination with a dual cavity PIV laser was employed to provide data in 20 mm thick sections in both vertical and horizontal directions above the burner. From four simultaneous views of the illuminated particles a 3D array of light intensity discretized over voxels was reconstructed. With two successive reconstructed voxel spaces the three-component velocity vector distribution and the full gradient tensor were calculated by means of the Least Squares Matching (LSM) algorithm. The average volumetric flow field data visualized the bowl shaped low-speed region where the flame can propagate. Instantaneous data captured the complex flow generated by the swirler and the 3D shape of coherent structures in the shear layer surrounding the lifted flame. In the post-flame region the instantaneous flow field displayed an alternating direction of the axial velocity component along the centerline. On average a symmetric stagnation region was identified approximately 60 mm above the nozzle. Large coherent structures identified as parts of a vortex ring were detected downstream of the stagnation region. A local reverse flow through a vortex ring was presented as a possible mechanism for the oscillation along the center axis in the post-flame region and for the instantaneous position of the stagnation plane.

## Introduction

The possibility to perform measurements of the 3D velocity field in relatively large volumes has increased the understanding of complex flow fields and the nature of coherent structures. Most combustion devices, e.g. gas turbines, rely on swirling flow fields for flame stabilization and for generation of turbulence to enhance large- and small scale mixing of fuel and oxidizer (maximize fuel-air mixing). Ever more stringent emissions legislation has led to significant changes in modern combustor design and an increased research in new combustion concepts. New designs of the main mixer arrangement can include several annular swirlers e.g. generating co- and counter rotating air flows [1]. Fundamental studies of new designs can be performed in atmospheric test rigs and include investigation of the flow field for cold and reacting cases. A well characterized flow field is also necessary as boundary condition and for validation of Large Eddy Simulations (LES). To characterize such flow fields in detail requires advanced techniques such as volumetric or tomographic flow field measurements.

Stereo-PIV (2D, 3 velocity components) and when possible dual-plane stereo-PIV can be used as first step to investigate complex flows [2]. Different techniques have been explored to gain access to the full 3D flow field. A natural extension of the planar techniques is based on a scanning-light sheet capturing information in multiple-planes with a speed so that the flow can be considered frozen during one sweep [3]. This approach requires costly high-speed systems to image a sufficient number of planes over the volume. An alternative so called tomographic approach is to illuminate the entire volume and image the entire volume (seeding particles in the volume) at once, from several different views simultaneously [4]. From the simultaneous views of the illuminated particles a 3D array of light intensity

discretized over voxels is reconstructed. With two exposures separated in time the intensities representing the particles in the volume can then be analyzed by means of e.g. an iterative algorithm to calculate the three-component velocity vector distribution over the measurement volume [5][6][7].

## Specific Objectives

In the present study volumetric flow field measurements were applied to study turbulent low-swirl lean premixed methane/air flames. Various versions of the low-swirl burner have been used in several research groups to study the fundamental structure of turbulent premixed flames. Characteristic for the low-swirl flames is the diverging flow field creating a low-speed region where the flame can propagate. Combined with an interaction of the flame with coherent structures emanating from the nozzle the flame dynamic is complex. In a joint LES and single-shot PIV/OH PLIF study [11][12] it was found that the large scale structures generated in the inner shear layer could be responsible for the flame to be stabilized at a relatively low height. The lack of data capturing gradients out of the measurement plane has also limited earlier analysis. This has motivated the present investigation in which we perform volumetric flow field measurements in two different flame conditions.

## Experimental Set-up and Methods

To generate the low-swirl flame the burner set-up presented in previous work performed at Lund University was used [10][11][13]. An overview of the burner design is shown in Figure 1a. The low-swirl flow is created by an outer annular swirler where ~60 % by volume of the mixture passes, with eight swirl-vanes, in combination with an inner perforated plate that allows for about 40% by volume of the mixture to pass

through, see Figure 1b. After passing the swirler/perforated plate the premixed methane and air mixture of equivalence ratio 0.62 discharges through a nozzle (diameter of 50 mm) into a co-flow of air. The resulting outflow from the nozzle has an inner low velocity non-swirling region ( $X < 10$  mm) and an outer region with higher axial and tangential velocities. The investigated turbulent flames are categorized in the laminar flamelet (leading edge of the flame) and the distributed reaction-zone regimes (typically at the trailing edge of the flame) of the turbulent premixed flame regime diagram. The low-swirl flames have previously been investigated in several publications [10-14].

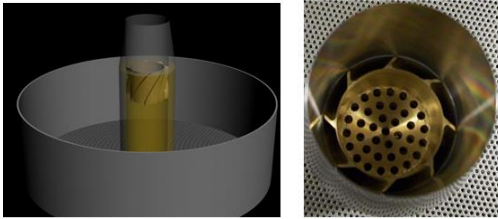


Figure 1. (a) The low-swirl burner placed in a co-flow region of air. (b) The swirler arrangement and the perforated plate.

A volumetric velocimetry system (Dantec Dynamics) was employed to provide data in 20 mm thick sections in both vertical and horizontal directions above the burner. The measurement system consists of four cameras with a resolution of 4 Megapixels (FlowSense EO 4M), mounted on Scheimpflug adaptors to ensure the overlapping of the different depth-of-fields. A dual cavity PIV laser was used for illumination. To ensure that the measurement volume was imaged with the same resolution by all the cameras, a cross like camera setup arrangement was chosen. Moreover, the cameras were facing the illumination source so that the light scattered from the seeding particles was received in forward scattering. The opening angle between the cameras was set to about 110 degrees, ensuring an optimum tomographic reconstruction quality [4]. The optical arrangement around the lifted flame is shown in Figure 2.



Figure 2. Photo of the experimental arrangement. Note the lifted flame above the burner nozzle.

The measurement volume was imaged through 60 mm lenses at a working distance of about 450 mm. According to diffraction-limited optics, the depth of field  $\Delta z$  of the optical setup can be calculated using the following equation:

$$\Delta z = 4.88 \cdot \lambda \cdot f\#^2 \left( 1 + \frac{1}{M} \right)^2$$

with  $M$  being the magnification,  $\lambda$  the illumination wavelength and  $f\#$  the numerical aperture of the lens. Therefore, a  $f\#$  of 11 was chosen giving a depth-of-field of 20 mm and ensuring that the light reaching the camera sensor is significant.

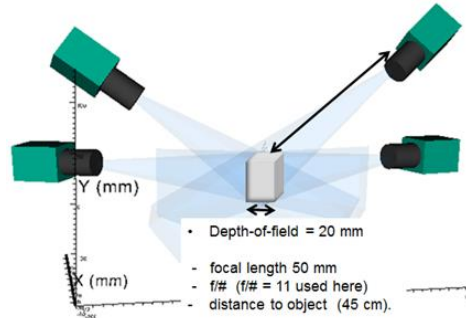


Figure 3. Schematic view of the experimental arrangement and the imaged volume.

Dedicated illumination optics was used to create a ~20 mm thick light sheet across the burner and illuminating the seeding particles in the volume. As the reader can notice, the illumination was optimized for the depth-of-field, ensuring that the imaged particles are in focus. The effective measurement volume was approximately  $50 \times 45 \times 20$  mm<sup>3</sup> with the presented setup. A schematic diagram of the experimental setup is shown in Figure 3. The camera system was calibrated by traversing and imaging a target in eight planes over the depth-of-field.

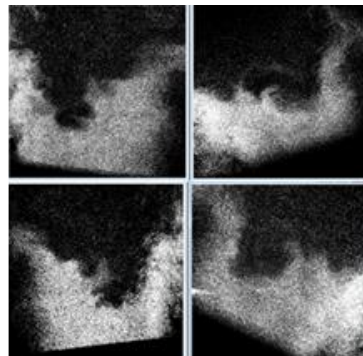


Figure 4. Integrated view of the illuminated particles in the volume seen by the four cameras. The region with low seeding density corresponds to the expanded burnt region of the flame.

From the four camera views (see example in Figure 4), the particles positions were reconstructed via a tomographic technique in an array of typically  $500 \times 440 \times 300$  voxels. Two successive reconstructed voxel spaces were then analyzed by means of the Least Squares Matching (LSM) algorithm, returning the three-component velocity vector distribution as well as the full gradient tensor over the measurement volume (Figure 5). See Westfeld et al. [7], Kitzhofer et al. [6], Kitzhofer et al. [9] and Jaunet et al. [8], for more precise information on the LSM algorithms.

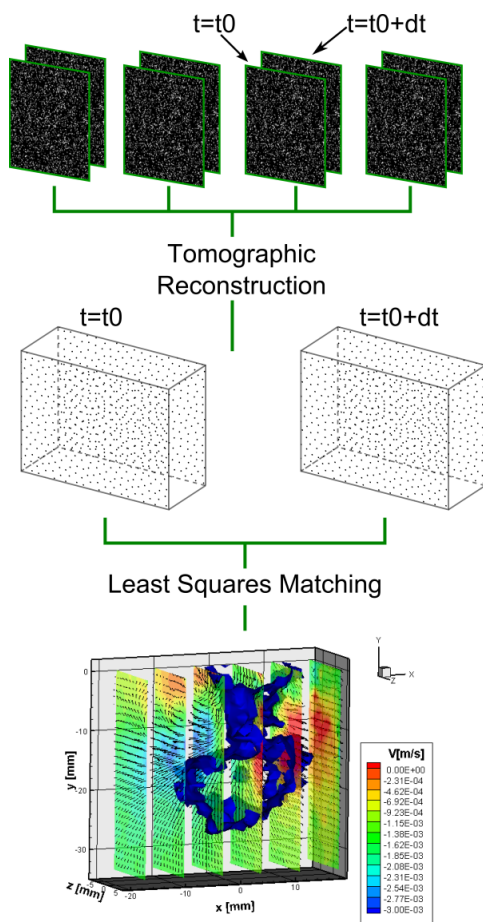


Figure 5. Reconstruction of the volume from four simultaneous views of the particles. With two successive reconstructed voxel spaces the three-component velocity vector distribution as well as the full gradient tensor is calculated by means of the LSM algorithm.

As flow tracer  $\sim 1 \mu\text{m}$ -sized zirconium oxide particles were used, giving a particle size of about 2 pixels ensuring an optimal reconstruction quality [5]. Figure 4 above shows the integrated view of the illuminated particles in the volume as seen by the 4 cameras. The

region with low seeding density in the figure corresponds to the expanded burnt region. To assure a sufficient seeding density in this region the density in the flow leaving the nozzle must be higher than for corresponding non-reacting experiments. To avoid a large number of overlapping particles in the reconstruction of the densely seeded region a four camera system was required [4].

## Results and Discussion

Two methane/air flames are investigated both with an equivalence ratio of 0.62. The Reynolds numbers ( $Re$ ) based on the bulk flow velocity (6.2 and 9.3 m/s) and diameter at the burner exit are about  $Re=20\,000$ , and  $Re=30\,000$ . An overview of the flow field and a schematic flame position is given in Figure 6. Mean flame position at the centerline is 32 mm above the nozzle for  $Re=20\,000$ , and 30 mm for  $Re=30\,000$  [11]. Characteristics for the low-swirl flames are that the interaction between turbulence eddies and the chemical reactions occur in both the laminar flamelet (leading edge of flame) and the distributed reaction-zone regimes (trailing edge of flame) of the turbulent premixed flame regime diagram.

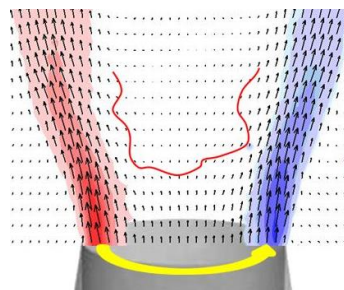


Figure 6. The mean velocity field from stereoscopic PIV and a schematic flame. Background color corresponds to the tangential velocity component (swirl). A stagnation plane (axial velocity = 0) is located in the very upper part of the image. Nozzle diameter = 50 mm.

The volumetric flow field data in Figure 7 clearly visualizes the bowl shaped low-speed region created by the diverging flow field. The corresponding cold flow field (not shown) shows a slightly slower divergence of the flow [11]. The contours in Figure 7 show how the axial flow slows down with height along the center line, reaching a very slow zone in the core towards the upper part of the flow field. In mean the tangential component (swirl) is close to zero in the inner part ( $X < 10$  mm) of the flow field, see also Figure 6. At the centerline the leading edge of the flame is in mean positioned 32 mm above the nozzle for  $Re=20\,000$ . The mean flame position is a combination of that the flow has slowed sufficiently (around 1m/s, [13]) and that the flame is wrinkled by the interacting with large coherent structures and turbulence increasing the flame area [14].

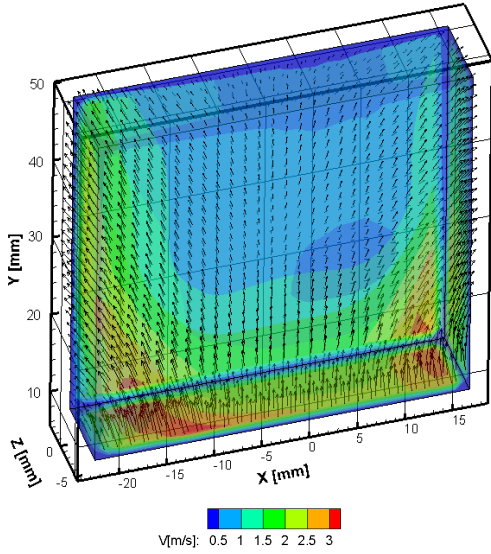


Figure 7. The average volumetric flow field visualizing the bowl shaped low-speed region created by the diverging flow field.  $Re=20\,000$ .  $V$  is the axial velocity component.

The expansion due to the heat release is visualized by the jump in seeding density in the raw images in Figure 4 above. However, even with the expansion in the post-flame region the mean volumetric flow field in Figure 8 visualizes a symmetric stagnation region approximately 60 mm above the nozzle. This is in agreement with the stagnation plane in the overall 2D flow field shown in Figure 6.

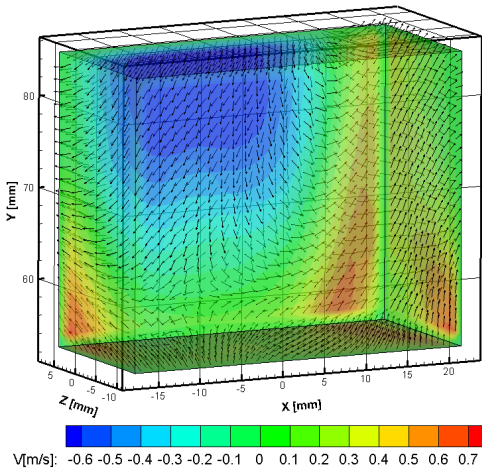


Figure 8. The stagnation zone in the post-flame region, average of 200 images.  $Re=20\,000$ .  $V$  is the axial velocity component. Velocity vectors are presented with a uniform length.

In Figure 9 below the average flow field in a horizontal section capturing the central part of the flame brush region above the nozzle, is shown (corresponds to the flow field in Figure 7). It can be noted that the average data taken within the flame brush has contributions from both burnt and unburnt regions due to the fluctuation of the flame front position. The inner low-speed region at the mean flame height,  $Z=32$  mm, is visualized by the contours representing the axial velocity ( $V$ ). Previous work has shown that the signatures of the flow passing the swirler vanes are present as the flow exits the nozzle [12]. The drawn ellipsis in Figure 9 shows that these high-speed regions, following helical paths due to the swirl component, are still found in the flow around the flame region.

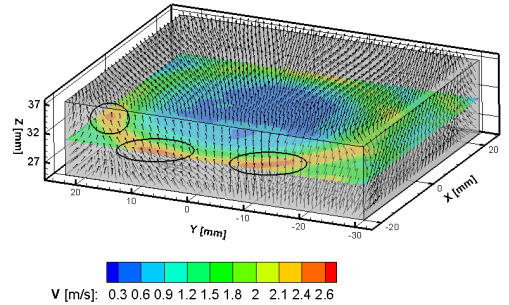


Figure 9. Horizontal section at the mean flame height. The contours represent the axial velocity ( $V$ ). The ellipsis indicates high speed regions originating from the jets leaving the eight swirler vanes inside the nozzle.  $Re=20\,000$ . This is an average of 150 images, not fully converged. Velocity vectors are presented with a uniform length.

In Figure 10 an example of the instantaneous volumetric vector field capturing the inner low-speed region ( $X < 10$  mm) and part of the outer region with higher velocities. The shear layer between the inner and outer region originates from the swirler arrangement (Figure 1b) and develops in the downstream direction. Previous simulations (LES) and time-resolved PIV (2D) have shown that coherent structures in the shear layer are emanating from the nozzle and convected downstream [14]. The iso-surfaces in Figure 10 visualize the vorticity magnitude identifying the vortex cores and thus the 3D structure of such coherent structures in the flow. The vortex detection is performed with the Q-criterion [15] utilizing the information from the velocity gradient tensor generated with the LSM algorithm. The interaction between coherent structures and the flame is previously analyzed via LES and modal decomposition of time-resolved flow field data [14]. The results in Petersson et al. [14] indicated how the leading and trailing edge of the flame was pulled radially and upstream by coherent structures with characteristics correlated to the structures presented in Figure 10. A result of the interaction between the flame and coherent structures is that the flame in average will be positioned at a much lower height above the nozzle

then indicated by the mean flow field and its fluctuations (root mean square values).

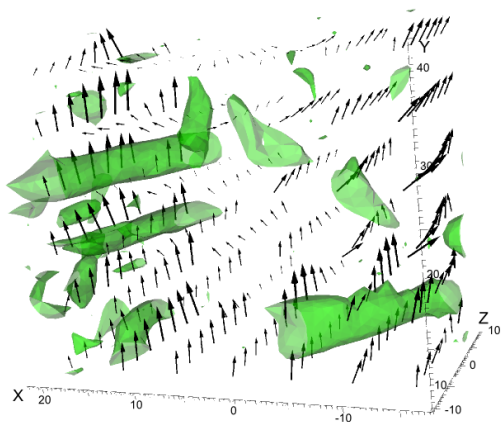


Figure 10. Instantaneous flow field with iso-surfaces visualizing complex coherent structures surrounding the inner low-speed region.

The instantaneous flow field and large coherent structures in the post-flame region are displayed in Figure 11 and 12. A reverse axial flow in the center between the surrounding structures is clearly shown above the instantaneous stagnation region 70 mm above the burner in Figure 11. The direction of rotation of the large structure correlates with the created reverse flow in the center for  $Y > 75$  mm i.e. above the stagnation plane. This is further discussed in connection with Figure 12 below.

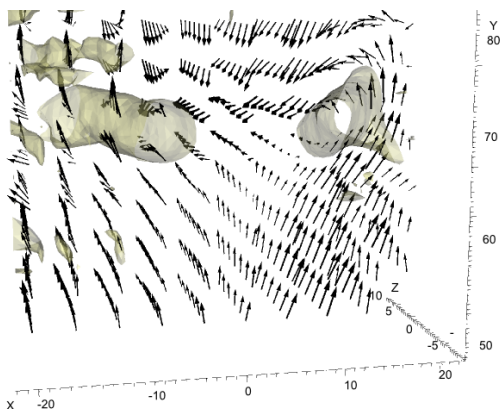


Figure 11. Instantaneous flow field with large coherent structures positioned in the stagnation region. The iso-surfaces represent the vorticity magnitude identifying the vortex cores. The rotation direction of the vortex cores is the same as illustrated in Figure 12.

In Figure 12 the stagnation region is at a lower position and only just captured in the lower part of the image. A part of a large vortex structure (compare with Figure

11), assumed to be half of a vortex ring, positioned in the X-Z plane, is by its rotation guiding the flow radially inwards,  $Y=70$  mm, and upstream (reverse axial flow) along the center axis towards the created instantaneous stagnation region at  $Y=50$  mm. The direction of rotation of the large coherent structures in both Figure 11 and 12 is consistent with that of a vortex ring with an upstream rotation direction towards the center axis. Thus this large vortex structure is contributing to an upstream (reverse) transport of fluid (for  $Y > 50$  mm) and involved in the formation of instantaneous stagnation regions at different heights with time. Note that the diverging flow field due to the swirl is the primary mechanism for the stagnation. It can be mentioned that Therkelsen et al. [16] reported shedding of vortex rings from the nozzle rim in an enclosed version of the low-swirl burner. These vortex rings, detected by phase-resolved PIV, was found to be convected in the outer shear layer leaving a dominant frequency peak in the acoustic and flame oscillation spectra [16].

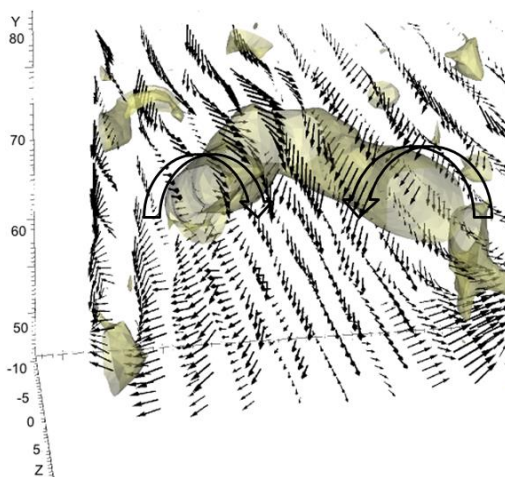


Figure 12. Instantaneous flow field and large coherent structure in the post-flame region. The iso-surfaces represent the vorticity magnitude identifying the vortex cores. The rotation direction of the vortex cores is consistent with a vortex ring.

An alternative view of structures active around the stagnation region is shown in Figure 13. With only one plane of vectors plotted and the volume tilted in the Z-direction details of coherent structures in the measurement volume can be studied. The instantaneous structures in the upper part of Figure 13 are complex, partly including segments with double vortex cores, which can be an effect of merging of interacting vortices. The rotation direction of the two upper structures in Figure 13 is the same as illustrated in Figure 12, here further visualized by the local vector field.

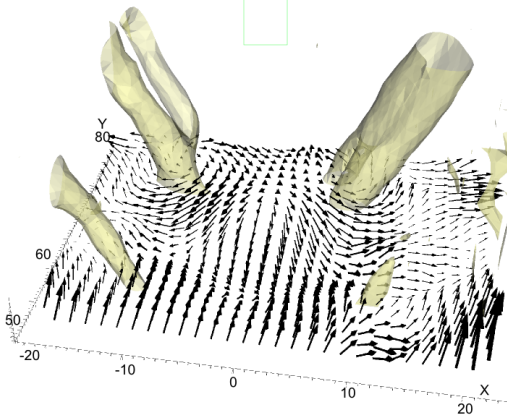


Figure 13. Details of coherent structures active around the stagnation region. Only one plane of vectors in the measurement volume is presented to increase visibility. The iso-surfaces represent the vorticity magnitude identifying the vortex cores.

### Conclusions

Volumetric velocimetry was successfully performed in lifted turbulent premixed low-swirl flames. With the four camera system the reconstruction of the densely seeded regions was achieved with high quality. The mean flow field captures the inner low-speed region housing the flame and the stagnation region in the post-flame region. The complex flow generated by the swirler and nozzle including the coherent structures surrounding the flame region and its influence on the flame dynamics have been better understood. Large coherent structures identified as parts of a vortex ring were detected downstream of the stagnation region. A local reverse flow through the center of a vortex ring was presented as a possible mechanism for the oscillation along the center axis in the post-flame region and for determining the instantaneous position of the stagnation plane.

Planned future work includes tests with combined volumetric flow field and 3D flame surface visualization to capture the flame flow interaction in 3D.

### Acknowledgements

This work was supported by the Swedish Energy Agency and the Swedish Foundation for Strategic Research through CECOST (Centre for Combustion Science and Technology), and the Swedish Research Council.

### References

[1] P. Iudiciani, S.M. Hosseini, R.Z. Szasz, C. Duwig, L. Fuchs, R. Collin, A. Lantz, M. Alden, E. Gutmark. Proceedings of ASME TurboExpo 2009: Power for Land, Sea and Air. June 8-12, USA (2009).

[2] M.P. Arroyo, C.A. Greated. Meas. Sci. Technol. 2:1181-1186 (1991).

[3] C. Brücker. Exp. In fluids 19:255-263 (1995).

[4] G.E. Elsinga, B.W. van Oudheusden, F. Scarano. 13th Int. Symp. on Applications of Laser Techniques to Fluid Mechanics, Lisbon, (2006).

[5] F. Scarano. Meas. Sci. Technol., 24. doi:10.1088/0957-0233/24/1/012001, (2013).

[6] J. Kitzhofer, P. Westfeld, O. Pust, H. G. Maas, C. Brücker. 16th Int. Symp. on Applications of Laser Techniques to Fluid Mechanics, Lisbon (2010).

[7] P. Westfeld, H.-G. Maas, O. Pust, J. Kitzhofer and C. Brücker. 16th Int. Symp. on Applications of Laser Techniques to Fluid Mechanics, Lisbon (2010).

[8] V. Jaunet, J. Kitzhofer, T. I. Nonn, B. B. Waltz, G. Ergin, P. Dupont, J.F. Debiève. European Fluid Mechanics Conference (EFMC9), Rome, September (2012).

[9] J. Kitzhofer, G. Ergin, V. Jaunet. 16th Int. Symp. on Applications of Laser Techniques to Fluid Mechanics, Lisbon, (2012).

[10] K.J. Nogenmyr, C. Fureby, X.S. Bai, P. Petersson, R. Collin, M. Linne. Combust. Flame, 156, 1 (2009), 25-36.

[11] P. Petersson, J. Olofsson, C. Brackman, H. Seyfried, J. Zetterberg, M. Richter, M. Aldén, M. A. Linne, R. K. Cheng, A. Nauert, D. Geyer, A. Dreizler. Appl. Opt. 46 (19) (2007) 3928-3936.

[12] K.J. Nogenmyr, P. Petersson P, X.S. Bai, A. Nauert, J. Olofsson, C. Brackman, H. Seyfried, J. Zetterberg, Z-S. Li, M. Richter, A. Dreizler, M. Linne, M. Aldén. Proc. Combust. Inst. 31 (2007) 1467-1475.

[13] K.J. Nogenmyr, P. Petersson, X.S. Bai, C. Fureby, R. Collin, A. Lantz, M. Linne, M. Aldén. Proc. Combust. Inst. 33 (2011) 1567-1574.

[14] P. Petersson, R. Wellander, J. Olofsson, H. Carlsson, C. Carlsson, B. Beltoft Watz, M. Richter, M. Aldén, L. Fuchs, X-S Bai. 16th Int. Symp. on Applications of Laser Techniques to Fluid Mechanics, Lisbon, (2012).

[15] J.C.R. Hunt, A.A. Wray, P. Moin. Center of Turbulence Research Report CTR-288: 193-208 (1988).

[16] P.L. Therkelsen, J.E. Portillo, D. Littlejohn, S.M. Martin, R.K. Cheng. Combust. Flame 160 (2012) 307-321.

# Paper VIII



# Experimental analysis of flashback in lean premixed swirling flames: conditions close to flashback

A. Nauert · P. Petersson ·  
M. Linne · A. Dreizler

Received: 29 November 2006 / Revised: 9 May 2007 / Accepted: 9 May 2007 / Published online: 5 June 2007  
© Springer-Verlag 2007

**Abstract** Swirling lean premixed flames are of practical relevance due to their potential for low nitric oxide (NO<sub>x</sub>) emissions. Unfortunately, these flames have various drawbacks. One critical attribute is the possibility for flashback of the reacting flow into the nozzle. Advanced numerical simulations should be able in the future to predict the transition from stable flames to flashback. For a better understanding of the process itself and for validation of numerical simulation a well-documented generic benchmark experiment is needed. This study presents a burner configuration that has already been studied extensively in the past. By minor geometrical adaptations, and via the possibility to vary the swirl intensity in a controlled way, the transition from stable flames to flashback is now accessible to detailed characterisation using advanced laser diagnostics. In a first part of this study the different states of the flame were classified. In the second part, both a stable and a precessing flame very close to flash back were compared in terms of flow and scalar field. The variation of the swirl intensity on the flame is discussed. Because the flame is strongly influenced by its inflow conditions additional velocity measurements inside the nozzle were carried out. This is of special importance for subsequent

numerical simulations to match the experimental conditions. The quantitative investigation of the flame during flashback is subjected to consecutive experiments where planar laser diagnostics at high repetition rates will be exploited.

## 1 Introduction

Lean premixed combustion offers the potential for low NO<sub>x</sub>-emissions. In practical realizations, premixed flames are usually stabilized by internal recirculation zones generated by vortex breakdown associated with swirling flows reviewed by Lucca-Negro and O'Doherty (2000). When exceeding critical geometry-dependent swirl numbers, coherent flow structures evolve that precess around the central axis of the swirl-generating nozzle (precessing vortex core, PVC). In premixed combustion these coherent flow structures can cause the flame to move upstream into the nozzle. This process is known as flashback.

Obviously, flashback can cause serious problems in any kind of practical application and must be avoided during all operational conditions of a combustor. Advanced design tools based on numerical simulation of turbulent combustion should therefore be able to determine the PVC, the stability limits of the premixed flame, the onset of flashback and the upstream flame propagation during flashback in a physically correct manner.

Flashback is a complex phenomenon not yet fully understood. Different mechanisms causing flashback have been identified and are described in Thibaut and Candel (1998), Fritz et al. (2001), Kröner et al. (2002), Kieseewetter et al. (2003), Sommerer et al. (2004), Davu et al. (2005)

---

A. Nauert · A. Dreizler (✉)  
FG Energie- und Kraftwerkstechnik, TU Darmstadt,  
Petersenstr. 30, Darmstadt 64287, Germany  
e-mail: dreizler@ekt.tu-darmstadt.de

P. Petersson  
Department of Combustion Physics,  
Lund Institute of Technology, 221 00 Lund, Sweden

M. Linne  
Sandia National Laboratories, Combustion Research Facility,  
MS 9051, PO Box 969, Livermore 94551-0969, USA

and Domingo and Vervisch (2007): flashback by autoignition, flashback in the boundary layer, turbulent flame propagation in the core flow, flashback due to combustion instabilities and flashback induced by vortex breakdown. These different mechanisms are briefly reviewed by Sommerer et al. (2004). Flashback by vortex breakdown, relevant for the flashback phenomenon observed in this study, is associated with a density jump due to combustion-induced heat release. Occasionally negative axial velocities located ahead of the vortex breakdown region occur and push the flame upstream. Negative axial velocity is due to azimuthal vorticity produced primarily through baroclinic torque (Hasegawa et al. 2002; Konle et al. 2006; Domingo and Vervisch 2007). If this process continues the flame proceeds farther and farther upstream. It is important to note that this scenario is inherently transient in nature. A description based on global parameters such as probability density function (PDF) of velocity components or turbulent flame speed is not only inappropriate but in contradiction to experimental findings.

Recent advances in large eddy simulation (LES) allow an accurate prediction of complex turbulent flows including coherent structures in a wide range of frequencies (see for example Janicka and Sadiki 2005 or Wegner et al. 2004). The inclusion of combustion models, mostly transferred from RANS (Reynolds-averaged Navier Stokes), within the LES approach has become a high-priority issue of current research. For premixed flames, among others, the *G-equation* by Pitsch and de Lageneste (2002), Wang and Bai (2005) and Freitag and Janicka (2007) or the *artificial thickened flame*-approach by Veynante and Vervisch (1997) were successfully used to predict flow and scalar field characteristics. As demonstrated by Sommerer et al. (2004) for inherently transient cases such as flashback, combustion LES is the most promising predictive design tool.

As for any simplifying model, combustion LES must be validated properly. Exemplified in the TNF-Workshop series (2006) for non-premixed flames a validation should be based on different generic burner geometries and flame series that cover a range of different Reynolds numbers (flames D–F) and/or fuel compositions. For non- and partially premixed flames a broad and reliable database has already been developed to meet the needs of model validation. Examples are described in Barlow (2007), Geyer et al. (2005), Cabra et al. (2002), Dally et al. (1998) and Tacke et al. (1998). For turbulent premixed flames fewer databases are available such as Chen et al. (1996), Cheng et al. (2002) or Schneider et al. (2005). To best of the authors' knowledge, none of these databases include detailed insight into flames that approach or achieve flashback.

The aim of the present investigation therefore, was to study turbulent premixed flames near or during flashback.

For this purpose an unconfined swirled premixed lean methane/air flame was selected. The swirler includes design features typical of practical devices. A crucial design benefit is the use of a moveable block for swirl generation. It allows a continuous variation of the theoretical swirl number in a range from 0 to 1.98 and thereby flame series measurements with variable swirl intensity. The same basic nozzle geometry was used in previous experimental (Schneider et al. 2005; Nauert and Dreizler 2005) and numerical studies (Wegner et al. 2004; Freitag et al. 2006a, b; Freitag and Janicka 2007). These studies were focused on non-reacting and stable combusting conditions at various Reynolds numbers but at fixed swirl number. The present study has been focused on variable swirl intensity but fixed Reynolds number. It benefits from the improved understanding of this complex fluid flow and the tools developed during previous research. By Thibaut and Candel (1998), Sommerer et al. (2004) and Freitag et al. (2006b) the combustion LES approach has already demonstrated its potential to predict the transition from stable combustion to flashback.

This paper is organized as follows: in section two the background of the previous studies with the most important aspects with regard to flashback are summarized. In the third section, minor changes of the nozzle design are highlighted and different flame operating conditions ranging from stable, meta-stable (precessing flame) to flashback are discussed. Diagnostic methods for the investigation of the operating conditions prior to flashback are described in section four. In the fifth section the focus is on flow and scalar field characteristics of the stable and precessing flame operating condition.

A correct prediction of the flame characteristics at the precessing flame condition very close to flashback is seen as an important step in the validation sequence of combustion LES. In a subsequent paper to be published separately, attention will be devoted to the transient phenomenon of flashback utilizing recent advances in high-speed optical diagnostics highlighted by Upatnieks et al. (2002), Wäsle et al. (2005), Konle et al. (2006) or Smith and Sick (2007).

## 2 Starting point

As pointed out in the introduction the present investigation continues previous studies of turbulent non-reacting and reacting atmospheric swirling flows. A cross-sectional view of the original nozzle used throughout the previous studies is shown in Fig. 1a. Upstream of the moveable block methane was injected into the 300 K airflow by a perforated tube. It was experimentally confirmed that methane and air were perfectly mixed. Downstream of the

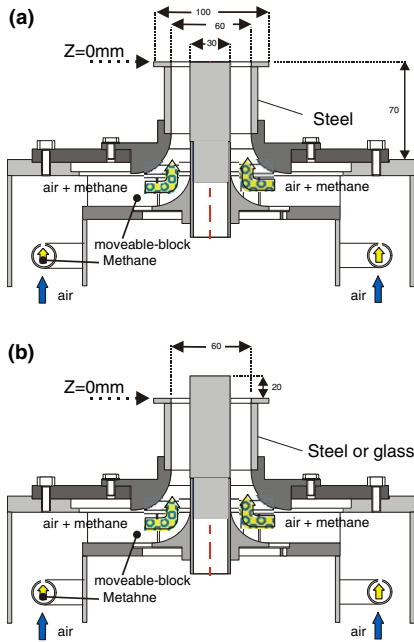


**Fig. 1** *Top* cross-sectional view of the nozzle used in previous studies for stable flame operation. *Bottom* adapted nozzle by extended central bluff-body and optical access to the annular slot

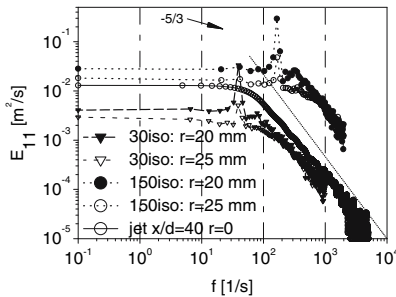


**Fig. 2** Power spectral density ( $E_{1,1}$ ) as function of frequency ( $f$ ) deduced from temporal auto-correlation measurements by LDV recording the axial velocity component. The measurements were conducted 1 mm downstream the nozzle presented in Fig. 1a. The corresponding radial position is labelled in the legend. 30 iso corresponds to a non-reacting case with  $Re = 10,000$ . 150 iso labels the non-reacting case with  $Re = 42,300$ . Characteristic frequencies are at 38 and 195 Hz. Reproduced from Schneider et al. (2005)

mixing chamber the flow passed the swirler assembly. Subsequently the flow reached a cylindrical, vertically oriented, and 15 mm wide annular slot enclosing a 30 mm-

diameter central bluff-body. To achieve constant and reproducible boundary conditions the bluff-body was water-cooled to 353 K. Downstream of the nozzle exit the flow expanded due to the circumferential momentum of the swirled flow. At sufficiently high swirl and/or Reynolds numbers a vortex breakdown generated an internal recirculation zone located in mean above the bluff-body.

For a lean methane/air mixture using an equivalence ratio of  $\phi = 0.833$  statistically stable flames were achieved up to a theoretical swirl number  $S_{th}$  (see Leuckel (1967)) of 0.8. These stable flames were anchored in the vicinity of the rim of the central bluff-body at the nozzle exit. By increasing the swirl number beyond 0.8 the flame flashed back into the annular slot quickly and was finally stabilized at the swirler assembly.

For  $S_{th} = 0.75$  and  $\phi = 0.833$  (stable flames) a thorough investigation of the flow field has been carried out by Schneider et al. (2005). In the reacting cases power spectra of the axial velocity component (gained from one- and two-point LDV correlation measurements) showed no appearance of any coherent structures. Switching to non-reacting flows under otherwise identical conditions, however, the power spectra showed characteristic frequencies that scaled with the Reynolds number (Fig. 2). The associated Strouhal-numbers were approximately 0.25 and independent of the Reynolds number as expected for fully developed turbulence. The observation of characteristic frequencies in the power spectra was associated with the occurrence of precessing vortex cores (PVCs). It was hypothesized that the stable combusting case did not show a PVC for the same nozzle setting because the effective swirl number was reduced by the variation in density.

Based on these previous findings the working hypothesis for the present investigation was that flashback observed at swirl numbers exceeding a critical value could be associated with the onset of a PVC, analogous to the non-reacting case, causing a coherent precession of the flame and eventually reaching back into the annular slot. At the leading edge of the flame streamlines diverge due to combustion-induced volume expansion. In addition, azimuthal vorticity might be generated close to the flame tip such that negative axial velocities push the flame against the oncoming fluid. An experimental review of this hypothesis necessitated slight adaptations of the nozzle described in the next section.

### 3 Adapted nozzle geometry and operation conditions

Reaching the critical swirl number in the reacting case causes a sudden and rapid flashback upstream into the annular slot. This prohibits a thorough investigation of the transition from stable to flashback conditions. For this

reason the original design of the nozzle shown in Fig. 1a was changed by extending the central bluff-body by 20 mm (Fig. 1b). By this measure the transitional regime between stable and flashback (termed ‘meta-stable’ and associated with a precession of the flame) was extended and made experimentally accessible for sufficiently long observation times. To allow optical observation of the transient flame during flashback, the outer cylindrical wall of the annular slot was replaced in some of the experiments by a cylindrical glass tube. The inner diameter of 60 mm was matched to its stainless-steel counterpart. For easy control of the swirl number the moveable block was equipped with an electrical stepper motor. By an additional gear reduction the theoretical swirl number could be changed in increments of  $\Delta S_{th} = 0.02$ . This was sensitive enough to reproduce the various operational modes of the flame as detailed below.

For a global characterization of flame stability, the equivalence ratio and the Reynolds number were varied. The top of Fig. 3 shows the critical theoretical swirl number  $S_{th,crit}$  for a fixed Reynolds number of 10,000 (based on hydraulic diameter and bulk nozzle exit velocity). At the bottom  $S_{th,crit}$  is presented for fixed equivalence ratios but varying Reynolds numbers. Operation of the

flame in regions below the experimental data points corresponds to statistically stable conditions, the regions above the data points correspond to flashback. Due to limitations in the laboratory environment the maximum thermal load of the rig was restricted to 35 kW. For  $\phi = 1$  this was reached at  $Re = 10,000$ . Therefore, higher Reynolds numbers or richer mixtures were not investigated.

In a range from  $\phi = 0.7$  to 0.9  $S_{th,crit}$  decreases monotonically. This finding is attributed to the influence of the density jump between unburned and burnt gases across the flame front ( $\rho_d/\rho_b$ ). Flame propagation speed along a fine vortex was shown by Hasegawa et al. (2002) (and references therein) to depend on  $\rho_d/\rho_b$ : an increasing value of the density jump increases baroclinic torque that was identified as the initiating mechanism causing the premixed flame propagating into the vortex. The higher the density jump, the higher is the negative axial velocity generated by azimuthal vorticity. In a later study by Domingo and Vervisch (2007) this finding was confirmed for cases where turbulence was superimposed onto the vortex interacting with the flame.

Exceeding  $\phi = 0.9$ ,  $S_{th,crit}$  increases again and reaches a value of  $S_{th,crit} \approx 1.0$  at  $\phi = 1.0$ . This finding is in contrast to the explanation above as the largest density jump is expected to occur closer to  $\phi = 1$ . The present data, however, is insufficient to draw any final explanation for this observation.

At  $\phi = 0.833$  the critical swirl number was  $S_{th,crit} \approx 1.0$ . This corresponds to a 25% increase relative to the original nozzle geometry (Fig. 1a) and can be attributed to changes in the flow field by the extended bluff-body.

For a fixed equivalence ratio (bottom in Fig. 3)  $S_{th,crit}$  increases approximately linearly with the Reynolds number. From this finding one can conclude that larger bulk velocities retard the onset of flashback. The propagation speed in vortex tubes was found to be proportional to the maximum circumferential velocity (Hasegawa et al. 2002 and references therein). The proportionality factor is a positive function of the density jump across the flame and the Reynolds number of the vortex. Based on numerical simulations Hasegawa et al. (2002) showed that the dependence of the proportionality factor on the Reynolds number is a rather weak function (compare Fig. 8 in Hasegawa et al. 2002). Assuming that their findings for non-turbulent vortex tubes can be conferred to the present case, increasing Reynolds numbers only marginally increase the negative axial velocity generated by azimuthal vorticity. Drawing the balance between increased axial momentum due to higher Reynolds numbers and negative axial momentum due to azimuthal vorticity, net negative flame propagation into the annular slot is obtained only when swirl is increased. This mechanism broadens the region of stable operation at higher Reynolds numbers to higher values of  $S_{th,crit}$ .

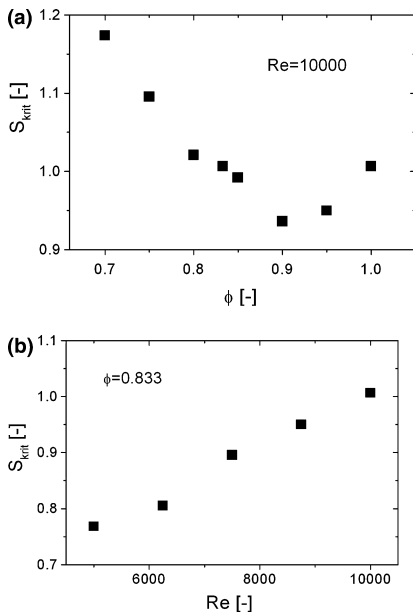


**Fig. 3** Critical theoretical swirl numbers  $S_{th,crit}$  where flashback occurs. *Top* fixed  $Re$ , varying equivalence ratio. *Bottom* fixed equivalence ratio, varying  $Re$

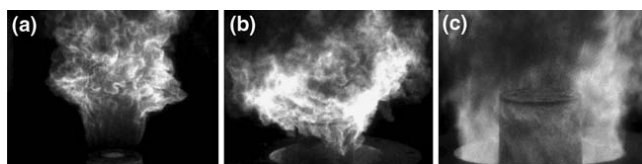


**Fig. 4** Snapshots of turbulent premixed methane/air flames:  $Re = 10,000$ ,  $\phi = 0.833$ . *Left* no swirl, no precession of the flame, flame is stabilized at the rim of the bluff-body. *Middle*  $S_{th} \approx 0.8$ , prior

to flashback, flame precesses around the cylindrical bluff-body. *Right*  $S_{th} > S_{th,crit}$ , flame after flashback

**Fig. 5** Flame luminescence monitored by intensified CMOS camera at a frame rate of 7 kHz. Only six exposures of a full cycle are shown. The cycle duration was  $\sim 7.5 \pm 0.6$  ms

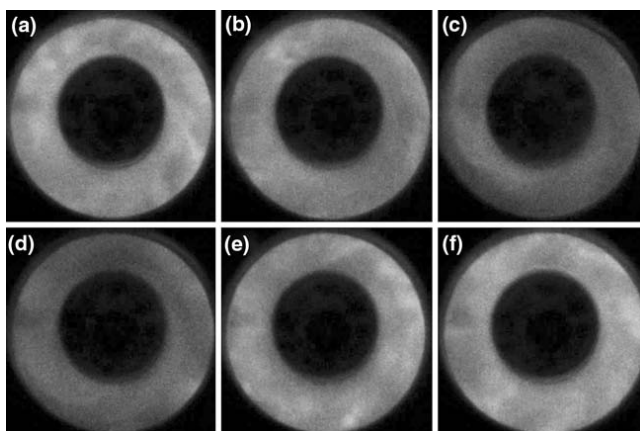
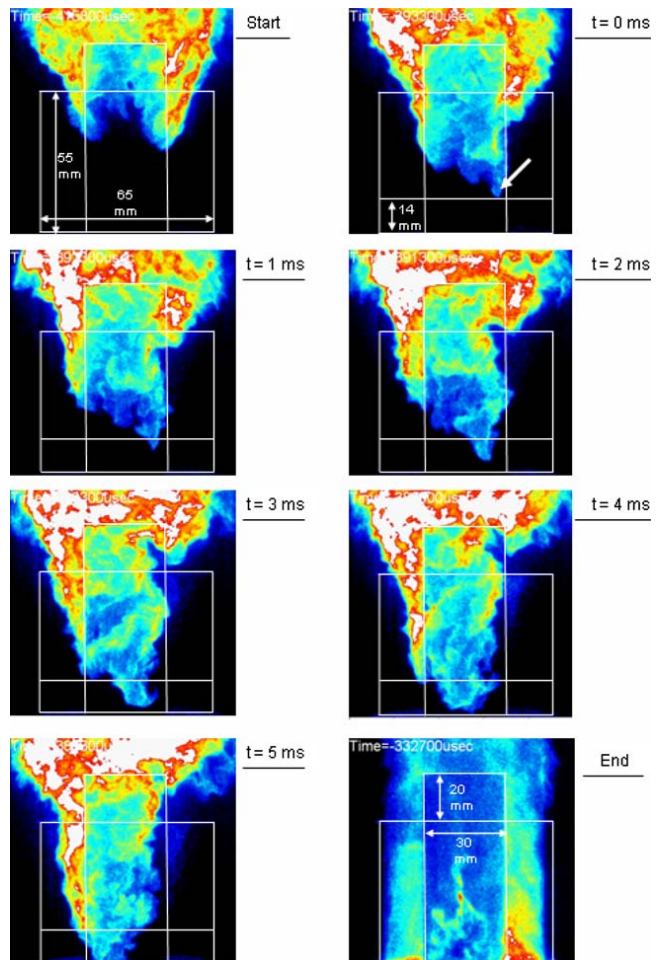


Figure 4 gives a visual impression of the three different operational modes by imaging the spectrally integrated chemiluminescence in the visible and near UV. These images were taken with an intensified high-speed CMOS camera system (LaVision). Exposure times for these examples were 100  $\mu$ s. Figure 4a shows the flame without any swirl acting as an annular jet flame. It was anchored at the front side of the central bluff-body. No precession of the flame was observable. At the instant of time presented in Fig. 4a vortex shedding created the mushroom-like structure of chemiluminescence. Increasing the theoretical swirl number to values in a range between 0.8 and 1.0, the farthest upstream position of the flame left the rim of the bluff-body and moved upstream. As is obvious in Fig. 4b the flame stabilized freely in the diverging flow field beside the shell of the bluff-body. The stabilization point was highly transient and it precessed around the bluff-body. The average leading edge flame position depended sensitively on the swirl number. For  $S_{th,crit} \approx 1.0$  only a slight increase of the swirl could cause the flame to reach back into the annular slot. Once the combustion zone was located partly in the annular slot the flow dilatation just upstream the flame tip was expected to accelerate the flow at neighbouring radial and circumferential locations in the

slot. Furthermore, this situation might promote the production of azimuthal vorticity due to baroclinic torque pushing the flame upstream. To confirm this expectation high-speed particle image velocimetry (PIV) conditioned on the heat release zone is planned for the near future to unambiguously identify vorticity ahead of the flame tip as suggested by recent DNS (compare Fig. 5 in Domingo and Vervisch 2007).

When the critical swirl number was met or passed the flame suddenly flashed back into the nozzle and stabilized upstream at the swirler assembly. Figure 4c shows the chemiluminescence after the flashback. In this mode a combustion instability was observed producing rumbling at rather low frequencies. By high-speed imaging at several kHz a clear oscillation of chemiluminescence intensity was observed that was associated with heat release oscillation causing the rumbling. Figure 5 shows one cycle of time resolved chemiluminescence monitored with the intensified CMOS at a repetition rate of 7 kHz. The view was from top but slightly tilted to prevent damaging of the optics due to hot exhaust. That is why the slot appears slightly asymmetric. Based on 14 consecutive cycles, the mean cycle duration was 7.5 ms with a standard deviation of 0.6 ms ( $\sim 133 \pm 10$  Hz).

**Fig. 6** Temporal sequence of flame during flashback lasting from “Start” to “End” 83.1 ms. The sequence between  $t = 0$  and 5 ms shows only the section where the flashback occurs. White lines sketch the extensions of the central bluff-body and the outer wall of the annular slot. The actual flashback is triggered by the leading edge of the flame highlighted by an arrow in the second image ( $t = 0$  ms). Within 5 ms approximately 14 mm were covered corresponding to a flame propagation speed of nearly 3 m/s



To obtain a closer view of the flame dynamics during flashback time-resolved chemiluminescence sequences were monitored through the glass tube as detailed above. Figure 6 shows snapshots of the flame dynamics in steps of 1 ms (notice that the data rate was 10 kHz, in the sequence from 1 to 5 ms only every tenth exposure is shown). The starting point of the sequence shows the flame stabilization region located in the annular slot. It precessed around the bluff-body. Flashback was associated with a rather small flame region identified as the flame tip and highlighted by an arrow in the image at  $t = 0$  ms. This part of the flame subsequently propagated upstream during the precession in a very fast manner. In this individual example the propagation speed in negative axial direction of the leading edge

was nearly 3 m/s. In other individual realizations, propagation speeds up to 12 m/s were observed. However, at the end of the sequence shown in Fig. 6 the flame was anchored by the swirler assembly similar to the example shown in Fig. 4c.

To investigate whether this fast propagation can be caused simply by global turbulent burning velocity  $s_T$ , the relation derived by Gouldin (1987) can be used:

$$\frac{A_T}{A} = \left( \frac{\varepsilon_0}{\varepsilon_f} \right)^{D_f - 2} \quad (1)$$

where  $D_f$  is the fractal dimension. According to Gülder (1999)  $D_f$  is smaller than 7/3. Pointed out by Peters

(2000), there is common agreement that the outer cut-off scale  $\varepsilon_0$  should be the integral length scale. However, in this study the filtered burning velocity has been observed: flame front wrinkling smaller than the optical resolution is not resolved (if the wrinkling would have been fully resolved laminar flamelets would have been observed). Therefore, at the leading edge of the upstream propagating flame  $\varepsilon_0$  is given more correctly by the actual resolution of the experimental set up. With respect to the inner cut-off  $\varepsilon_i$  there is disagreement among various authors. Following Peters (1986) the Gibson length describing the smallest scalar scales should be used whereas most experimental studies favour the Kolmogorov scale as summarized by Gülder (1999). Using the two-point correlation measurements from Schneider et al. (2005) recorded in the shear layer 1 mm above the nozzle exit for the configuration presented in Fig. 1a and  $Re = 10,000$ , Kolmogorov as well as Gibson lengths were approximately equal and amount to  $50 \mu\text{m}$ . Using the longitudinal length scales measured in the same study of  $L_{11,x} = 10 \text{ mm}$  as the worst case scenario the global flame surface ratio is  $A_T/A \approx 5.8$  (the filtered flame surface ratio is much smaller). Using a spatial resolution of typically  $400 \mu\text{m}$  as a conservative estimate for  $\varepsilon_0$ ,  $A_T/A$  is only two. With a laminar burning velocity at  $\phi = 0.833$  of  $0.36 \text{ m/s}$  and following the pioneering work of Damköhler (1940)

$$s_T = s_L \frac{A_T}{A}, \quad (2)$$

the maximum global turbulent burning velocity was estimated to be less than  $2.1 \text{ m/s}$  (for  $\varepsilon_0 = 10 \text{ mm}$ ) and  $<0.8 \text{ m/s}$  (for  $\varepsilon_0 = 0.4 \text{ mm}$ ), respectively. In any case these values are well below the observed propagation speeds during flashback. Following the idea of the kinematic balance between flame propagation velocity (as visualized by high-speed chemiluminescence imaging), flow velocity and burning velocity the mismatch between estimated maximum turbulent burning velocity and observed flame propagation speed suggests that upstream-oriented convection at the leading edge of the precessing flame most certainly caused by baroclinic torque plays a significant role for the observed flashback phenomena. This hypothesis will be tested by high-speed laser diagnostics in a subsequent study.

Coming back to the stable and meta-stable operation conditions of the flame, a numerical simulation must reliably determine the flow and scalar field prior to flashback. For validation purposes diagnostic methods and the characterisation of some important flow and scalar field features are described in the following sections.

## 4 Diagnostic methods

### 4.1 Hot wire anemometry

In a first step of this validation sequence the non-reacting flow and turbulence field should be considered. For locations downstream of the nozzle, comprehensive LDV measurements by Schneider et al. (2005), using the configuration presented in Fig. 1a are believed to be appropriate for this purpose: a numerical simulation successful in predicting the flow field of the original nozzle will be able to predict the cold flow of the nozzle with the extended bluff body. However, one deficiency in this data set is the missing information from inside the annular slot, as the inflow conditions determine the flow and scalar field tremendously. For this reason hot wire anemometry (HWA) measurements were performed at various locations inside the annular slot complementing the data from Schneider et al. (2005). A standard commercial HWA (Dantec) was used with a single-wire probe. Following the procedure summarized by Bruun (1995) axial and tangential velocity components were determined by HWA-measurements at two different angles. This procedure assumed that the radial velocity component inside the annular slot was close to zero. According to Fig. 4 in Schneider et al. (2005) 1 mm above the nozzle exit, the mean radial velocity component was less than 10% of the peak axial component. Therefore, the assumption is justified that inside the annular slot axial and tangential components define the mean-flow direction.

### 4.2 Particle image velocimetry (PIV)

For the two-component PIV measurements the beams from two frequency doubled Nd:YAG lasers (Quantel) were overlapped to provide successive Mie scattering from added seed particles. The energy in each pulse was set to  $65 \text{ mJ}$ . With a time separation of  $20 \mu\text{s}$  between consecutive pulses and by using a relatively large sheet thickness of  $1.5 \text{ mm}$ , out-of-plane losses of imaged particles could be minimized. An interline-transfer CCD camera (Flowmaster 3S, La Vision) with  $1,280 \times 1,024$  pixels was used for imaging, typically imaging an area of  $70 \times 57 \text{ mm}^2$  in the flow. A cross-correlation algorithm with an adaptive multipass method (LaVision) was applied for the evaluation of the velocities. The spatial resolution for the PIV measurements equals the sizes of the interrogation windows, here  $32 \times 32$  pixels, and the sheet thickness. Hence, the spatial resolution is about  $1.75 \times 1.75 \times 1.5 \text{ mm}$ .

Dry  $\text{ZrSiO}_4$  particles of  $0.5 \mu\text{m}$  were used as seed material. Velocity fluctuations up to  $7 \text{ kHz}$  could thus be resolved with a slip of less than 1%. To assure stable and

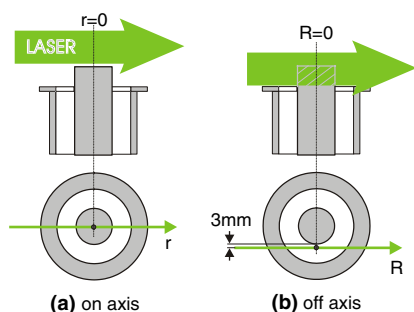


**Fig. 7** Illustration of the two PIV planes. *Top* shows a side-view, *bottom* a top-view. *Left* “on axis” arrangement. *Right* “off axis” arrangement

reproducible seeding densities,  $\text{ZrSiO}_4$  was sieved into a bypass of the gas flow. For this purpose a combination of static mesh and rotating brush was installed at the bottom of an adequately dimensioned  $\text{ZrSiO}_4$  storage tank. The speed of the motor driving the rotating mesh and the bypass-ratio determined the seeding density. The seeding density was adjusted to meet the standard PIV criterion (see Keane and Adrian 1990) of a minimum of 10 particles in the interrogation windows, even in the hot expanded region.

Two planes were used for PIV measurements. As illustrated in Fig. 7 the first plane was centred in top of the central bluff-body (“on-axis”). In this configuration axial ( $u$ ) and radial ( $v$ ) velocity components were monitored at various radial profiles. The second PIV plane intersected the flow at the exit of the annular flow (“off-axis”). Here the closest distance to the side of the bluff body was approximately 3 mm. As obvious from the illustration for  $|R| > 0$  mm the horizontal component comprises a mixture of radial and tangential ( $w$ ) components. A purely tangential component was observed at  $R = 0$  mm.

#### 4.3 Planar laser induced fluorescence (PLIF)

Detailed insights into the scalar field of a turbulent flame can be gained best from quantitative multi-scalar single shot Raman/Rayleigh measurements. Because this study is an extension of previous studies, the interested reader is referred to Freitag et al. (2006a) and Gregor (2006) for more detailed scalar measurements, where the nozzle presented in Fig. 1a was used. However, for a global characterization of the scalar field at varying swirl numbers using the adapted nozzle geometry (Fig. 1b), the average OH distributions give access to the topology of the flame brush. In connection with the previous scalar measurements, information on the flame brush is seen in this context as a suitable benchmark to test numerical simulations.

OH distributions were measured by planar laser-induced fluorescence (PLIF). For this purpose a frequency doubled Nd:YAG laser pumped a dye-laser (Sirah) operating on a Rhodamine 590 dye solution in methanol. The output from the dye laser was then frequency doubled. The UV laser beam was formed into a sheet of thickness  $\sim 500$   $\mu\text{m}$  in the probe volume region. OH radicals were excited via the  $Q_1(8)$  transition of the (1,0) band in the A-X system at approximately 283 nm with a fairly temperature-insensitive population distribution in the  $J = 8$  level. Fluorescence from the A-X (1,1) and (0,0) bands was detected using a UV lens (Nikkor  $f = 105$  mm,  $f/\# = 4.5$ ). In front of an ICCD camera (Hadland), a bandpass filter and a *UG11*-filter (Schott) suppressed spurious light efficiently.

For each investigated flame condition 1500 PIV and OH-LIF sequences were collected in order to generate statistics.

## 5 Results and discussion

In a first step it was verified that the HWA measurements reproduced the previous non-reacting LDA measurements detailed in Schneider et al. (2005). Figure 8 shows radial profiles of the mean axial and tangential velocity components for the non-reacting case at  $Re = 10,000$ , measured 1 mm downstream from the nozzle exit. Obviously there is excellent agreement between both measurements. This provides confidence that the flow facility operates in a repeatable way.

Velocity measurements inside the annular slot at locations  $-15$  and  $-30$  mm upstream of the nozzle exit are presented at the bottom of Fig. 8. The extension of the HWA probe prohibited measurements closer than 1.8 mm from the wall. Mean axial and tangential components show similar profiles up to  $r = 22$  mm. Their variation with different axial positions within the annular slot was rather low. The profiles are asymmetric with respect to the mean radius at  $r = 22.5$  mm. The mean axial velocity peaked at  $r = 25$  mm whereas the tangential component peaked at  $r = 23$  mm. These profiles can be used to confirm correct inflow boundary conditions in numerical simulations.

PIV was conducted in the reacting flow field as well. As sketched in Fig. 7 two different measurement planes were selected. At the on-axis position on top of the central bluff-body Figs. 9 and 10 compare various radial and axial profiles of the mean axial ( $u$ ) and radial velocities ( $v$ ), fluctuations as well as co-variances for  $S = 0$  (no swirl) and  $S = 1.0$  (close to critical swirl number resulting in rapid flash back). In the absence of swirl the maximum mean axial velocity does not show any significant radial shift with increasing axial height as it does in case with swirl. The spreading of the flow in case of high swirl is a feature

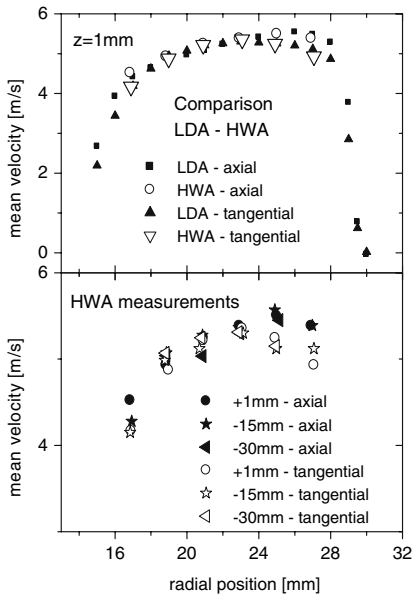


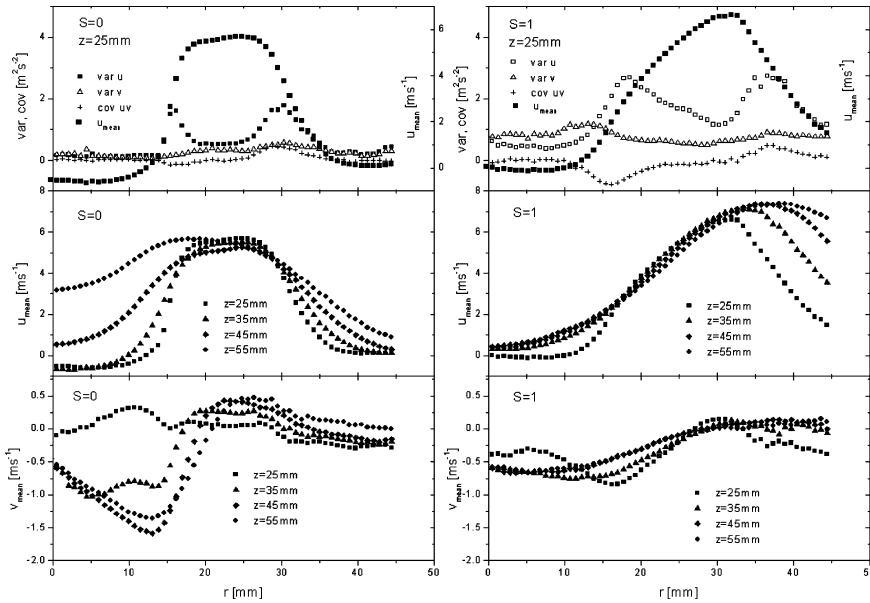
**Fig. 8** Mean axial and tangential velocity components. The radial position  $r = 0$  mm is at the symmetry axis of the nozzle. The annular slot extends from  $r = 15$  to  $30$  mm. The mean radius is located at  $r = 22.5$  mm. *Top* measurements  $1$  mm above the nozzle, comparison of recent LDA and HWA measurements of the present study. *Bottom* additional HWA measurements inside the annular slot at  $-15$  and  $-30$  mm

well known from many previous studies. The maximum mean velocity for  $S = 0$  was constant with axial height, whereas, for  $S = 1$  the maximum increases by approximately  $10\%$  within the domain considered. Mean radial velocities at  $S = 0$  show distinct negative values especially for  $z > 35$  mm in a radial range up to  $20$  mm. This indicates the presence of a recirculation bubble above the central bluff body. Indeed, negative axial velocities associated with a recirculation were observed up to  $z \approx 42$  mm. For  $S = 1$  the mean radial velocities show smaller absolute values compared to  $S = 0$ . However, they are negative up to  $r \approx 25$  mm slightly broadened versus the  $S = 0$ -case and in accordance with the spreading of the swirled flow. Intense shear layers are indicated by peaks in the respective radial profiles of the velocity fluctuations. In case of  $S = 0$  these peaks were observable primarily for the axial velocity component as the radial component was relatively small. Co-variances at the inner shear layer were negative but positive at the outer shear layer. This corresponds to the radial transport of axial momentum in the gradient direction. This observation was more pronounced in case of the high swirl.

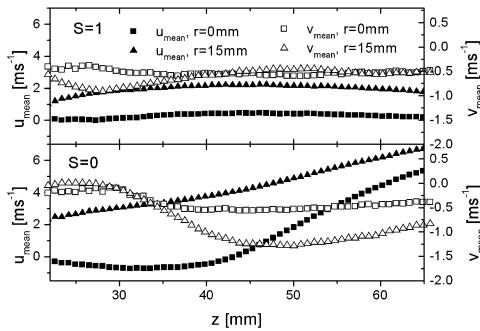
Axial profiles of the two velocity components are compared in Fig. 10. As obvious from the profiles at  $r = 0$  mm, the inner recirculation zone was less pronounced for the case with  $S = 1$ . For the high swirl the constant  $u_{\text{mean}}$ -profile at  $r = 15$  mm indicates that the position of the inner shear layer was fixed in the radial direction. This finding is supported by the constant radial position of the maximum of the variance of the axial velocity component at different heights (not shown).

Figure 11 shows axial profiles of the PIV measurements at the off-axis position. As noticed before for values with  $|R| > 0$  mm the horizontal velocity comprised a mixture of radial and tangential velocity components complicating the interpretation. Therefore, only the axial profiles that comprise the axial and pure tangential velocity components at  $R = 0$  are presented. The tangential velocity components are negative in Fig. 11 due to the frame of reference. For  $S = 0$  the mean axial velocity declined in axial direction by  $\sim 10\%$ . The small deviation of the mean tangential component from zero over the entire axial range shown is attributed to experimental imperfections. In case of  $S = 1$  the mean axial component decreased rapidly in the close vicinity of the nozzle exit. This observation is attributed to the spreading of the strongly swirled flow. After this initial decay the mean axial component was constant for  $z > 10$  mm. The absolute value of the tangential component decayed similar to the axial component. Constant values of approximately  $3$  m/s were measured for  $z > 15$  mm. The variances of both swirl intensities were relatively flat over the entire axial range considered. For the higher swirl the respective values were significantly larger. The associated increased turbulence level would be expected to widen the flame brush. Additionally, this would promote mixing with ambient air similar to observations by Freitag et al. (2006a) for the nozzle configuration presented in Fig. 1a.

Binary images were generated in post-processing of the instantaneous relative OH radical distributions measured by PLIF. For this procedure, normal corrections such as background subtraction or normalisation on the mean profile of the laser sheet were applied along with a thresholding for the identification of the local flame front. From typically  $200$  single-shots a two-dimensional probability map for the occurrence of the flame front was calculated. By integration along radial cuts of the probability map the mean reaction progress variable  $\langle c \rangle$  was obtained. For the on-axis measurement position Fig. 12 compares radial profiles of  $\langle c \rangle$  at different axial positions and the cases  $S = 0$  and  $S = 1$ . For the absence of any swirl the little spreading of the flow caused a thin flame brush evident by the steep radial gradients of  $\langle c \rangle$ . The apex angle relative to the vertical symmetry axis of the flow determined for the  $\langle c \rangle = 0.5$  iso-contour was  $13^\circ$ . Taking the axial position of  $z = 35$  mm for example, the location  $\langle c \rangle = 0.5$  coincided



**Fig. 9** Radial profiles for variances, covariances, mean axial and radial velocity components at different axial heights measured by PIV at the on-axis location as indicated in Fig. 7. At the left-hand side the case  $S = 0$  is presented, at the right-hand side  $S = 1$



**Fig. 10** Axial profiles for mean axial velocity components for swirl numbers of 0 and 1 at two radial positions as measured by PIV

approximately with the steepest gradient of the mean axial velocity component at the inner shear layer. For the case  $S = 1$  the flame brush was significantly widened. Unfortunately, the field of view in the PLIF experiments was not sufficient to follow the profiles up to  $\langle c \rangle = 0$ . However, the  $\langle c \rangle = 0.5$  contours were shifted significantly to larger radii. The apex angle was increased to approximately  $23^\circ$ . Compared to the mean axial velocity profile at  $z = 35$  mm, the  $\langle c \rangle = 0.5$ -location matched with the velocity maximum.

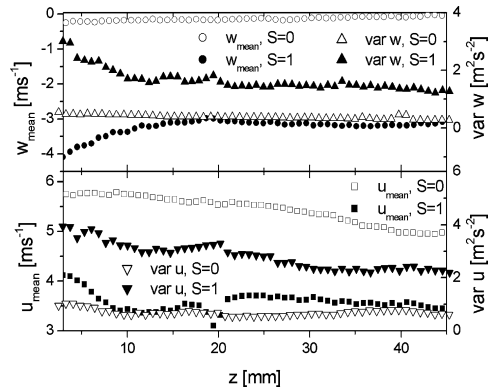


**Fig. 11** Axial profiles of axial and tangential velocity components measured with PIV at the off-axis position highlighted in Fig. 7. The cases with  $S = 0$  and  $S = 1$  are compared. Data at  $R = 0$  are considered only. For  $S = 1$  the mean axial velocity component exhibits at  $z \approx 19$  mm outliers due to experimental artefacts

Apparently the mean flame location moved with increased swirl out of the shear layer. For future investigations it might be worth investigating the impact of the mean flame position on its degree of wrinkling.

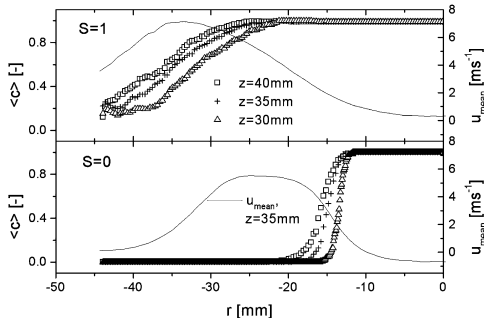


**Fig. 12** Radial profiles of the mean reaction progress deduced from planar OH distributions. Profiles are shown for different axial heights as measured at the on-axis position. For comparison of relative positions, the mean axial velocity component measured at  $z = 35$  mm is superimposed

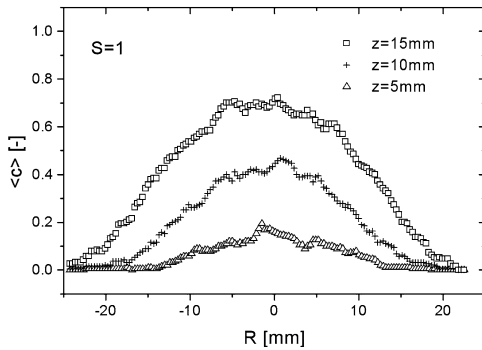


**Fig. 13** Mean reaction progress profiles at different axial locations measured at the off-axis position. Only results of  $S = 1$  are shown as for  $S = 0$  the flame was not present alongside the superficial surface of the bluff body at any time

The mean reaction progress at the off-axis position is presented in Fig. 13. Recall that the co-ordinate  $R$  does not correspond to the radius denoted by  $r$ . The profiles are symmetric with respect to  $R = 0$ . This indicates that the turbulent flame was axi-symmetric. The maximum of  $\langle c \rangle$  was at its maximum for  $R = 0$  independent of  $z$ . From this it follows that the flame stabilized close to the shell of the bluff body. This is in accordance with the snapshot of the flame presented in Fig. 4b. At position  $z = 5$  mm the flame was observed rarely. Therefore, values of  $\langle c \rangle$  are low. With increasing height the probability of finding the flame increases. At  $z = 15$  mm the maximum of  $\langle c \rangle$  reached 0.7.

## 6 Conclusions

In this paper a previous investigation of lean premixed swirling flames was extended by variation of the swirl number. When a critical swirl number was exceeded the flame flashed back into the annular nozzle. The critical swirl number depended on conditions such as equivalence ratio and geometric features. In the original configuration presented in Schneider et al. (2005) a rapid turnover between stable flame and flashback was observed. Conditions very close to flashback for this reason were not accessible for characterisation using relatively slow (e.g., pulsed at low duty cycle) laser diagnostic experiments. By the extension of the central bluff body by 20 mm a metastable flame could be realized. A particular feature of this state was the precession of the flame around the bluff body.

In the first part of this work, the different states of the flame were classified. At low swirl the flame stabilized in top of the bluff body. At sufficiently high swirl numbers the flame moved upstream and stabilized beside the shell of the bluff body and precessed. A small increase of the swirl number caused the flame to move into the annular slot. From this position a flashback could occur very rapidly. Using an optically transparent nozzle the flashback velocities were measured by transient flame luminosity using a CMOS camera at a frame rate of up to 10 kHz. The filtered burning velocity was estimated and found much lower than the measured flashback velocity. Therefore, the flashback was assisted by an upstream-directed convection. Comparing this observation to previous studies in the literature the upstream flame propagation most certainly is caused by azimuthal vorticity. This hypothesis needs to be confirmed by planar velocity measurements at high repetition rates. For this purpose PIV conditioned on the local flame front position is scheduled for future experiments to identify vorticity production in the vicinity of the flame tip.

In the second part of this study HWA, PIV and OH PLIF measurements of the stable flame with  $S = 0$  and the precessing flame with  $S = 1$  were performed. Quantitative features of the flow and scalar field were compared and the influence of different swirl intensities was discussed. These data serve for validation of numerical simulation aiming to predict the transition from stable flames to flashback. Combustion large eddy simulation (CLEs) has already proven its potential for this challenging task as shown by Sommerer et al. (2004) and Freitag et al. (2006b).

**Acknowledgments** The authors are grateful for financial support through Deutsche Forschungsgemeinschaft (DR374/4-1) and the European Union Large Scale Facility in Combustion (LTH Lund) is gratefully acknowledged. For the HWA measurements the authors appreciate assistance by J. Fabricius.

## References

- Barlow RS (2007) Laser diagnostics and their interplay with computations to understand turbulent combustion. *Proc Combust Inst* 31:49–75
- Bruun HH (1995) Hot-wire anemometry, principles and signal analysis. Oxford University Press, Oxford
- Cabra R, Myhrvold T, Chen JY, Dibble RW, Karpets AN, Barlow RS (2002) Simultaneous laser Raman-Rayleigh-LIF measurements and numerical modeling results of a lifted turbulent  $H_2/N_2$  jet flame in a vitiated flow. *Proc Combust Inst* 29:1881–1888
- Chen YC, Peters N, Schneemann GA, Wruck N, Renz U, Mansour MS (1996) The detailed flame structure of highly stretched turbulent premixed methane-air flames. *Combust Flame* 107:223–244
- Cheng RK, Sheperd IG, Bédard B, Talbot L (2002) Premixed turbulent flame structures in moderate and intense isotropic turbulence. *Combust Sci Tech* 174:29–59
- Dally BB, Fletcher DF, Masri AR (1998) Flow and mixing fields of turbulent bluff-body jets and flames. *Combust Theor Model* 2: 193–219
- Damköhler G (1940) Der Einfluß der Turbulenz auf die Flammgeschwindigkeit in Gas-gemischen. *Z Elektrochem* 46: 601–652
- Davu D, Franco R, Choudhuri A, Lewis A (2005) Investigation of flashback propensity of syngas premixed flames. *AIAA Paper* 2005–3585
- Domingo P, Vervisch L (2007) DNS of partially premixed flame propagating in a turbulent rotating flow. *Proc Combust Inst* 31: 1657–1664
- Freitag M, Klein M, Gregor M, Geyer D, Schneider C, Dreizler A, Janicka J (2006a) Mixing analysis of a swirling flow using DNS and experimental data. *Int J Heat Fluid Flow* 27: 636–643
- Freitag M, Dreizler A, Janicka J (2006b) Numerical investigations of a strongly swirled flow. In: Eighth international workshop on measurement and computation of turbulent nonpremixed flames, Heidelberg, Germany
- Freitag M, Janicka J (2007) Investigation of a strongly swirled unconfined premixed flame using LES. *Proc Combust Inst* 31: 1477–1486
- Fritz J, Kröner M, Sattelmayer T (2001) Flashback in a swirl burner with cylindrical premixing zone. *ASME Turbo Expo New Orleans*
- Geyer D, Kempf A, Dreizler A, Janicka J (2005) Turbulent opposed-jet flames: a critical benchmark experiment for combustion LES. *Combust Flame* 143: 524–548
- Gouldin FC (1987) An application of fractals to model premixed turbulent flames. *Combust Flame* 68: 249–266
- Gregor MA (2006) Laserspektroskopische Untersuchungen technologisch relevanter Flammen. Department of Mechanical Engineering, TU Darmstadt
- Gülder ÖL (1999) Fractal characteristics and surface density of flame fronts in turbulent premixed combustion. In: Mediterranean combustion symposium, Ankara
- Hasegawa T, Nakamichi R, Nishiki S (2002) Mechanism of flame evolution along a fine vortex. *Combust Theor Model* 6: 413–424
- Janicka J, Sadiki A (2005) Large eddy simulation of turbulent combustion systems. *Proc Combust Inst* 30: 537–547
- Keane RD, Adrian RJ (1990) Optimization of particle image velocimeters. Part 1: double pulsed system. *Meas Sci Technol* 1:1202–1215
- Kiesewetter F, Hirsch C, Fritz J, Kröner M, Sattelmayer T (2003) Two-dimensional flashback simulation in strongly swirling flows. *ASME Turbo Expo Atlanta, Georgia*
- Konle M, Winkler A, Kiesewetter F, Wäsle J, Sattelmayer T (2006) CIVB flashback analysis with simultaneous and time resolved PIV-LIF measurements. 13th Int symp on applications of laser techniques to fluid mechanics, Lisbon, 26–29 June
- Kröner M, Fritz J, Sattelmayer T (2002) Flashback limits for combustion induced vortex breakdown in a swirl burner. *ASME Turbo Expo, Amsterdam*
- Leuckel W (1967) Swirl intensities, swirl types, and energy losses of different swirl generating devices. *IRF Doc. Nr. G02/a/16*
- Lucca-Negro O, O'Doherty T (2000) Vortex breakdown: a review. *Prog Energy Combust Sci* 27: 431–481
- Nauert A, Dreizler A (2005) Conditional velocity measurements by simultaneously applied laser Doppler velocimetry and planar laser-induced fluorescence in a swirling natural gas/air flame. *Z Phys Chem* 219:635–648
- Peters N (1986) Laminar flamelet concepts in turbulent combustion. *Proc Combust Inst* 21:1231–1250
- Peters N (2000) *Turbulent combustion*. Cambridge University Press, Cambridge
- Pitsch H, Duchamp de Lageneste L (2002) Large-eddy simulation of premixed turbulent combustion using a level-set approach. *Proc Combust Inst* 29: 2001–2008
- Schneider C, Dreizler A, Janicka J (2005) Fluid dynamical analysis of atmospheric reacting and isothermal swirling flows. *Flow Turbulence Combust* 74: 103–127
- Smith, J D, Sick, V (2007) Quantitative dynamic fuel distribution measurements in combustion-related devices using laser-induced fluorescence imaging of biacetyl in iso-octane. *Proc Combust Inst* 31: in print
- Sommerer Y, Galley D, Poinot T, Ducruix S, Lacas F, Veynante D (2004) Large eddy simulation and experimental study of flashback and blow-off in a lean partially premixed swirl burner. *J Turbulence* 5:1–21
- Tacke MM, Linow S, Geiss S, Hassel EP, Janicka J, Chen JY (1998) Experimental and numerical study of highly diluted turbulent diffusion flame close to blowout. *Proc Combust Inst* 27: 1139–1148
- Thibaut D, Candel S (1998) Numerical study of unsteady turbulent premixed combustion: application to flashback simulation. *Combust Flame* 113: 53–65
- TNF Workshop (2006) International workshop on measurement and computation of nonpre-mixed flames, <http://www.ca.sandia.gov/TNF/abstract.html>
- Upatniaks A, Driscoll JF, Ceccio SL (2002) Cinema particle imaging velocimetry time history of the propagation velocity of the base of a lifted turbulent jet flame. *Proc Combust Inst* 29: 1897–1903
- Veynante D, Vervisch L (1997) Reynolds averaged and large eddy simulation modeling for turbulent combustion. In: Métais O, Ferziger J (eds) *New tools in turbulence modeling*. Springer, Berlin, pp 105–140
- Wäsle J, Winkler A, Sattelmayer T (2005) Spatial coherence of the heat release fluctuations in turbulent jet and swirl flames. *Flow Turbulence Combust* 75: 29–50
- Wang P, Bai X S (2005) Large eddy simulations of turbulent premixed flames using level-set G-equation. *Proc Combust Inst* 30: 583–591
- Wegner B, Maltsev A, Schneider C, Sadiki A, Dreizler A, Janicka J (2004) Assessment of unsteady RANS in predicting swirl flow instability based on LES and experiment. *Heat Fluid Flow* 25: 528–536

# Paper IX



A. OMRANE<sup>1</sup>  
P. PETERSSON<sup>1,✉</sup>  
M. ALDÉN<sup>1</sup>  
M.A. LINNE<sup>2</sup>

## Simultaneous 2D flow velocity and gas temperature measurements using thermographic phosphors

<sup>1</sup> The Division of Combustion Physics, Lund Institute of Technology, P.O. Box 118, 22100 Lund, Sweden

<sup>2</sup> Sandia National Laboratories, P.O. Box 969, Livermore, CA 94551-0969, USA

Received: 7 January 2008/Revised version: 10 April 2008  
Published online: 30 May 2008 • © Springer-Verlag 2008

**ABSTRACT** In this paper a new approach for simultaneous 2D velocity and temperature measurements using phosphoric particles is presented. The phosphoric particles respond to the temperature changes in the flow while acting as tracers for velocity mapping. The temperature sensitive particles were seeded into a heated flow and were excited by a pulsed UV laser. The subsequent red shifted emission was detected and analyzed to infer temperature using calibration procedures for lifetime and emission spectra against temperature. The diameter of the temperature sensitive particles, usually in the range of 1–10  $\mu\text{m}$ , makes them useful for velocity measurements using particle image velocimetry (PIV). As such, simultaneous measurement of temperature and flow velocity of a gaseous flow were performed and presented.

**PACS** 42.62.-b; 47.80.Cb; 47.80.Fg

### 1 Introduction

Temperature is one of the most frequently measured parameters in a wide variety of applications. It impacts the physical, chemical and biological world in numerous ways. Over the last two decades optical diagnostic techniques have emerged as feasible tools for remote and accurate measurements of flow quantities and they have allowed researchers and engineers worldwide to deepen their understanding of fluid dynamics and combustion. In fluid dynamics and combustion, measurement of only one scalar quantity such as temperature or concentration is usually not sufficient. Simultaneous measurement of a scalar quantity and the associated velocity field is valuable for understanding and validating turbulence models [1]. In particular, a correlation between temperature and velocity information would give a direct insight into the turbulent heat flux terms. In combustion applications, characterization of local flame parameters requires conditioning upon the burnt or un-burnt regions across the flame front [2]. With simultaneous temperature and velocity measurements the possibility to produce such conditional information is improved.

Gas thermometry using laser-induced fluorescence is usually based on monitoring the physical characteristics of molecules and/or radicals intrinsic to the flow such as OH and NO or seeded species such as 3-pentanone, acetone and indium atoms e.g., see [3–5]. In this work we present a technique based on seeding the flow with temperature sensitive particles known as thermographic phosphors. The advantage of many of these particles over the previously mentioned techniques is the non-sensitivity to quenching by oxygen or pressure up to 10 bar [6], which makes the technique suitable for thermometry even in harsh environments e.g. in internal combustion engines. Thermographic phosphors are based on the use of temperature sensitive particles doped with rare-earth materials. The micrometer sized particles exhibit high temperature sensitivity from cryogenic temperatures up to 1600 °C. Once excited by suitable UV light, the fluorescence decay lifetime [7, 8] or the intensity ratio [9] between two or several emission lines, assuming thermal equilibrium, can be compared against previous calibration measurements in order to infer the actual temperature. The technique has gained a wide acceptance for surface thermometry during the last two-decades and recently some efforts have been made to further extend the technique for droplets [10] and spray thermometry [11, 12].

For mapping a 2D velocity field with high spatial resolution particle image velocimetry (PIV) is a well-established technique. With the present ultra-high-framing-rate cameras and high-repetition rate lasers PIV systems can also provide a high temporal resolution. PIV tracks groups of particles, “seeded” to the flow, within small regions of the image so called interrogation areas. The cross-correlation between the corresponding interrogation areas in two images separated in time is computed and the displacement is determined from the location of the strongest correlation peak. Thus only one mean velocity vector is produced for each interrogation area. To get a reliable velocity  $\sim 20$  particles per interrogation area are required. Tracer or seeding particles are supposed to accurately follow the motion of the flow. Various seeding materials are available and the choice depends on the fluid properties and flow regime to study [13]. In combustion applications metal oxide powder such as  $\text{TiO}_2$  and  $\text{Al}_2\text{O}_3$  are often used due to high melting points. These powders have a density of 3500–3970  $\text{kg}/\text{m}^3$  and for particles to follow the flow properly the particle size should be  $\sim 1 \mu\text{m}$  or smaller.

✉ Fax: +46-46-222 4542, E-mail: per.petersson@forbrf.lth.se

With a smaller size the light scattering decreases and there is a trade-off between scattering efficiency and how true the particle follows the flow [13].

In this paper a new approach for simultaneous 2D velocity and temperature measurements using phosphoric particles is presented. The phosphoric particles respond to the temperature changes in the flow and also act as tracers for the velocity mapping.

## 2 Experimental set-up

A 300 mm long heated tube with a diameter of 20 mm was used to produce a hot air flow. Two simple flow configurations were used for this proof of concept study – a jet flow and, by mounting a bluff body above the tube exit, a recirculating turbulent flow.

The thermographic phosphor  $\text{Mg}_4\text{FGeO}_6\text{:Mn}$ , in this investigation used both for temperature measurements and as flow tracers, were seeded into the flow using a nebulizer fitted to the bottom of the tube. The particles were dispersed in alcohol and transported by compressed air streaming through the nebulizer creating a fine spray carrying the particles. During the passage through the heated tube the alcohol evaporated and particles and air were heated gradually (to approximately  $400^\circ\text{C}$ ) before exiting into the ambient. The seeding density using this technique was relatively low which limited the data to include only averaged velocity data and temperature of the two flow configurations.

Two separate laser and detector systems were used for the simultaneous velocity (PIV) and temperature measurements, see Fig. 1. The counter-propagating laser beams were formed into overlapping sheets to illuminate a planar region along the centerline of the flow to be investigated. By lowering the heated tube the overlapping sheets could be positioned to image different parts of the flow.

For PIV the beams from two frequency doubled Nd:YAG lasers (Quantel) were overlapped to provide successive Mie scattering images from the phosphoric particles. In the probe volume the light sheets had a height of 45 mm and a thickness of  $\sim 700\ \mu\text{m}$ . The energy in each pulse was set to 40 mJ

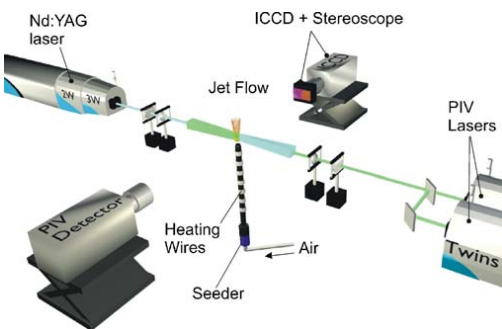


**FIGURE 1** Experimental setup: thermographic phosphors were seeded and carried out with a streaming air flow through a heated tube. The third harmonics of an Nd:YAG laser at 355 nm were used to excite the particles while mie-scattering at 532 was collected from a double pulsed laser system to register the image displacement of the  $\mu\text{m}$  size particles

and the pulse separation was  $\Delta t = 50\ \mu\text{s}$ . For imaging an interline-transfer CCD camera (PCO) was used and the pixel resolution with the field-of-view used in this investigation was  $58\ \mu\text{m}/\text{pixel}$ . For the evaluation of the velocities, a cross-correlation algorithm with an adaptive multipass method developed by LaVision was used.

For temperature measurements the third harmonic generation of an Nd:YAG laser at 355 nm, with a pulse duration of 7 ns and a repetition rate of 10 Hz, was used to excite the particles at the outlet. The thermometry light sheet matched the sheet for the PIV measurements, with a height of 45 mm and a thickness of  $\sim 700\ \mu\text{m}$ . The subsequent phosphorescence emission was detected by an intensified CCD camera (Princeton Instruments IMAX with a Nikon objective lens of 50 mm) together with an imaging stereoscope. The collected emission first passes through separate filters before encountering a  $45^\circ$  mirrors and a prism positioned inside the stereoscope, producing identical images of the same object on corresponding halves of the CCD chip. The reflection curve of the mirror surface shows a constant reflection in the wavelengths range of the incoming phosphorescence. Interference filters (632/657 nm, FWHM = 10 nm) were placed in front of each entrance of the stereoscope in order to detect phosphorescence signals at these wavelengths. After registration of the images, both background measurement and special reference images were needed. For each measurement, the background was subtracted from the signal and the resulting image was digitally divided by a reference image. These flat-field images have thus been corrected for the non-uniformity introduced by the detector, the stereoscope and the optics employed. Then a geometrical manipulation of the images was performed in order to allow for pixel-to-pixel registration. The resulting temperature ratio image was finally inferred from a previously recorded calibration curve.

## 3 Results and discussion

In this proof of concept study only a limited amount of data was collected (50 single shot). This was a large enough sample to produce a converged mean velocity field but not enough to generate a converged temperature field. For the velocity evaluation an interrogation area of  $32 \times 32$  pixels was applied and the seeding density was sufficient (typically 30–40 particles were used in the cross-correlation) for an accurate velocity calculation. However, the seeding density was too low for a pixel resolved temperature evaluation. The sparse seeding resulted in pixel areas with a lack of valid temperature data in the single shot images. A higher seeding density or a larger sample would be required to produce a converged mean temperature field.

In Fig. 2 the simultaneous measurements of temperature and velocity fields of 50 instantaneous samples were averaged and presented. The field-of-view for the simultaneous measurements was approximately  $45 \times 35\ \text{mm}^2$  and measurements were performed at two different heights to produce the data in the figure. At the exit of the nozzle the measured temperature and flow velocities are the highest (in the center: approx. 10 m/s and  $400^\circ\text{C}$ ) and both decrease gradually owing to the entrainment of surrounding ambient air into the jet. It should be noted that the ambient was not seeded and therefore only

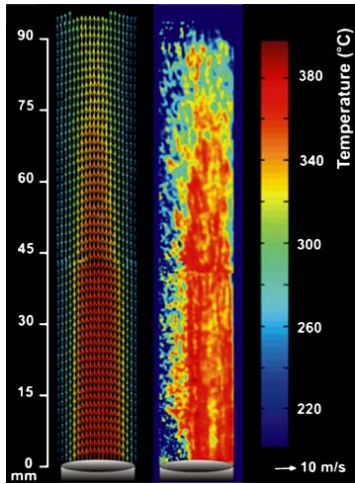


FIGURE 2 The temperature and velocity field in the jet flow, 50 instantaneous images are used to produce the averaged data

the main part of the slowly spreading jet is presented in Fig. 2. Without seeding in the ambient air PIV measurements will in turbulent flows be biased towards high velocity as entrained eddies will not be represented in the measurements. A similar bias effect can be expected to influence the temperature measurements in this case. The asymmetric temperature field is believed to be an effect of non-uniform particle density and/or non uniform heating of the particles during the passage of the pipe.

Also one-point measurements using a temporal decay method were performed. The ICCD camera in the experimental setup was replaced by a photomultiplier. After excitation, the phosphorescence was directed into the PMT and digitized by an oscilloscope (TDS 640). The phosphorescence decay was analyzed and compared against previous calibration data of lifetime versus temperature. The measurements were performed at different heights from the outlet and results from these tests are presented in Fig. 3. The error bars represent the standard deviation of 50 samples. The total error in the measurements was difficult to estimate partly due to a fluctuating temperature due to the simple (no regulation) heating system used.

The technique was also tested on a re-circulating flow with a higher degree of mixing than the previously presented jet flow. A conical bluff body was centered and placed 5 mm above the outlet from the heated tube, creating a flow with a recirculation zone in the centre, see Fig. 4. The flat top surface of the 25 mm cone was situated in the lower part of Fig. 4. The data were produced by averaging 50 instantaneous samples. As can be seen in the figure the flow was not perfectly symmetric and the highest velocities (and mass flow) were found on the right-hand side. This also influences the temperature field with higher maximum temperatures and a larger area with temperatures above 300 °C. In the central recirculation zone areas with lower average temperature than the flow passing outside are found. This could be caused by cooling from

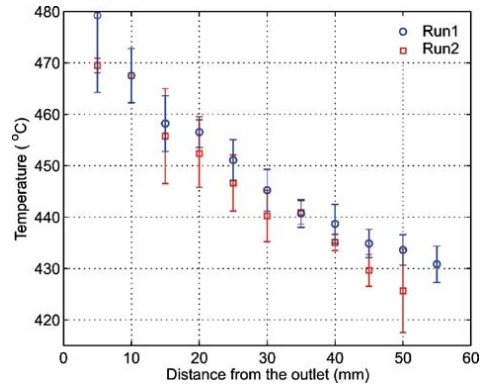


FIGURE 3 Temperature profiles as measured by the temporal method. As the flow progresses from the outlet, ambient air is entrained and the temperature decreases

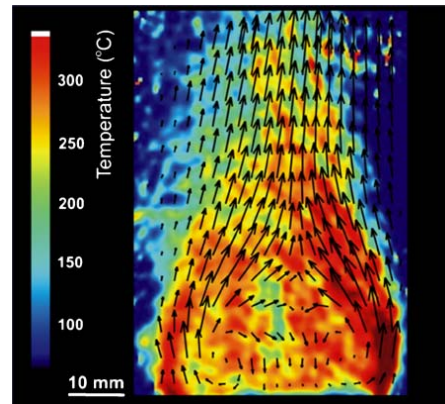


FIGURE 4 Simultaneous measurements of temperature and velocity of the turbulent flow behind a conical bluff body

the metallic bluff body or by entrainment of cooler air into the recirculation zone.

This thermal flow diagnostic relying upon a seed is based on the assumption that the small seed particles should have the same temperature relative to the surrounding medium. However, fundamental investigations of the sensitivity of the particles for various gas-phase measurements are necessary. The authors have addressed this subject, initially by using simple heat transfer calculations based on heat convection from the surrounding flow to a suspended or a free falling particle, and found that particle diameter and density contribute to the measurement sensitivity to temperature change. For example particles having a 1  $\mu\text{m}$  diameter and a density of 2  $\text{g}/\text{cm}^3$  would yield a response time of 10  $\mu\text{s}$  when subjected to a 400 °C step change. Smaller diameters and lower densities generate a shorter response time. For an accurate measurement of both velocity and temperature the particles used should be as small as possible. For metal oxide powders often used for PIV, it is vital that the size is around 1  $\mu\text{m}$  or smaller for the particles to follow rapid fluctuations in a flow

properly [13]. As discussed previously it is also important for both the velocity and temperature measurements that the seeding density is sufficient and that all parts of the flow, e.g. coflow and main flow are seeded uniformly to avoid biasing effects.

It should also be noted that the life time of  $\text{Mg}_4\text{FGeO}_6:\text{Mn}$  in the present temperature range is in the order of 1 ms (see e.g. figure 6 in [6]) which is of the same order as the integral time scales ( $\sim 450 \mu\text{s}$ ) in the investigated flows. With a more sensitive phosphor and with a shorter decay time the temporal resolution and measurement accuracy could have been improved. Very recent experiments in the authors laboratory have revealed “new” thermographic phosphors with much shorter decay times (ns) as well as higher temperature sensitivity. For future temperature/velocity experiments this phosphor is clearly an alternative and probably a better than the one used above,  $\text{Mg}_4\text{FGeO}_6:\text{Mn}$ , for applications in highly turbulent flows [14].

#### 4 Conclusions

Simultaneous measurement of temperature and velocity profiles are presented using thermographic phosphors as temperature sensitive particles for gas thermometry, and for acting as tracer particles for velocity measurements as well. The technique seems to be promising for use in harsh environments such as internal combustion engines where other

optical techniques may encounter difficulties due to the high temperature and pressure.

**ACKNOWLEDGEMENTS** The financial support by the Centre of Excellence in Combustion Science and Technology, CECOST, through the Swedish Foundation for Strategic Research, SSF, and the Swedish Energy Agency, STEM, are gratefully acknowledged.

#### REFERENCES

- 1 H. Hu, M.M. Koochesfahani, “Molecular Tagging Technique for the Simultaneous Measurements of Flow Velocity and Temperature Fields”, *4th AIAA Aerospace Sciences Meeting and Exhibit*, AIAA-2006-0041
- 2 P.A.M. Kalt, Y.-C. Chen, R.W. Bilger, *Combust. Flame* **129**, 401 (2002)
- 3 U.E. Meier, D. Wolff-Gassmann, W. Stricker, *Aerosp. Sci. Technol.* **4**, 403 (2000)
- 4 M.C. Thurber, F. Grisch, B.J. Kirby, M. Votsmeier, R.K. Hanson, *Appl. Opt.* **37**, 4963 (1998)
- 5 C.F. Kaminski, J. Engström, M. Aldén, “Quasi-instantaneous two dimensional measurements in a spark ignition engine using 2-line atomic fluorescence”, *27th Symp. (Int.) on Comb./Combust. Inst.* (1998), pp. 85–93
- 6 J. Brübach, A. Dreizler, J. Janicka, *Meas. Sci. Technol.* **18**, 764 (2007)
- 7 A. Omrane, F. Ossler, M. Aldén, *Proc. Combust. Inst.* **29**, 2653 (2002)
- 8 T. Husberg, A. Omrane, S. Girja, I. Denbratt, J. Engström, M. Aldén, SAE paper, 2005-01-1646
- 9 A. Omrane, G. Juhlin, M. Aldén, G. Jossesfsson, B. Timothy, J. Engström, SAE paper, 2004-01-0609
- 10 A. Omrane, G. Juhlin, F. Ossler, M. Aldén, *Appl. Opt.* **43**, 3523 (2004)
- 11 A. Omrane, G. Särner, M. Aldén, *Appl. Phys. B* **79**, 431 (2004)
- 12 J. Brübach, A. Patt, A. Dreizler, *Appl. Phys. B* **83**, 499 (2006)
- 13 A. Melling, *Meas. Sci. Technol.* **8**, 1406 (1997)
- 14 G. Särner, M. Richter, M. Aldén, unpublished



